Novel silane additive and mixed antisolvent processes for air-fabricated perovskite solar cells with magnetron-sputtered silver contacts

A thesis submitted to Cardiff University in the candidature for the degree

of

Doctor of Philosophy

By

Martin Chinweokwu Eze

School of Engineering

Cardiff University

June 2023

Acknowledgement

I want to thank my supervisors, Prof Gao Min, and Dr Victoria Rocha, for allowing me to pursue PhD research at Cardiff University and for their continuous and immeasurable support at every research stage. I am also grateful for their patience, motivation, and immense knowledge.

I profoundly appreciate the Federal Government of Nigeria's financial support for this PhD research under the Petroleum Technology Development Fund scholarship. This research would have been impossible without this financial support.

I am also very thankful to all my research colleagues for their support during my research, especially at the early stage. Finally, thanks to Dr Alex Evans and Dr Mohammad Alnajideen for offering me world-class training on using DC magnetron, AFM, and I-V characterisation. I also thank Dr Meng Li and Dr Zhe Li for their immense contributions to this research.

I thank Dr D Sapsford and Mr J Rowland for their assistance in XRD and UV-Visible spectroscopy measurements. In addition, I thank Dr E. Brousseau, Guillermo M. Rodriguez and Dr Daniel Zabek for their help in SEM measurements. I am also incredibly grateful to Dr Barbe Jeremy for the training offered at Swansea University at the early stage of my research. Finally, I am also thankful to Marc Walker for the UPS measurement conducted for me at Warwick University.

I want to thank the members of the electrical and mechanical workshops who always helped me repair faulty equipment and manufacture items I designed for my experiments. I especially appreciate Malcolm Seaborne and Andrew Rankmore for their immense support.

I will not forget to thank the Engineering Finance and Research Office members Engineering Finance and Research Office members, especially Aderyn Reid, for their outstanding support in administrative, financial, and procedural matters.

Lastly, I appreciate my wife, parents, and siblings for their moral and spiritual support throughout my PhD research. I am also thankful to my friends who offered their help in diverse ways.

Finally, I thank all those who directly or indirectly played a role in the smooth completion of this research.

Abstract

A systematic investigation was conducted on the effect of sputtering power, argon flow rate, sputtering duration, and argon pressure on the performance of the perovskite solar cells (PSCs) with sputtered silver (Ag) contacts. The results show that PSCs prepared in the air at high relative humidity (RH) achieved a high power conversion efficiency (PCE) of 18.35%. The devices also exhibit an excellent short-current density of 22.56 mA/cm^2, an open-circuit voltage of 1.10 V and a fill factor of 73.7%. Furthermore, this study demonstrates that depositing metal contacts using magnetron sputtering with optimised parameters could be valuable in preparing highly efficient PSCs.

An investigation was also conducted on the effect of a novel chlorodimethyl (pentafluorophenyl)silane (CPFS) additive on the performance of PSCs prepared in the air at high RH. The results reveal that PSCs modified with 3 µl of CPFS additive achieved a PCE of 17.82% compared to 18.07% obtained for control devices. Furthermore, the stability study shows that the devices modified with 3 µl of CPFS additive exhibit degradation in PCE of 23% after 1035 hours of storage, compared to 33% degradation achieved for the control devices. This study proves that PSCs with improved stability could be prepared in the air at high RH using CPFS additive process.

A study was conducted on how treating perovskite films with a mixture of methyl ethanoate and trichloromethane antisolvents affects the PCE and stability of PSCs prepared at high relative humidity. The results show that PCE increased from 17.1% for the devices treated with methyl ethanoate (100%) to 18.6% for those treated with a mixture of methyl ethanoate (70%) and trichloromethane (30%). The stability study shows that the PCE of devices treated with methyl ethanoate (85%) mixed with trichloromethane (15%) degraded by 7% after 552 hours of storage. Conversely, PSCs treated with methyl ethanoate (100%) suffered a PCE degradation of 22% after the same period. This study demonstrates that preparing devices using a suitable mixture of methyl ethanoate and trichloromethane antisolvent improves the PCE and stability of air-fabricated PSCs.

Table of Contents

List of Figures

List of Tables

List of Abbreviations

Abbr.	Meaning	Abbr.	Meaning
AFM	Atomic force microscope	MET	Methyl ethanoate
AM	Air mass	MAI	Methylammonium iodide
ASTM	American Society for Testing and Materials	$MAPbI_3$	Methylammonium lead iodide
CBZ	chlorobenzene	PbI_2	Lead iodide
CB	Conduction band minimum	PSCs	Perovskite solar cells
TCM	Trichloromethane	RH	Relative humidity
CPFS	Chlorodimethyl (pentafluorophenyl)silane	RMS	Root-mead square
DMM	Dimethyl methanamide	$SnCl_2.2H_2O$	Tin (II) chloride dihydrate
DMSO	Dimethyl sulphur (IV) oxide	SnO_2	Tin (IV) oxide
IS	Impedance spectroscopy	Spiro-OMETAD	2,2′,7,7′-tetrakis(N, N-di-p-methoxyphenyl-amine)9,9′-spirobifluorene
ETL	Electron transport layer	UPS	Ultraviolet photoelectron spectroscopy
SEM	Scanning electron microscope	XRD	x-ray diffraction

FK209	tris(2-(1H-pyrazol-1-yl)-2-methylpropan-4-yl pyridine) cobalt (III) tris(bis(trifluoromethylsulfonyl) amine)	MPPD	2-methyl propan-4-yl pyridine
FTO	Fluorine-doped tin oxide	TCO	Transparent conducting oxide
FTIR	Fourier Transform infrared	TCFPS	Trichloro(3,3,3-trifluoropropyl)silane
GHG	Greenhouse gas	TF	Thin film
HTL	Hole transport layer	MBZ	Methylbenzene
Li-TFSI	Lithium bis(trifluoromethanesulfonyl) amine	TiO2	Titanium (IV) oxide
VB	Valence band		
R_{dc_f}	Equivalent dc resistance of the solar cell when the diode is forward-biased		
R_{dc_r}	Equivalent dc resistance of the solar cell when the diode is reverse-biased		

List of Symbols

Symbol	Meaning	Symbol	Meaning
A	Device active area	R_p	Shunt resistance
C_r	Chemical capacitance	T_x	Transmittance
d	Film thickness	T	Temperature
D	Diffusion coefficient	V	Voltage
e	Electron charge	V_{bi}	Barrier voltage
E	Light energy	E_{loss}	Mismatch loss
E_g	Energy bandgap	V_{oc}	Open-circuit voltage
E_{max}	Energy emission onset	WF	Work function
EQE	External quantum efficiency	z	Grain size
FF	Fill factor	$Z(\omega)$	Impedance
I	Current	θ_s	Sun angle
J	Current density	2θ	Diffraction angle
J_{sc}	Short-circuit current density	χ	Extinction coefficient
J_m	Current density at the maximum PowerPoint	α	Absorption coefficient
J_o	Diode saturation current	τ	carrier lifetime
J_{ph}	Photocurrent density	μ	Carrier mobility
k_B	Boltzmann constant	ε_r	Dielectric constant
L	Carrier diffusion length	ϕ	Photon flux
P_{in}	Incident light irradiance	β	Full-Width Half Maximum
P_m	Power at the maximum PowerPoint	ρ	Grain shape constant
PCE	Power conversion efficiency	$\Delta VB_{i\text{-}p}$	VB mismatch at i-p
R	Load resistance	$\Delta CB_{n\text{-}i}$	CB mismatch at n-i
R_s	Series resistance		

Chapter 1: Introduction

1.1. Background

Carbon dioxide emission from fossil fuels (Coal, Liquid fuels, Natural gas etc.) is a central cause of global warming and the greenhouse gas (GHG) effect [1]. Since 1900, global warming and GHG effects have worsened as carbon dioxide emission has increased exponentially. In 2019, the International Energy Agency (IEA) reported 33 gigatonnes (Gt) of global energy-related emissions [2]. The increase in global warming and other associated disasters resulted in the United Nations (UN)-led 2015 Paris Agreement aimed at reducing global warming by cutting GHG emissions [3]. A reliable method of reducing GHG emissions is through partial or total replacement of fossil fuel technologies (coal plants, gas plants, diesel plants, automobile engines etc.) with clean energy technologies (wind energy, hydro energy, solar energy etc.) [4]. Among all the clean energy sources, energy from the sun is the most readily available, cost-effective and easily convertible.

The most cost-effective and efficient method for harvesting energy from the sun is using solar cell technologies, which are cost-effective and have excellent power conversion efficiency (PCE). The development of solar cells started with the production of single-junction crystalline silicon (c-Si) solar cells with a PCE of 6% in 1954 by Chapin et al. [5]. Consequently, Yoshikawa et al. reported a PCE of 26.7% for a single-junction c-Si solar cell in 2017 [6]. The abundance, high stability, and non-toxicity of the c-Si have made the material indispensable in solar cell industries. Over the years, the cost/kWh of c-Si solar cells has decreased significantly due to massive research and development (R&D) investment and technology maturity of the c-Si technology [7]. Hence, PV magazine reported a cost of 0.32/Wp in 2019 [8], whereas PVinsights reported 0.155/Wp in 2022 [9] for monocrystalline silicon photovoltaic systems.

Despite the low cost-per-watt of c-Si solar cells, there is ongoing research to develop alternative solar cell technologies. Examples of alternative solar cell technologies are gallium arsenide, indium phosphide, copper indium gallium selenide, gallium indium phosphide, organic, quantum dot and perovskite solar cells [10]. Most alternative solar cell technologies use ultra-thin film (≤1000nm) photovoltaic materials deposited on supporting substrates to generate charge carriers from incident photon energy [11,12]. One of the most efficient alternative solar cell technologies is GaAs, and an efficiency of

29.1% was reported for single-junction GaAs solar cells in 2020 [13]. However, toxicity, scarcity and high cost have limited the applications of gallium arsenide in solar cell technology.

One of the most promising solar cell technologies is perovskite solar cells (PSCs) which contain perovskite as the active element. Perovskite has a generic chemical formula of ABX_3, where A represents monocations (e.g. methyl ammonium ion), B represents dications (e.g. lead ion), and X represents monoanions (e.g. iodide ion) [14]. The high absorption coefficient, excellent carrier properties, high dielectric constant, tunable and near-optimum energy bandgap (1.48 – 1.6 eV), the abundance of materials and low-cost fabrication processes have attracted research interest in PSCs [15–17]. An energy bandgap (E_g) is an energy gap between the valence band (VB) and conduction band (CB), where no electronic states exist. E_g indicates the minimum energy that is required to excite an electron from the valence band to the conduction band. The E_g of perovskite materials could be tuned by changing perovskite composition.

The high absorption coefficient (absorbance per unit material thickness) of perovskite materials enables an ultra-thin film (thickness ≤ 500nm) to absorb nearly all the incident photons with energy (E) ≥ E_g [18]. Similarly, the low cost of materials for PSCs has significantly reduced the overall cost of the technology. Also, the adaptability of the technology to solution-processing and low-temperature treatment allows the use of low-cost fabrication equipment like spin-coating and hotplates (for heat treatment) for solar cell development. Thus, combining thin-film requirements, low cost of materials, and fabrication processes arguably made PSCs one of the most economically viable solar cell technologies [19,20].

Also, excellent carrier properties of perovskite materials, such as long carrier lifetime, diffusion length, and fast carrier mobility and diffusion coefficient, ensure efficient charge carrier extraction [21]. While tunable and near-optimum E_g also guarantees efficient light energy utilisation and carrier extraction [22]. The combination of excellent carrier properties, tunable and near-optimum E_g of perovskite materials has improved PCE from 3.8% in 2009 [23] to 25.2% in 2021 [24].

Despite the numerous advantages of PSCs, the instability caused by moisture and the high cost of facilities for inert fabrication negatively affect the viability of PSC technology [14,25–32]. Hence, air fabrication is a promising method of eliminating the cost of inert

facilities and minimising the overall cost of PSCs. However, air-fabricated PSCs have low efficiency and poor instability as perovskite materials are moisture-sensitive. They quickly decompose at high relative humidity because of the weak intermolecular bonds in the materials [33]. Furthermore, light accelerates the degradation of perovskite materials caused by moisture. Consequently, developing techniques for improving the efficiency and stability of air-fabricated PSCs is crucial to improving the commercial prospect of the technology.

Reports have shown that humidity-resistant antisolvent, additive, and passivation techniques can enhance the efficiency and stability of PSCs prepared in ambient air [14,25–32,34–37].

Humidity-resistant antisolvents protect sensitive perovskite/dimethyl sulphur (IV) oxide (DMSO) adducts from moisture interference during air fabrication. High water solubility and vapour pressure of humidity-resistant antisolvents make them effective in protecting $MAPbI_3$/DMSO adduct from moisture during spin-coating of perovskite films, particularly at high relative humidity [34,37,38]. Mixing an antisolvent with a high dipole moment and another with a low dipole maximises the effectiveness of humidity-resistant antisolvents [35]. The mixed antisolvent process minimises the removal of DMSO from $MAPbI_3$/DMSO adducts while retaining the antisolvent's moisture protection. Hence, the mixed antisolvent approach enhances film quality and crystal packing, minimises moisture penetration into the films, and enhances the PCE and stability of air-fabricated PSCs [34,37–39].

A few researchers have employed non-silane additives like $Pb(SCN)_2$ [40–42] and silane additives such as decaphenyl cyclopentasilane [43,44] in enhancing the PCE and stability of air-fabricated PSCs [26,40–50]. This method involves adding the additive material in the perovskite solutions before deposition. Additives strengthen the intermolecular bonds in perovskite film, making films more resistant to moisture decomposition [51,52]. In addition, additives with silyl and fluoride groups also form strong crosslinking bonds with perovskite materials, thereby minimising the deterioration of perovskite films in the presence of moisture [53].

Surface passivation is another method of improving the efficiency and stability of air-fabricated PSCs. Passivation involves depositing a thin layer of passivating materials on top of perovskite films to fill some pinholes and grain boundaries, thereby protecting the

surface from moisture ingress. In addition, the technique reduces perovskite/HTL interface defects that act as moisture entry points and charge traps, which play a severe role in PSCs' performance degradation at ambient conditions [54].

Reports have shown that non-silane materials like iodopentafluorobenzene, methyl ammonium bromide and ethylammonium chloride effectively passivate perovskite layers [42,55,56]. In addition, silane materials such as trichloro(octyl)silane and trichloro(3,3,3-trifluoropropyl)silane have also demonstrated their effectiveness in passivating perovskites layers [51,52,57].

Besides improving the stability of PSCs, reproducibility is also a critical factor affecting the technology's commercial prospects. The metal contact deposition process enhances perovskite solar cells' reproducibility. Magnetron sputtering (MS) is a viable method of depositing metal contacts to achieve reproducible and scalable PSCs. MS has the advantages of improved film adhesion, precise deposition parameter control, scalability and, consequently, superior metal contact morphology over thermal evaporation [58–61].

Currently, the PCE and stability of the perovskite solar cells fabricated in the air are not as good as those manufactured in an inert atmosphere. Also, the metal electrodes of most PSCs are fabricated using thermal evaporation. The method for preparing the metal electrodes of PSCs using magnetron sputtering is not widely employed, and the PCE achieved using the technique is relatively low based on limited reports [58,61–66]

1.2. Motivation

This study is motivated by the desire to develop new processes for preparing more stable and efficient PSCs in the air at high relative humidity. This research focuses on developing approaches for perovskite solar cell preparation in the air at high humidity because air fabrication benefits future low-cost, large-scale, and commercial production.

1.3. Objectives

The objectives of this study include the following:

- To establish the suitable process, optimal solution parameters, and antisolvent treatment for preparing perovskite solar cells in ambient air.
- To determine the optimal magnetron sputtering parameters for depositing silver contacts on the perovskite solar cells.

- To determine the optimum volume of chlorodimethyl(pentafluorophenyl)silane additive for preparing perovskite solar cells with improved stability in ambient air.
- To establish an optimal mixture of methyl ethanoate and trichloromethane antisolvents for preparing perovskite solar cells in ambient air.

1.4. Thesis structure

This thesis describes a detailed experimental investigation of novel silane additive and mixed antisolvent processes for air-fabricated perovskite solar cells with magnetron-sputtered silver contacts. It comprises eight chapters and adopts the International Union of Pure and Applied Chemistry (IUPAC) nomenclature for all the chemicals used in this study. This subsection summarises the purpose of each chapter as follows:

Chapter 1

Chapter 1 introduces the background and motivation for the research. It also presents the research's key objectives and the thesis's structure.

Chapter 2

Chapter 2 presents an extensive literature review on solar energy conversion. It summarised the fundamentals and principles of operation of solar cells, solar cell equivalent circuits, photovoltaic parameters and factors that affect the performance of solar cells. It also elaborates on perovskite solar cells (PSCs) and structures, energy band matching, thin-film deposition methods and the characterisation of films and PSCs. The review finally focuses on recent progress in metal contact deposition using magnetron sputtering, silane additive process and mixed antisolvent treatment.

Chapter 3

Chapter 3 describes the experimental techniques and processes developed and applied for preparing and characterising perovskite solar cells in this project. It also provides detailed descriptions of the facilities employed for the films and solar cells characterisation with the testing results to demonstrate the reliability of the equipment. Materials, their sources, and percentage purity are provided in this chapter to allow for a reproduction of the experiments.

Chapter 4

Chapter 4 presents the preliminary studies that guided the initial trial of methods and procedures for preparing efficient perovskite solar cells in the air at Cardiff University. The chapter describes the effect of depositing Ag contact at very high and low sputtering power on the performance of perovskite solar cells prepared at high relative humidity. The chapter also comparatively investigated the impact of FTO (TEC-8) and FTO (TEC-15) on the performance of devices. The studies also presented results from calibrating the hotplate used for the annealing process. Finally, this chapter also shows the impact of Petri dish-controlled annealing of SnO_2 and $MAPbI_3$ films on the performance of PSCs.

Chapter 5

Chapter 5 describes a systematic experimental investigation of the effect of solution parameters on the performance of perovskite solar cells. It includes the impact of tin (II) chloride dihydrate ($SnCl_2.2H_2O$) concentration on the properties of the prepared tin (IV) oxide (SnO2) films and PSCs, the influence of methyl ammonium lead iodide ($MAPbI_3$) concentration on the properties of $MAPbI_3$ films and the photovoltaic performance of PSCs, the impact of the amount of tris(2-(1H-pyrazol-1-yl)- 2-methylpropan-4-yl pyridine) cobalt (III) tris(bis(trifluoromethylsulfonyl) amine) (FK209) additive incorporated in Spiro-OMETAD solution on the properties of Spiro-OMETAD films, and the performance of the prepared devices. The chapter also provides a detailed discussion of the results and a summary of the developed optimal parameters for preparing SnO_2, $MAPbI_3$ and Spiro-OMETAD films and perovskite solar cells.

Chapter 6

Chapter 6 describes the experimental efforts to determine the optimum sputtering parameters for preparing high-quality silver contact for efficient perovskite solar cells. The investigation includes the effect of sputtering power, argon flow rate, sputtering duration, and argon pressure on the photovoltaic characteristics of PSCs and the impact of these sputtering parameters on the properties of silver films. It also presented a detailed description of the results and a summary of the optimal magnetron sputtering parameter for Ag contacts deposition for efficient PSCs.

Chapter 7

Chapter 7 describes a novel attempt to use the chlorodimethyl(pentafluorophenyl) silane (CPFS) additive to improve the stability of perovskite solar cells prepared in the air at high relative humidity. It presented the methods for preparing the MAPbI films and devices in the study, the physical properties of MAPbI films, and the photovoltaic performance and stability of the devices. This chapter established the optimal volume of CPFS additive required to achieve good stability.

Chapter 8

Chapter 8 describes the suitable antisolvent treatment for preparing perovskite solar cells with improved efficiency and stability. It also investigated the impact of chlorobenzene, trichloromethane, methyl ethanoate and methylbenzene on the performance of PSCs and the properties of $MAPbI_3$ films. Furthermore, the research demonstrates the benefit of mixing methyl ethanoate and trichloromethane antisolvents on the stability and efficiency of PSCs.

Chapter 9

Chapter 9 summarises the main findings and conclusions of this research. It also provides recommendations for future work to explore.

Chapter 2: Literature Review

2.1. Introduction

This chapter begins with a brief introduction to the fundamental aspects of solar cell operation and the key factors affecting their performances, followed by a comprehensive review of perovskite solar cells (PSCs) technology, the research topic of this project. It also elaborates moisture degradation routes of perovskite solar cells and the mitigation procedures. Finally, the review focuses on the recent progress in developing high performance perovskite solar cells in air, including PSC structures, energy band structure, energy band matching, thin-film deposition methods, films, and characterisation methods.

2.2. Fundamentals of solar cells

Among clean energy technologies, solar energy technology is the most promising as the average energy of 3,400,000 exajoule (EJ) reaches the earth's surface yearly from the sun [67]. This energy is much more than the annual global energy consumption projected by Statista from 2005 to 2040, as shown in Table 2.1 [68].

Table 2.1: Projected global energy consumption from 2005 to 2040 [68]

	Energy consumption (EJ)					
Year	Hydro	Nuclear	Renewable	Natural gas	Oil	Coal
2005	28	27	4	99	169	130
2010	32	26	10	114	173	151
2015	35	23	18	125	184	158
2018	38	24	27	138	190	158
2025	43	26	48	154	191	155
2030	46	27	70	166	190	149
2035	47	28	89	175	187	145
2040	49	29	114	180	182	138

The abundance, ease of harvesting and environmental friendliness of solar energy have led to the development of cost-effective and efficient solar cell technologies [69]. Solar cells convert photon energy (E) to electrical energy via the photovoltaic effect, first observed by French Physicist Edmund Becquerel in 1839 [70–72]. Photovoltaic materials

sandwiched between the electrodes perform energy conversion in solar cells. Photovoltaic materials are semiconductors with an energy bandgap (E_g) that allow a substantial number of incident photons with energy $E \geqslant E_g$ to excite electrons from the valence band (VB) to the conduction band (CB) [22]. When electrons (negative charge) are excited from VB to the CB, holes (positive charges) are left on the VB, resulting in electron-hole pairs [22]. Electrons are excited to CB when $E \geqslant E_g$ for direct bandgap materials (e.g. perovskite) and $E > E_g$ for indirect bandgap materials (e.g. silicon) [22,73,74]. Figure 2.1 demonstrates the excitation of electrons and the creation of electron-hole pairs in photovoltaic materials. External quantum efficiency (EQE) represents the photon-electron conversion efficiency of materials. Equation (2.1) expresses EQE, the ratio of the number of electrons collected to the number of incident photons on solar cells. EQE is easier to determine than internal quantum efficiency (IQE), which represents the ratio of the number of electrons collected to the number of photons absorbed by the solar cell [75]. IQE determination is challenging because it is difficult to determine the number of photons absorbed by a material accurately.

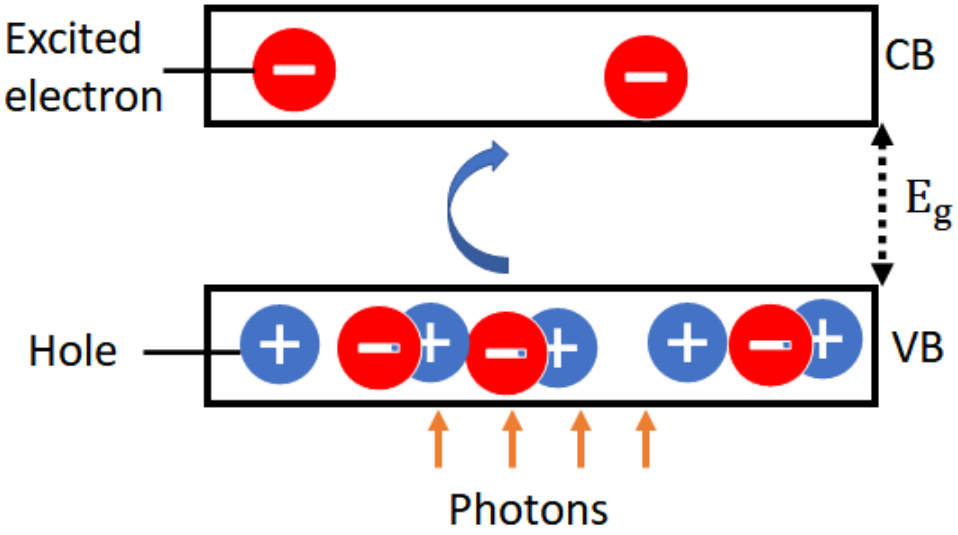

Figure 2.1: Electron-hole pair generation in photovoltaic materials

$$\text{EQE} = \frac{\text{Numer of collected electrons/second}}{\text{Number of incident Photons/second}} \qquad (2.1)$$

Efficient photovoltaic materials operate within a 380 nm-1100 nm wavelength range, as most electromagnetic spectra are within this region, according to the American Society for Testing and Materials (ASTM) [76–78]. Figure 2.2 shows the spectra distribution of

the electromagnetic spectrum. The Air mass zero (AM0) spectrum represents the spectrum in space where there is a negligible amount of air molecules and consequently low spectrum absorption (due to O_3). Air mass 1.5 (AM1.5) global spectrum describes the total solar irradiance that reaches the earth's surface (sea level) from the sun on a clear day when the sun is about 48.2° from the zenith (vertical) [79]. It has an integrated power density of 1000 W/m^2 and represents standard reference irradiance for testing flat solar photovoltaics in the laboratory. The AM1.5 direct spectrum refers to solar irradiance that reaches the earth's surface (sea level) from the sun's disk on a clear day when the sun is about 48.2° from the zenith [79]. It has an integrated power density of 900 W/m^2 and is the standard reference irradiance for testing concentrated solar photovoltaics. The AM1.5 spectrums in Figure 2.1 have deeps due to selective absorption by atmospheric gas (O_2, CO_2 and H_2O) as the spectrum travels through the atmosphere [72].

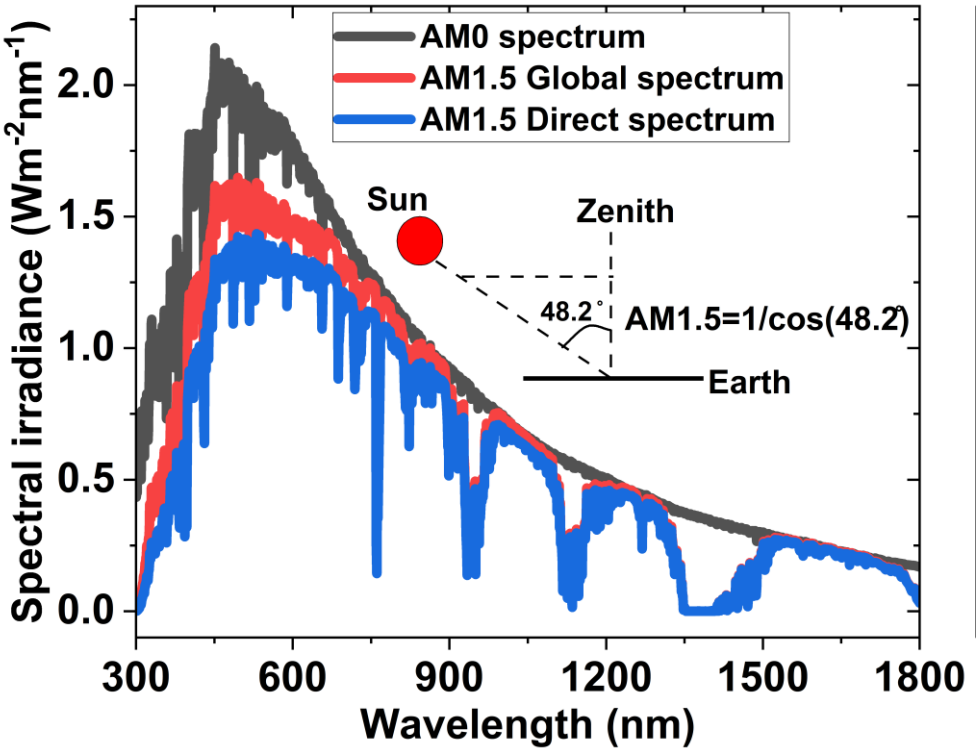

Figure 2.2: ASTM G173-03 reference spectral derived from SMARTS v.2.9.2 [80]

2.2.3. Operation of solar cells

Solar cells are specialised diodes that convert photon energy (E) to electrical energy (direct current) via the photovoltaic effect. Solar cells' photovoltaic materials (e.g., organic and perovskite) generate electron-hole pairs when electrons are excited from the VB to the CB. The n-type and p-type in the junctions facilitate the separation of electron-hole pairs and charge collection [81]. In perovskite solar cells, perovskite acts as an i-type material. However, experiments have shown that the Fermi level of perovskite has an offset of 0.23 eV from the CB and an offset of 1.35 eV from the VB, suggesting that it is probably not intrinsic material [82]. Intrinsic material has equal numbers of electron and hole carriers, and the Fermi level is mid-way between the VB and CB. The n-type materials have electrons as the majority carriers, while p-type materials have holes as the majority carriers. Junctions provide the electric field that separates the electron-hole pairs generated in i-type material and causes the movement of electrons to the n-type side and the holes to the p-type side, as shown in Figure 2.3 [22,71,83,84]

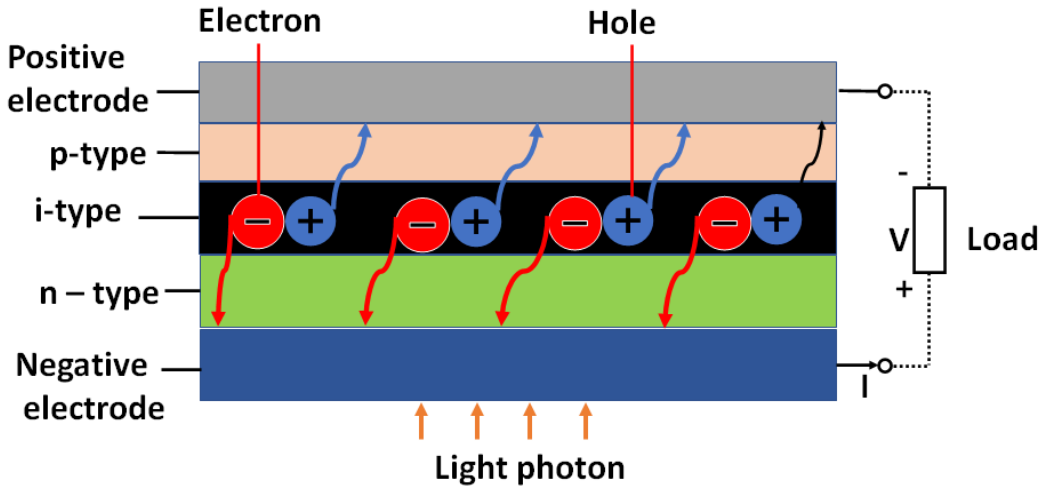

Figure 2.3: Basic operation of perovskite solar cells

The movement of these charge carriers results in the development of photocurrent (I_{ph}), the maximum electric current generated by solar cells when exposed to light irradiance. I_{ph} increases with an increase in incident irradiance as photovoltaic materials generate more charge carriers when the intensity (number) of incident photons with $E \geq E_g$ is

increased [85]. However, a fraction of I_{ph} is supplied as load current (I) to the load (R), while the rest is lost as leakage current through the diode and shunt resistance (R_p) of the solar cells [86]. Similarly, the voltage drop across the series resistance (R_s) reduces the voltage (V) developed across R.

To facilitate direct comparison among solar cells that have different active areas (A), the current density (J), defined by equation (2.2), is employed, which represents the current generated by a solar cell of a unit area [87].

$$J = \frac{I}{A} \qquad (2.2)$$

2.2.4. Equivalent electrical circuits of solar cells

The equivalent circuit of solar cells is a representation of solar cells using electrical circuits and discrete electrical components. It consists of R_p in parallel with the diode, a current source (charge generator) and $R_{s,}$ which is in series with the load (R).

The R_s represents losses due to the interface resistances, the resistance of the electrodes, and connecting wires and causes the loss in load voltage (V). Conversely, R_p relates to various recombination losses inside a solar cell and reduces the load current due to leakages [88]. In solar cells, large R_p relates to low recombination and reduced loss in load current, while low R_s indicate a decrease in the loss of load voltage [89–91]. Figure 2.4(a) presents a single-diode model of a solar cell connected to a load [92]. Equation (2.3) shows the expression for the current density (J) through R, where J_D represents the current density leakage via the diode, and J_p is the current density leakage through the R_p [22,87,93]. However, J_D exists when the diode is forward-biased.

$$J = J_{ph} - J_D - J_p \qquad (2.3)$$

Figure 2.4(b) shows the Thevenin equivalent of a single-diode model of solar cells under dc conditions [94], where R_j represents the dc resistance of the diode junction. Typical solar cells have $R_j \ll R_p$ when the diode is forward-biased and $R_j \gg R_p$ when the diode is reverse-biased.

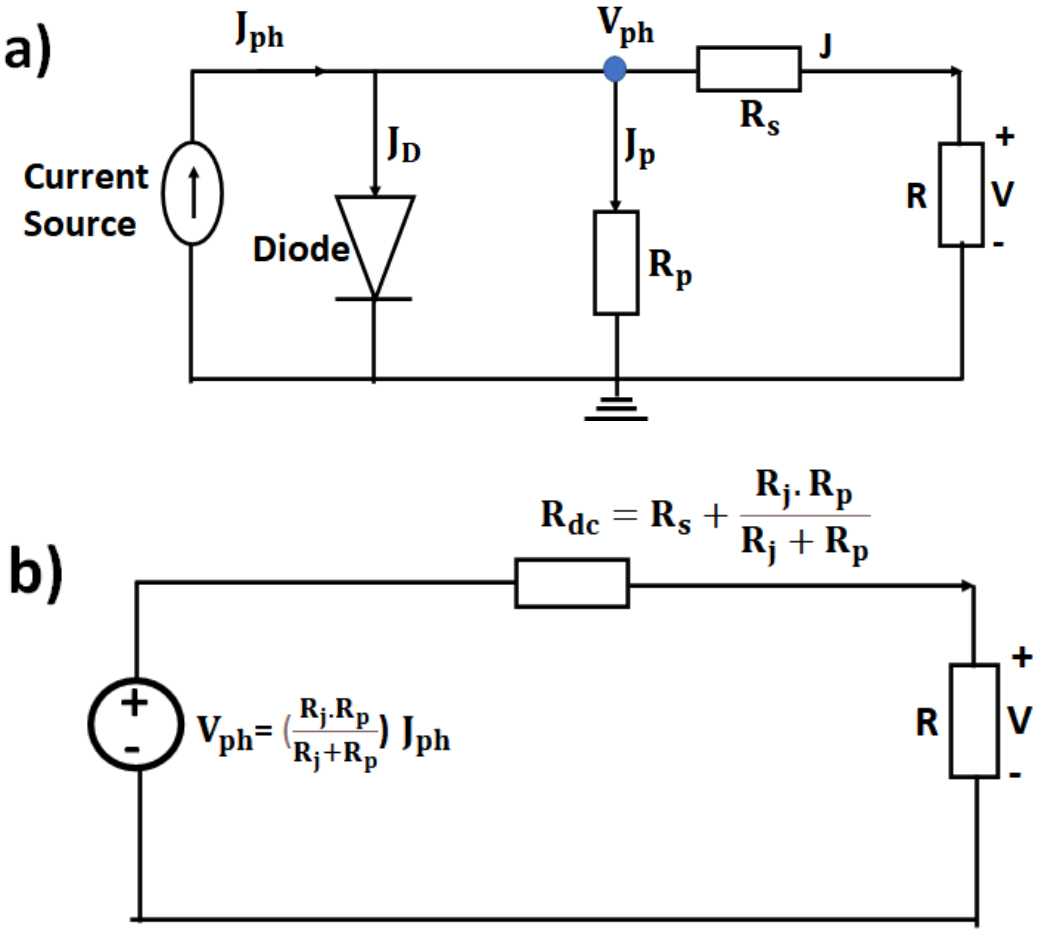

Figure 2.4: (a) A single-diode model of solar cells and (b) Thevenin equivalent circuit of the single-diode model [94].

2.3. Performance characteristics of solar cells

The key performance characteristics of solar cells are open-circuit voltage (V_{oc}), short-circuit current density (J_{sc}) and fill factor (FF). The current density at maximum power point (J_m), the voltage at maximum power point (V_m), maximum power (P_m), R_s, R_p, junction resistance (R_j) and junction capacitance (C_j) of solar cells also impact performance. Subsections 2.3.1 to 2.3.9 review these performance characteristics of solar cells. Figure 2.5 presents a J-V curve of a typical perovskite solar cell with some performance parameters. R_{dc_r} and R_{dc_f} represent the dc equivalent resistances of the solar cell when the diode in Figure 2.4(a) is reverse and forward biased respectively.

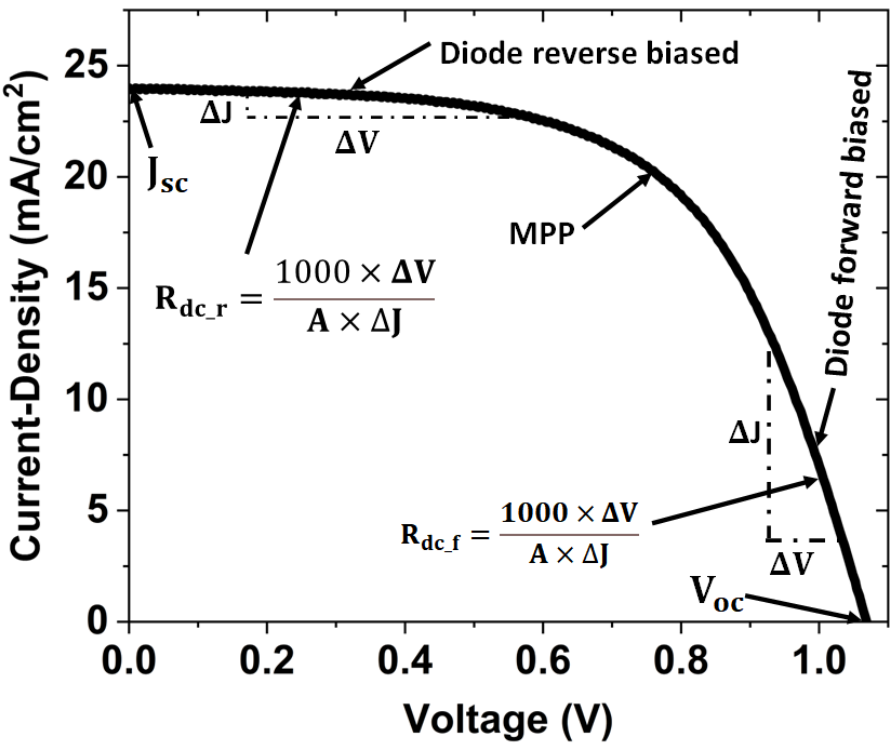

Figure 2.5: J-V curve of a typical perovskite solar cell, showing the key features of the J-V curve of solar cells.

2.3.1. Open-circuit voltage

V_{oc} is a crucial factor that affects the performance of solar cells. It is the voltage across the output of the solar cells in an open-circuit condition (J = 0). Figure 2.6 shows a single-diode model of a solar cell in an open-circuit state. Equation (2.4) is the expression of V_{oc} derived from a single-diode model at an open circuit [95].

$$V_{oc} = R_p(I_{ph} - I_D) \qquad (2.4)$$

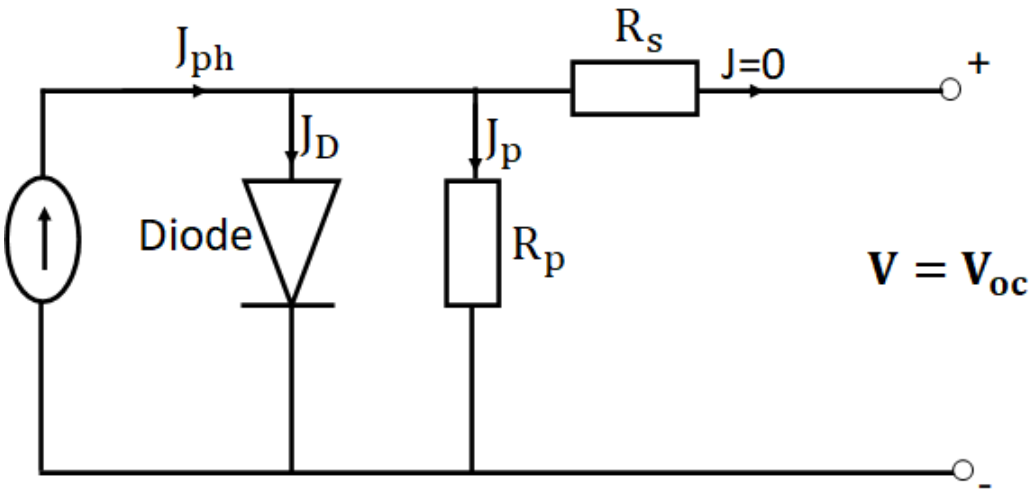

Figure 2.6: Single diode model of a solar cell in open circuit condition

The V_{oc} can be measured experimentally using a source measure unit (SMU) and a solar simulator. SMU is electronic equipment that can generate current/voltage and simultaneously measure them accurately [96]. V_{oc} represents the point where the curve crosses the V-axis in J-V curves. The V_{oc} of a solar cell depends on the energy band mismatch, film morphology, R_p and the work function of the electrodes [22,73,97–100]. For example, poor film morphology results in low V_{oc} due to short-circuiting (low R_p). In addition, the energy losses due to mismatch also decrease the V_{oc} [101].

2.3.2. Short-circuit current density

Short-circuit current density (J_{sc}) is the current density measured at the output of a solar cell when the terminals are shorted (R = 0 and V =0). Experimentally, the J_{sc} of a solar cell can be measured directly using an SMU in conjunction with solar simulators. J_{sc} represents the maximum current density a solar cell can supply and is the intercept on the J-axis of a J-V curve. Figure 2.7 presents a single-diode model of a solar cell in short-circuit conditions.

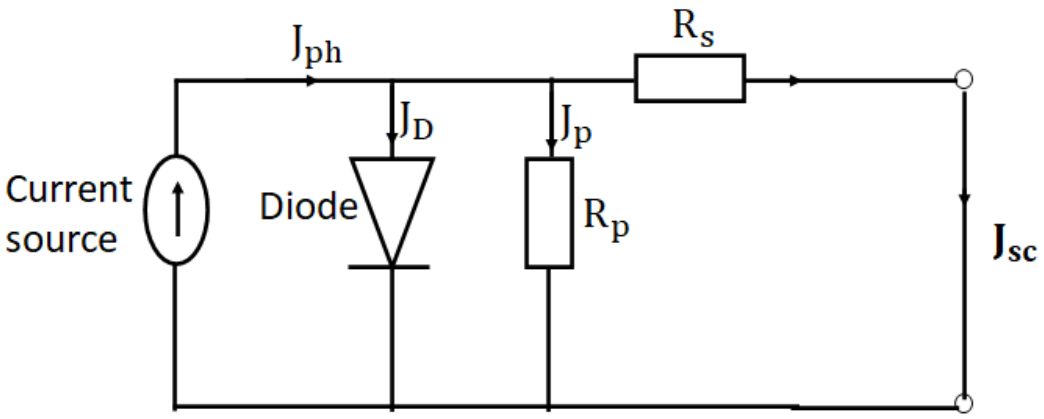

Figure 2.7: Single diode model of solar cell in short-circuit state [95]

$$J_{sc} = \frac{R_p}{R_p + R_s}(I_{ph} - I_D) \qquad (2.5)$$

Equation (2.5) presents the expression for J_{sc} derived from Figure 2.7. J_{sc} depends on the incident photons, the absorption coefficient of photovoltaic materials, diode current, R_s and the R_p of the solar cell [102]. It depends on the incident photons and the absorption coefficient of materials because more electron-hole pairs are generated when the intensity of incident photons with $E \geq E_g$ and the absorption coefficient of photovoltaic material increases. Low R_s and large R_p support efficient current flow through the load.

2.3.3. Maximum power point

Maximum power point (MPP) is a point on the J-V curve where the solar cell transfers maximum power to the load. It corresponds to a point along the J-V curve where the impedance of solar cells closely matches the load impedance [95].

2.3.4. Voltage at the maximum power point

The voltage at the maximum power point (V_m) is the output voltage of the solar cell at MPP.

2.3.5. Current density at the maximum power point

The current density at the maximum power point (J_m) is the current density supplied to the load at MPP.

2.3.6. Maximum power density

Maximum power density (P_m) is the power density transferred to the load at MPP. It is the maximum power delivered to a load by a solar cell of a unit area. Equation (2.6) gives the expression for calculating P_m from the experimental data using V_{oc}, J_{sc} and FF.

$$P_m = V_{oc}.J_{sc}.FF \qquad (2.6)$$

2.3.7. Fill factor

The fill factor (FF) is an important parameter that indicates the quality of solar cells [103]. It is a measure of how closely the maximum power output (P_m) of a real solar cell matches the maximum power output (V_{oc}. J_{sc}) of an ideal solar cell [93]. Furthermore, FF is affected by resistive and recombination losses [104,105]. Equation (2.7) shows the expression for calculating the FF from experimental data.

$$FF = \frac{P_m}{V_{oc}.J_{sc}} \quad (2.7)$$

2.3.8. Series and shunt resistance

Resistance represents the opposition to the flow of electric current in electrical circuits. Series resistance (R_s) and shunt resistance (R_p) represent resistive and recombination losses in solar cells. A large R_s indicates a significant power consumption inside the solar cell, leading to less power delivered to the load. A small R_p represents a significant current loss due to recombination internally, resulting in a smaller current delivered to the load. Therefore, it is desirable to have a small R_s and large R_p for an efficient solar cell [89–91,106].

2.3.9. Power conversion efficiency

Power conversion efficiency (PCE) is the maximum power density (P_m) supplied to a load by a solar cell divided by the incident solar irradiance (P_{in}) [107–109]. The PCE is also a function of solar cells' FF, V_{oc} and J_{sc}. For standardization, I-V measurement of solar cells is conducted at incident solar irradiance of 1000 W/m^2 (AM1.5 global spectrum) [22]. Equation (2.8) presents the expression for calculating PCE from measured photovoltaic parameters.

$$\text{PCE} = \frac{P_m}{P_{in}} \times 100 \qquad (2.8)$$

2.4. Factors that affect the performance of solar cells

The performance of solar cells depends on photon absorption characteristics, carrier transport properties, charge carrier separation, energy bandgap, energy band alignment, R_s, and R_p. These factors are discussed in detail in subsections 2.4.1 to 2.3.5.

2.4.1. Energy bandgap of photovoltaic materials

The Energy bandgap (E_g) of photovoltaic materials is a crucial factor that influences the performance of solar cells because of Shockley-Queisser's limitation. Shockley-Queisser limit is the maximum theoretical efficiency of single-junction solar cells illuminated by a black body with a surface temperature (T_s) of 6000K when the only loss mechanism is radiative recombination [73]. Radiative recombination is the emission of photons by electrons when they transition from the CB to the VB [110]. Every material radiates photons via the black-body radiation effect when its temperature is above absolute zero (0K or -273°C). Equation (2.9) presents the expression for the Shockley-Queisser limit (PCE_{limit}) for solar cells (2.10) [111]. The Shockley-Queisser limit model assumes that every photon with $E \geq E_g$ generates an electron-hole pair [111].

$$\text{PCE}_{\text{limit}} = \frac{\text{Absorbed photon/s} - \text{Radiated photon/s}}{\text{Incident photon/s}} \qquad (2.9)$$

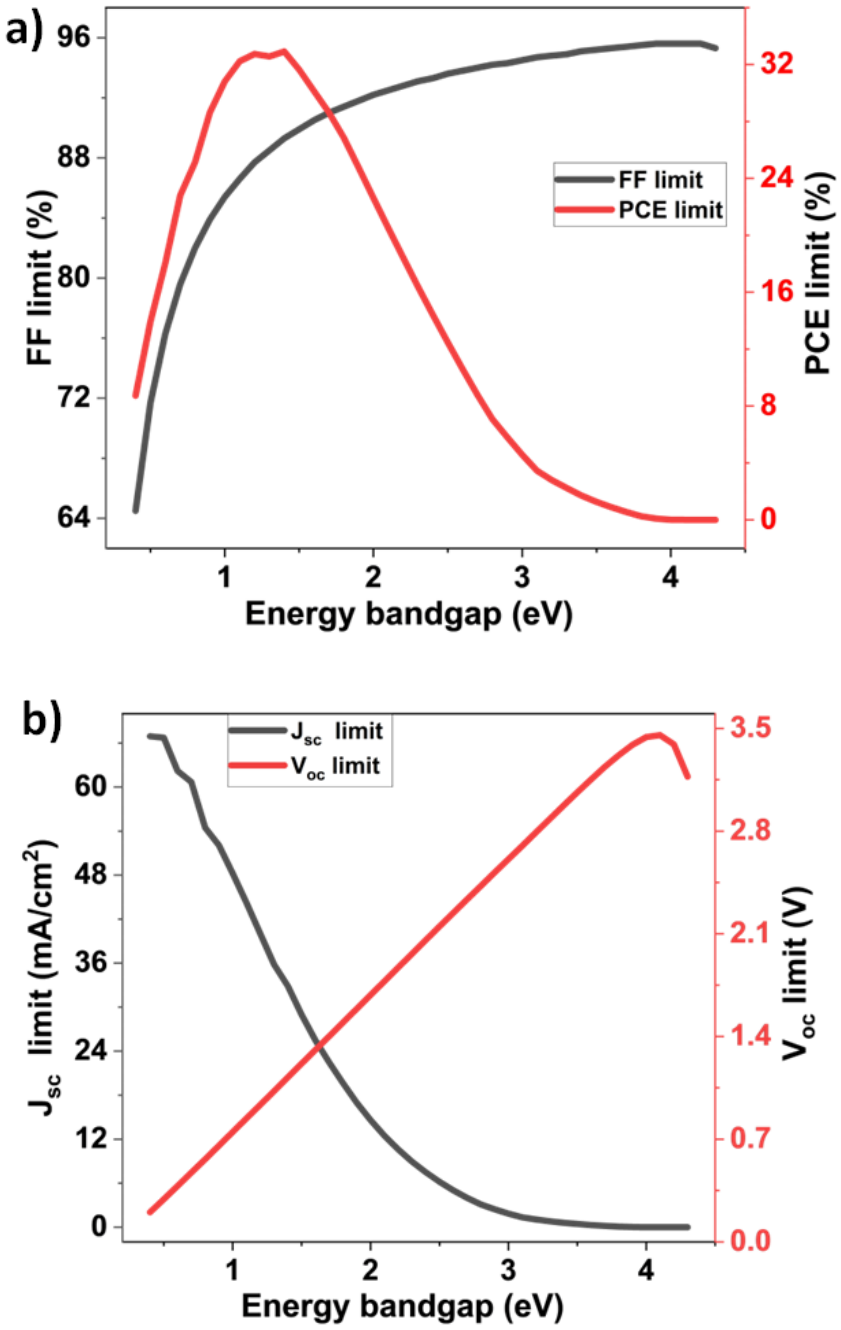

Figure 2.8: (a) FF and PCE limits and (b) J_{sc} and V_{oc} limits as a function of energy bandgap [73,112]

Existing studies have shown that to achieve excellent PCE from solar cells, the E_g of photovoltaic materials must be within $1.2 \leq E_g \leq 1.6$ eV, with 1.48 eV as the optimum energy bandgap [22,73,112,113]. Photovoltaic materials with $E_g < 1.2$ eV have efficient charge generation properties (due to narrow E_g) but reduced charge extraction characteristics (due to short delay before excited electrons return to VB). Nevertheless, materials with $E_g > 1.6$ eV have decreased charge generation properties (due to wide E_g)

but excellent charge extraction characteristics (due to the long delay before excited electrons return to VB) [22]. Hence, the FF and V_{oc} limits of solar cells increase when the E_g of the photovoltaic materials increases because of the improvement in charge extraction characteristics. However, solar cells' short-circuit current density (J_{sc}) limit decreases when the E_g of the photovoltaic materials increases due to reduced charge generation [73]. Figures 2.8(a) and 2.8(b) present V_{oc}, PCE, FF and J_{sc} limits of solar cells as a function of E_g of the photovoltaic materials [73].

2.4.2. Photon absorption characteristics

Absorption coefficient (α) and film thickness (d) play crucial roles in the photon absorption characteristics of photovoltaic materials. The α determines the amount of incident photon absorbed by a unit thickness of material [114]. Figure 2.9 presents the absorption coefficient for common photovoltaic materials. Materials with low absorption coefficients (e.g., crystalline silicon) require thick films (about 200 μm). In contrast, materials with large absorption coefficients (e.g., perovskite) require ultra-thin films (about 500 nm) to absorb incident photons efficiently. For efficient photon absorption, d must be greater than the material's absorption length (1/α) [18].

In addition to the absorption coefficient and film thickness, the morphology of films affects their photon absorption properties. Hence, films with poor morphology severely decrease photon absorption because their rough surfaces cause light scattering [115–117].

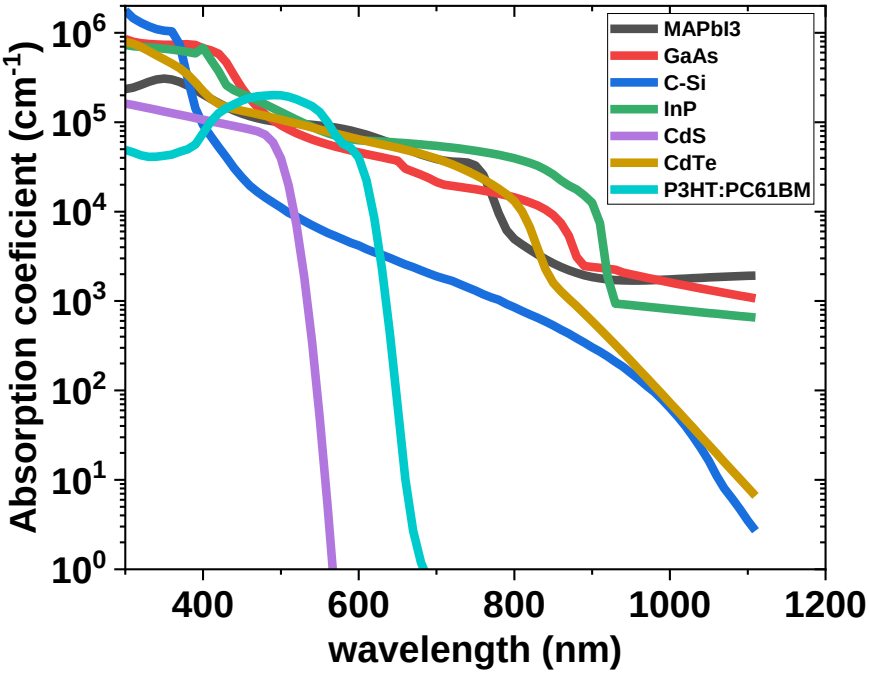

Figure 2.9: Absorption coefficient of materials as a function of wavelength [114,118–121]

2.4.3. Charge carrier properties

Diffusion length (L), carrier lifetime (τ), electron density (N), carrier mobility (μ) and carrier diffusion coefficient (D) are some carrier properties that affect the PCE of solar cells [122]. L is the average distance carriers can move from the region of the generation before recombination, while τ is the time between carrier generation and recombination [21]. μ quantifies how fast carriers can move in semiconductors when subjected to an external electric field [123]. L, τ, μ and D magnitudes determine the effectiveness of charge extraction from devices and the optimum thickness of photovoltaic materials [124,125]. For excellent solar cell performance, the thickness of photovoltaic materials must be optimised to enhance efficient photon absorption without compromising carrier extraction. Hence, $d > 1/\alpha$ and $L \gg d$ to ensure efficient light absorption and carrier extraction [18,126]. Equation (2.10) gives the mathematical relationship between L and μ, τ and D, where k_B is the Boltzmann constant (1.38064×10^{-23} m^2 kg s^{-2} K^{-1}) and T is the temperature (in Kelvin) [18].

$$L = \sqrt{D.\tau} = \sqrt{k_B.\mathrm{T}.\mu.\tau} \qquad (2.10)$$

2.4.4. Charge carrier separation

Electron-hole pairs generated in photovoltaic materials could be weakly or strongly bound by electrostatic force. An electrostatic force is the force of attraction/repulsion between two static charges. The strength of the electrostatic force binding electron-hole pair depends on the exciton binding energies of the photovoltaic materials. The exciton binding energy is required to separate an electron-hole pair into free charge carriers [127]. Materials with weak exciton binding energies produce weakly bound electron-hole pairs [128–130], while strongly bound electron-hole pairs (excitons) are generated in materials with strong exciton binding energies [128].

Consequently, organic materials (e.g. P_3HT: $PC_{61}BM$) generate strongly bound electron-hole pairs, while perovskite materials (e.g. $MAPbI_3$) produce weakly bound electron-hole pairs as a result of partial charge pair separation [81]. Hence, organic materials need strong electric fields, while c-Si requires a weak electric field to separate electron-hole pairs. Figure 2.10 shows the plots of exciton binding energies of common photovoltaic materials.

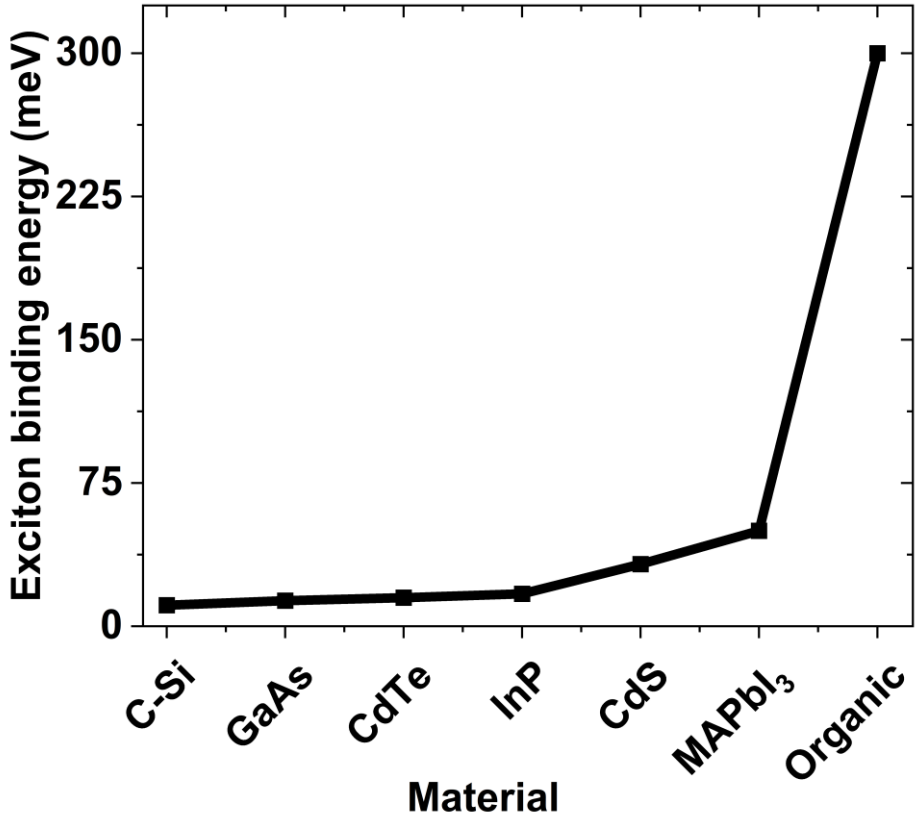

Figure 2.10: Exciton binding energies of some photovoltaic materials [128–134]

For efficient charge separation in solar cells, n-type and p-type materials are combined to form junctions that provide the electric fields required to separate the electron-hole pairs [81]. The n-p, n–i–p and p–i–n junctions are commonly used for charge separation in solar cells [22,71,83]. In the n–i–p junction, n, p, and i represent the electron transport layer (ETL), hole transport layer (HTL) and photovoltaic materials (e.g., perovskite), respectively.

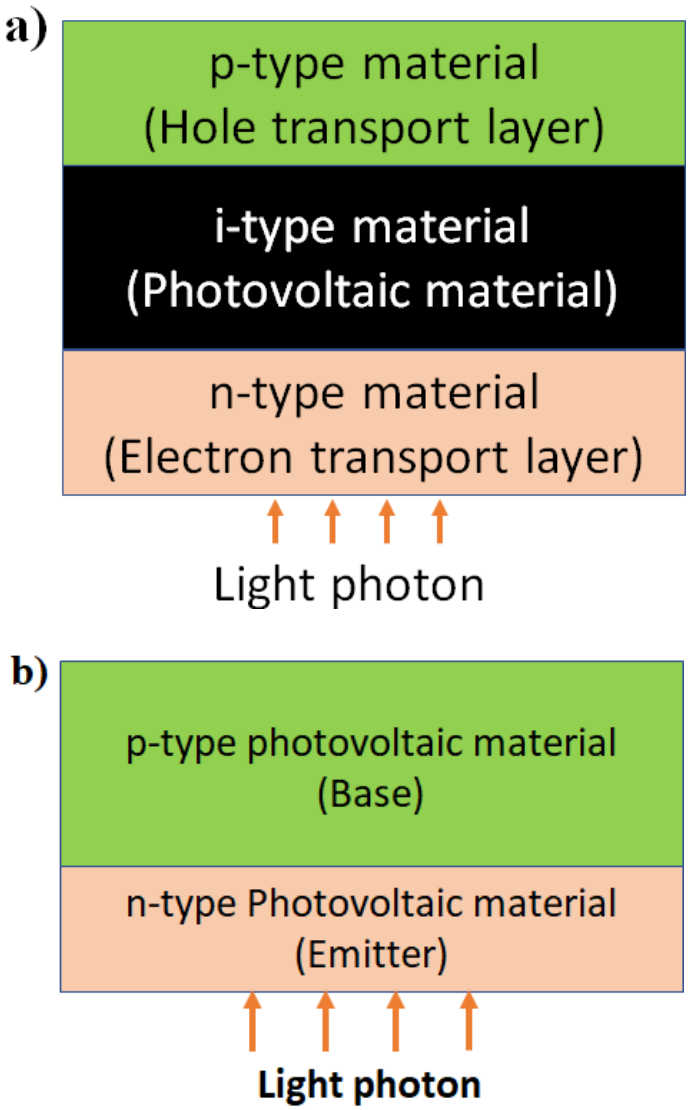

Figure 2.11: (a) n–i–p junctions and (b) n–p junctions. These diagrams were drawn in this thesis to demonstrate the differences between n–i–p and n–p junctions.

Similarly, n and p represent the emitter (very thin) and base (very thick) layers in the n–p junction. Figure 2.11(a) shows an n–i–p junction preferred in solar cells when the photovoltaic material has a short carrier diffusion length (e.g., perovskite material). On the other hand, Figure 2.11(b) presents an n–p junction which is quite efficient when the photovoltaic material has a long carrier diffusion length (e.g. c-silicon) [22].

Barrier voltage (V_{bi}) develops from the junction in solar cells. V_{bi} arises from the difference between the work function of p-type (WF_p) and the work function of n-type (WF_n) before junction formation [22,135]. Equation (2.11) presents the expression for calculating V_{bi} from work functions of the n-type and p-type materials, where e is the electron charge (1.602×10^{-19} C).

$$V_{bi} = \frac{WF_n - WF_p}{e} \qquad (2.\ 11)$$

V_{bi} provides the electric fields that overcome the electrostatic force binding the electron-hole pair together and drives electron carriers towards n-type material and hole carriers toward p-type materials in solar cells [22,71,83,84]. The strength of the electric field developed in a junction is proportional to the magnitude of V_{bi}. Consequently, high V_{bi} is beneficial for efficient electron-hole pair separation and transportation [22,97,107]. Figures 2.12 (a) and 2.12 (b) show the energy band diagram of a typical perovskite solar cell at open-circuit conditions, operating under dark and illumination, respectively [82,135–137].

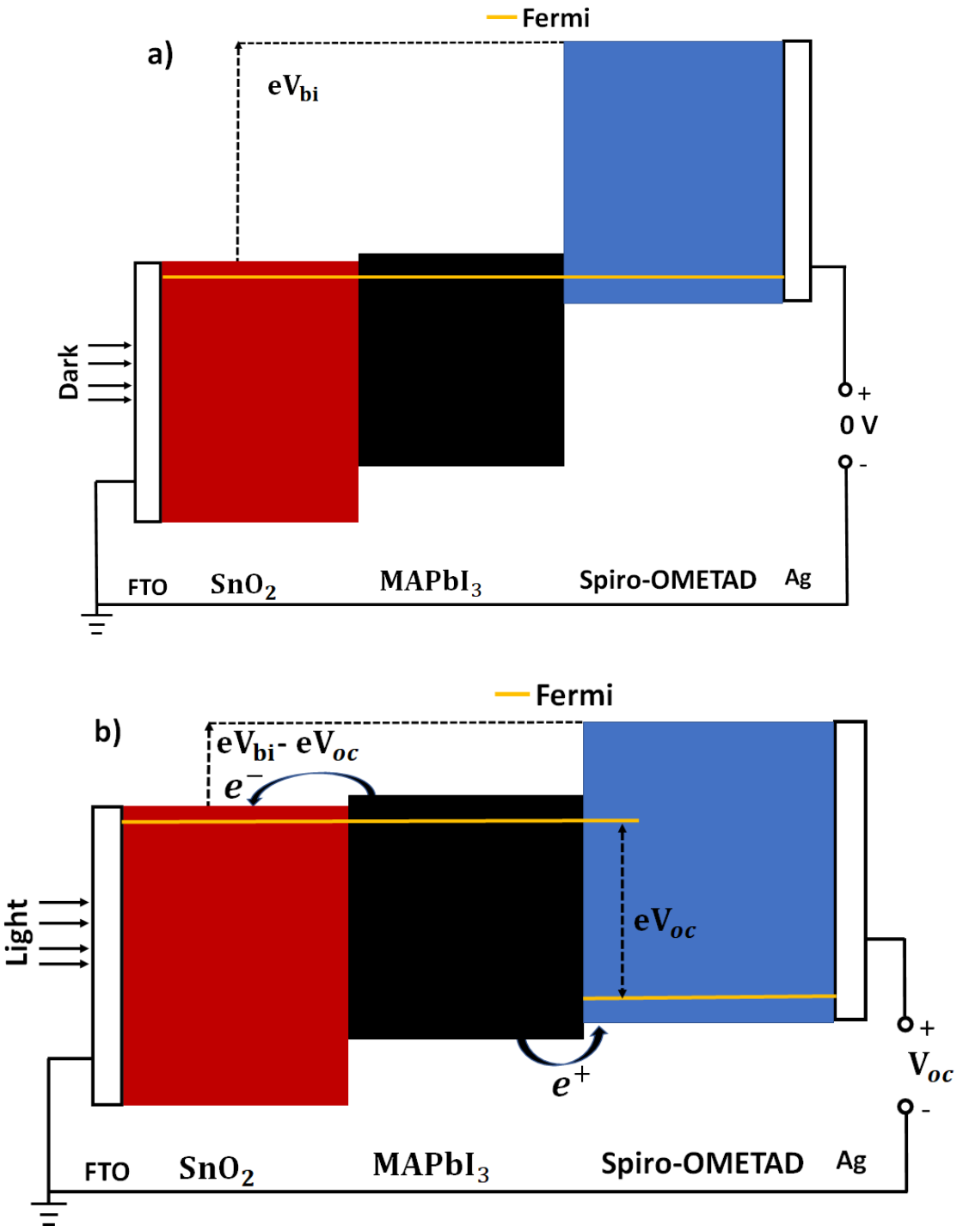

Figure 2.12: Energy band diagram of n–i–p junction under (a) dark (b) illumination at open-circuit conditions [82,135–137].

2.4.5. Energy band matching

Energy band matching represents the extent to which the CB of the n-type material aligns with the CB of the i-type material and the degree to which the VB of the p-type material matches

the VB of the i-type material. It is an essential factor influencing the PCE of solar cells with n–i–p junctions.

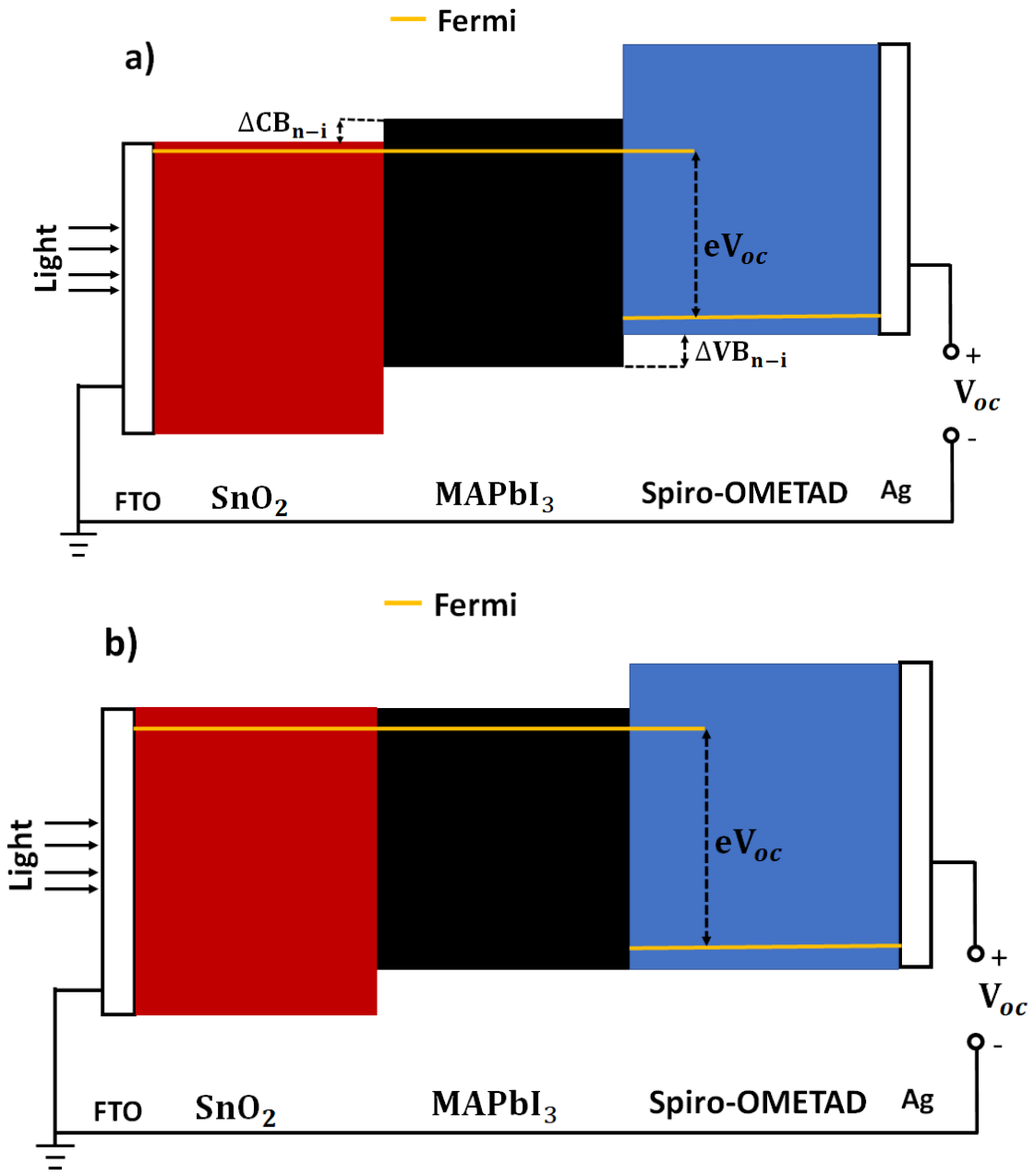

Figure 2.13: An n–i–p junctions of illuminated PSC with (a) CB and VB mismatch relative to perovskite and (b) no CB and VB mismatch relative to perovskite [138–140].

Mismatching in solar cells reduces the V_{oc} by causing recombination losses because of charge accumulation and the reverse flow of charges [141–143]. Figure 2.13(a) shows the

energy band diagram of a solar cell with a CB mismatch at the n–i junction and a VB mismatch at the i–p junction. Equation (2.12) presents the expression for estimating the resultant energy loss (E_{loss}) due to these mismatches [138–140].

$$E_{loss} = \Delta CB_{n-i} + \Delta VB_{i-p} \qquad (2.12)$$

Minimizing CB and VB mismatch at n–i and i–p junctions improves solar cells' charge extraction and V_{oc} [144,145]. Figure 2.13(b) presents the energy diagram of a solar cell with matched CB and VB at n–i and i–p junctions respectively.

2.5. Basics of perovskite solar cells

Perovskite solar cell technology is promising for low-cost and efficient solar energy conversion to electricity [30]. The photovoltaic materials in perovskite solar cells are perovskite. The perovskites have an absorption coefficient of about 1.1×10^5/cm at a wavelength of 600 nm, suggesting that ultra-thin perovskite films are required for high-performing devices [19,20]. Currently, the PCE of single-junction PSCs has grown from 3.8% in 2009 to 25.8% in 2021 [23,24,45,146–156].

2.5.1. Components of perovskite solar cells

Perovskite solar cells (PSCs) consist of a top electrode, hole transport layer (HTL), perovskite layer, electron transport layer (ETL) and fluorine-doped tin oxide (or indium-doped tin oxide) layer. These layers are systematically arranged to achieve the preferred device structure. PSCs could have a regular or inverted structure [157–159]. In regular structure (n–i–p), the ETL (n-type) is deposited on the FTO substrate.

Figure 2.14(a) presents the regular structure of PSCs. The regular structure is preferred when the ETL deposition process may remove or alter the composition of the perovskite layer. Conversely, in an inverted structure (p–i–n), the HTL (p-type) is deposited on the FTO substrate. Figure 2.14(b) presents the inverted structure of PSCs [157–159]. Transport layers with low energy band mismatch relative to the perovskite materials are chosen in PSCs to minimise charge accumulation and recombination losses. These layers are discussed in detail in subsections 2.5.1.1. to 2.5.1.5.

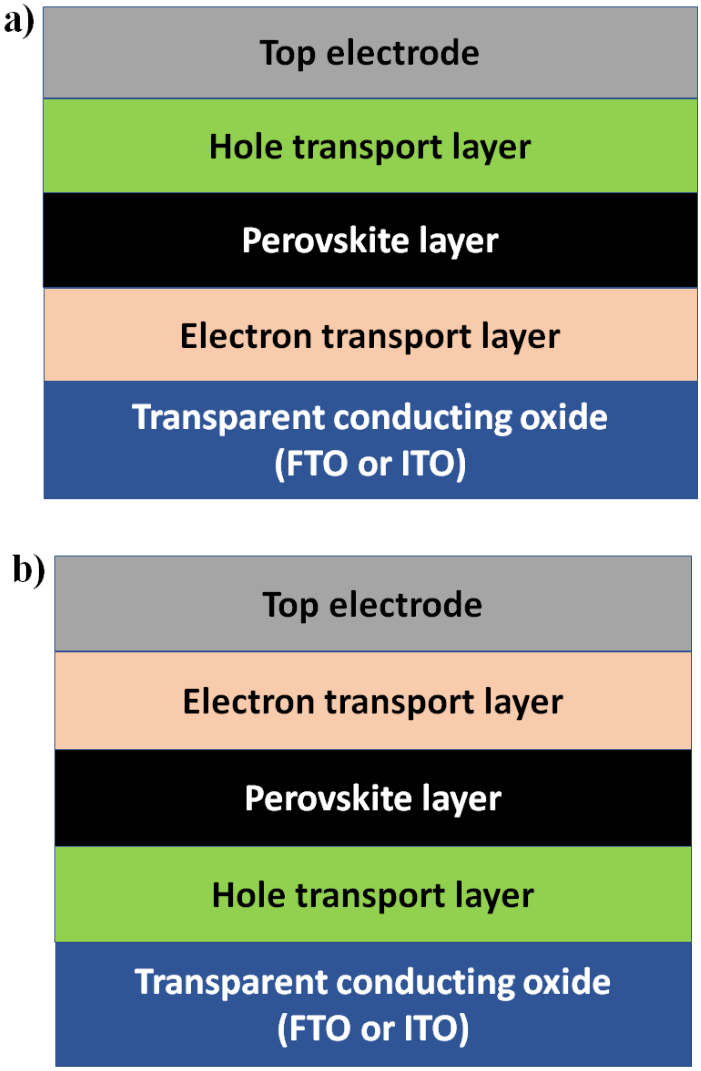

Figure 2.14: (a) Regular PSC structure and (b) Inverted PSC structure [140,157–159].

2.5.1.1. Fluorine-doped tin oxide

Fluorine-doped tin oxide (FTO) is a transparent conductive oxide (TCO) with high-temperature stability, excellent electrical conductivity, wide E_g and high optical transparency. It has applications as a working electrode in PSCs and electronic displays [40,160–164]. The functions of FTO substrates in solar cells include admitting light photons into the solar cells and transporting charges generated in the devices to the external circuits. In addition, FTO substrates have wide E_g which ensures that a broad spectrum of photons is admitted into the PSCs.

FTO substrates are classified based on their sheet resistance, root-mean-square (RMS) roughness, thickness, and transparency. Table 2.2 presents the properties of TEC-8 and TEC-15 FTO substrates. FTO substrates are vital in most critical applications due to their mechanical hardness, high-temperature resistance, and low cost [161,165–167].

Table 2.2: The properties of TEC-8 and TEC-15 FTO substrates [168,169]

Class	Sheet resistance (Ω/sq.)	Average RMS (nm)	Average thickness (nm)	Transmittance (%) at 550 nm
TEC-8	8	34.8	600	76.4
TEC-15	15	12.5	330	82.5

2.5.1.2. Electron transport layer

The n-type semiconductors are generally applied as the electron transport layers (ETLs) in PSCs [170,171]. ETL allows electrons to flow from the CB of the perovskite layer to the FTO. However, it blocks the flow of holes from the VB of the perovskite layer to the FTO [40]. ETL materials are to have very low CB and large VB mismatches at the ETL/perovskite interface to minimise electron accumulation and electron-hole recombination [172–175]. Also, ETL must not be too thin as this may result in multiple pinholes that lead to electron-hole recombination and low R_{dc_r}, whereas films that are too thick increase the R_{dc_f} of the devices [176]. Reports have shown that ETL materials achieve adequate hole blocking when their thickness is larger than the RMS of FTO [177]. Table 2.3 presents typical materials for electron transport layers.

Notwithstanding the availability of many materials for ETLs, TiO_2 and SnO_2 are most extensively studied for PSC applications [178–182]. These materials have low CB mismatch relative to most perovskites and excellent electron mobility, conductivity, transmittance and wide bandgap [158,166,180,183–185]. Over the years, the efficiency of devices based on TiO_2 has improved from 3.8% in 2009 to 23.2% in 2018 [23,151]. However, the high annealing temperature (≥ 450°C) requirement of TiO_2 has limited the application in perovskite solar cells.

Table 2.3: Typical materials of electron transport layers [185–189]

Material	VB (eV)	CB (eV)	E_g (eV)
Titanium (IV) Oxide (TiO_2)	-7.20	-4.00	3.20
Zinc (II) oxide (ZnO)	-7.67	-4.30	3.37
Tin (IV) oxide (SnO_2)	-8.61	-4.21	4.40
Graphene oxide (GO)	-6.60	-3.60	3.00

Because of the high-temperature requirement of TiO_2, SnO_2 with a low annealing temperature (180℃) requirement was introduced [180,185]. Reports have shown that SnO_2 films annealed at low temperatures effectively block hole transportation through it [189–192]. Hence, the PCE of devices based on SnO_2 has improved from 13.27% in 2015 to 25.8% in 2021 [45,149,193,194].

2.5.1.3. Perovskite layer

The perovskite layers generate electron-hole pairs required to operate PSCs [195,196]. The composition and morphology of the perovskite layer play substantial roles in the performance and stability of PSCs [113,172,177,197,198]. The perovskite composition influences the E_g and the film's intermolecular bond strength. Perovskite materials have high absorption coefficients, excellent carrier properties, and low processing costs, and the materials are readily available [15–17]. Similarly, most perovskite materials have CB and VB that closely match the CB and VB of commonly applied ETL and hole transport layers. Table 2.4 presents the energy bands of some perovskite materials.

Table 2.4: Energy bands of some perovskite materials [199–203]

Perovskite materials	VB (eV)	CB (eV)	E_g (eV)
Methylammonium lead iodide ($MAPbI_3$)	-5.43	-3.93	1.50
Methylammonium lead bromide ($MAPbBr_3$)	-5.60	-3.40	2.20
Caesium lead Iodide ($CsPbI_3$)	-5.44	-3.45	1.99
Caesium lead bromide ($CsPbBr_3$)	-5.85	-3.35	2.50

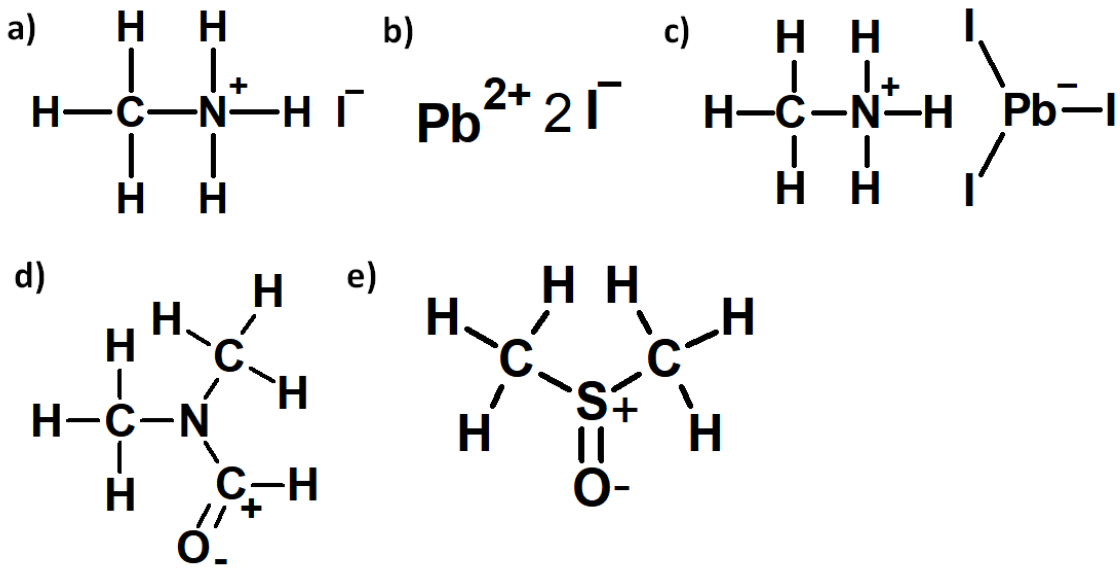

Figure 2.15: Chemical structures of (a) methylammonium iodide, (b) lead iodide, (c) methylammonium lead iodide, (d) dimethyl methanamide and (e) dimethyl sulphur, (IV) oxide. These chemical structures were drawn using ACD/Chemsketch software.

Perovskite layers require low-cost materials and are adaptable to solution processing because the materials are very soluble in polar solvents [14,36,195,204–206]. Perovskite materials are soluble in polar solvents because they are ionic. Figures 2.15(a) – 2.15(c) show the molecular structures of methyl ammonium iodide (MAI), lead iodide (PbI_2), methyl ammonium iodide ($MAPbI_3$), dimethyl methanamide (DMM) and dimethyl sulphur (IV)oxide (DMSO). Carbon/oxygen double bonds (C=O) in DMM and DMSO molecules make them polar and suitable as solvents for perovskite materials.

2.5.1.4. Hole transport layer

The hole transport layer (HTL) is a p-type material that blocks the flow of electrons from the CB of perovskite to the top electrode through its CB but permits the flow of hole from the VB of perovskite to the top electrode via its VB. Hence, low VB mismatch and large CB mismatch at the perovskite/HTL interface are required to minimise electron-hole recombination and hole accumulation [177,207]. Table 2.5 presents some HTL materials with widespread application in PSCs.

Table 2.5: Typical materials for hole transport layers [187,199,208]

HTL Material	VB (eV)	CB (eV)	E_g (eV)
Spiro-OMETAD	-5.30	-2.05	3.25
Poly(triaryl)amine	-5.25	-2.30	2.95
Nickel (II) oxide	-5.40	-2.40	3.00

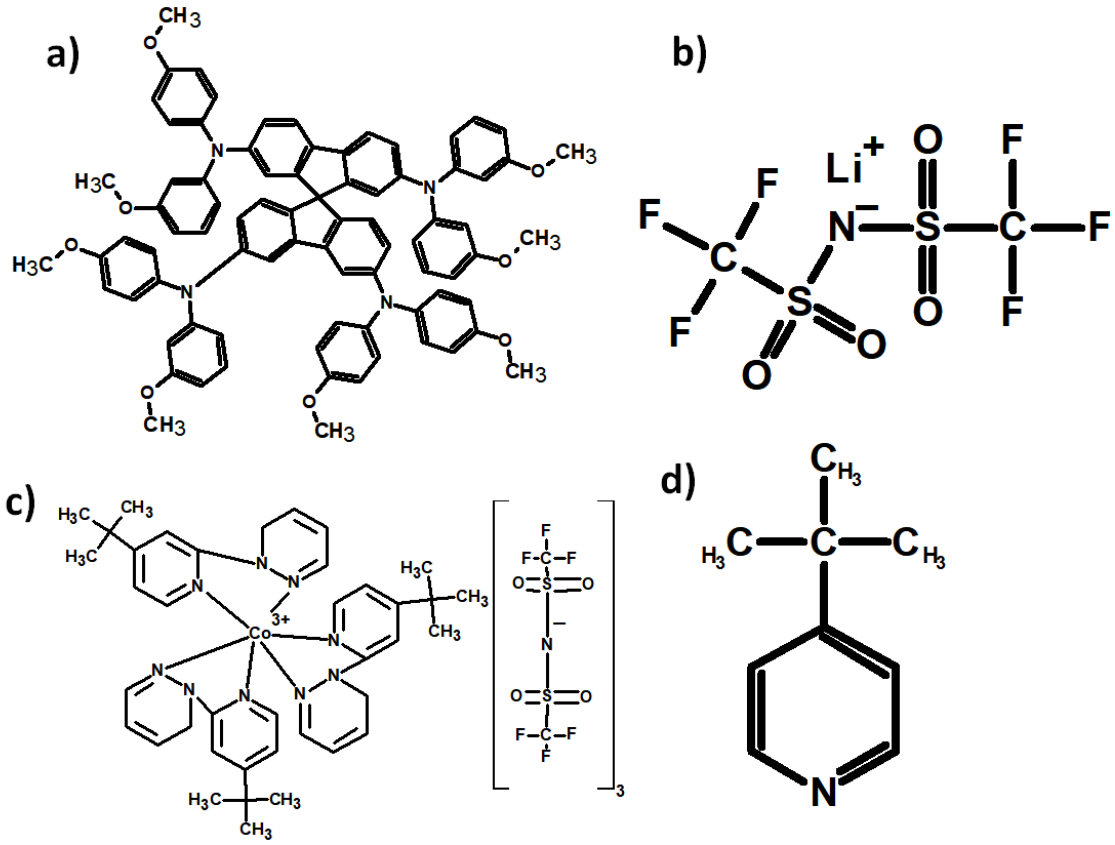

Figure 2.16: Chemical structures of (a) Spiro-OMETAD, (b) Li-TFSI, (c) FK209, and (d) MPPD.

Spiro-OMETAD has extensive application in PSCs because of its low cost, large CB mismatch and low VB mismatch relative to perovskite. In addition, adding additives is an effective method of modifying the conductivity, CB, VB, and work function of Spiro-OMETAD. Some common additives for Spiro-OMETAD are lithium bis(trifluoromethanesulfonyl)amine (Li-TFSI), 2-methylpropan-4-yl pyridine (MPPD) and tris(2-(1H-pyrazol-1-yl)- 2-methylpropan-4-yl pyridine) cobalt (III)

tris(bis(trifluoromethylsulfonyl) amine) (FK209) additives [209–215]. Reports have indicated that devices based on Spiro-OMETAD have reasonable PCEs [41,216–219].

A problem with Spiro-OMETAD is that it employs hydrophilic additive (especially Li-TFSI), which hasten its degradation and reduces the stability of the perovskite layer [220–223]. Figures 2.16(a) – 2.16(d) present the chemical structures of Spiro-OMETAD, Li-TFSI, FK209 and 2-methylpropan-4-yl pyridine (MPPD), respectively. Currently, nickel oxide, which is low-cost and stable, is being adopted in inverted architecture [89,224,225].

2.5.1.5. Top electrode

Top electrodes receive the electrons from an external circuit and transport them through the HTL to the perovskite layers. The key factors determining the top electrode's choice are conductivity, work function, and cost. Top electrodes with high work function are more resistant to oxidation [106], and this explains the improved stability for PSCs with Gold (Au) contacts [41,146,155,156,226–228]. Low cost, high conductivity and good work function alignment relative to the VB of HTL have made Ag the most widely used electrode in PSCs [204,216,229–231]. Table 2.6 presents typical metals employed as top electrodes in PSCs.Thermal evaporation, e-beam and sputtering techniques are some techniques for depositing top electrodes [61–63,146,151,219,232].

Table 2.6: Metals for top electrodes and their properties [233,234]

Metal	**Work Function (eV)**	**Resistivity (Ωm)**
Gold	5.33	2.4×10^{-8}
Silver	4.53	1.6×10^{-8}
Aluminium	4.32	2.8×10^{-8}
Copper	4.90	1.7×10^{-8}
Platinum	5.65	10.6×10^{-8}

2.5.2. Air-fabrication of perovskite solar cells

Air-fabrication of PSCs is a viable method of reducing the overall cost of perovskite solar cell technology and encouraging large-scale production for commercial applications. However, PSCs prepared in the air have low PCE and suffer from severe degradation

because of moisture interference. This challenge has limited the adoption of the air-fabrication process. Subsections 2.5.2.1 and 2.5.2.2 detail the degradation mechanisms of PSCs due to moisture and the mitigation methods.

2.5.2.1. Degradation of air-fabricated perovskite solar cells

Perovskites severely decompose when exposed to moisture during or after the perovskite film nucleation processes [48,235]. Perovskite films deteriorate when exposed to moisture because it has weak intermolecular bonds. Also, exposure to moisture during preparation causes the perovskite films to have poor morphology and many pinholes. These pinholes act as entry points for water molecules and hasten the rate of decomposition [236,237]. An example of perovskite is methylammonium lead iodide ($MAPbI_3$).

In the presence of moisture, $MAPbI_3$ decomposes to form different products depending on the light condition [238–242]. For example, Lang et al. and Christians et al. reported that the exposure of $MAPbI_3$ to moisture in the dark causes it to decompose into methylammonium iodide (MAI) and lead iodide (PbI_2) (see equation (2.13)) [241,242]. However, in the presence of moisture and light, $MAPbI_3$ decomposes to produce PbI_2, methyl amine (CH_3NH_2) and hydroiodic acid, as in equation (2.14) [240]. Consequently, the effort to mitigate the damaging effect of moisture on the perovskite films is an essential aspect of developing PSC technology.

$$CH_3NH_3PbI_3 \xrightarrow{H_2O+\ dark} CH_3NH_3I\ (aq) + PbI_2(s) \qquad (2.13)$$

$$CH_3NH_3PbI_3 \xrightarrow{H_2O\ +\ light} CH_3NH_2(g) + PbI_2(s) + HI(aq) \quad (2.14)$$

2.5.2.2. Methods of minimising degradation of air-fabricated PSCs

Different methods have been developed and employed to minimise the degradation of air-fabricated perovskite solar cells. These methods aim to exclude moisture from the perovskite films during nucleation and strengthen the perovskite's intermolecular bonds. Similarly, a combination of these routes could result in enhanced device stability and PCE. Sections 2.5.2.2.1 – 2.5.2.2.3 elaborate on some of these methods.

2.5.2.2.1. Humidity-resistant antisolvent method

Humidity-resistant antisolvents protect against moisture interference during perovskite film deposition and enhance the film's long-term stability. These antisolvents have high water solubility and vapour pressure, which make them effective in protecting the $MAPbI_3$/DMSO adduct from moisture during perovskite film deposition, particularly at high relative humidity [34,37]. The high vapour pressure accelerates the evaporation of DMM and moisture around the films, while high water solubility enhances moisture absorption around the films [37]. By protecting the films against moisture, these antisolvents promote the formation of films with compact grains and quality morphology. These are vital in minimising moisture ingress into the films and enhancing long-term stability and PCE of air-fabricated films PCSs [34,37,243].

Troughton et al. introduced humidity-resistant antisolvent treatment for PSCs prepared in ambient air. The researchers reported that PSCs treated with ethyl ethanoate antisolvent have improved PCE and stability compared to devices treated with methylbenzene [34]. In addition, research has shown that devices treated with ethyl ethanoate have improved PCE and stability because of the high water solubility and vapour pressure of antisolvent. In 2018, Yang et al. reported that devices prepared using methyl ethanoate have improved stability and PCE over devices treated with ethyl ethanoate antisolvent. This observation is because methyl ethanoate has higher vapour pressure and water solubility than ethyl ethanoate[37]. Wang et al. showed that ethoxyethane antisolvent treatment makes the perovskite film deposition process reasonably insensitive to moisture at RH $\leq$ 50% [38]. In 2019, Yang et al. demonstrated that for RH$\leq$30%, perovskite film deposition using trichloromethane antisolvent is humidity insensitive [244]. Trichloromethane was only effective within this range because it has low water solubility, despite its high vapour pressure.

Besides using a single antisolvent, mixed antisolvents effectively improve the PCE and stability of PSCs prepared in ambient air [35]. Mixing an antisolvent of high dipole moment with an antisolvent of low dipole moment reduces the removal of DMSO from the solution, thereby improving the perovskite film quality and the performance of PSCs [39,245–249].

Table 2.7: Properties of typical antisolvents for perovskite film treatment [250,251]

Antisolvent	Vapour pressure (mmHg) at 23℃	Water solubility (%) at 23℃	Boiling point (℃)	Dipole moment (D)
Chlorobenzene	9	0.05	131.00	1.55
Trichloromethane	160	0.50	61.15	1.04
Methyl ethanoate	173	25.00	56.90	1.71
Methylbenzene	21	0.07	110.00	0.38
Ethyl ethanoate	73	10.00	77.22	1.78
Ethoxyethane	440	8.00	34.44	1.28
1-butoxybutane	4.8	0.03	141.00	1.26
Propyl ethanoate	25	2.00	101.67	1.86
Butyl ethanoate	10	1.00	125.56	1.87
2-Butanol	12	16.00	99.44	1.62

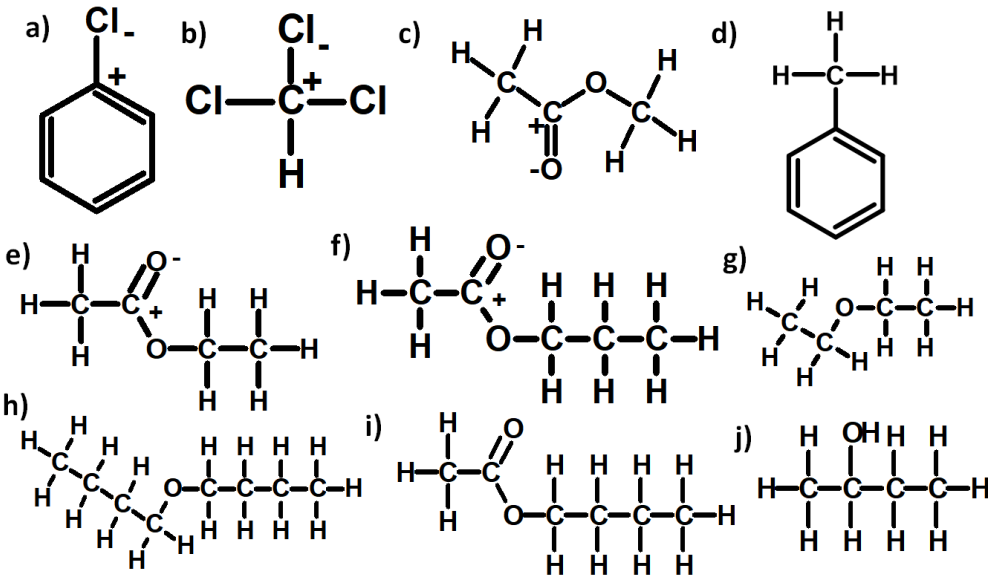

Figure 2.17: Chemical structures of (a) chlorobenzene (b) trichloromethane (c) methyl ethanoate (d) methylbenzene (e) ethyl ethanoate (f) propyl ethanoate (g) ethoxyethane (h) 1-butoxybutane (i) butyl ethanoate and (j) 2-butanol

In 2021, Jung *et al.* reported improved stability and PCE of 20.55% for devices treated with 1-butoxy butane (30%) mixed with ethoxy ethane (70%) antisolvents at relative humidity > 40% [39]. Table 2.7 shows the physical properties of typical antisolvents frequently used to fabricate perovskite solar cells. Figures 2.17(a) – 2.17(j) present the corresponding chemical structures.

2.5.2.2.2. Additive technique

The additive technique is another method of enhancing the stability of air-fabricated PSCs. In the additive process, additives are introduced in the perovskite solution to achieve a homogenous solution before film deposition. Additive materials can enhance the stability of air-fabricated PSCs through two routes. In one method, non-silane additives are added to the perovskite solution to delay nucleation. Optimal delay in nucleation increases grain sizes and reduces the film pinholes, consequently minimising the entry points for moisture [226,252–255]. In the second instance, silane additives crosslink and strengthen the intermolecular bonds of perovskite films, thereby making the films less prone to decomposition [43,52,256,257]. Bag et al. conducted the first study on applying the non-silane additive process in PSCs in 2016 [255]. The researchers reported PCSs with improved stability and PCE when the perovskite materials contained sodium bromide (NaBr) additive. In 2017, Sun et al. enhanced the PCE and stability of PSCs by adding lead (II) thiocyanate ($Pb(SCN)_2$) in the perovskite solution [252]. In 2018, Zhang et al. reported PSCs with improved PCE and stability when perovskite films were modified with sodium thiocyanate (NaSCN) and potassium thiocyanate (KSCN) additives [226]. The investigators explained that the improvement in PCE and stability is due to the large grain sizes and the fewer pinholes on the perovskite films with these additives. Finally, in 2021, Salim et al. demonstrated that lead (II) sulphide (PbS) additive is beneficial in air fabrication [258].

Silane additives are becoming quite popular due to their ability to form a cross-linking bond with perovskite and delay the nucleation process [43,44]. Studies indicate that silane materials become more effective when they contain both silyl and fluoride groups. These groups form strong crosslinking bonds with perovskites and reduce the decomposition rate in the presence of moisture [53]. Oku et al. conducted the first study applying silane additives in PSCs, and the researchers reported that using decaphenylcyclopentasilane

additive enhanced the PCE of devices from 5.82% to 10.46% [43]. In 2021, Zheng et al. improved the PCE of the devices from 18.85% to 20.72% by applying a 3-aminopropyltrimethoxysilane additive [44]. The researchers also reported that the additive improved the stability of the devices prepared at 50-60% relative humidity by 40% compared to the control devices after 400 hours of storage. Figures 2.18(a) and 2.18(b) present the chemical structures of decaphenylcyclopentasilane and 3-aminopropyltrimethoxysilane.

2.5.2.2.3. Passivation technique

Surface passivation involves depositing a thin layer of passivating materials on perovskite films to fill pinholes and gaps between grain boundaries. By filling some of the pinholes and the cracks between grain boundaries, the passivation technique minimises the degree of moisture ingress into the films and enhances device stability [54].

The first application of surface passivation in PSCs reported improved PCE for devices with films passivated using iodopentafluorobenzene and pyridine [46,55]. The researchers attributed the improvement in PCE to the fluoride and nitride groups which protected the perovskite films from moisture [53]. In 2015, Jeong et al. reported that passivating the perovskite films with polytetrafluoroethene resulted in devices with improvement in PCE and stability [259]. They explained that the polymer layer repels H_2O molecules, thereby significantly enhancing the stability of the PSCs.

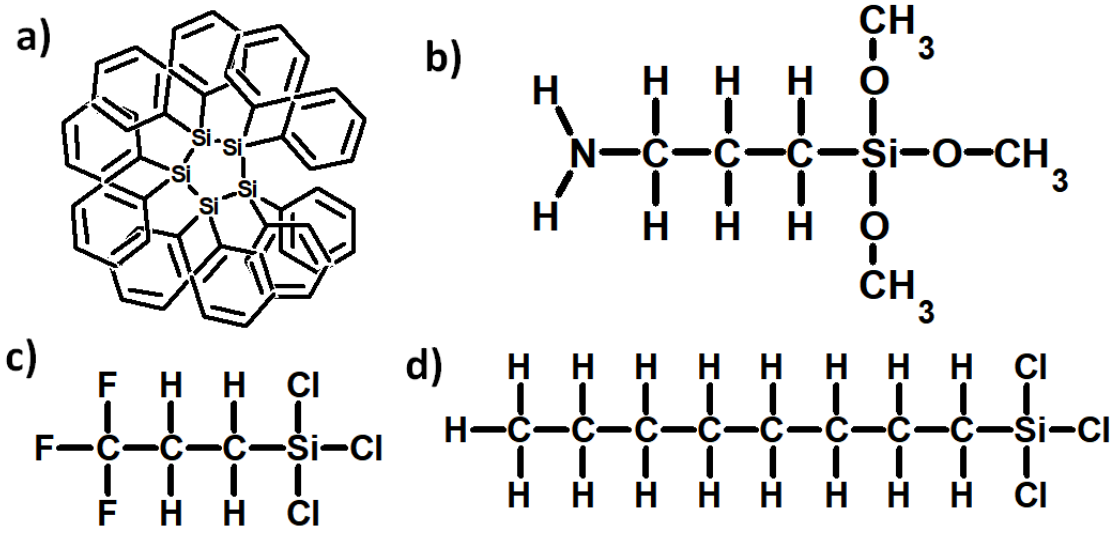

Figure 2.18: Chemical structures of (a) decaphenylcyclopentasilane, (b) 3-aminopropyltrimethoxysilane (c) trichloro(3,3,3-trifluoropropyl) silane and (d) Octyl trichlorosilane

In 2017, researchers reported enhanced PCE and stability for devices passivated using (2-hydroxyethyl)trimethylammonium chloride [260]. This ammonium salt enhances the PCE and stability by reducing trap densities and moisture ingress into the films. Finally, in 2019, ethylammonium iodide was reported to improve the PCE and stability of devices [261].

Few studies have demonstrated that silane materials are effective passivation agents for enhancing the PCE and stability of devices [52,57]. The first study on silane passivation reported improved PCE and stability when trichloro(3,3,3-trifluoropropyl)silane was used [52]. In the same year, Zhao et al. achieved enhanced PCE and stability by applying trichloro(octyl)silane [57]. Octyl trichlorosilane and trichloro(3,3,3-trifluoropropyl) silane effectively passivate perovskite layers since they form crosslinking bonds with perovskites [52,57]. Figures 2.18(c) and 2.18(d) present the chemical structures of trichloro(3,3,3-trifluoropropyl) silane and octyl trichlorosilane.

2.6. Film deposition methods

Spin-coating, inkjet printing, slot-die coating, blade coating, screen printing, spray-coating, and magnetron sputtering are some film deposition techniques for PSC fabrication. This project used the spin-coating method because of its reproducibility [262–264]. Similarly, the benefits of improved film adhesion, scalability, reproducibility and precision made magnetron sputtering suitable for this study [58–61]. In this section, spin-coating and magnetron sputtering techniques are described in detail because these two techniques are relevant to this project.

2.6.1. Spin-coating

Spin-coating is a laboratory standard, reproducible, fast, solution and low-temperature technique for depositing uniform and quality thin films on flat substrates using the interaction between surface tension and centrifugal force as substrate rotates [264–266].

Table 2.8: Solvents for the spin coating process [267–270]

Solvent	Boiling point (℃)	Molar mass (g/mol)	Density (g/ml)	Required spin time (s)
Propan-2-ol	82.6	60.10	0.79	30
Methylbenzene	110.6	92.14	0.87	30
Dimethyl methanamide	153	73.09	0.94	>30
Dimethyl sulphur (IV) oxide	189	78.13	1.10	>30
Ethane nitrile	82	41.05	0.79	30
Chlorobenzene	131	112.56	1.11	30
Methoxybenzene	153	108.14	1.0	>30

In spin-coating, a known volume of the coating solution is spread on a substrate, and the substrate is then spun at high speed to distribute the applied solution uniformly on the substrate. For uniform and pinhole-free film, substrates must be thoroughly cleaned, the solution must be filtered, and sufficiently enough solution must be applied on the substrate. Using too little solution on the substrate leads to uncoated areas, while solid particles due to an unfiltered solution or improperly cleaned substrate result in films with numerous pinholes [271].

A practical method of spin-coating quality films is mixing a primary solvent with a moderately low boiling point and a minor solvent with a relatively high boiling point [268,272]. However, using a volatile solvent only leads to fast nucleation, while using a solvent with a high boiling point alone leads to delayed nucleation and rewetting [273,274]. Table 2.8 presents effective solvents for spin-coating processes during PSC preparation and the required spin-coating time.

2.6.2. Magnetron sputtering

Magnetron sputtering (MS) is a scalable, reproducible, and precise method for depositing films on a substrate at ultrahigh vacuum chamber pressure. It uses magnetic field-

accelerated gaseous ions (e.g. argon ions) to eject atoms or molecules to be deposited from target materials [275]. The operation of magnetron sputtering is as follows:

- Magnetron system generates high-power microwave energy.
- The high-power microwave energy ionises the inert gas in the chamber to create gaseous ions (positive ions).
- A strong magnetic field accelerates the gaseous ions towards the target material (cathode).
- The accelerated gaseous ions eject atoms from the target materials.
- The ejected particles travel towards the substrate at high speed and get deposited.

Direct current (DC), pulsed DC and radio frequency (RF) magnetron sputtering are the classes of magnetron sputtering. The target is always negatively charged in DC magnetron sputtering, making it only suitable for sputtering conducting materials. DC magnetron sputtering is not used for low-conducting and insulating materials because these materials cause positive ions to accumulate on the target, resulting in the non-passing of current through the target materials. In RF magnetron sputtering, the polarity of the target alternates at high frequency, thereby preventing charge accumulation and ensuring that current flows through the target materials. RF magnetron sputtering is suitable for depositing insulators, conducting materials, polymers, and ionic and covalent compounds [276]. Titan magnetron sputtering systems can operate in RF, pulsed DC, and DC magnetron sputtering modes [277].

Magnetron sputtering has the advantages of improved film adhesion, precise deposition parameter control, scalability and superior morphology over other metal contact deposition methods [58–61]. However, researchers rarely use MS to deposit contacts on perovskite solar cells because it causes damage to the organic HTLs and HTL/perovskite interfaces [58,61,64].

2.7. Characterisation techniques

This section describes techniques applied in studying thin films and solar cells prepared in this project.

2.7.1. Atomic force microscopy

Atomic force microscopy (AFM) is a 3-dimensional imaging technique that uses the force of interaction between the probe and the sample molecules to measure the topology and morphology of the sample surface [278]. It uses probes (which consist of a cantilever and tips) installed in a probe holder for image capturing [279]. Tapping and contact modes are the two most common operational modes of AFM, and in each case, the probe oscillates at its resonance frequency.

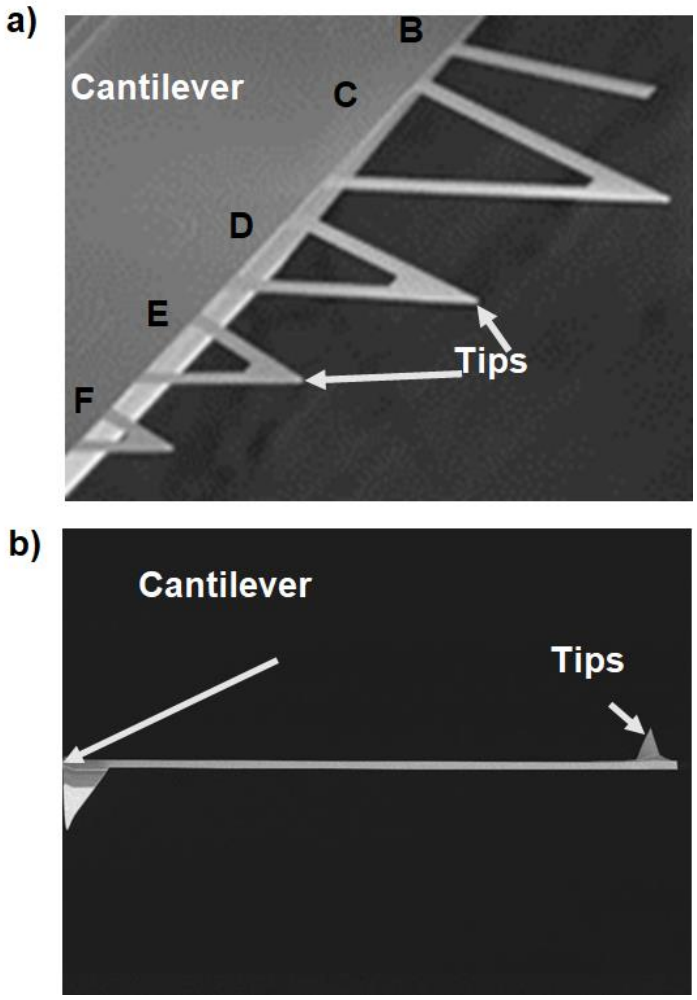

Figure 2.19: (a) Schematic of the MLCT probe and (b) schematic of SCM-PIT-V2 probe [280,281]. This project applied these probes.

In tapping mode, the oscillating probe tip lightly taps the sample surface, unlike in contact mode, where the tip has direct mechanical contact with the sample surface. Although tapping mode is valuable for soft and hard samples, it is crucial for soft samples that get

damaged when captured in contact mode. Also, probes with a small spring constant are preferred for soft samples [279].

AFM is vital in perovskite solar cell study as it helps determine and visualise film morphology, crystal sizes and thickness of the layers. It also provides visual evidence of pinholes and degradation in the films. Figures 2.19(a) and 2.19(b) present the schematics of the MLCT probe (for capturing soft samples) and SCM-PIT-V2 probe (for capturing hard samples), respectively. This project applied these probes for AFM studies.

2.7.2. Ultraviolet-Visible spectroscopy

Ultraviolet-Visible (UV-Vis) spectroscopy is a technique for determining the optical absorbance (Abs) and transmittance (T_x) of samples across the ultraviolet and visible regions of the electromagnetic spectrum [282]. It operates by measuring the intensity of light transmitted through a sample (I_o) and comparing it with the intensity of the incident light (or light transmitted through the reference) (I_i) [283]. Equation (2.15) shows the expression for calculating transmittance (T_x) from measured data [284].

$$T_x = \frac{I_o}{I_i} \times 100 \qquad (2.15)$$

Depending on the purpose of the study, the samples are deposited on suitable substrates such as FTO substrate, glass, or quartz glass (fused silica). For example, for energy bandgap (E_g) measurement, FTO and glass substrates are suitable for materials with narrow E_g (e.g., perovskite and Spiro-OMETAD), while quartz glass (fused silica, $193 \leq \lambda \leq 2000$ nm transmission) is required for materials with wide E_g (e.g., SnO_2).

Equation (2.16) presents an expression for determining the E_g from a plot of α^2E^2 against E for direct bandgap material. Equation (2.17) estimates E_g from a plot of $\alpha^{1/2}E^{1/2}$ against E for indirect bandgap material [285–287]. Other reports have shown that absorption coefficient (α) with absorbance [288] or absorption [289,290] against E also gives accurate E_g from the Tauc plots.

$$[\alpha(\lambda).E(\lambda)]^{\mathbf{2}} = \mathrm{K}\big[E(\lambda) - E_g\big] \qquad (2.16)$$

$$[\alpha(\lambda).E(\lambda)]^{\frac{\mathbf{1}}{\mathbf{2}}} = \mathrm{K}\big[E(\lambda) - E_g\big] \qquad (2.17)$$

UV-Vis spectroscopy is essential in PSC studies as it gives vital information on the absorbance characteristics, the perovskite layer's quality and the transport layers' transparency. It also gives information about the E_g of the layers and provides indirect evidence of layer degradation.

2.7.3. Fourier Transform Infrared Spectroscopy

Fourier Transform Infrared (FTIR) spectroscopy gives spectral and vibrational information relating to the functional groups, bond types, unique compositions, and quantity of the material in organic and inorganic samples. It operates in the mid-infrared region ranging from 400 cm^{-1} (25 µm wavelength) to 4000 cm^{-1} (2.5 µm wavelength) [291].

FTIR works in either transmission or attenuated total reflection (ATR) mode. In the transmission mode, the infrared spectrum is transmitted through samples deposited on substrates (e.g. zinc sulphide, potassium chloride, sodium chloride etc.) [292]. The problem with the transmission mode is that all the suitable substrates are expensive and brittle [293]. Conversely, ATR mode uses low-cost and highly reflective substrates (e.g. silver and aluminium) [294]. In ATR mode, the infrared beam transmitted through the sample gets reflected by the substrate and then re-transmitted through the sample [293]. FTIR technique is quite relevant in perovskite solar cell study as it provides information about the functional groups, bond types and the degree of formation of the samples. It also gives direct evidence of layer degradation.

2.7.4. X-ray diffraction

X-ray diffraction (XRD) is valuable for the phase identification of crystalline material. It provides information on the dimension of unit cells, atomic spacing, strain (shift in peak position, peak broadening), film thickness, degree of crystallization (peak intensity), preferred orientation (peak position) and grain size (peak broadening and dislocation density) using constructive interference of X-ray scattered by the material [177,295]. Target material (e.g. copper, iron, nickel, Zirconium and Molybdenum) emits X-rays when bombarded by high-energy electrons from the heated cathode of the X-ray machines [296]. The wavelength of X-rays is characteristic of the target materials.

$$z = \frac{\rho.\lambda}{\beta\cos\theta} \qquad (2.18)$$

Equation (2.18) estimates grain size (z) from the XRD pattern [297] where β is the Full-Width Half Maximum (FWHM), $\boldsymbol{\lambda}$ is the x-ray wavelength of the target, θ is half of the angle at the peak position and ρ is the grain shape constant which is 0.9 for a spherical crystal [297].

In PSCs study, XRD provides vital information on each layer's crystallinity, thickness, crystal sizes and orientation. It also provides direct evidence of the degradation of the perovskite layers.

2.7.5. Ultraviolent photoelectron spectroscopy

Ultraviolet photoelectron spectroscopy (UPS) measures the kinetic energy spectra of electrons emitted from a sample material when the electrons on the VB of the material absorb incident ultraviolet photons of sufficient energy. This technique is vital in determining the sample's VB, Fermi level and WF. UPS equipment uses aluminium Kα radiation (hf=1486.7 eV) for the measurement of the core levels as well as another discharge lamp (e.g. Neon, Helium I, Neon II and Helium II) that provides the ultraviolet photon (Kα) [298–301]. Equation (2.19) is the expression for estimating VB from UPS spectra where E is the photon energy, WF is the work function, and E_{max} is the onset energy [302]. For accurate work function determination, a negative bias voltage (-2 V to -5 V) is applied to the sample to enable the measurement of the secondary electron cut-off [303].

$$VB = -(E + WF) + E_{max} \qquad (2.19)$$

In the perovskite solar cell study, the UPS provides vital information on the films' work function (WF), Fermi level and VB.

2.7.6. Field emission scanning electron microscopy

Scanning electron microscopy (SEM) is a characterisation method that captures the images of samples using an accelerated electron beam [304]. Field emission scanning electron microscope (FE-SEM) and thermionic emission scanning electron microscope

(TE-SEM) are the two types of scanning electron microscopes. FE-SEM is an ultra-high-resolution electron microscope that scans and captures sample images using a high-energy electron beam from a field emission electron gun (cold cathode) [305]. It has a much higher resolution than TE-SEM as a field emission electron gun produces about 1000x more electrons than the thermionic emission electron gun (hot cathode) used in TE-SEM [305,306]. Also, FE-SEM requires much higher vacuum conditions than thermionic emission scanning electron microscope (TE-SEM) [306]. A high electric field applied across the cathode causes the emission of electrons from the field emission gun, unlike thermionic emission guns (hot cathodes) that emit electrons from heated cathodes [307]. Top-view SEM images provide vital information on surface morphology, crystal sizes, grain compactness, grain boundaries and pinholes, which are relevant in perovskite solar cell study. Also, the cross-sectional view measurement gives vital information about the thickness of each layer in perovskite solar cells.

2.7.7. 4-Probe measurement

The 4-Probe is an instrument that uses four electrodes to measure the resistivity, sheet resistance and conductivity of either bulk or thin-film materials. It uses the voltage difference (potential drop) between two of the four electrodes to determine the sheet resistance (conductivity or resistivity) of test samples [308]. 4-Probes work by passing current (I) through the samples from the two outer probes (current probes) and measuring the voltage (V) across the inner probes (voltage probes). The sheet resistance of samples measured using 4-Probe is independent of the contact resistances of the probes and connectors [309]. Equation (2.20) shows the expression for estimating the sheet resistance of a sample with the thickness (d) $\leq$ 0.4x using 4-Probe [308,310–312]. Figure 2.20 presents the generic schematics of the 4-probe.

$$\text{Sheet resistance } = \frac{\pi}{\ln(2)} . \frac{V}{I} \qquad (2.20)$$

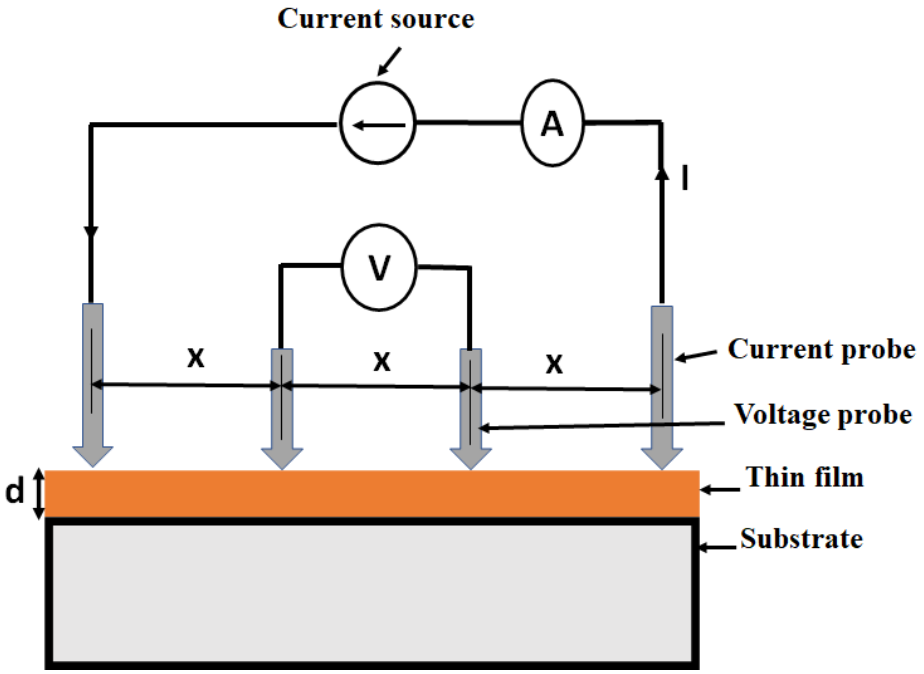

Figure 2.20: Generic schematics of 4-probe [309].

On the other hand, a 2-Probe (e.g. Ohmmeter) uses two electrodes as both current and voltage probes to measure the resistive properties of samples [313,314]. As a result, the 2-Probe measurement depends on the contact resistances of the probes and connectors. The accuracy of the 4-Probe technique made it suitable for this project [313].

2.7.8. Current-voltage measurements

Current-voltage (I-V) measurement is a technique for determining the I-V characteristics of electrical/electronic devices. The I-V measurement involves supplying increasing voltages across the device and measuring the current that flows through the device at each voltage level. In this measurement, a voltmeter connected in parallel to the device measures the voltage across the device. In contrast, an ammeter connected in series to the device measures the current through the device [315]. For devices with sourcing ability, switching circuits (e.g. transistors) regulate the devices' voltage and current output while voltameters and ammeters measure these parameters[316]. For example, Figure 2.21 shows a simple circuit for measuring the I-V characteristics of sourcing devices. The circuit works as follows [316,317]:

- An increasing ramp voltage (V_{ramp}) is applied to the Op-amp to increase the gate voltage of the field-effect transistor (FET).

- As the FET gate voltage increases, the current flow from the solar cell via the Source-Drain pins of the FET transistor also increases.
- The oscilloscope measures the voltage (V) across the solar cell and the voltage (V_R) that drops across the resistor (R) connected in series to the solar cell at each V_{ramp},
- The current (I) supplied by the solar cells is computed using equation (2.21).

$$I = \frac{V_R}{R} \qquad (2.21)$$

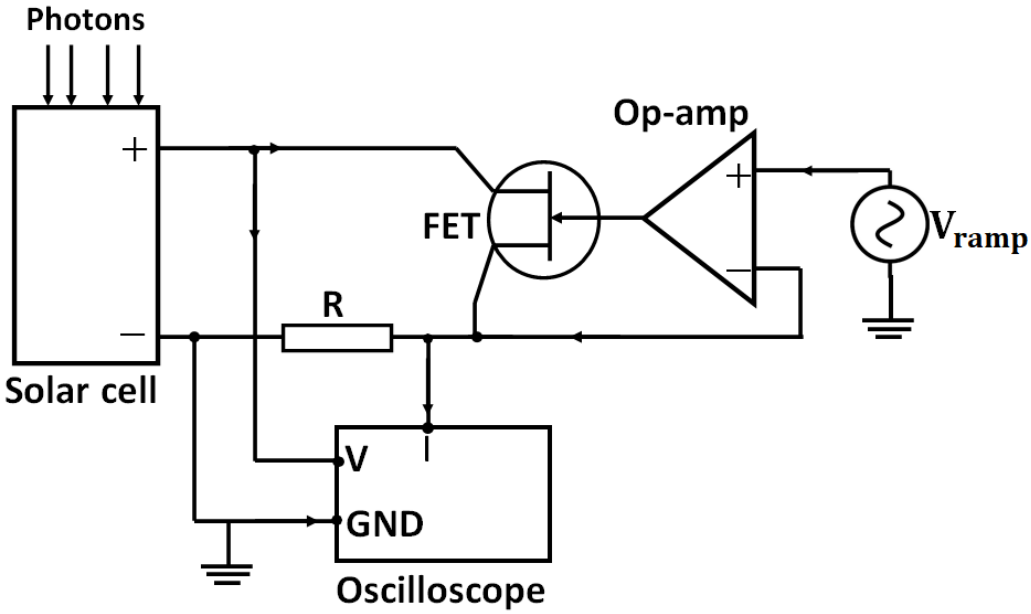

Figure 2.21: A circuit for measuring I-V characteristics of solar cells [316]

In practice, the SMU (e.g. Autolab PGSTAT32, Keithley 2400 and Keysight B2912A) [318–321] measures the I-V characteristics, while a solar simulator (e.g. Newport Oriel LCS-100) provides the AM1.5 global spectrum. The I–V measurement error depends on the characteristics and resolution of both SMU and the solar simulator.

A solar simulator is a controllable indoor test facility that provides illumination that approximates the AM1.5 global spectrum under laboratory conditions for testing photovoltaic devices. Solar simulators are classified using spectral mismatch, spatial non-uniformity, and temporal instability of the illumination. Table 2.9 presents ASTM E927-10 classification of spectra qualities of Newport solar simulators [77,78,321]. Xenon,

halide, quartz tungsten halogen and light-emitting diode lamps are widely used in solar simulators because they have good spectral qualities [77].

Table 2.9: ASTM classification of Newport solar simulators.

Solar simulator	Spectral mismatch (%)	Spatial Non-Uniformity (%)	Temporal Instability (%)	Class
Oriel Sol3A	0.75–1.25	2	2	AAA
Oriel VeraSol-2	0.75–1.25	2	2	AAA
Oriel MiniSol LSH-7320	0.75–1.25	5	2	ABA
Oriel 94042A	0.75–1.25	5	2	ABA
Oriel LCS-100	0.75–1.25	5	5	ABB

2.7.9. Impedance spectroscopy

Impedance spectroscopy (IS) is a technique for measuring the impedance characteristics and frequency response of electrical/electronic devices over a frequency range. IS measurement involves supplying sinusoidal voltage input V(t) to a device at different illumination conditions and measuring the sinusoidal current output I(t) from the device [18,322,323]. Equation (2.22) presents the expression for calculating the complex impedance parameters of the device from the Fourier transform of V(t) and I(t) [18,92,324].

$$Z(\omega) = \frac{V(\omega)}{I(\omega)} \qquad (2.22)$$

IS measurement provides information on the impedance model, parameters and frequency response of devices [325]. In IS measurement, the impedance measured at the upper cut-off frequency relates to the R_s of the solar cell. In contrast, the impedance at the lower cut-off frequency is associated with the junction resistance (R_j), shunt resistance and series resistance of the solar cells [326]. At the resonance frequency, the measured impedance relates to the impedance characteristics of the junction and shunt resistance

[326,327]. IS measurement could be conducted at different dc voltage biases and illumination to reveal some inherent properties of the device [18,322,323].

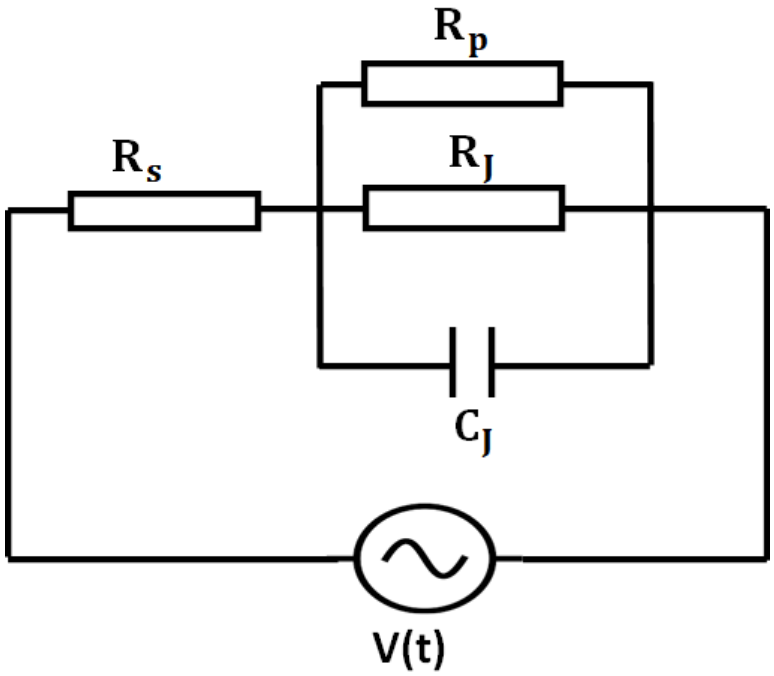

Figure 2.22: AC equivalent circuit of a forward-biased PSC [328].

Figure 2.22 shows the ac equivalent circuit of a solar cell, with C_J representing the capacitance of the n – i – p junction [328]. The circuit oscillates at resonance frequency when the reactance (X_c) of the junction capacitance is equal to the resultant resistance of R_j and R_p which are in parallel. The resonant frequency is the natural frequency at which an RC circuit oscillates at the highest amplitude [329]. Equation (2.23) presents the expression for extracting junction capacitance (C_J) from impedance spectroscopy (IS) measurement [330].

$$C_J = \frac{1}{\omega . X_C} \qquad (2.23)$$

The junction capacitance (C_J) is directly proportional to the carrier density (N) of the devices, as reported in the literature [18].

2.8. Review of recent literature relevant to the key studies

Many studies have reported new processes for preparing efficient and stable PSCs in the air [26,34,37,38,245–248,331–333]. For example, reports have shown that additive processes enhance the efficiency and stability of devices. Hence, Tai et al. showed that modifying $MAPbI_3$ layers with $Pb(SCN)_2$ additive improves the stability of air-fabricated PSCs by 26.7% [26]. Also, Oku et al. reported that modifying $MAPbI_3$ layers with decaphenylcyclopentasilane increased the PCE of devices by 5% [43]. In contrast, Zheng et al. improved the PCE of the devices by 2% by modifying the perovskite material with 3-aminopropyltrimethoxysilane [44].

Reports showed that humidity-resistant antisolvent treatment improved the performance of PSCs prepared in ambient air. Consequently, Troughton et al. reported enhanced efficiency and stability for devices based on $MAPbI_3$ layers treated with ethyl ethanoate antisolvent [34]. Later, Yang et al. demonstrated that devices treated with methyl ethanoate have improved PCE and stability relative to devices treated with ethyl ethanoate [37]. Studies have also reported that mixed antisolvent treatment improves device performances [245–248]. In addition, studies show that magnetron sputtering improved film adhesion, precise deposition parameter control, scalability and superior metal contact morphology [58–61].

This section reviews only works of literature on silane additive and mixed antisolvent processes for improving the performance of perovskite solar cells and metal contact deposition by magnetron sputtering. These three areas of literature are relevant to the key studies in the project.

2.8.1. Recent studies on metal contact deposition by magnetron sputtering

Magnetron sputtering (MS) has the advantages of improved film adhesion, precise deposition parameter control and scalability, which may offer a better quality metal contact over thermal evaporation [58–61]. However, magnetron sputtering causes damage to the soft organic hole transport layer (HTL) and perovskite layers when the deposition parameters are not suitably optimised [63,66]. This damaging effect is due to the impact of high kinetic energy metal atoms from the sputtering target. Consequently, MS has limited application in PSC fabrication. In addition, the HTL gets damaged when metal particles remove some HTL or dope into the HTL/perovskite interface to form

recombination sites [64]. The extent of penetration and the number of metal dopants in the HTL/perovskite interface depend on the particle kinetic energy and deposition rate, respectively [58]. Numerous metal particles dope in the perovskite layer at remarkably high kinetic energy, leading to severe performance degradation. Because of this, only a few research studies reported using magnetron sputtering for depositing metal contact in PSCs [58,61–66]. To date, most of these studies focused on the effect of magnetron sputtering of different metal contacts on the performance of PSCs [62,63,65,66]. In addition, a few studies investigated the dependence of PSC performance on the thickness of metal electrodes [65,66] and the influence of deposition rate [58]. However, few authors have conducted comparative studies of PSCs with metal contacts deposited using thermal evaporation, magnetron sputtering and e-beam techniques [58,61,64]. Furthermore, these researchers conducted their studies in a controlled laboratory environment (glovebox), and the best efficiencies reported were 18.32% and 15.97% for devices with sputtered Au [58] and Ag contacts [63]. Notwithstanding these reports, a systematic study of the effect of metal contact sputtering parameters on the performance of PSCs is still lacking, especially for devices processed in ambient laboratory environments relevant to real-life manufacturing conditions.

2.8.2. Recent studies on performance enhancement using silane additive

Studies showed that modifying perovskite layers with silane additives improved the PCE and stability of PSCs [43,44,51–53,334]. This is because silyl groups readily form crosslinking bonds with perovskite molecules, enhancing the bond strength and protecting against humidity [51,52]. Furthermore, reports show that a fluoride group enhances silane additives' effectiveness in strengthening intermolecular bonds in perovskites and minimising decomposition [53]. Therefore, silane materials are applied as passivation agents or additives in perovskite layers to enhance the stability of the layers. However, despite the benefits of silane materials in strengthening the bond strengths in perovskites, quite a few studies have investigated the effect of silane additives on the performance of PSCs [43,44,334]. Oku et al. conducted the first study on the silane additive process. The researchers reported devices with PCE that improved from 5.82% to 10.46% when the decaphenyl cyclopentasilane additive was incorporated in $MAPbI_3$ layers [43]. In 2019, Xie et al. reported improved stability and PCE for devices based on perovskite layers modified with a 3-Mercaptopropyltrimethoxysilane additive [334]. In

2021, Zheng et al. improved the PCE of the devices from 18.85% to 20.72% by adding 3-aminopropyltrimethoxysilane in perovskite [44]. In addition, the researchers demonstrated that devices with 3-aminopropyltrimethoxysilane additives degraded by about 40% after 400 hours at 50-60% compared to about 80% degradation for control devices.

Although these studies contributed immensely to silane additive processes for preparing PSCs with enhanced PCE and stability, the researchers conducted their fabrications in inert atmospheres, where exposure to moisture is negligible. Hence, a systematic study of the effect of silane additives on the PCE and stability of PSCs fabricated in the air at high relative humidity, relevant to real-life manufacturing conditions, is still lacking.

2.8.3. Recent studies on performance enhancement via mixed antisolvents

Antisolvents play significant roles in improving the PCE and stability of PSCs. The effectiveness of any antisolvent depends on its vapour pressure, water solubility and dipole moment at room temperature [37]. The high water solubility of methyl ethanoate and ethyl ethanoate has proven effective in protecting $MAPbI_3$/DMSO adduct from interacting with moisture during perovskite film deposition, particularly in high relative humidity [37]. Antisolvents with high vapour pressure and low boiling point accelerate the evaporation of DMM and moisture around the films [37]. However, these antisolvents have high dipole moments that enable them to dissolve and quickly extract DMSO from the perovskite solution, resulting in less DMSO in the $MAPbI_3$/DMSO adduct. Quick extraction of DMSO from the adducts could lead to a fast nucleation process and poor film morphology [35,36].

Additionally, antisolvents with high dipole moments remove more MAI from perovskite solution, leading to low grain compactness [137,205,335,336], reduction in the film thickness and introduction of lead (II) iodide particles [337–339]. On the other hand, antisolvents with relatively low dipole moments (e.g. trichloromethane and methylbenzene) dissolve less DMSO. Therefore, they cannot extract DMSO quickly from the perovskite solution, leaving excess DMSO in the $MAPbI_3$/DMSO adduct. Excess DMSO in $MAPbI_3$/DMSO adduct can result in significant rewetting, a slow nucleation process, poor film morphology and low grain compactness, especially at high humidity [35,36]. Therefore, mixing different antisolvents helps optimise the amount of DMSO in

the $MAPbI_3$/DMSO adduct [36]. A convenient method of reducing the solubility of DMSO in humidity-resistant antisolvents without affecting their moisture protection ability is by adding other antisolvents with a lower dipole moment [35]. This approach has been applied to the fabrication of PSCs to achieve improved performances [245–248]. Wang et al. conducted the first study on the effect of antisolvent mixing on PSC performance in 2017. They reported that devices treated with chlorobenzene mixed with 2-propanol achieved the best PCE of 17.8%, while PSCs treated with chlorobenzene (100%) attained the best PCE of 16.1% [245]. Similarly, Yu et al. reported that devices treated with trichloromethane mixed with hexane exhibited a PCE of 17.1%, whereas devices treated with trichloromethane (100%) achieved a PCE of 15.8% [249]. In 2018, Chen et al. reported improved performance for the devices treated with 2-butanol mixed with chlorobenzene or 2-butanol mixed with ethoxyethane antisolvents [35]. Since 2018, reports have shown that mixed antisolvents such as methylbenzene mixed with ethoxyethane [246], methylbenzene mixed with dichlorobenzene [246], and 2-methyl pentane mixed with ethyl ethanoate improve the PCE and stability of devices. Although these studies contributed immensely to developing antisolvent mixing techniques for PSC fabrication, they were all conducted in a glovebox of exceptionally low humidity (0.1 – 1.0 ppm or 0.00001 - 0.0001%). Very recently, Jung *et al.* reported that at relative humidity > 40%, devices treated with 1-butoxybutane (30%) mixed with ethoxyethane (70%) achieved improved stability and PCE of 20.55% [39]. However, despite recent studies, extensive study of the effect of mixed antisolvent on the PCE and stability of PSCs processed in ambient environments is still lacking.

2.9. Summary

This chapter conducted the overview of the operation, factors that affect the performance cells, energy band diagram, energy band matching, junction formation and performance characteristics and precisely presented the observations and explanations. Furthermore, this chapter discussed the basics of PSCs, structures, fabrication, and characterisation techniques. Finally, the moisture degradation routes of perovskite solar cells and the mitigation procedures, which are highly relevant to the key study of this thesis, are reviewed and discussed.

Chapter 3: Materials and Methods

3.1. Introduction

This chapter describes the procedures for preparing perovskite solar cells (PSCs) in ambient air and measurement techniques used for characterisation. This chapter will extensively elaborate on processes for cleaning FTO substrates and preparing electron transport layers, perovskite layers, hole transport layers, and top electrodes. The equipment employed for solar cells and film characterisation is discussed, together with the test results, to demonstrate the reliability of the equipment. It will also provide information on materials, their sources, and other relevant details to allow for a reproduction of the experiments.

3.2. Perovskite solar cell fabrication

This section discusses the cleaning of FTO substrates and the preparation of other layers in PSCs. Figure 3.1 shows the FTO/SnO_2/$MAPbI_3$/Spiro-OMETAD/Ag structure applied for PSCs fabrication in this project. This structure was adopted from the study reported by Yang et al. [37], except for replacing gold electrodes with silver electrodes.

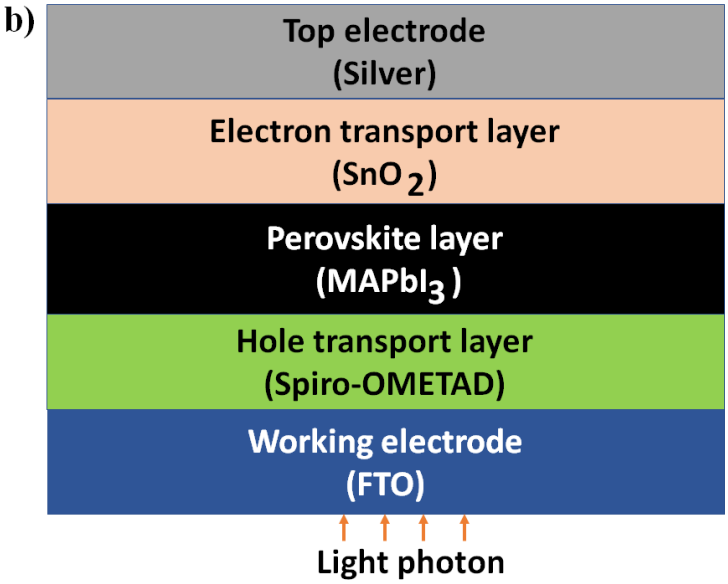

Figure 3.1: Structure of devices fabricated in this project.

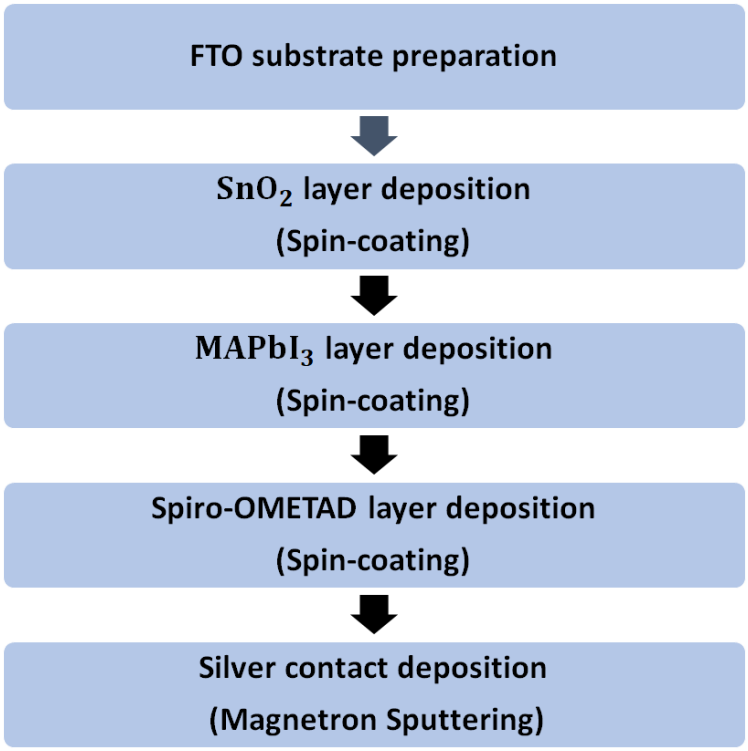

Figure 3.2: Flow chart of PSCs fabrication

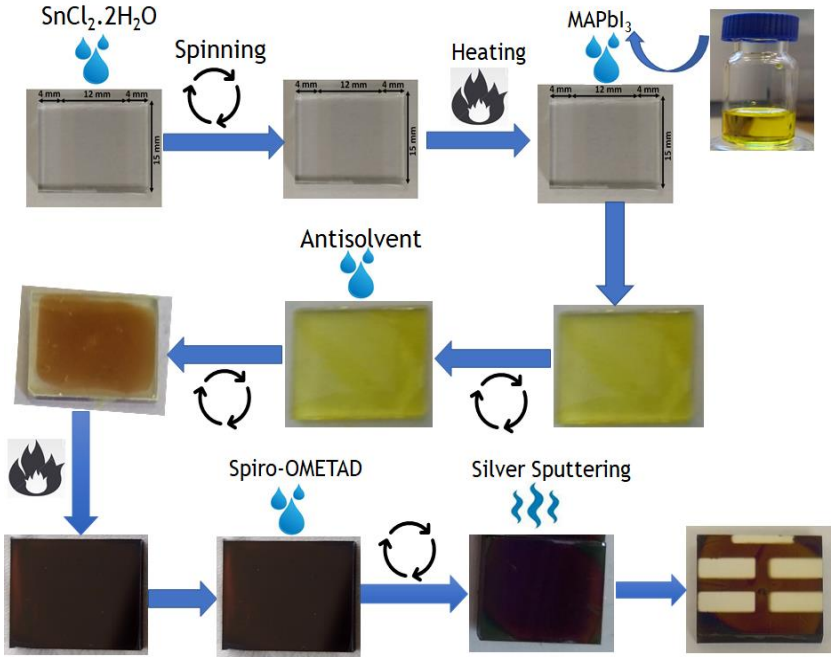

Figure 3.3: Products at each step of device fabrication

Figures 3.2 and 3.3 show the fabrication flow chart of the PSCs and the products at each stage of the fabrication process. Figure 3.4 presents the Laurell spin-coater (WS-650Hz-23NPPB) utilized in depositing solution-processed layers (SnO_2, $MAPbI_3$ and Spiro-

OMETAD). All the solution-processed films were deposited at relative humidity (RH) ranging from 40-55% (see Chapters 4 -8 for the actual RH range for each study).

Figure 3.4: Laurell spin-coater used for depositing solution-processed layers

3.2.1. Cleaning of Fluorine-doped Tin Oxide substrates

Pingdingshan Mingshuo Technology Co. Ltd (TEC-15), and Kintec Company LTD (TEC-8) supplied the Fluorine-doped Tin Oxide (FTO) substrates. The FTO substrates have dimensions of 15 mm×20 mm. This project used Laser-patterned FTO substrates to reduce the likelihood of edge defects and short-circuiting problems in the devices. Figures 3.5(a) and 3.5(b) show the design and a sample of the FTO substrate with dimensions. The FTO substrates were thoroughly cleaned before device fabrication for a clean surface. Firstly, the FTO substrates were cleaned using diluted Hellmanex (III) solution and then rinsed thrice with deionized water. Later, the FTO substrates were successively sonicated in deionized water, 2-propanone, and 2-propanol at 50℃ for 10 minutes using an ultrasonic bath (Allendale ultrasonic bath, US-CU-DI-9L). Finally, the FTO substrates were dried using nitrogen gas (with an air gun) before they were treated in the ultraviolet (UV)-ozone cleaner (Ossila UV-ozone cleaner, L2002A2-UK) for 10 minutes to improve surface energy and wettability [340–344]. Figures 3.6(a) and 3.6(b) show the ultrasound bath and UV-ozone cleaner used for the experiments.

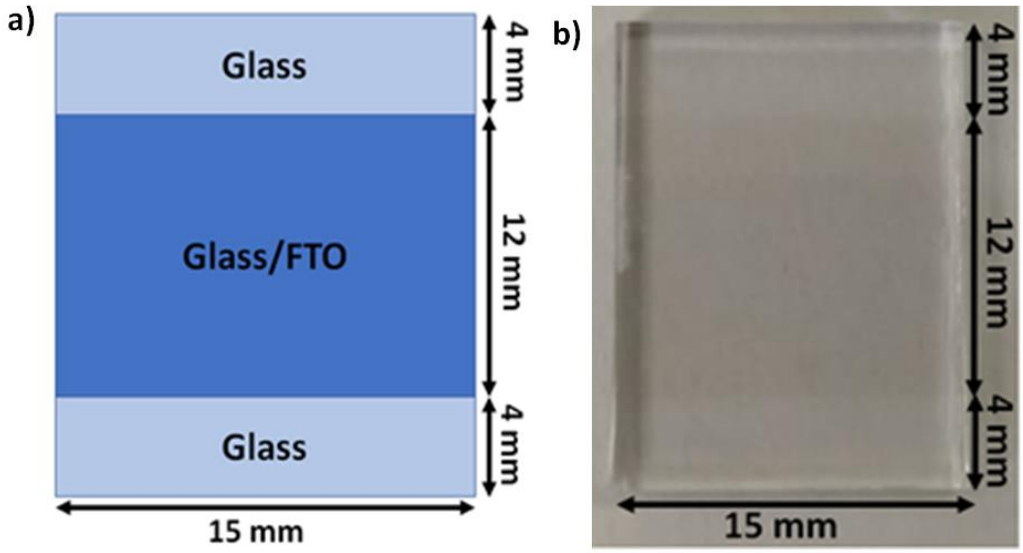

Figure 3. 5: (a) The design of the FTO substrate and (b) a picture of a sample FTO substrate

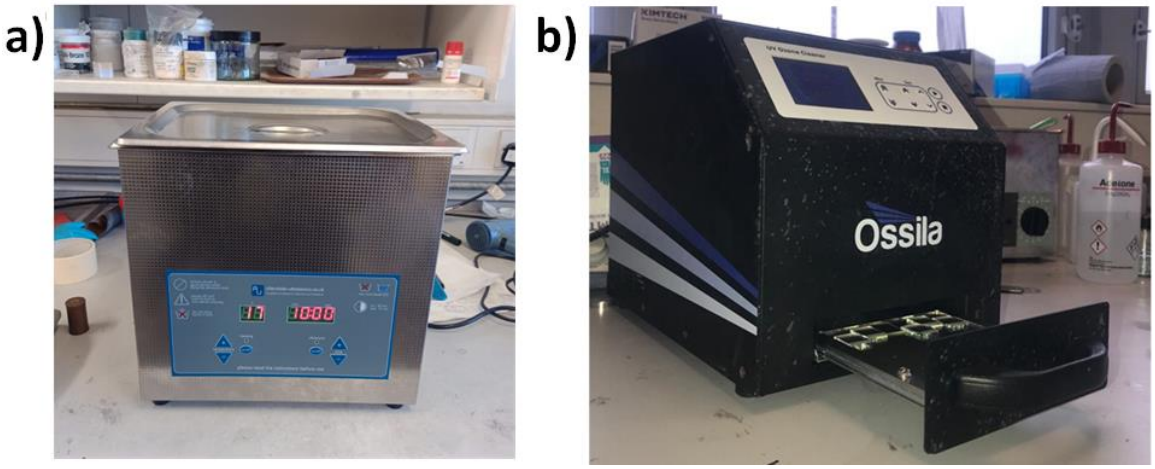

Figure 3.6: (a) Allendale ultrasonic bath and (b) Ossila UV-ozone cleaner

3.2.2. Electron transport layer preparation

The SnO_2 layers were prepared from tin(II) chloride dihydrate ($SnCl_2.2H_2O$, 99.995%) bought from Sigma Aldrich and absolute ethanol purchased from Fisher Scientific. Figures 3.7(a) and 3.7(b) and Table 3.1 presents the chemical structure and properties of ethanol and $SnCl_2.2H_2O$.

The required amount of $SnCl_2.2H_2O$ (see Chapters 4-8 for the exact amount) was dissolved in ethanol. Next, the solution was stirred at 50 ℃ and 300 rpm (using Corning™ Hot Plate Stirrer, Glass Ceramic, 1150 rpm) for 4 hours to achieve

homogenous solutions before being filtered using 0.45 µm syringe filter (nylon). Then, 90 µl of the $SnCl_2.2H_2O$ solution was spin-coated on the FTO substrates at 4000 rpm for 30 seconds.

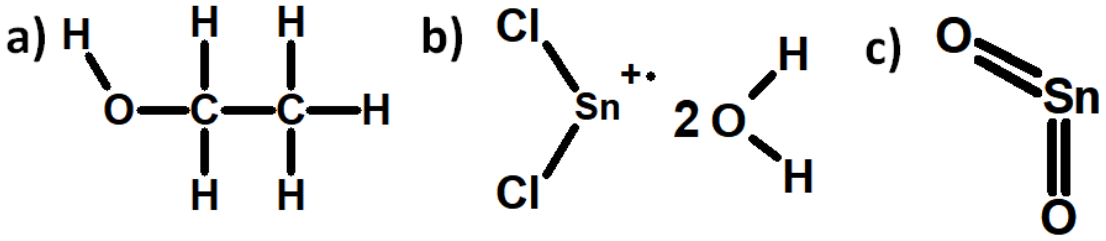

Figure 3. 7: Chemical structures of (a) ethanol, (b) tin(II) chloride dihydrate and (c) tin(IV) oxide

The samples were placed on the hotplate at 110℃ (Corning™ Hot Plate Stirrer, Glass Ceramic, 550℃), covered with a petri dish to ensure uniform temperature distribution, and annealed at 180℃ for 60 minutes to convert the $SnCl_2.2H_2O$ films to the SnO_2 films. The chemical structure of the SnO_2 formed is shown in Figure 3.8(c). The annealed samples were allowed to cool to 110 ℃ before being removed from the hotplate to avoid the likelihood of cracks arising from non-uniform expansion. The deposited SnO_2 layers were treated in a UV-ozone cleaner for 10 minutes before the deposition of the perovskite layer.

3.2.3. Perovskite layer preparation

The $MAPbI_3$ layers were prepared from lead(II) iodide (PbI_2, 99.999%) sourced from Alfa Aesar and methylammonium iodide (MAI, 99%) bought from Sigma Aldrich. Across Organics supplied dimethyl methanamide (DMM, 99.8%), chlorobenzene (99.6%) and methyl ethanoate (99%). Fisher Scientific provided methylbenzene, trichloromethane and chlorodimethyl(pentafluorophenyl)silane (CPFS, 96%). Alfa Aesar delivered dimethyl sulphur(IV) oxide (DMSO, 99.8%). This project used CPFS as an additive for the perovskite layer (see Chapter 7 for details). Figures 3.8(a) - 3.8(i) and Table 3.1 show these materials' chemical structures and properties.

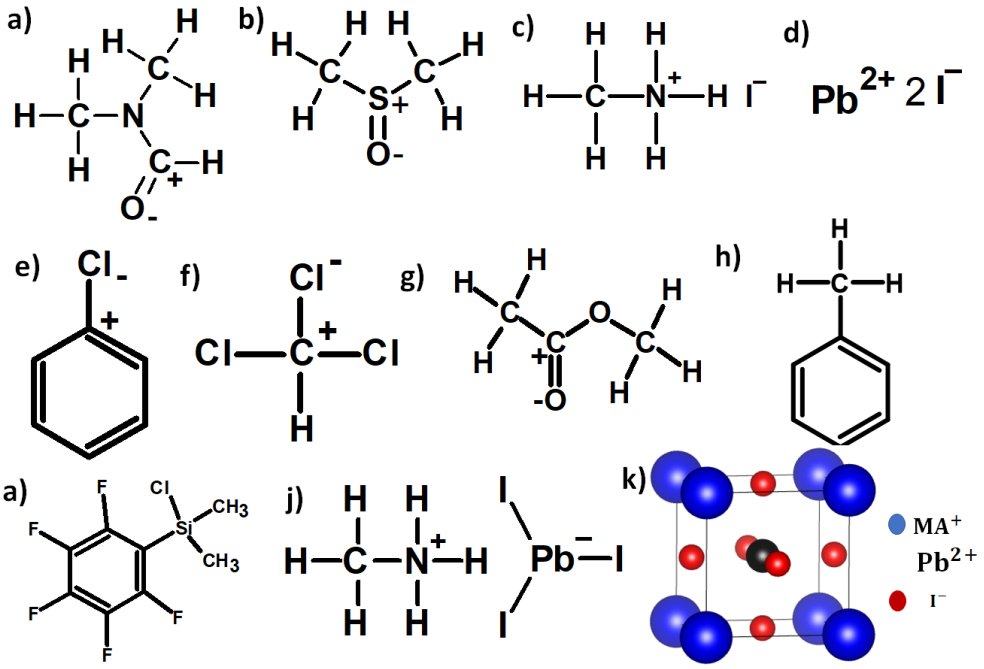

Figure 3.8: Chemical structures of (a) dimethyl methanamide, (b) dimethyl sulphur(IV) oxide, (c) methylammonium iodide, (d) lead(II) iodide, (e) chlorobenzene, (f) trichloromethane, (g) methyl ethanoate, (h) methylbenzene, (i) chlorodimethyl(pentafluorophenyl)silane, (j) $MAPbI_3$ and (k) crystal structure of $MAPbI_3$

The MAI, PbI_2 and chlorodimethyl(pentafluorophenyl)silane (see chapters 4-8 for the exact amount of solutes) were dissolved in a mixture of solvents containing 800 µl of DMM and 200 µl of DMSO. The perovskite solution was stirred at 50 °C and 300 rpm for 11 minutes to achieve a homogenous solution before filtering using a 0.45 µm syringe filter (nylon). Later, 90 µl of perovskite solution was spin-coated on the surface of the SnO_2 layer at 4000 rpm for 30 seconds. The antisolvents (see the exact volume and antisolvents in chapters 4-8) were dropped on the spinning perovskite films after the first 15 seconds to induce supersaturation and crystallisation. In addition, the antisolvent was dropped from a height of 2 mm above the film surface to minimise the impact force on the wet film and hence the resultant damage. Finally, the samples were placed on a hotplate, covered with a petri dish, and then annealed at 110 °C for 15 minutes to form dark $MAPbI_3$ films. Figures 3.8(j) and 3.8(k) present the chemical and crystal structure of $MAPbI_3$. The crystal structure has a tetrahedral shape, with the MA^+ occupying the vertexes of the cube, Pb^+ occupying the cube's centre, and I- occupying the cube's six (6) faces.

3.2.4. Hole transport layer preparation

Borun New Materials supplied the 2,2',7,7'-tetrakis (N, N -di-p -methoxyphenylamino)-9,9'- spirobifluorene (Spiro-OMETAD, 99.8%) for hole transport layers. Alfa Aesar delivered lithium bis(trifluoromethylsulfonyl) amine (Li-TFSI, 98%). Sigma Aldrich provided Tris(2-(1H-pyrazol-1-yl)- 2-methylpropan-4-yl pyridine) cobalt (III) tris(bis(trifluoromethylsulfonyl) amine) (FK209, 98%) and 2-methylpropan-4-yl pyridine (MPPD, 96%). This project used Li-TFSI, FK209 and MPPD as additives for Spiro-OMEAD. Figures 3.9(a) – 3.9(d) and Table 3.1 present the chemical structures and properties of Spiro-OMETAD, Li-TFSI, FK209 and MPPD, respectively.

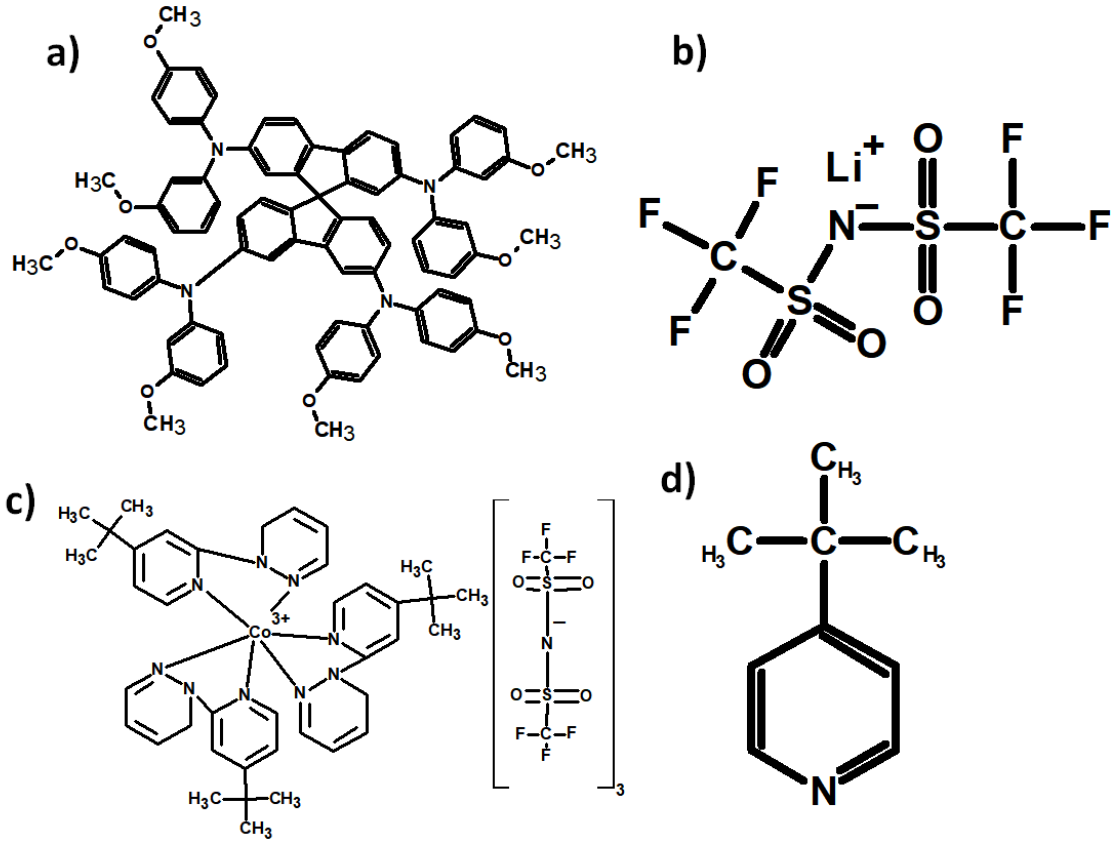

Figure 3. 9: Chemical structures of (a) Spiro-OMETAD, (b) Li-TFSI, (c) FK209 and (d) 2-methylpropan-4-yl pyridine.

90 mg of Spiro-OMETAD powder was dissolved in 1 ml of chlorobenzene. The Spiro-OMETAD solution was doped with 36 µl of MPPD, 22 µl of Li-TFSI solution (520mg/ml in ethane nitrile), and FK209 solution (300mg/ml in ethane nitrile) (see Chapters 4-8 for the amounts of FK209 solution). Li-TFSI, FK209 and MPPD additives were added to the Spiro-OMETAD solution to enhance the electrical and energy band properties of the HTL

[212,213]. The HTL solution was stirred at 30℃ and 300 rpm for 30 minutes. Next, a 90µl of the HTL solution was spin-coated on the perovskite layers at 4000 rpm for 30 seconds. Finally, the HTL films oxidized in a desiccator for 10 minutes before the deposition of the silver contacts.

Table 3. 1: Properties of chemicals used in this project

Material	Vapour pressure (mmHg) at 23℃	Water solubility (%) at 23℃	Boiling point (℃)	Dipole moment (D)
Chlorobenzene	9	0.05	131.00	1.55
Trichloromethane	160	0.50	61.15	1.04
Methyl ethanoate	173	25.00	56.90	1.71
Methylbenzene	21	0.07	110.00	0.38
Ethanol	44.6	Miscible	79	1.66
Chlorodimethyl (pentafluorophenyl) silane	0.5	hydrolyse	253.7	
Dimethyl sulfoxide	0.42	miscible	189	3.96
Dimethyl methanamide	3.87	Miscible	153	3.86
2-methylpropan-4-yl pyridine	0.5	6.9mg/ml	196.5	3.29
Lead (II) iodide		0.76 mg/ml		
Tin (II) chloride dihydrate		839mg/ml		
Methylammonium iodide		N/A		
FK209		N/A		
Li-TFSI		6000mg/ml		
Spiro-OMETAD		sparingly soluble		

3.2.5. Top electrode sputtering

Silver contacts were deposited from a 2-inch diameter, 0.125-inch-thick silver sputtering target (Ag, 99.99%) purchased from Kurt J. Lesker Company Ltd. Figures 3.10 shows a picture of the Pulsed Laser Deposition system (PLD2000) with Titan magnetron sputtering subsystem used for Ag contact deposition. First, the sputtering chamber was evacuated to a pressure of 10 µTorr and then refilled with argon gas before the deposition of Ag contacts at 20°C (see Chapters 4-8 for details of other sputtering parameters). Next, the Ag contacts were sputtered on the Spiro-OMETAD layer using a 2.2-inch substrate holder that simultaneously accommodates four 20 mm ×15 mm substrates. The holder was also designed to deposit four devices of 0.15cm^2 active area on each substrate (the mask for preliminary studies in Chapter 4 has a different design). Figures 3.11(a) and 3.11(b) show the substrate holder used for Ag contact deposition and a substrate with four deposited active devices, respectively.

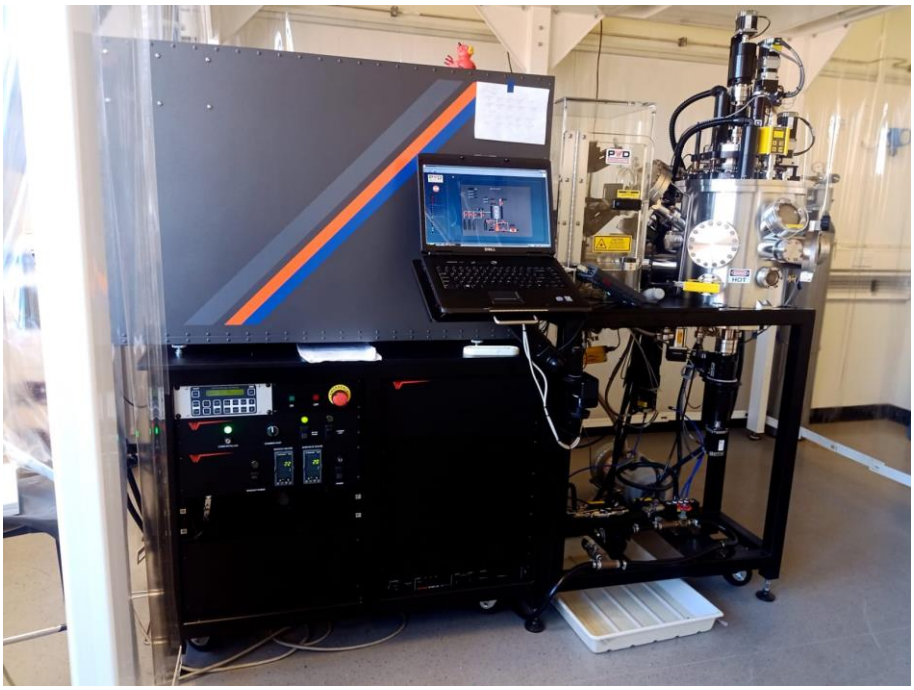

Figure 3.10: Pulsed Laser Deposition system with Titan magnetron sputtering subsystem.

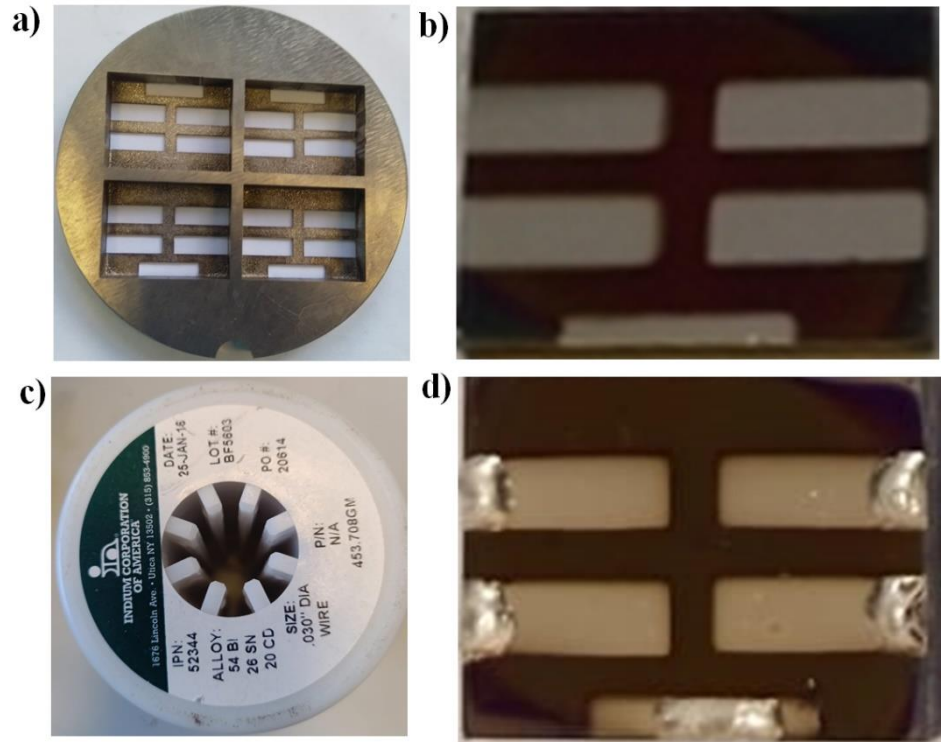

Figure 3.11: (a) Ag sputtering mask, (b) substrate with four deposited active devices, (c) low-melting-point $Bi_{0.54}Sn_{0.26}Cd_{0.2}$ soldering wire and (d) substrate with soldered active devices.

Figure 3.11(c) shows a low melting-point (157°C) Bismuth Tin Cadmium Alloy ($Bi_{0.54}Sn_{0.26}Cd_{0.2}$) soldering wire, used for soldering the contacts of the active devices to protect the Ag contacts from damage during testing. Figure 3.11(d) presents the substrate with solder-protected active devices. During soldering, high temperature removes the $MAPbI_3$ and Spiro-OMETAD layers around the soldered area to ensure that the solder/Ag layer made good contact with FTO (cathode) and the glass/Ag (at the anodes).

3.3. Equipment and Characterisation

This project employed various techniques to characterise the films and devices prepared in this project to ensure they have the required electrical, optical, morphological, and photovoltaic properties. Figure 3.12 presents schematically all the equipment employed in this study. The function and reasons for using these facilities are discussed briefly in subsections 3.3.1 to 3.3.9 below.

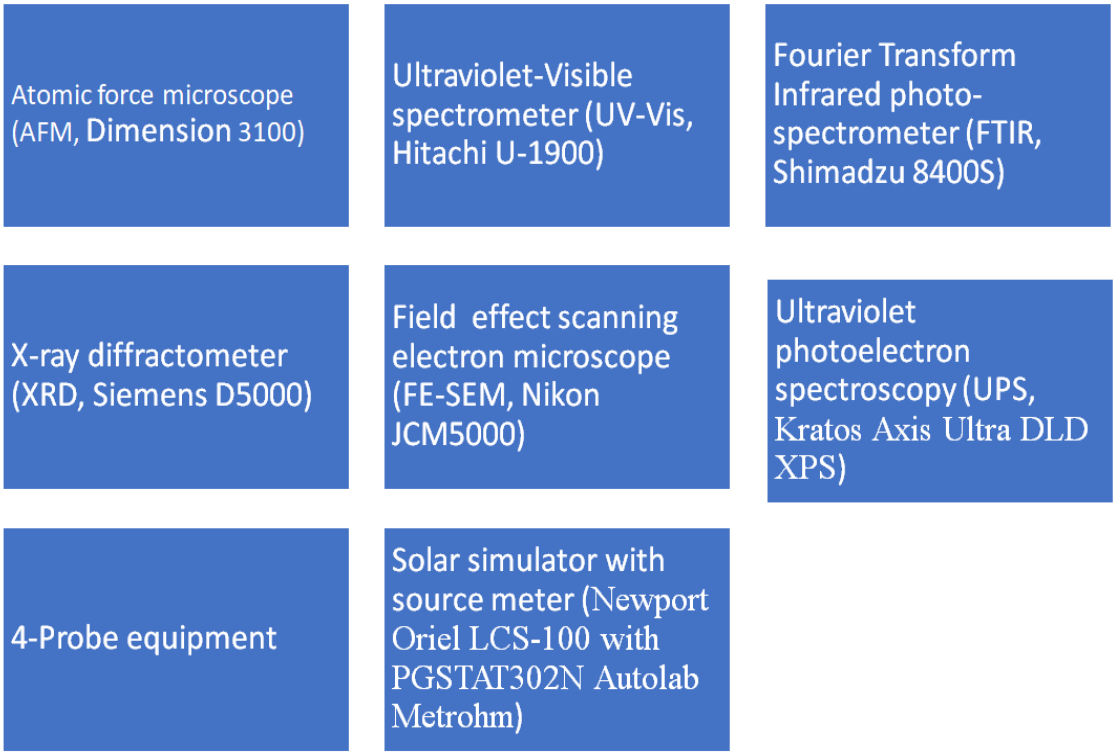

Figure 3.12: Equipment applied for films and device characterisation.

3.3.1. Atomic force microscopy

An atomic force microscope (AFM) uses the force of interaction between the probe and the atoms of the sample surface to measure the morphology of the sample surface [278]. It determines the surface morphology of samples as follows [345]:

- The probe raster scanned the surface line by line
- At each point, the probe tip bends due to interaction with atoms on the sample surface
- As the probe tip bends, the reflection angle of the laser light from the tip changes
- The photodiode detects laser light reflected by the tip
- The AFM reproduces the surface image of the sample from the detected laser light.

This project used a dimension 3100 atomic force microscope to study the morphology of FTO, Ag, SnO_2, $MAPbI_3$ and Spiro-OMETAD films.

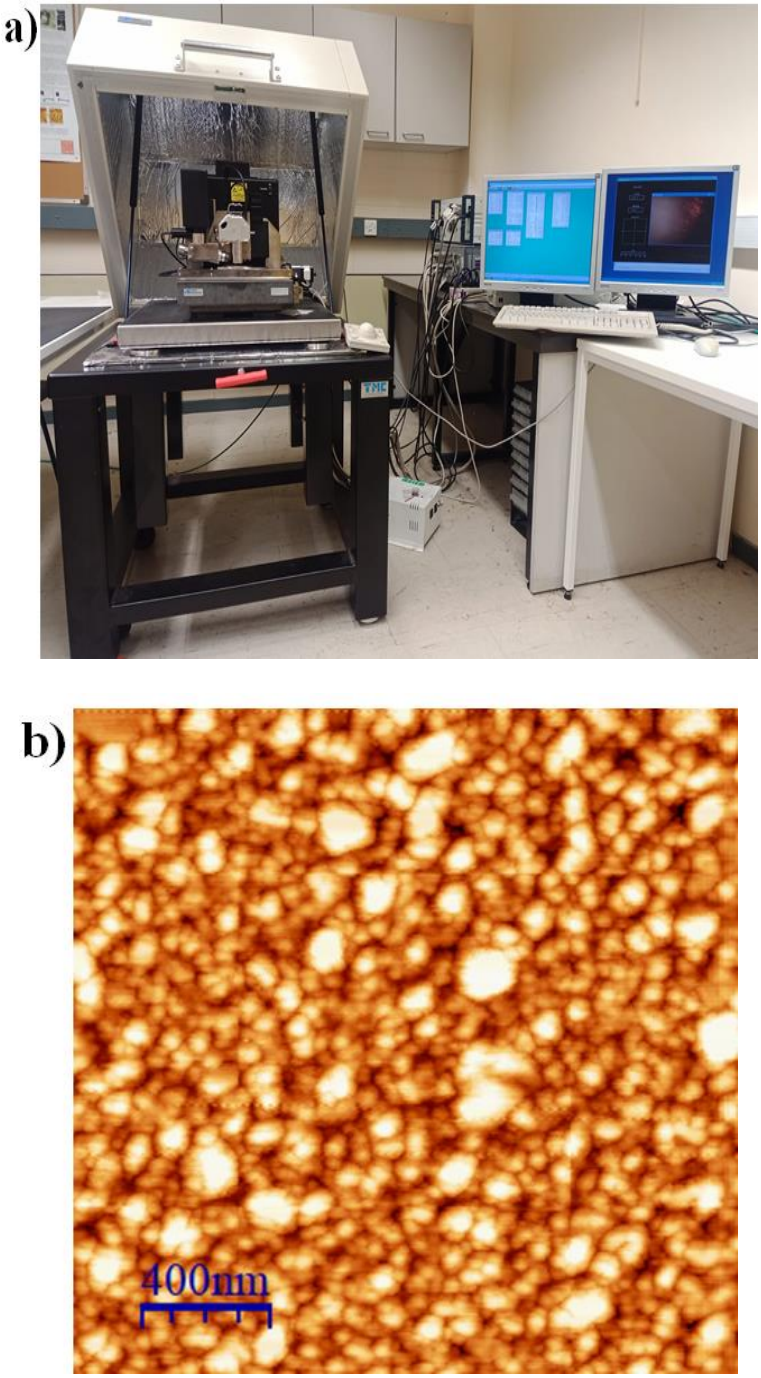

Figure 3.13: (a) Dimension 3100 AFM for morphology measurement and (b) an AFM image of silver film on a glass substrate

This project conducted AFM measurement in tapping mode and laser sum of 4.0 V. It utilized MLCT probes (consisting of silicon nitride cantilever and silicon nitride tips) in studying $MAPbI_3$, Spiro-OMETAD and Ag films (soft samples), and SCM-PIT-V2 probes (made of platinum-indium coated tips) for FTO and SnO_2 films (hard samples).

The studies used glass substrates for Ag samples and FTO substrates for SnO_2, $MAPbI_3$ and Spiro-OMETAD samples. The WSxM and Gwydion applications were used to analyse the AFM images to obtain root-mean-square (RMS) roughness and pit heights. Figure 3.13(a) shows the Dimension 3100 AFM setup. Figure 3.15(b) presents an AFM image of Ag film obtained using the setup to demonstrate the suitability of this facility for characterising surface morphology.

3.3.2. Ultraviolet-Visible spectroscopy

Ultraviolet-Visible (UV-Vis) spectroscopy determines the absorbance, transmittance and energy bandgap of materials across the ultraviolet and visible regions of the electromagnetic spectrum [282]. The operation of a UV-Vis spectrometer involves the following phases [283]:

- The source lamps emit UV and visible light.
- The light spectrums are filtered with monochromatic filters to transmit a single wavelength at a time.
- The filtered light (incident light) is focused on the sample of interest using sets of lenses.
- The intensity of light transmitted through a sample is measured and compared with the intensity of the incident light.

Figure 3.14(a) shows the image of the Hitachi U-1900 UV-Visible spectrometer used for determining the optical absorbance, transmittance, reflectance, and energy bandgap (E_g) of samples in this project.

This project employed a UV-Vis spectroscopy to determine the absorbance of $MAPbI_3$ and transmittance (transparency) of SnO_2, FTO, Ag, and Spiro-OMETAD films. The instrument is also vital in estimating the E_g of $MAPbI_3$, SnO_2, and Spiro-OMETAD films using Tauc plots. For all the measurements, the equipment was operated in wavelength scan mode. Figure 3.16(b) presents a typical absorbance spectrum of $MAPbI_3$ films to demonstrate the reliability of the setup.

For E_g determination, the SnO_2 films were deposited on quartz substrates (Corning HPFS 7980, Kintec Ltd), while FTO substrates were used for measuring the optical transmittance of SnO_2 films [346,347]. FTO substrates were applied to study optical characteristics and E_g of $MAPbI_3$ and Spiro-OMETAD films. The glass substrates were employed when measuring the transparency of Ag films.

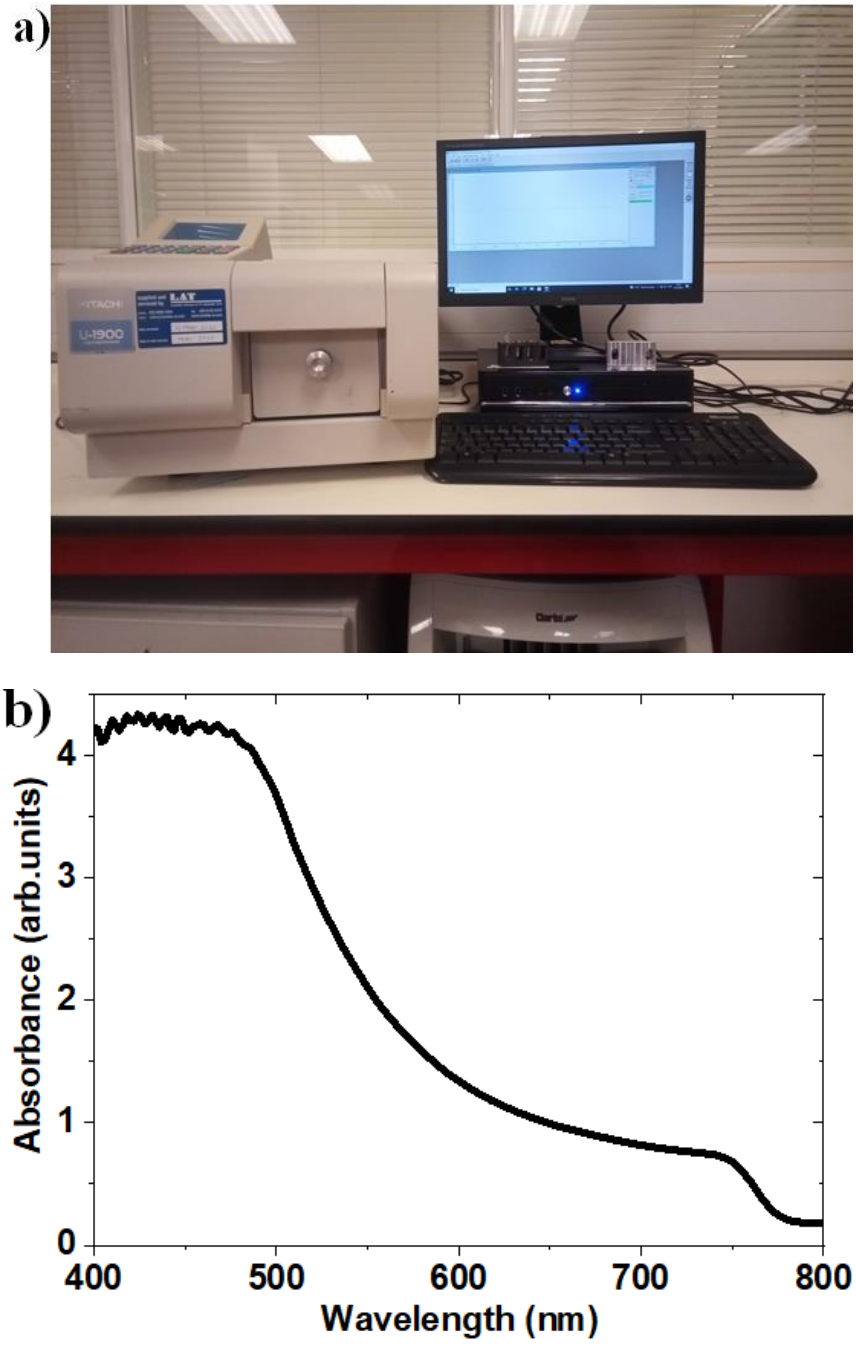

Figure 3.14: (a) Hitachi U-1900 Spectrophotometer and (b) absorbance spectrum of $MAPbI_3$ film deposited on FTO substrates

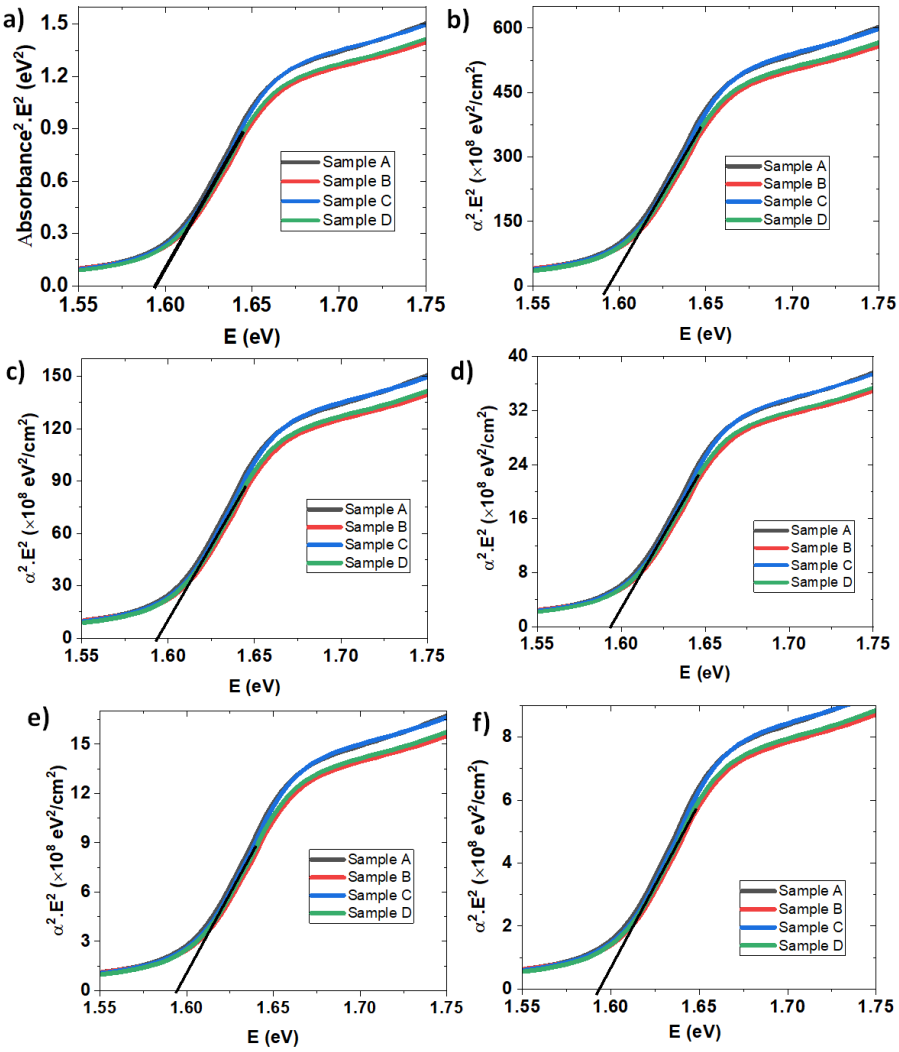

Figure 3.15: (a)Tauc plot using absorbance (b) Tauc plot using absorption coefficient with a thickness (d)= 50 nm (c) Tauc plot using absorption coefficient with d = 100 nm (d) Tauc plot using absorption coefficient with d = 200 nm (e) Tauc plot using absorption coefficient with d = 300 nm and (f) Tauc plot using absorption coefficient with d = 400 nm

A Tauc plot is a graphical method of determining the E_g from the absorbance spectra of the materials. In this project, the E_g of the films was estimated from Tauc plots obtained using equation (3.1), where K is a constant. This method has been reported to be accurate in E_g determination [288–290], and it is convenient as it does not require the knowledge of film thickness. The E_g estimated from equation (3.1) is practically the same as the E_g obtained from equation (2.20), as demonstrated in Figures 3.15(a) - 3.15(f). These figures show that the knowledge of film thickness is not necessary when determining the E_g of

materials using Tauc plots. This is because dividing the absorbances with a constant does not change the energy characteristics of the materials under investigation.

$$[\text{Absorbance}(\lambda).\,\text{E}(\lambda)]^2 = \text{K}.\,\text{E}(\lambda) \qquad (3.1)$$

3.3.3. Fourier Transform Infrared Spectroscopy

Fourier Transform Infrared (FTIR) spectroscopy gives spectral and vibrational information relating to the functional groups, bond types, and quantity of the material in organic and inorganic samples. It operates in the mid-infrared region ranging from 400 cm^{-1} (25 µm wavelength) to 4000 cm^{-1} (2.5 µm wavelength) [291]. The operation of the FTIR spectrometer involves the following stages:

- The infrared light source emits the infrared (IR) spectrum.
- The emitted IR spectrum is filtered with monochromatic filters to transmit a single wavelength at a time.
- The filtered IR light (incident IR light) is focused on the sample of interest using lenses.
- The IR light transmitted through the sample (I_o) is measured and compared with the incident IR light (or light transmitted through the reference) (I_i).

Figure 3.16(a) shows the Shimadzu FTIR-8400S spectrometer employed in this project. This FTIR was used to determine the bond types, structures, and functional groups in SnO_2, $MAPbI_3$, and Spiro-OMETAD layers. It was also used to determine the presence of silver iodide (AgI), which is direct evidence of $MAPbI_3$ degradation when in contact with Ag. The FTIR spectrometer was operated in attenuated total reflection (ATR) mode from 500 to 4000 cm^{-1}. Silver substrates were used in this study because silver is highly reflective and applied as the devices' top electrode. Figure 3.16(b) presents the transmittance spectra of $MAPbI_3$ film to demonstrate the reliable performance of the setup.

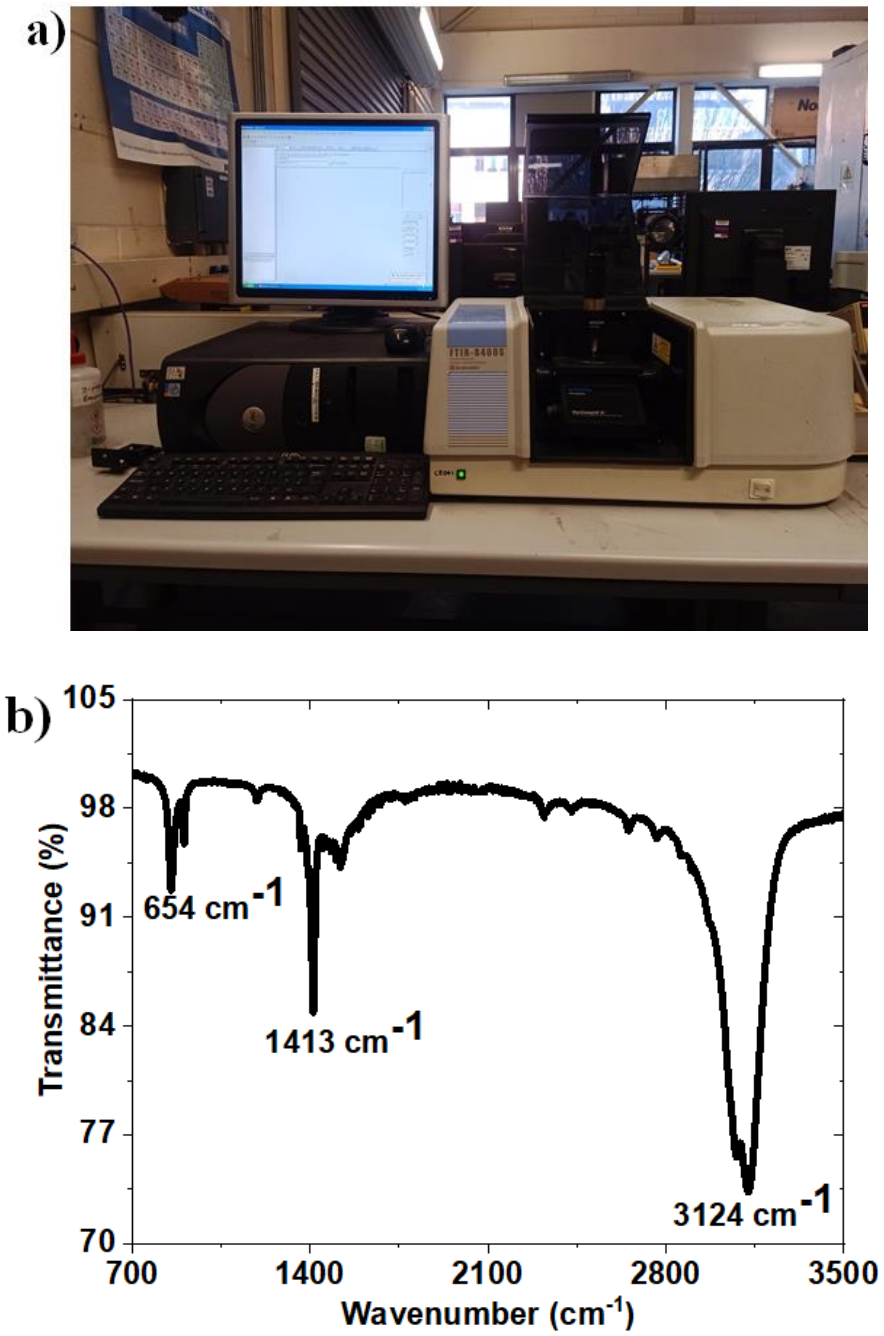

Figure 3.16: (a) FTIR measurement facility and (b) typical FTIR spectra of $MAPbI_3$ film on a silver substrate.

3.3.4. X-ray diffraction

X-ray diffraction (XRD) is used for phase identification of crystalline samples using constructive interference of monochromatic X-rays scattered by the material. XRD provides information on the dimension of unit cells, atomic spacing, strain (shift in peak position, peak broadening), film thickness, degree of crystallization (peak intensity),

preferred orientation (peak position) and grain size (peak broadening and dislocation density) [177,295]. The operation of XRD involves the following processes:

- Electron emission guns (cathode) emit electrons.
- The emitted electrons are accelerated toward the anode (target material) by applying 35 to 40 kV voltage between the cathode and the anode. Copper, iron, nickel, Zirconium and Molybdenum are the typical target materials for XRD.
- The high-speed electrons interact with the k-shell electrons of the target materials to emit X-rays.
- Lenses focus the generated X-ray on the samples.
- The crystals and atoms in the sample scatter the incident X-ray.
- The scattered X-ray undergoes constructive and destructive interferences.
- Intensities and angles (2θ) of the x-ray pattern that resulted from constructive interferences are recorded [296].

Figure 3.17(a) presents the Siemens D5000 X-ray diffractometer utilised in this project for XRD measurement. This XRD machine diffractometer was used to determine the structure of the $MAPbI_3$, Ag and SnO_2 films by identifying the peak intensity, peak position, and preferred orientation. The equipment was operated at a current of 35 mA and a voltage of 40 kV (voltage applied between the cathode and the anode).

Copper (Cu, CuKα radiation of 1.5418 Å) was the target material. FTO was used as the substrate for $MAPbI_3$ film studies, and the diffraction patterns were acquired within $10° \leq 2\theta \leq 50°$ as $MAPbI_3$ films have peaks within this region. XRD patterns were measured within $10° \leq 2\theta \leq 80°$ for SnO_2 films deposited on FTO substrates to capture all the possible peaks, as few studies have been reported on the XRD structure of low-temperature processed SnO_2 films. XRD data capture from $10° \leq 2\theta \leq 50°$ was performed for SnO_2 films on glass substrates to verify some bumps observed in spectra of SnO_2 films on FTO substrates. Glass substrates were used for Ag film studies, and the data were acquired within $10° \leq 2\theta \leq 80°$ because Ag has peaks within this region. The acquired XRD spectra were processed using X'Pert HighScore Plus, while the XRD formats were converted to Excel formats using a POWDLL converter. Figure 3.17(b) shows typical XRD spectra of $MAPbI_3$ films on FTO substrates to demonstrate the facility's reliability.

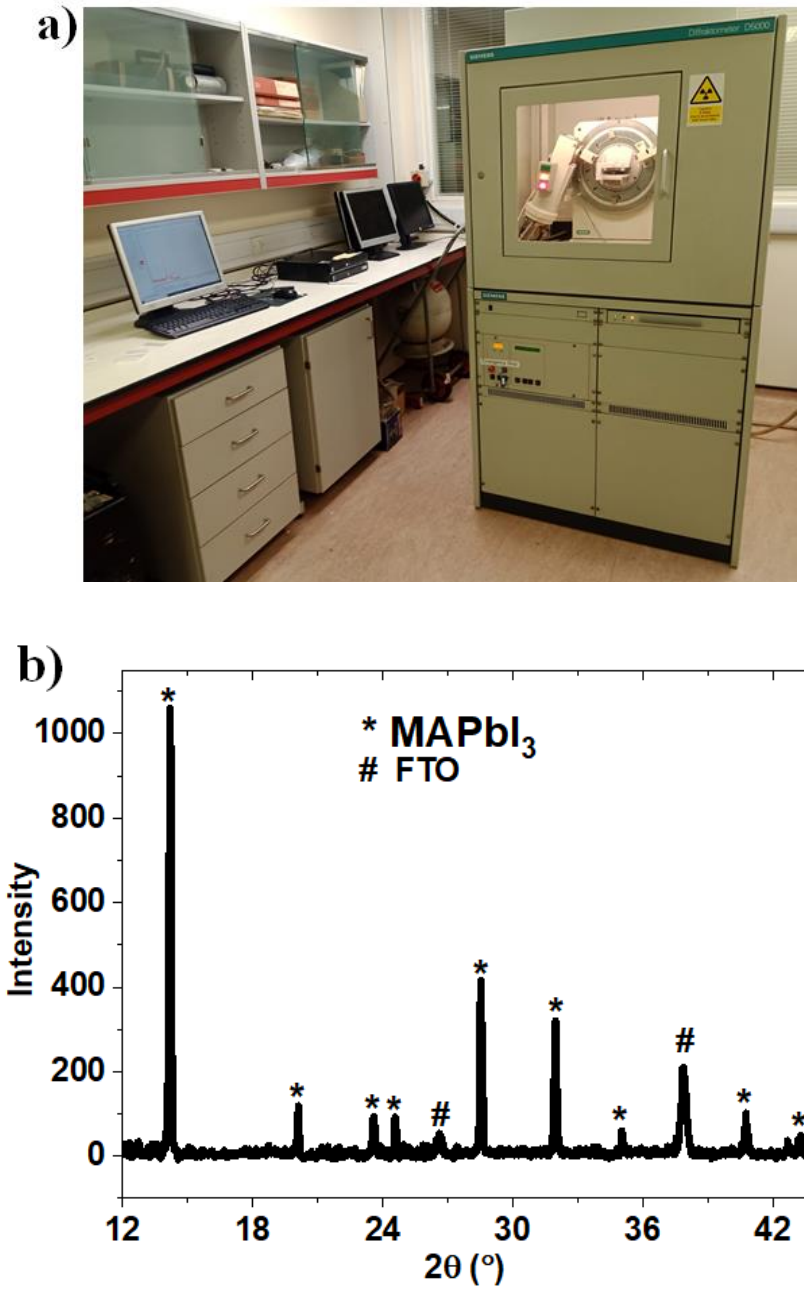

Figure 3.17: (a) Siemens D5000 X-ray diffractometer and (b) A typical XRD spectra of $MAPbI_3$ film on FTO substrate.

3.3.5. Ultraviolent photoelectron spectroscopy

Ultraviolet photoelectron spectroscopy (UPS) measures the kinetic energy spectra of electrons emitted when electrons on the VB of material absorb ultraviolet photons. The UV spectrum for UPS is generated from Neon, Helium I, Neon II or Helium II light source [298–301].

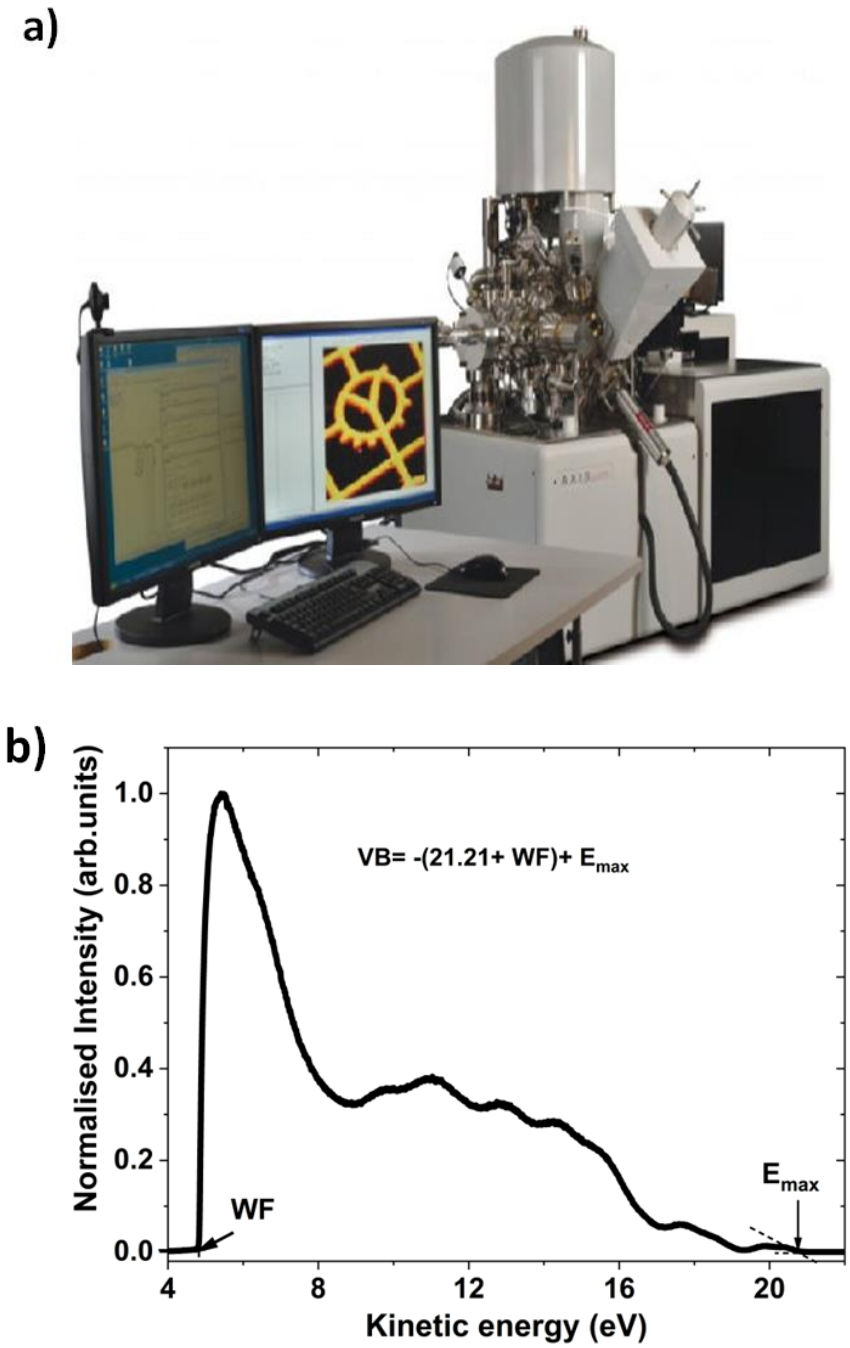

Figure 3.18: (a) Kratos Axis Ultra DLD XPS spectrophotometer, and (b) a typical UPS spectra for Spiro-OMETAD film on FTO substrate

This technique helps determine the VB, Fermi level and WF of materials. In conjunction with a UV-Vis spectrometer, UPS also provides vital information on the CB of the material. The operation of UPS involves the following processes [298–301]:

- A UV light source emits the UV spectrum.
- A narrow beam of the UV spectrum (Kα) is focused on a test sample.
- Electrons are emitted from the VB of the sample when the material absorbs the UV light.
- The kinetic energy and intensity of the emitted electrons are measured using a detector.

Figure 3.18(a) shows the Kratos Axis Ultra DLD XPS spectrophotometer (with UPS capability) at Warwick University used for the UPS measurements in this project. Helium I discharge lamp was the ultraviolet photon source. This technique was used to determine the VB and work function of SnO_2, $MAPbI_3$, Spiro-OMETAD, FTO and Ag films. FTO substrates were used for SnO_2, $MAPbI_3$ and Spiro-OMETAD films, while glass substrates were used for FTO and Ag films. The VB of the materials was calculated from the UPS spectra using equation (2.20). Figure 3.18(b) shows a UPS spectrum obtained using this facility from Spiro-OMETAD film deposited on FTO substrates to demonstrate the instrument's effectiveness.

3.3.6. Field emission scanning electron microscopy

A field emission scanning electron microscope (FE-SEM) is an ultra-high-resolution electron microscope that captures sample images using a high-energy electron beam emitted from a field emission electron gun (cold cathode) [304,305]. FE-SEM has a high resolution and requires high vacuum conditions to operate effectively [305,306]. The operation of FE-SEM involves [348]:

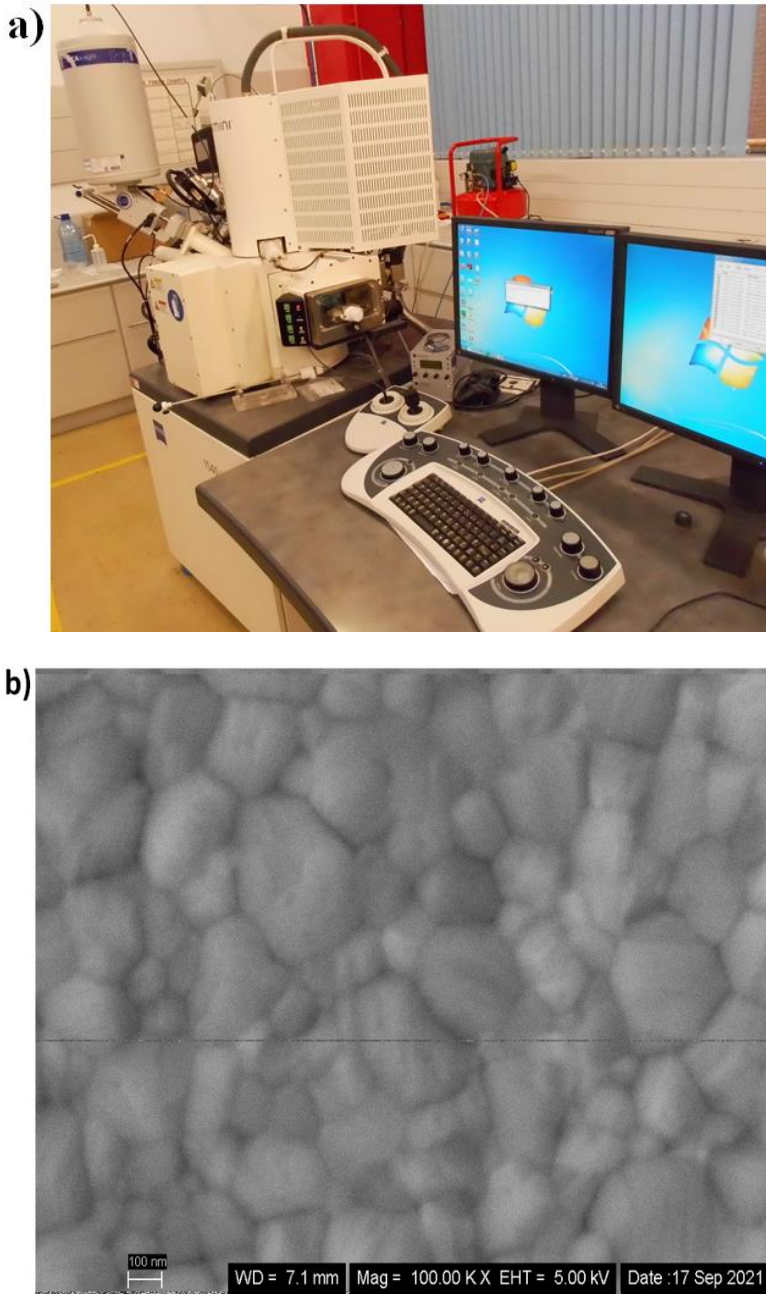

Figure 3.19: (a) Carl Zeiss 1540XB FE-SEM system and (b) Top view SEM image of $MAPbI_3$ film

- The emission of primary electrons from field emission electron guns
- The primary electrons are accelerated to high velocity using a high electric field.
- A narrow beam of the primary electrons is focused on the test sample.
- Secondary electrons are emitted when the primary electrons bombard the test sample.
- The detector measures the angle and velocity of the secondary electrons. These parameters define the surface structure of the sample.

- The SEM image of the sample is reconstructed from the angle and velocity.

Figure 3.19(a) shows the Zeiss 1540 XB Crossbeam Field emission scanning electron microscope (FE-SEM) system used in this project. The setup was used to capture the top-view images of $MAPbI_3$ films and cross-sectional view images of PSCs. The top-view SEM image of $MAPbI_3$ films was performed to identify the grain sizes, morphology, and the presence of pinholes in the films. Similarly, cross-sectional SEM images of PSCs were used to estimate the thickness of FTO, $MAPbI_3$, Spiro-OMETAD and Ag films in the devices using ImageJ. For top-view SEM measurement, the Working Distance (WD) and Electron High Tension (EHT) were set at 7.1 nm and 5.0 kV, respectively. Figure 3.19(b) presents a typical top-view SEM image of $MAPI_3$ film obtained using this system.

3.3.7. The 4-probe

The 4-Probe can measure the sheet resistance, conductivity and resistivity of test samples with reasonable accuracy [308]. It works by passing current (I) through the samples from the outer probes (current probes) and measuring the voltage drop (V) across the inner probes (voltage probes). Since the voltmeter connected in series to the voltage probes has high input resistance, virtually all the current supplied from the current probes will flow through the sample while only negligible current flows through the voltage probes. Hence, the voltage difference measured across voltage probes accurately relates to only the potential drop across the sample. This is because the voltage drop across the connectors and probes of the voltage probes is relatively negligible.

Figure 3.20 shows the 4-probe setup for sheet resistance measurement in this project. The 4-probe instrument was a homemade facility developed at Cardiff University, and it can measure the sheet resistance and resistivity of materials. The 4-Probe was applied to measure the sheet resistance of Ag films deposited on glass substrates. The sheet resistance was chosen for measurement because it does not require the knowledge of film thickness, unlike conductivity and resistivity.

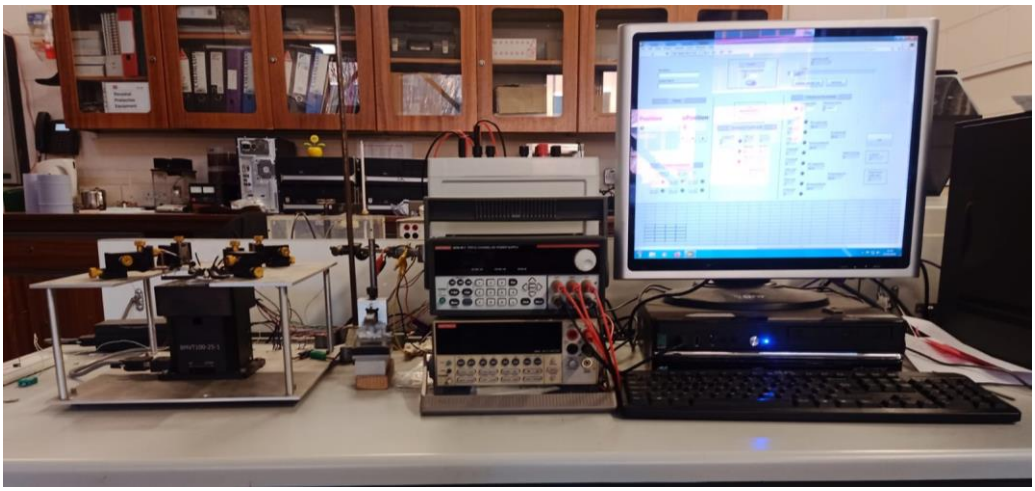

Figure 3.20: 4-probe measurement setup, developed at Cardiff University.

3.3.8. Current-voltage measurement

Current-voltage (I-V) measurement is a technique for determining the I-V characteristics of electrical/electronic devices. The I-V measurement involves increasing voltages across the device and measuring the current that flows through it at each voltage level. In this measurement, a voltmeter connected in parallel to the device measures the applied voltage. In contrast, an ammeter connected in series measures the current through the devices [315]. For devices with sourcing ability, the I-V measurement uses a switching device (e.g. transistors) to control the device's voltage and current output [316]. For high accuracy, SMU is used for this measurement.

Figure 3.21(a) shows the setup for the I-V measurement in this project. The I-V measurement was conducted using AUTOLAB (Metrohm, PGSTAT302N) in conjunction with Newport Oriel LCS-100 solar simulator (Class ABB, xenon lamp as the light source) providing the standard solar irradiance of 1000 W/m^2 (i.e., AM1.5G). Figure 3.21(b) presents the current density-voltage (J-V) curve of a typical PSC calculated from the I-V curve and device active area.

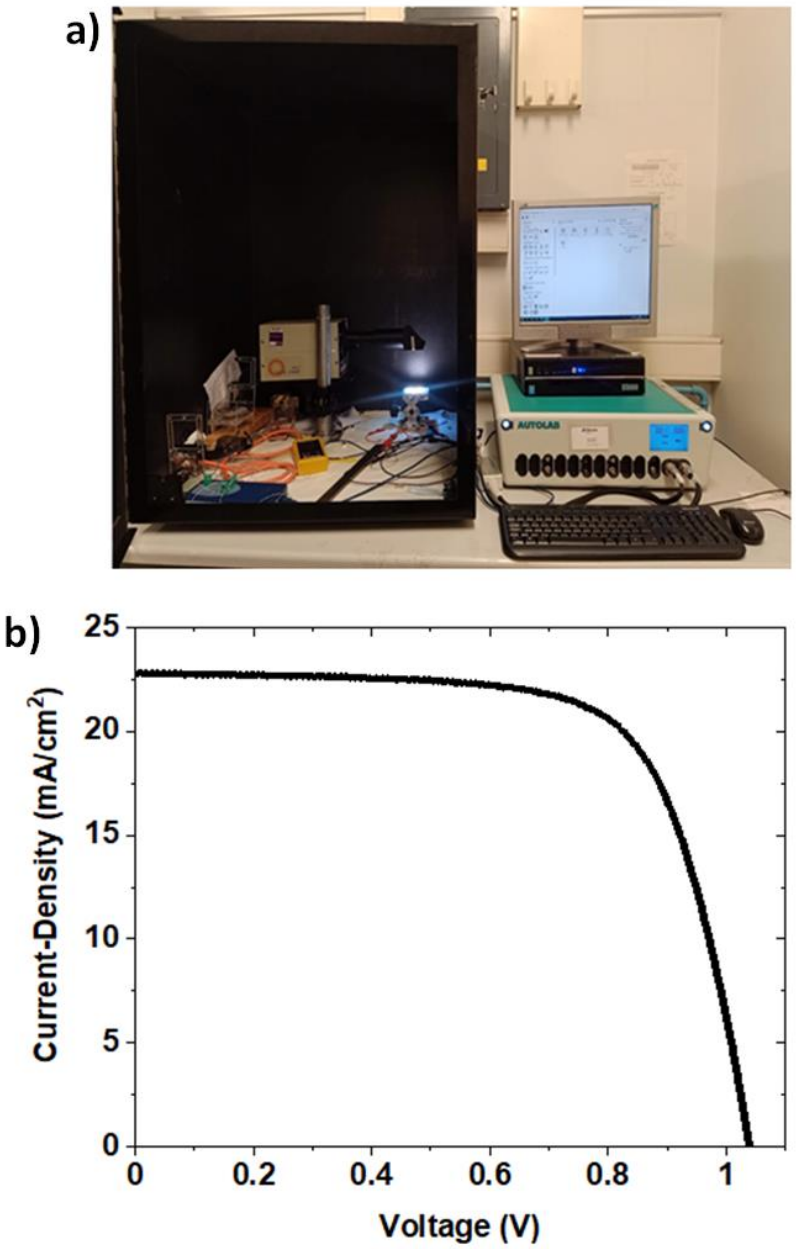

Figure 3.21: (a) Newport Oriel LCS-100 solar simulator/PGSTAT302N Autolab Metrohm setup for I-V measurement system (b) J-V curve calculated from I-V curve measured at 1000 W/m^2

3.3.9. Impedance spectroscopy

Impedance spectroscopy (IS) is a technique for measuring the impedance characteristics and frequency response of electrical/electronic devices over a frequency range. IS measurement involves applying a combination of sinusoidal input (low frequency to high

frequency) and a dc voltage input to the device and determining the impedance characteristics of the device at different illumination conditions [18,322,323]. In IS measurement, the impedance measured at the upper cut-off frequency relates to the resistance of the contacts and the wires. In contrast, the impedance measured at the lower cut-off frequency is associated with the resistance of the solar cell under dc conditions [326]. At the resonance frequency, the measured impedance is related to the impedance characteristics of the junction [326,327].

Figure 3.23(a) shows a simple electronic circuit for impedance spectroscopy of solar cells, and the operation involves the following steps [349]:

- A low amplitude sinusoidal input, V(t) and direct current voltage, $V_{dc,}$ are applied to the positive inputs of the summing operational amplifier (OP1) to generate a frequency-dependent superimposed voltage, $V(t) + V_{dc}$ (see Figure 2.23(b)).
- The output of OP1 is connected positive terminal (Ag contact) of the solar cells.
- The solar cells' negative terminal (FTO substrate) is connected to the positive input of the operational amplifier buffer (OP2) to protect the solar cell from overloading.
- The output of the OP2 is passed through a capacitor to filter off the dc voltage.
- The ammeter measures the sinusoidal current (I(t)) flowing through the solar cell.
- The complex impedance parameters of the solar cell are calculated from the Fourier transform of V(t) and I(t).

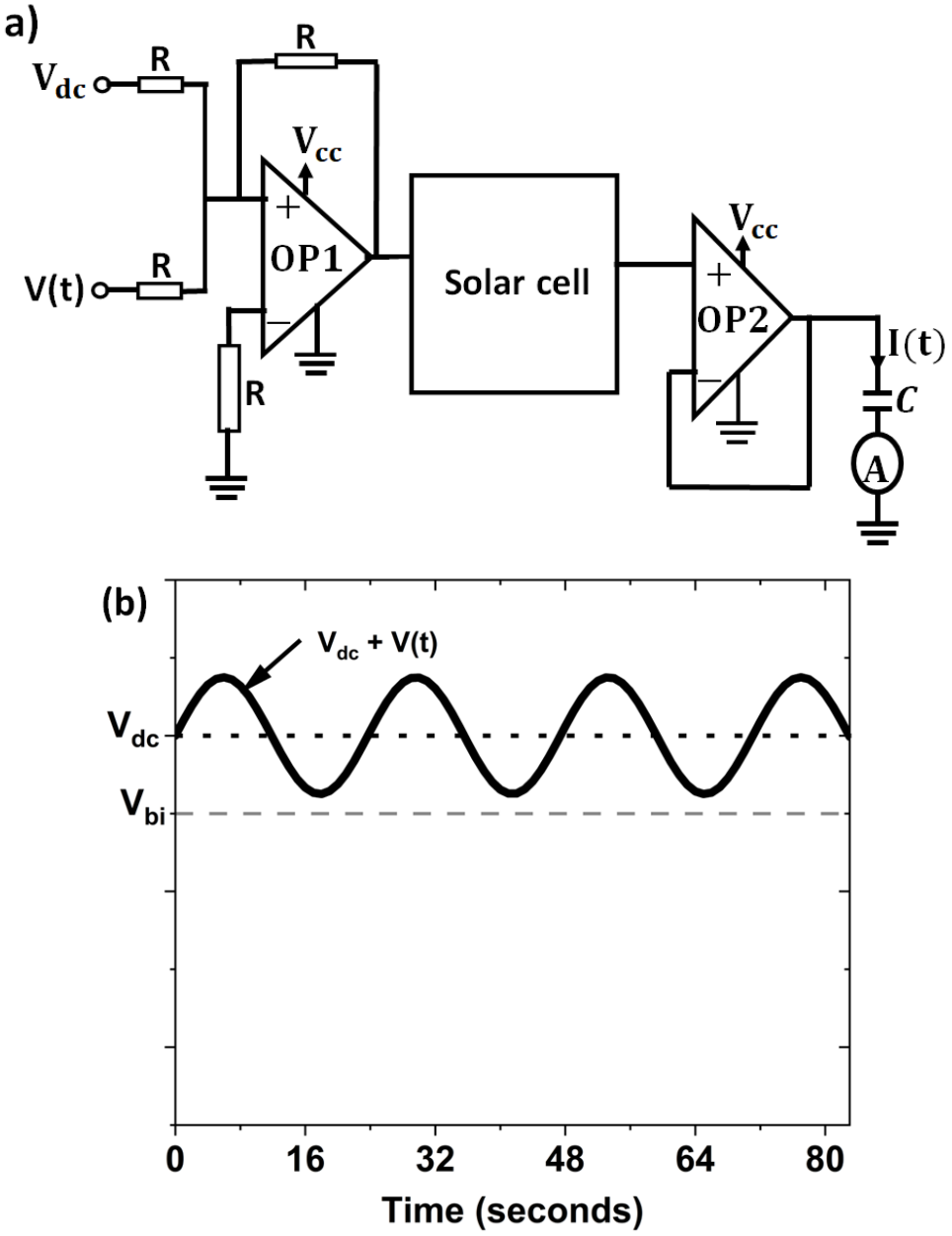

Figure 3. 22: (a) A simple circuit for measuring impedance spectroscopy of solar cells and (b) Superimposition of V(t) and V_{dc}.

This project used Figure 3.21(a) setup to measure the impedance spectroscope (IS). Input sinusoidal signal with an amplitude of 75 mV and frequency varying from 10 Hz - 1.0 MHz was applied to the devices. Forward dc bias (1.0 V) and low sinusoidal input (75 mV) were applied to the devices to ensure the measurement was performed within the linear region. A dc bias of 1.0 V was chosen in this project to ensure that bias is sufficient to overcome the V_{bi} of PSCs (0.94 V). Figure 3.23 shows the energy band diagram of the perovskite solar cell during IS measurements in this project.

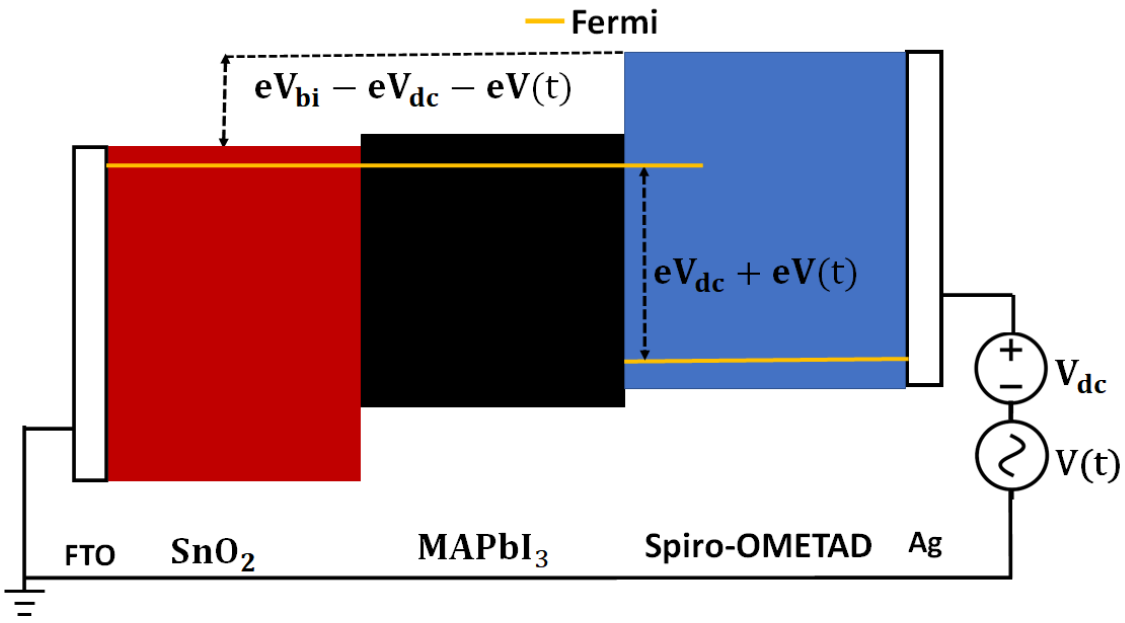

Figure 3.23: Energy band diagram of perovskite solar cell during IS measurements.

Figure 3.24(a) presents the dark I-V characteristics of a typical perovskite solar cell showing the V_{bi} and the position of the applied dc voltage bias during measurement. This project conducted IS measurements at an irradiance of 1000 W/m^2. In this project, the junction capacitance, which relates to the carrier density of the device, was extracted from the measured data using ZSimpWin software. ZSimpWin is an IS Data analysis software developed by Ametek Scientists Instrument. Figure 3.24(b) shows the impedance plot of a device measured at 1000 W/m^2 (AM1.5G spectrum) and dc bias of 1.0 V. The maximum point in the impedance plot represents the condition under which the circuit oscillates at the natural frequency.

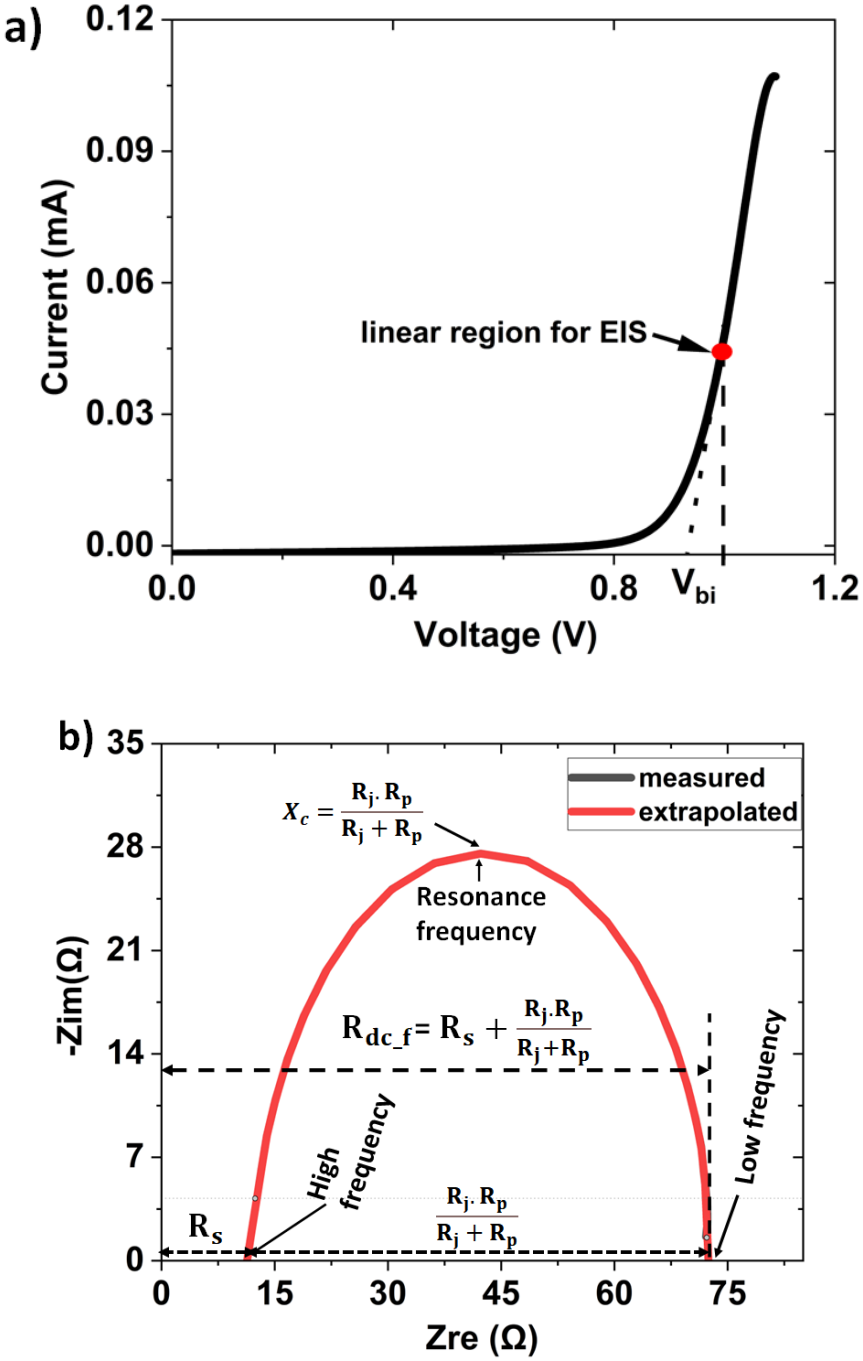

Figure 3.24: (a) Dark I-V characteristics of PSCs and (b) impedance plot of a perovskite solar cell obtained at 1000 W/m^2 and 1.0 V.

3.4. Summary

This Chapter explored and tested procedures suitable for fabricating and characterising perovskite solar cells at the Cardiff laboratory. It also evaluated the suitability,

accessibility and reliability of the established practical methodologies for future studies. This chapter also briefly explains the processes for cleaning FTO substrates and preparing SnO_2, $MAPbI_3$, Spiro-OMETAD layers, silver top electrodes and the equipment for films and solar cell characterisation. This chapter also presented typical results demonstrating the reliability of the developed fabrication procedures and characterisation techniques. Finally, this Chapter also provided information on the materials and the suppliers to allow for the reproducibility of the experiments. Chapters 4-8 will present and discuss the results from investigations conducted using these procedures and methods.

Chapter 4: Preliminary Studies

4.1. Introduction

This chapter presents the preliminary studies aiming at exploring suitable components and processes for fabricating perovskite solar cells at Cardiff University for the first time. The studies involve trial runs of preparing different layers of solar cells and whole devices to reveal the key issues and challenges for making efficient perovskite solar cells for further investigation. The results of this preliminary work will help identify suitable methods, components, and processing routes for systematic study in future research.

4.2. Film and device fabrication

The fabrication processes employed for the initial trial runs were designed based on the information collected from the literature and a brief training at Swansea University with consideration of the available facilities at Cardiff University. The devices prepared in this study adopted structures, transport materials, perovskite, and antisolvent reported by Yang et al. [37]. However, this project replaced the gold contact deposited by the thermal evaporator in [37] with low-cost silver contact deposited using magnetron sputtering. The key device and film fabrication steps are briefly explained as follows:

SnO_2 films were deposited on FTO substrates from 21 mg/ml of $SnCl_2.2H_2O$ solutions using a spin-coater. Next, $MAPbI_3$ layers were spin-coated on SnO_2 layers from a 1.5 M solution of $MAPbI_3$ solutions. Then, the spinning perovskite films were treated with 150 µl of methyl ethanoate antisolvent after the first 15 seconds. HTLs were spin-coated on $MAPbI_3$ layers from HTL solution containing 90 mg Spiro-OMETAD, 36 µl of MPPD, and 38 µl of FK209 solution (300 gm/ml) ethane nitrile) and 22 µl of Li-TFSI solution (520 mg/ml in ethane nitrile) in 1 ml of chlorobenzene. All the solution-processed layers were prepared in ambient air. Finally, Ag contacts with active areas of 0.15 cm^2 were deposited on HTLs at different sputtering powers. All Ag sputtering in this chapter will be performed at an argon flow rate of 15.0 sccm, pressure of 5.0 mTorr and sputtering duration of 60 minutes.

4.3. Feasibility of fabricating Ag contact by magnetron sputtering

This study was to explore the feasibility of fabricating Ag contacts using a magnetron sputtering facility available in our laboratory. FTO (TEC-8) substrates were used in this study on the assumption that their low sheet resistance will enhance the performance of devices. The SnO_2 and $MAPbI_3$ films were annealed at hotplate readings of 180°C and 110°C, respectively.

4.3.1. Photovoltaic performance of devices

In the first experiment, PSCs were prepared with the Ag contacts deposited using a sputtering power of 200 W, with the hypothesis that Ag contacts with low sheet resistance would benefit device performance. This is because low sheet resistance is achieved when Ag films are deposited using high sputtering power [350]. The Ag contacts were deposited using a sputtering mask used at the early stage of the research as shown in Figure 4.2(a) (with 8 slits for devices and a central slit for the common). Figure 4.2(b) presents an image of a substrate with 8 solar cells. The bright areas are the regions where the solar cells were fabricated, which become transparent after Ag deposition at 200 W, indicating the loss of perovskite/HTL layers. Figure 4.2(c) shows that the J-V curve obtained from devices with Ag contacts deposition at 200 W (black line) is almost straight lines with low V_{oc}, FF and J_{sc}. It corresponds to a very low PCE of 0.04% as shown in Table 4.1.

Consequently, further experiments were conducted with more devices prepared using sputtering power of 50.0 W, 10.0 W, 5.0 W and 1.0 W while keeping other parameters constant. The J-V curves of these devices are shown in Figure 4.2(c) and the corresponding parameters are presented in Table 4.1. The results show that the V_{oc}, FF and PCE were increased as the sputtering power was decreased, indicating less damage to perovskite/HTL layers when the sputtering power was reduced. Evidently, high sputtering power negatively affects the efficiency of the PSCs and a systematic investigation is needed to identify the optimal sputtering power of perovskite solar cell fabrication.

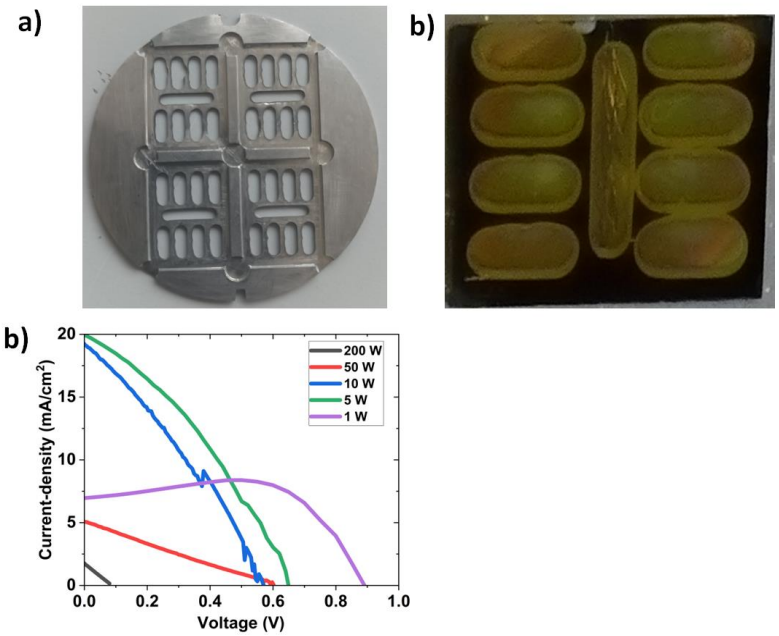

Figure 4.1: (a) Sputtering mask for Ag deposition in this study, (b) image of the devices immediately after contact deposition at a sputtering power of 200 W, (c) J-V curves of the devices with Ag contacts deposited at different suppering powers.

Table 4.1: Photovoltaic parameters of devices with Ag contacts deposited at different sputtering powers (the rows denoted "Best" represent the data obtained from the best solar cells of the batch; the rows denoted "Av" represent the average of all cells). The average parameters were calculated from 8 devices for each power.

Sputtering power		V_{oc} (V)	J_{sc} (mA/cm^2)	FF (%)	R_{dc_f} (Ω)	R_{dc_r} (Ω)	PCE (%)
200 W		0.08	1.76	26.82	338	320	0.04
50 W	Best	0.60	5.07	24.41	649	912	0.75
	Av	0.47±.10	3.60±1.04	24.8±1.65			0.44±0.21
10 W	Best	0.57	19.24	31.48	122	290	3.46
	Av	0.60±0.03	15.39±3.85	32.10±0.62			2.91±0.55
5 W	Best	0.66	20.22	33.17	135	434	4.43
	Av	0.64±0.02	15.69±4.54	41.81±8.64			3.96±0.47
1 W	Best	0.90	8.39	64.07	192	2673	4.84
	Av	0.95±0.05	7.99±0.40	60.56±3.50			4.58±0.25

4.4. Benefit of replacing FTO (TEC-8) with FTO (TEC-15)

Having used FTO (TEC-8) and varied the sputtering power from 200 W to 1 W without achieving good efficiency, I decided to try different FTO substrates while keeping other components and parameters constant. A trial was conducted using a few FTO (TEC-15) substrates collected from a research colleague who visited Cardiff University from Germany. The trial experiment resulted in promising results. Hence, more FTO (TEC-15) substrates were purchased from the same company (Pingdingshan Mingshuo Technology Co. Ltd) for further experiments. In this study, the parameters specified in section 4.2 were employed to deposit SnO_2, $MAPbI_3$ and Spiro-OMETAD layers. The SnO_2 and $MAPbI_3$ films were annealed at hotplate readings of 180°C and 110°C, respectively. A sputtering power of 1.0 W, which achieved the best PCE in the last experiments, was used to deposit the Ag contacts.

4.4.1. Properties of FTO substrates

Before the fabrication of PSCs, AFM, UV-Vis spectrometer and XRD were used to characterise the FTO substrates. Figures 4.2(a) and 4.2(b) present the AFM images of FTO (TEC-8) and FTO (TEC-15) substrates, respectively. The images indicate that the FTO (TEC-8) substrate has a larger grain size and rougher surface than the FTO (TEC-15) substrate.

The RMS roughness of the FTO surfaces estimated from the AFM images using WSxM software indicates that FTO (TEC-8) has an RMS roughness of 38.32 nm in contrast to 14.32 nm obtained from FTO (TEC-15). These RMS roughness details suggest that a more concentrated ETL solution is required to fill the rough surfaces of FTO (TEC-8) substrates, provide smooth surfaces, and reduce recombination [177]. A smooth surface between the SnO_2 and $MAPbI_3$ decreases the interface resistance at the SnO_2/$MAPbI_3$ junction.

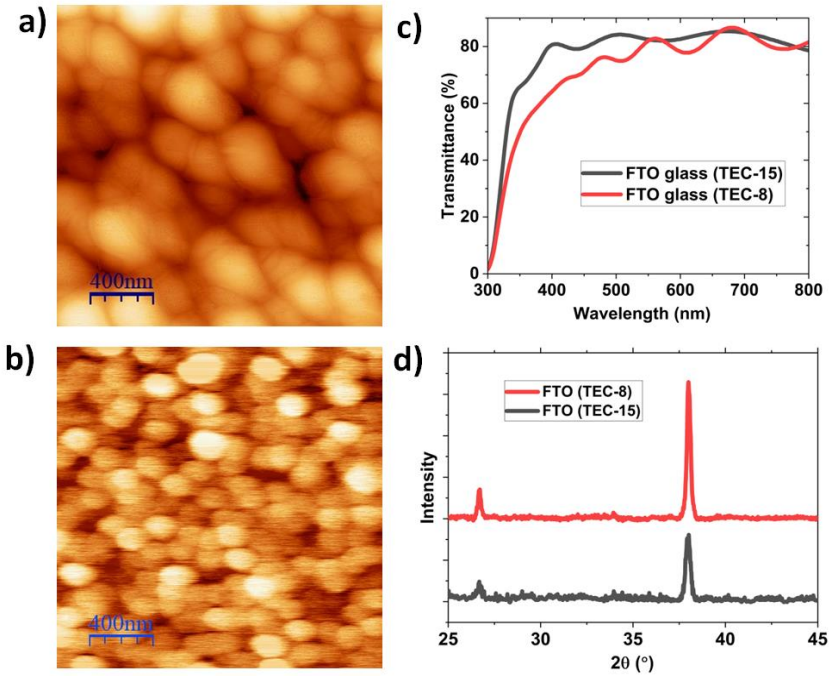

Figure 4.2: (a) AFM image of FTO (TEC-8) (b) AFM image of FTO (TEC-15) (c) Transmittance of FTO (TEC-8) and FTO (TEC-15) and (d) XRD spectra of FTO (TEC-8) and FTO (TEC-15)

Figure 4.2(c) shows that FTO (TEC-15) has better transmittance compared to FTO (TEC-8). This better transmittance indicates that devices prepared from (TEC-15) will likely have higher short-circuit currents as the active materials will receive more photons from the FTO (TEC-15) substrate. Figure 4.2(d) shows that the intensity of FTO (TEC-8) peaks at 38.2° and 26.71° are larger than the peak intensity of the corresponding peaks from FTO (TEC-15). This result indicates that FTO (TEC-8) films are thicker and have larger crystals than FTO (TEC-15) substrates.

4.4.2. Photovoltaic performance of devices

Devices were prepared using FTO (TEC-8) and FTO (TEC-15) substrates. Figure 4.3 presents the J-V curves and Table 4.2 summarises the photovoltaic parameters of the devices. The J-V curves show that devices prepared using FTO (TEC-8) have lower J_{sc} and V_{oc} than those fabricated using FTO (TEC-15). The lower J_{sc} of the devices based on FTO (TEC-8) could be due to the lower transmittance of FTO (TEC-8) (see Figure 4.2(c)). The low V_{oc} of the devices based on FTO (TEC-8) could also be due to poor charge extraction and high recombination caused by significant interface resistance at the SnO_2/$MAPbI_3$ junction.

Both J-V curves also show the presence of an s-shape. This could be due to the poor electrical conductivity of SnO_2, poor carrier mobility in $MAPbI_3$ and high interface resistance at SnO_2/$MAPbI_3$ or $MAPbI_3$/Spiro-OMETAD junction. The annealing temperature has significant influences on the charge transport properties of these layers. Hence, further studies will be needed to establish the impact of the annealing temperature of SnO_2 and $MAPbI_3$ films on the J-V characteristics.

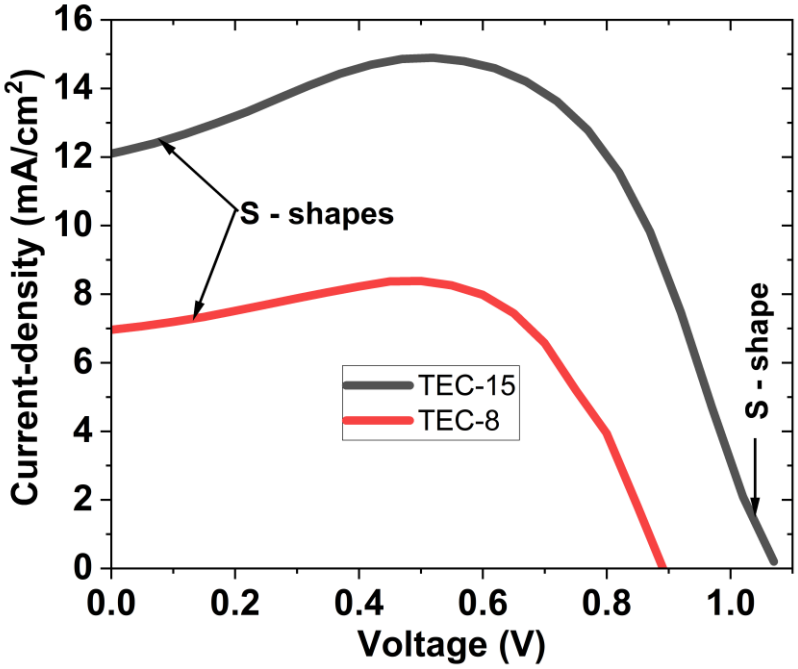

Figure 4.3: J-V curves of devices prepared using FTO (TEC-8) and FTO (TEC-15) substrates. The SnO_2 and $MAPbI_3$ were annealed with a hotplate with display temperatures of 180°C and 110°C, respectively.

Table 4.2: Photovoltaic parameters of PSCs prepared using different FTO substrates (the rows denoted "Best" represent the data obtained from the best solar cells of the batch; the rows denoted "Av" represent the average of all cells). The SnO_2 and $MAPbI_3$ films were annealed at hotplate readings of 180°C and 110°C, respectively

FTO substrate		V_{oc} (V)	J_{sc} (mA/cm^2)	FF (%)	R_{dc_f} (Ω)	R_{dc_r} (kΩ)	PCE (%)
TEC-8	Best	0.9	8.39	64.07	192	2.6	4.84
	Av	0.95±0.05	7.99±0.40	60.56±3.50			4.58±0.25
TEC-15	Best	1.07	11.98	76.74	139	1.2	9.84
	Av	1.07±0.00	10.26±1.73	66.39±10.35			7.48±2.36

4.5. Establishing the accurate hotplate setting for film annealing

This study aims to calibrate the hotplate to establish the correct temperature setting for annealing SnO_2 and $MAPbI_3$ layers. The PSCs prepared in this study applied the parameters reported in section 4.2 for SnO_2, $MAPbI_3$ and Spiro-OMETDA layers. The SnO_2 and $MAPbI_3$ layers were annealed at thermocouple readings of 180°C and 110°C, respectively. The Ag contact was deposited at 1.0 W, keeping other parameters the same.

4.5.1. Accuracy of thermocouple and hotplate reading

The hotplate for annealing was calibrated using a thermocouple. During the calibration, the thermocouple was attached to a copper plate (to ensure good contact and stability) which was placed in the centre of the hotplate and the reading was taken when the temperature reached a steady state. Figure 4.4 shows a plot of the thermocouple reading against the hotplate reading obtained from the calibration.

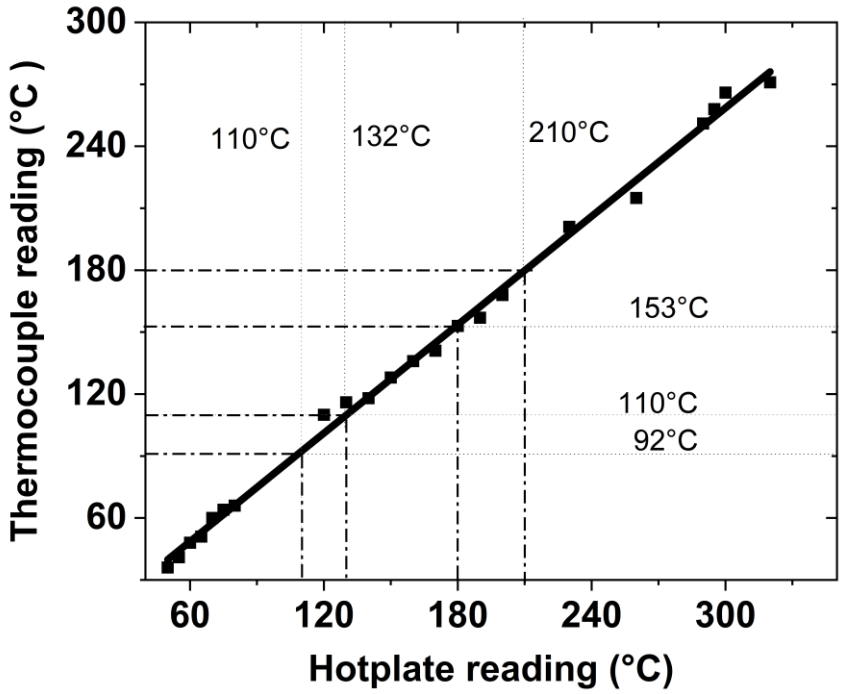

Figure 4.4: Thermocouple reading against the hotplate reading

The results show that the temperature display of the hotplate has a significant systematic deviation from the thermocouple reading. Hence, the SnO_2 and $MAPbI_3$ films annealed at hotplate readings of 180°C and 110°C respectively, were unintentionally annealed at

low temperatures of 153°C and 92°C. These temperatures are insufficient for achieving quality SnO_2 and $MAPbI_3$ layers with good electrical/carrier properties. Literature has reported that SnO_2 and $MAPbI_3$ films for efficient PSCs need annealing temperatures of approximately 180°C and 110°C [37,191,351].

4.5.2. Photovoltaic performance of devices

Further, PSCs were prepared from SnO_2 and $MAPbI_3$ films annealed at thermocouple readings of 180°C and 110°C. Figure 4.5 presents the J-V curves of 4 solar cells out of the 8 solar cells fabricated, while Table 4.3 summarises their photovoltaic parameters. The results show that the s-shape close to the J_{sc} (see Figure 4.3) seems to have disappeared, suggesting that the devices' charge collection properties have improved.

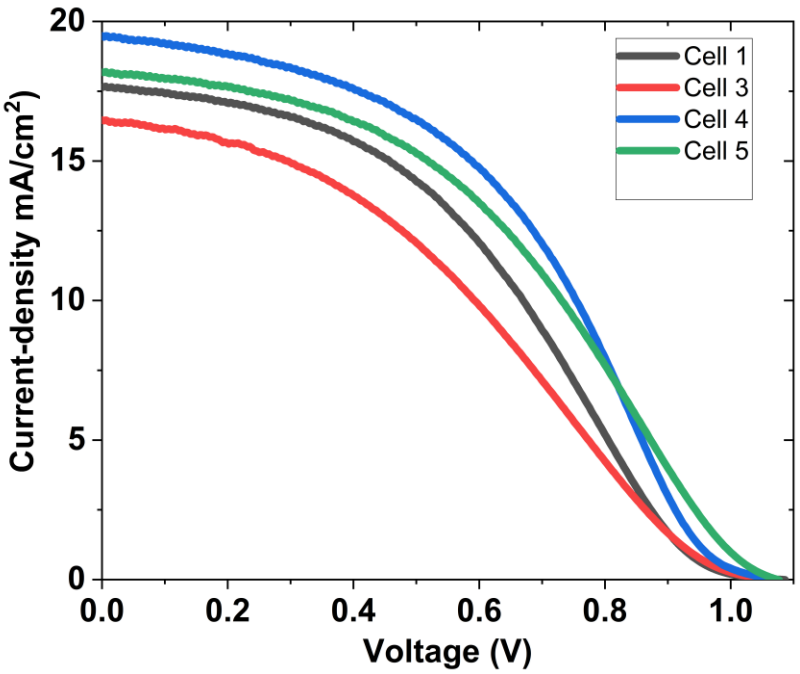

Figure 4.5: J-V curves of devices with SnO_2 and $MAPbI_3$ films annealed at hotplate reading or thermocouple readings of 180°C and 110°C.

Table 4.3: Photovoltaic parameters of devices with SnO_2 and $MAPbI_3$ films annealed at thermocouple readings of 180°C and 110°C (the rows denoted "Best" represent the data obtained from the best solar cells of the batch; the rows denoted "Av" represent the average of all cells). This average was estimated from 6 solar cells.

	V_{oc} (V)	**J_{sc} (mA/cm^2)**	**FF (%)**	**R_{dc_f} (Ω)**	**R_{dc_r} (kΩ)**	**PCE (%)**
Best	1.07	19.48	42.42	422	2.5	8.88
Av	1.08±0.01	18.45±0.76	40.63±1.84			8.10±0.64

This could be because the conductivity of SnO_2 increased, resulting in reduced interface resistance at the ETL/$MAPbI_3$ junction[352]. This result suggests that increasing the annealing temperature of SnO_2 and MAPbI3 films benefits the carrier extraction and PSCs performance. However, the s-shape about the V_{oc} remains, implying that there might be some issues at the $MAPbI_3$/HTL interface [352]. The problem at $MAPbI_3$/HTL interface could have resulted from moisture interfering with $MAPbI_3$ films during annealing. More studies will be needed to confirm this assumption.

4.6. Benefits of Petri dish-covered annealing of SnO_2 and $MAPbI_3$ films

This study explores the benefits of covering SnO_2 and $MAPbI_3$ films with a petri dish during annealing. This method was adopted from the annealing process developed in the literature [38]. In [38], the researchers reported that covering the films with a Petri dish during annealing protects them from moisture interference and ensures a uniform temperature.

This study used FTO (TEC-15) as substrates while SnO_2, $MAPbI_3$ and Spiro-OMETAD layers were deposited on it using the procedures and parameters specified in section 4.2. The SnO_2 and $MAPbI_3$ films were covered with a Petri dish and annealed at a thermocouple reading of 180°C and 110°C, respectively. The Ag contacts were deposited at a sputtering power of 1.0 W.

The PSCs prepared in this study were characterised at an irradiance of $1000W/m^2$. Figure 4.6 shows the J-V curve of 4 out of the 8 devices prepared and Table 4.4 presents the photovoltaic parameters of the devices. The results show an improvement in $V_{oc,}$ FF, J_{sc} and PCE for solar cells based on films annealed under petri dish covering, compared to

devices based on films annealed without petri dish covering (see Figure 4.5). It can be seen that the s-shape near both the V_{oc} and the J_{sc} has disappeared. Clearly, covering the $MAPbI_3$ films with a petri dish during annealing enhances the quality of $MAPbI_3$, minimises the interface resistance at $MAPbI_3$/HTL, and significantly benefits the device's performance.

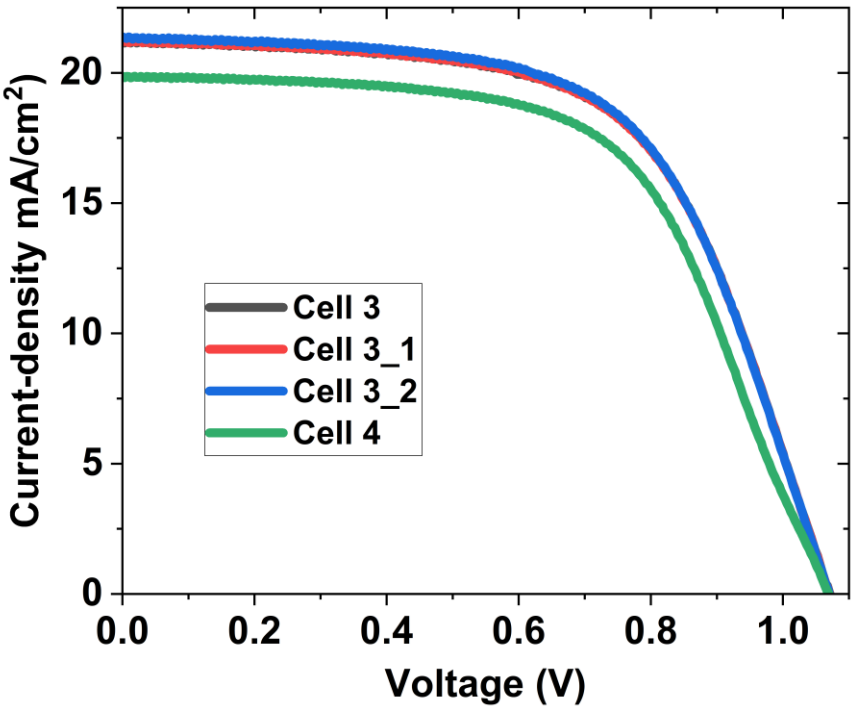

Figure 4.6: J-V curves of devices with SnO_2 and $MAPbI_3$ films annealed at thermocouple readings of 180°C and 110°C. The films were covered with a petri dish during annealing.

Table 4.4: Photovoltaic parameters of devices with SnO_2 and $MAPbI_3$ films were covered with a petri dish and annealed at thermocouple readings of 180°C and 110°C (the rows denoted "Best" represent the data obtained from the best solar cells of the batch; the rows denoted "Av" represent the average of all cells). The average parameters were estimated from 12 cells.

	V_{oc} (V)	J_{sc} (mA/cm^2)	FF (%)	R_{dc_f} (Ω)	R_{dc_r} (kΩ)	PCE (%)
Best	1.08	21.23	60.58	87	5.7	13.88
Av	1.07±0.01	19.38±2.6	60.33±0.92			12.52±1.84

4.7. Summery

This chapter presents the results of initial exploratory experiments to determine the suitable materials, processes and conditions for fabricating perovskite solar cells. The studies revealed that using a low sputtering power for depositing the Ag contacts is necessary to ensure satisfactory performance of PSCs. The study also shows that a better performance is obtained from using FTO (TEC-15) rather than FTO(TEC-8) as the substrate due to surface smoothness and transmittance. In addition, the initial exploratory work demonstrated that it is important to calibrate the temperature of the hotplate to ensure an accurate annealing temperature that has significant influences on the quality of the solar cell layers. Furthermore, a simple procedure of covering the films with a petri dish during annealing can improve the quality of the films, resulting in improved J-V characteristics. With these efforts, the efficiency of the fabricated cells has reached a value beyond 10%, indicating that the planned systematic investigations for in-depth optimisation studies can commence based on the findings from this work. In the following studies described in Chapters 5-8, FTO (TEC-15) is used as the substrate and all films are covered by a Petri dish during annealing with an accurate temperature measured by the calibrated thermocouple.

Chapter 5: Tailoring solution parameters for efficient perovskite solar cells

5.1. Introduction

The performance of PSCs is strongly affected by the thicknesses of electron transport layers (ETLs) and perovskite layers, which depend on the solution concentrations. In addition, the amount of additive in the Spiro-OMETAD also affects the PSCs characteristics. This chapter studies the effect of solution parameters on the performance of perovskite solar cells (PSCs). These studies include the impact of tin (II) chloride dihydrate ($SnCl_2.2H_2O$) concentration on the properties of tin (IV) oxide (SnO_2) films and PSCs and the influence of perovskite concentration on the properties of $MAPbI_3$ films and the photovoltaic performance of PSCs. This chapter will also explore the impact of the amount of FK209 additive in the Spiro-OMETAD solution.

5.2. Suitable $SnCl_2.2H_2O$ concentration for efficient devices

This study aims to establish the suitable $SnCl_2.2H_2O$ concentration for preparing PSCs with high performance. SnO_2 films and devices were fabricated from $SnCl_2.2H_2O$ solution in ethanol with concentrations varying from 10 mg/ml to 21 mg/ml to identify the optimal concentration for PSC fabrication.

5.2.1. Film and device fabrication

SnO_2 films were deposited on FTO substrates by spin-coating from 10, 13, 15, 18, and 21 mg/ml of $SnCl_2.2H_2O$ solutions, respectively. $MAPbI_3$ layers were spin-coated on SnO_2 layers from a 1.5 M solution, followed by the antisolvent treatment using 150 µl of methyl ethanoate. HTLs were deposited on $MAPbI_3$ layers from HTL solution containing 90 mg Spiro-OMeTAD, 36 µl of MPPD, and 38 µl of FK209 solution (300 gm/ml) ethane nitrile) and 22 µl of Li-TFSI solution (520 mg/ml in ethane nitrile) in 1 ml of chlorobenzene. All the fabrication processes were carried out in ambient air (50-55% relative humidity). Finally, Ag contacts with active areas of 0.15 cm^2 were deposited on HTLs at 1.0 W, 15.0 sccm and 5.0 mTorr for 60 minutes. Chapter 3 (section 3.2) gives the details of this fabrication.

5.2.2. Properties of the prepared SnO_2 films

This study investigates the crystallinity, transparency, and optical bandgap of low-temperature processed SnO_2 films.

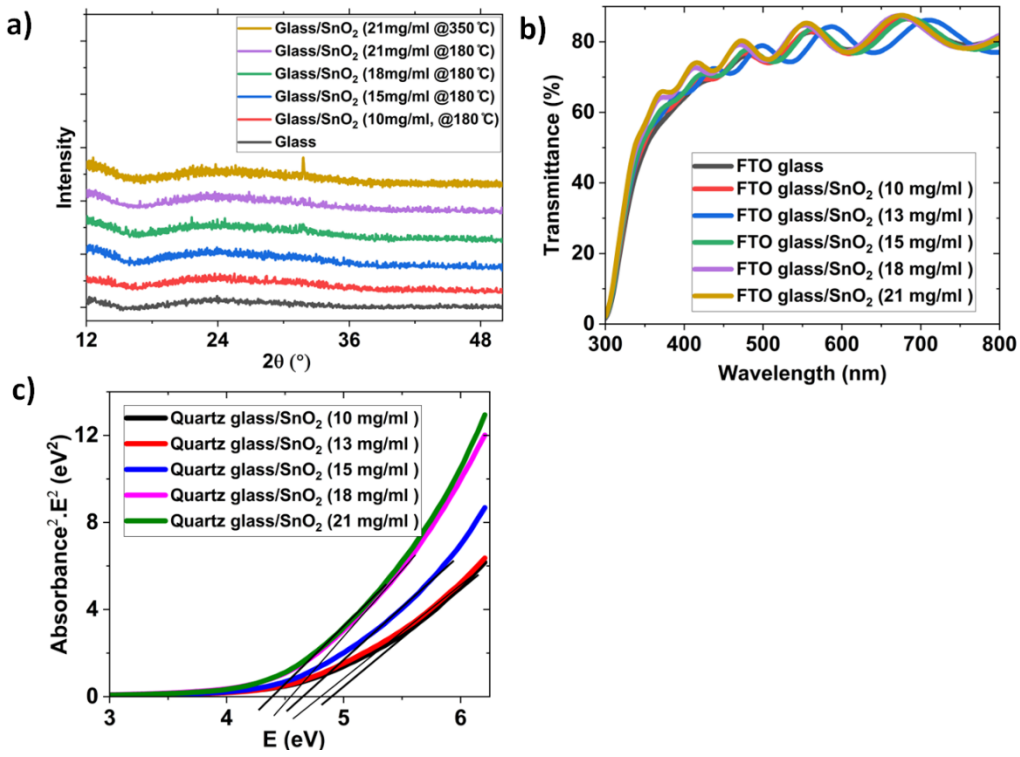

Figure 5. 1: (a) XRD spectra of glass/SnO_2 films, (b) Transmittance spectra of FTO substrate and FTO/SnO_2 films and (c) Tauc plots of SnO_2 films deposited on quartz as a function of $SnCl_2.2H_2O$ concentration.

XRD studies were performed to explore the crystallinity of the prepared SnO_2 films. Establishing the crystallinity of SnO_2 films is crucial, as amorphous SnO_2 films are required for effective electron-blocking [189]. XRD measurements were conducted on SnO_2 films deposited on glass substrates. Figure 5.1(a) presents XRD spectra of glass and SnO_2 films deposited on glasses from different $SnCl_2.2H_2O$ concentrations and annealed at 180°C and 350°C. The XRD spectra show the presence of only broad bumps at about 12° for both glass and glass with SnO_2 films annealed at 180°C. Consequently, these broad bumps agree with the bump at about 12° reported for glass in [353]. However, SnO_2 deposited on glass from 21 mg/ml of $SnCl_2.2H_2O$ and annealed at 350°C has a peak at 31.78°, closely matching the peak of 31.44° reported for SnO_2 annealed at 300°C in [354].

The XRD study suggests that SnO_2 films annealed at 180°C could have an amorphous structure. The report has shown that SnO_2 films annealed at 180°C were amorphous [189]. Amorphous SnO_2 is suitable for preparing effective electron transport (ETL) layers as it is a wide energy bandgap semiconductor, unlike SnO_2 with crystalline structures, which acts as a conductor.

Figure 5.1(b) shows the transmittance of SnO_2 films deposited on the FTO substrate as a function of $SnCl_2.2H_2O$ concentration. The results show that the SnO_2 films on FTO substrates have very high transparency [205]. The results also showed that the transmittance of FTO with SnO_2 layers slightly improved with increased $SnCl_2.2H_2O$ concentration. This could be because films deposited from high $SnCl_2.2H_2O$ concentration have a smoother surface and scatter less light as reported in [180]. Figure 5.1(c) presents the Tauc plots of SnO_2 films deposited on quartz. The results show that the energy bandgap (E_g) of SnO_2 films decreased from 4.75 eV to 4.3 eV as the concentration of $SnCl_2.2H_2O$ solution increased from 10 mg/ml to 21 mg/ml. These E_g closely match E_g of 4.4 eV reported elsewhere [189]. Therefore, all the SnO_2 films deposited showed high transmittance and wide E_g needed for efficient light transmission.

5.2.3. Photovoltaic performance of the devices

This study aims to determine the suitable $SnCl_2.2H_2O$ concentration for preparing efficient perovskite solar cells. Figure 5.2 presents the devices' J-V curves as a function of $SnCl_2.2H_2O$ concentration, with the device parameters summarized in Table 5.1. The results showed that, as the $SnCl_2.2H_2O$ concentration was increased from 10 to 15 mg/ml, there was a slight increase in open-circuit voltage (V_{oc}) and short-circuit current (J_{sc}) but a significant increase in the fill factor (FF) and power conversion efficiency (PCE) of the devices. The lower V_{oc} and FF observed for devices fabricated from 10 mg/ml of $SnCl_2.2H_2O$ are likely due to poor carrier extraction due to recombination losses arising from high interface defects and inefficient hole carrier blocking, as reported elsewhere [176,177]. The SnO_2 films prepared from 10 mg/ml of $SnCl_2.2H_2O$ would be quite thin and could have many pinholes. Also, the reduced J_{sc} might be caused by increased leakage current, resulting from large R_{dc_f} and low $R_{dc\_r,}$ as indicated in Table 5.1. Pinholes in SnO_2 films cause an increase in interface defects at SnO_2/perovskite, increasing R_{dc_f} and decreasing R_{dc_r} [355].

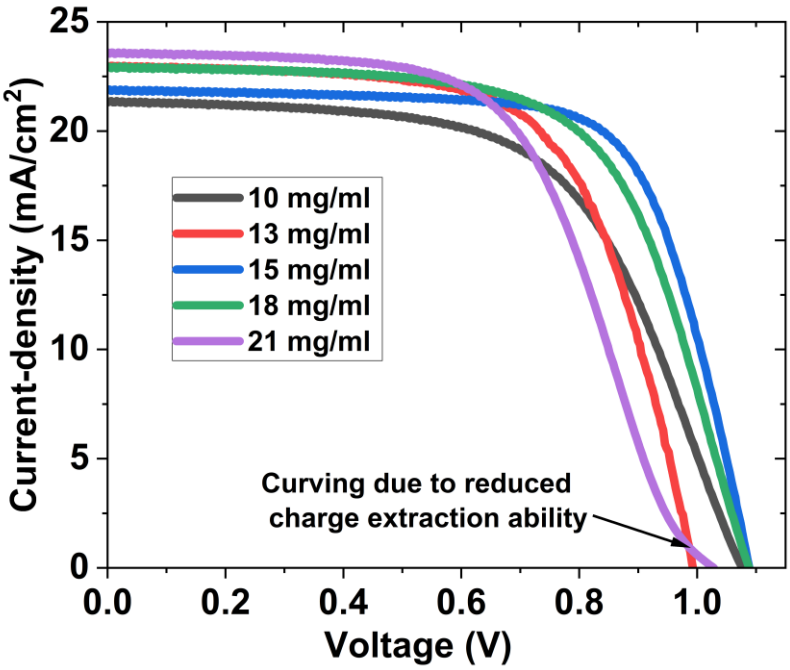

Figure 5.2: J-V curves of best devices as a function of $SnCl_2.2H_2O$ concentration. The J-V curve of the devices prepared from 21 mg/ml of $SnCl_2.2H_2O$ shows a typical s-shape near V_{oc}, indicating a significant barrier to charge extraction due to an increased thickness of SnO_2 films.

Table 5.1: Photovoltaic parameters of devices as a function of $SnCl_2.2H_2O$ concentration (the rows denoted "Best" represent the data obtained from the best solar cells of the batch; the rows denoted "Av" represent the average of all cells)

$SnCl_2.2H_2O$ (mg/ml)		V_{oc} (V)	J_{sc} (mA/cm^2)	FF (%)	R_{dc_f} (Ω)	R_{dc_r} (kΩ)	PCE (%)
10	Best	1.08	21.38	59.47	120	13.9	13.69
	Av	1.07±0.00	20.80±1.00	58.17±0.95			12.98±0.58
13	Best	0.99	23.01	64.24	57	22.5	14.69
	Av	0.99±0.03	22.67±0.80	62.62±1.32			13.99±0.67
15	Best	1.09	21.90	70.55	55	40.0	16.82
	Av	1.08±0.01	21.44±0.61	69.08±0.85			16.01±0.52
18	Best	1.09	22.96	64.04	90	19.0	16.00
	Av	1.09±0.00	22.65±0.30	62.64±0.72			15.40±0.36
21	Best	1.03	23.62	57.33	187	5.0	13.93
	Av	0.99±0.02	22.20±1.85	52.78±5.29			11.61±1.67

As the concentration increased from 15 to 18 mg/ml, the J_{sc} slightly improved while FF decreased. A reason for J_{sc} improvement for devices based on 18 mg/ml is due to the higher transmittance of the SnO_2 films (see Figures 5.2(c) and 5.2(d)). On the other hand, the FF decreased because of an increase in R_{dc_f} resulting from a probable rise in SnO_2 film thickness (see Table 5.1). An increase in R_{dc_f} leads to poor carrier extraction and, consequently, a decrease in FF [356,357]. Therefore, the PCE decreased because of a more pronounced reduction in FF compared to the increase in J_{sc}. When the concentration increased from 18 to 21 mg/ml, the J_{sc} increased further while the V_{oc} and FF degraded severely. The s-shape in the J-V curve provides evidence of poor carrier extraction for devices based on a 21 mg/ml of $SnCl_2.2H_2O$ solution. Hence, a combined effect of the decrease in FF and V_{oc} results in outstanding degradation in PCE. This observation indicates that at 21 mg/ml concentration, the impact of resistance of the SnO_2 films outweighs the benefits of improved transmittance, resulting in poor device performance. These results suggest that 15 mg/ml is a suitable concentration of $SnCl_2.2H_2O$ for preparing efficient perovskite solar cells.

5.3. Tuning $MAPbI_3$ concentration for efficient perovskite solar cells

This study aims to establish the best $MAPbI_3$ concentration for preparing the efficiency of PSCs and $MAPbI_3$ film properties. The perovskite films and devices were prepared using different $MAPbI_3$ concentrations ranging from 1.00 M to 2.00 M. Subsection 5.31 describes the device preparation, while subsections 5.3.2 and 5.3.3 present the results of the characterisation of the films and devices, respectively.

5.3.1. Film and device fabrication

SnO_2 films were deposited on FTO substrates from 15 mg/ml of $SnCl_2.2H_2O$ solution. $MAPbI_3$ layers were deposited on SnO_2 layers from 1.00 M, 1.25 M, 1.50 M, 1.75M and 2.00 M solutions. The $MAPbI_3$ films were treated with 150 µl of methyl ethanoate after 15 seconds of spinning. HTLs were spin-coated on $MAPbI_3$ layers from an HTL solution containing 90 mg Spiro-OMeTAD, 36 µl of MPPD, and 38 µl of FK209 solution (300 gm/ml) ethane nitrile) and 22 µl of Li-TFSI solution (520 mg/ml in ethane nitrile) in 1 ml of chlorobenzene. All the solution-processed layers were prepared at 50-55% relative

humidity. The Ag contacts with active areas of 0.15 cm^2 were sputtered on HTLs at 1.0 W, 15.0 sccm and 5.0 mTorr for 60 minutes (see Chapter 3, section 3.2 for fabrication details).

5.3.2. Properties of the prepared $MAPbI_3$ films

This study aims to determine the influence of $MAPbI_3$ concentration on the optical, morphological, and chemical properties of $MAPbI_3$ films.

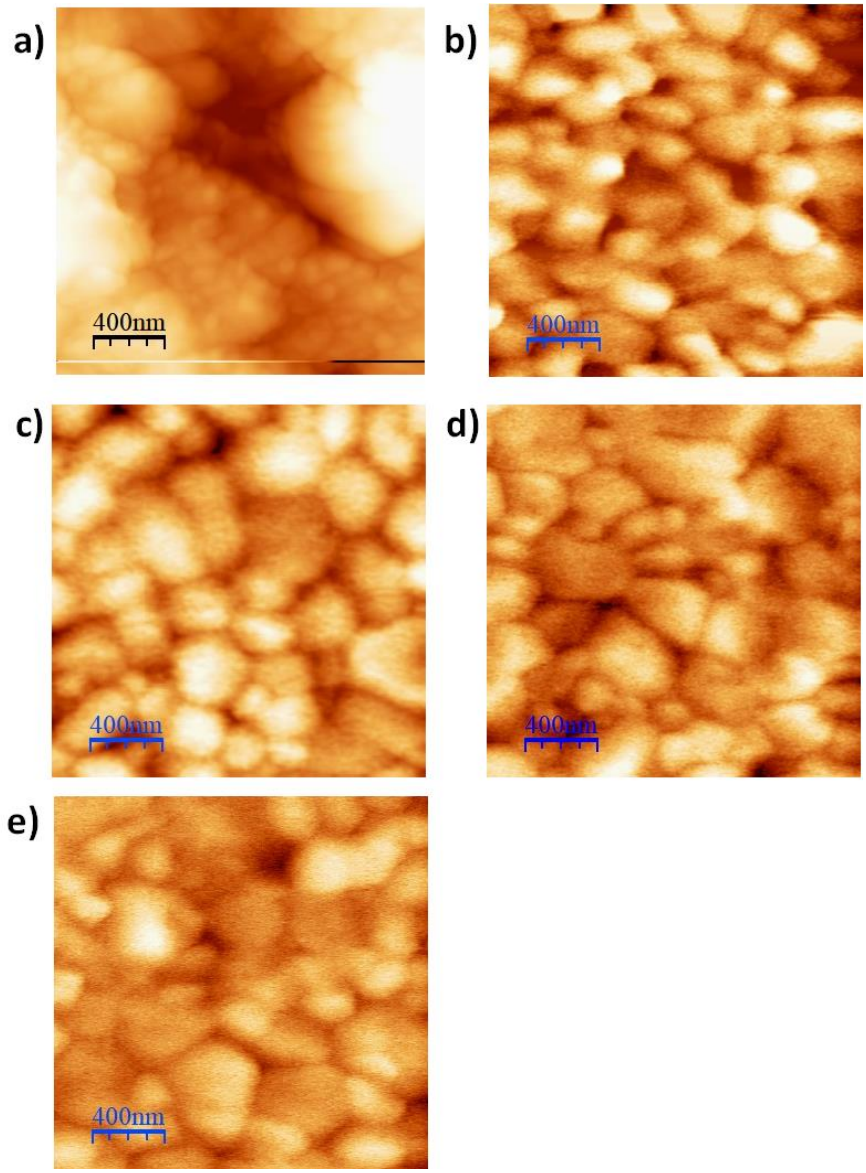

Figure 5.3: AFM images of $MAPbI_3$ films prepared using $MAPbI_3$ concentration at (a) 1.0 (b) 1.25 M (c) 1.5 M (d) 1.75 M and (e) 2.0 M solution s as a function perovskite concentration.

$MAPbI_3$ films were deposited on FTO substrates from 1.00 M, 1.25 M, 1.50 M, 1.75 M, and 2.00 M of $MAPbI_3$ solutions, respectively. The prepared films were rigorously studied using AFM, XRD and UV-Vis techniques. Figures 5.3(a) – 5.3(e) show the AFM images of the $MAPbI_3$ films as a function of solution concentration. The AFM images indicate that all the $MAPbI_3$ films have good morphology and nearly similar grain sizes, except the films deposited from 1.0 M solution, which appeared to have the poorest morphology. Also, the films deposited from 1.0 M seem to have the roughest surface, while those deposited from 2.0 M have the smoothest surface. This observation is because more perovskite molecules are available to cover the substrate surface when $MAPbI_3$ concentration increases.

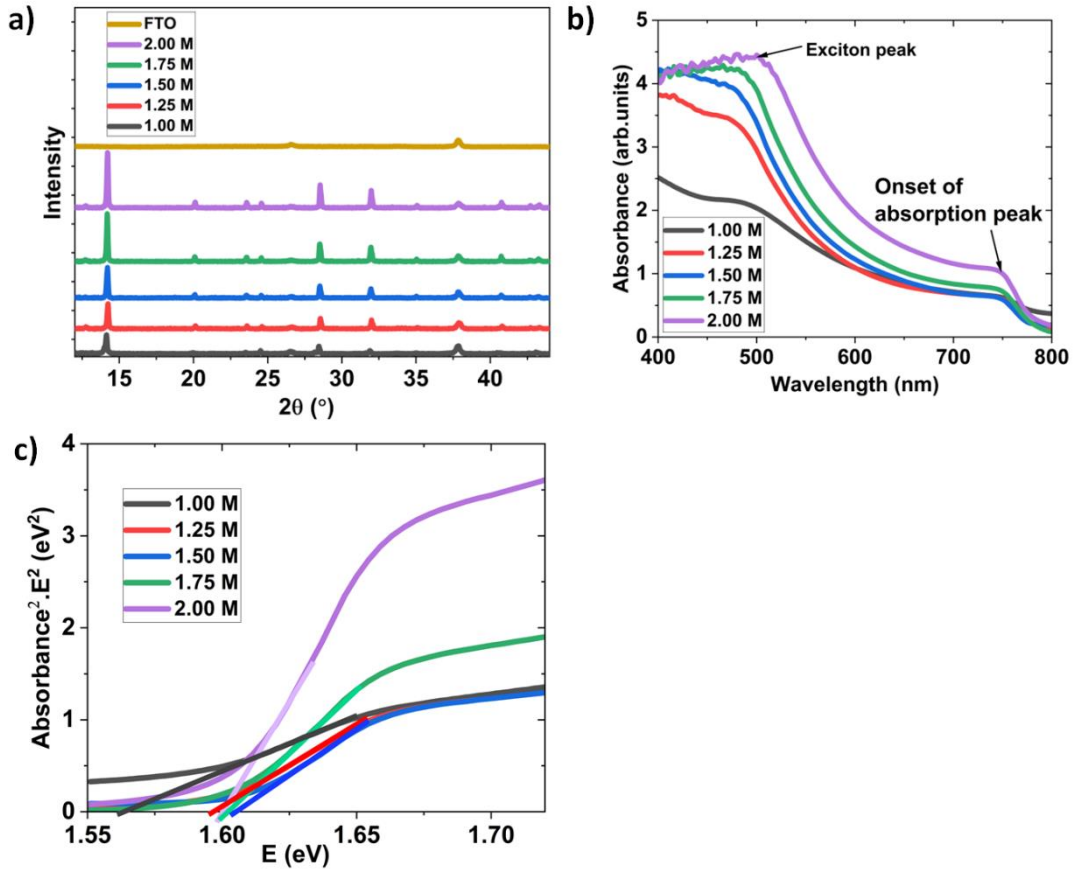

Figure 5.4: (a) XRD spectra of FTO/$MAPbI_3$, (b) absorbance spectra and (c) Tauc plots of $MAPbI_3$ films as a function of perovskite concentration.

Figure 5.4(a) presents the XRD spectra of $MAPbI_3$ films deposited on FTO substrates as a function of solution concentration. The XRD data show that $MAPbI_3$ peaks appeared at 2θ =14.2°, 28.4° and 31.8 ° while the FTO peaks occurred at about 2θ =26.7 and 38.2°.

These peaks closely agree with the 14.1°, 28.4° and 31.9° reported for $MAPbI_3$ [358] and 26.5° and 37.8° reported for FTO [359]. The results also indicate that the preferred crystal growth direction occurred at about 38.2° and 14.2° for FTO and $MAPbI_3$ films, respectively. The XRD measurements show that the ratio of the $MAPbI_3$ peak intensity at 14.02° to the FTO peak intensity at 37.9° increased as the $MAPbI_3$ concentration increased from 1.0 M to 2.0 M. Therefore, the ratio of $MAPbI_3$ intensity to FTO intensity was estimated to be 2.38, 4.16, 5.02, 8.60 and 11.96 for films deposited from 1.0, 1.25, 1.5, 1.75 and 2.0 M of $MAPbI_3$ solution, respectively. These results indicate that film thickness increases with an increase in solution concentration, as reported in [360].

Figures 5.4(b) and 5.4(c) present the absorbance spectra and the Tauc plots of $MAPbI_3$ films deposited on FTO substrates. Figure 5.4(b) indicates that the absorbance spectra of the films increased with the increase in the $MAPbI_3$ concentration, which is probably due to a rise in the film thickness [361,362]. The results also showed that each film has an absorption onset peak at about 722 nm-800 nm [363]. The absorption onset represents the wavelength where the films started absorbing the incident photons with $E \geq E_g$ of the photovoltaic materials. The results also show the presence of exciton peak within the wavelength ranging from 450 nm - 510 nm for green and purple curves. Exciton peaks represent the wavelength region with the highest incident photons and photogenerated charges [363]. Figure 5.4(c) also indicates that the films have E_g varying from 1.57 eV - 1.6 eV. These results closely agree with E_g of 1.59 eV reported in the literature [364]. Hence, this study demonstrates that the prepared films have good absorbance and E_g expected from excellent quality perovskite materials.

5.3.3. Photovoltaic performance of the devices

This study aims to determine the suitable concentration of $MAPbI_3$ solution for preparing highly efficient PSCs. Figure 5.5 shows the J-V curves of the devices for different concentrations of $MAPbI_3$ solution. Table 5.2 summarises the photovoltaic parameters of the devices. The results show that when the concentration of $MAPbI_3$ increased from 1.00 M to 1.50 M, the V_{oc}, FF and J_{sc} of the devices increased. A reason for the increase in J_{sc} could be due to the rise in photon absorption (see Figure 5.4(b)). On the other hand, FF and V_{oc} improved probably because of an enhanced charge carrier extraction, arising from probable decreased R_{dc_f} and increased R_{dc_r} that resulted from lower pinholes (see

Figures 5.3(a) - 5.3(c)) [355]. Hence, the combined enhancement in J_{sc}, V_{oc} and FF leads to improved PCE.

On the other hand, when the concentration of $MAPbI_3$ increased from 1.5 M to 2.0 M, the FF of the devices decreased further while the J_{sc} continued to rise. The increased J_{sc} is due to further enhancement in photon absorption from increased film thickness (see Figure 5.4(b)). Conversely, the FF decreased likely because of the decrease in charge carrier extraction properties of the devices due to an increase in R_{dc_f} (see Table 5.3).

The increase in R_{dc_f} as perovskite concentration was increased from 1.5 M to 2.0 M is likely because of an increase in film thickness beyond the optimum thickness of $MAPbI_3$ films, leading to poor charge carrier extraction [18]. Despite the slight rise in J_{sc}, the significant decrease in FF leads to a steady reduction in PCE as the $MAPbI_3$ concentration increased from 1.5 to 2.0 M. Therefore, this study suggests that 1.5 M is the best $MAPbI_3$ concentration for preparing efficient PSCs under the fabrication condition.

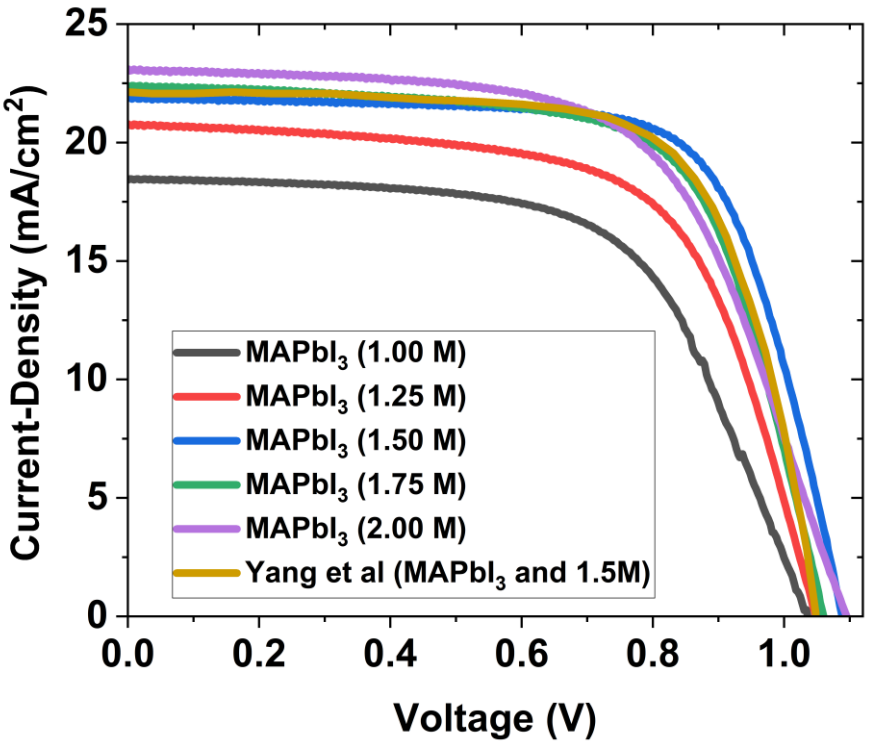

Figure 5.5: J-V curves of the best devices as a function of $MAPbI_3$ concentration and literature [37]. The perovskite films were spin-coated on FTO substrates at 4000 rpm for 30 seconds and annealed at 110°C for 15 minutes.

Table 5.2: Photovoltaic parameters of devices prepared from different $MAPbI_3$ concentrations (the rows denoted "Best" represent the data obtained from the best solar cells of the batch; the rows denoted "Av" represent the average of all cells). Also included in the table is the data from Yang et al. [37].

$MAPbI_3$ (M)		**V_{oc} (V)**	**J_{sc} (mA/cm^2)**	**FF (%)**	**R_{dc_f} (Ω)**	**R_{dc_r} (kΩ)**	**PCE (%)**
1.00	Best	1.04	18.47	61.50	100	12.4	11.78
	Av	1.03±0.02	17.75±0.58	59.92±1.12			10.97±0.46
1.25	Best	1.05	20.71	63.97	67	6.1	13.95
	Av	1.05±0.01	20.35±0.24	62.76±1.58			13.41±0.41
1.50	Best	1.09	21.90	70.55	55	40.0	16.82
	Av	1.08±0.01	21.44±0.61	69.08±0.85			16.01±0.52
1.75	Best	1.06	22.44	67.35	58	7.4	16.03
	Av	1.06±0.01	21.83±0.90	65.24±1.1.080			15.09±0.66
2.00	Best	1.10	23.10	61.62	84	6.5	15.62
	Av	1.08±0.04	21.99±1.14	59.80±3.21			14.16±1.21
Ref-1[37]	Best	1.05	22.21	70.00			16.30

Yang et al. [44] reported a PCE comparable to the PCE achieved in this project. This could be because similar materials, antisolvents, and laboratory conditions were used except for the replacement of gold deposited with thermal evaporation with silver deposited with magnetron sputtering.

5.4. How the addition of FK209 in Spiro-OMETAD affects the PCE of PSCs

This study aims to determine how the addition of an FK209 additive in Spiro-OMETAD affects the efficiency of PSCs. The Spiro-OMETAD solutions were modified using 0, 10, 20,20 and 38 µl of FK209 additive (300 mg/ml of ethane nitrile). Subsection 5.4.1 presents the fabrication process, while subsections 5.4.2 and 5.4.3 discuss the characterisation results obtained from the prepared Spiro-OMETAD films and PSCs in this experiment.

5.4.1. Film and device fabrication

SnO_2 layers were deposited on FTO substrates from 15 mg/ml of $SnCl_2.2H_2O$ solution. Next, $MAPbI_3$ layers were spin-coated on SnO_2 layers from a 1.5 M solution. Next, the spinning films were treated with 150 µl of methyl ethanoate. HTLs were deposited on $MAPbI_3$ layers from an HTL solution containing 90 mg Spiro-OMETAD, 36 µl of MPPD, 22 µl of Li-TFSI solution (520 mg/ml in ethane nitrile) and a varying amount of FK209 additive in 1 ml of chlorobenzene. Different HTL solutions were prepared using 0 µl, 10 µl, 20 µl, 30 µl and 38 µl of FK209 additive solution (300 mg/ml of ethane nitrile). All the solution-processed films were prepared in ambient air of 50-55% relative humidity. Finally, Ag contact with an active area of 0.15 cm^2 was deposited on HTLs at 1.0 W, 15.0 sccm and 5.0 mTorr for 60 minutes to form complete devices with $FTO/SnO_2/MAPbI_3$/Spiro-OMETAD/Ag structures.

5.4.2. Properties of Spiro-OMETAD films

This study aims to determine how the amount of FK209 additive added in the Spiro-OMETAD solution affects the E_g, VB and work function of HTL films. Spiro-OMETAD films deposited on FTO substrates were studied using UPS, AFM, UV-Vis and FTIR techniques. Figure 5.6 presents the UPS spectra of Spiro-OMETAD films deposited on FTO substrates while Table 5.3 summarises the energies of Spiro-OMETAD and $MAPbI_3$. The results show that the work function of HTL shifted from 4.6 eV to 4.85 eV as the amount of FK209 additives in Spiro-OMETAD films increased from 0 to 38 µl. The work function rose with the increase in the amount of FK209 additive because the number of p-type carriers increased. These results are consistent with the results reported in [365].

Equation (2.22) was used to calculate the VB of Spiro-OMETAD and VB of $MAPbI_3$ from UPS spectra). The data show that the VB of the Spiro-OMETAD downshifted from -4.97 eV to -5.22 eV when the amount of FK209 additive increased from 0 to 38 µl, agreeing with -5.22 eV reported in [365,366]. This is because the VB of Spiro-OMETAD is dependent on its oxidation level [367]. Research has shown that the FK209 additive oxidises neutral Spiro-OMETAD to Spiro-$OMETAD^{n+}$. The number of charges per molecule and the number of molecules oxidised is directly proportional to the amount of FK209 added [368,369].

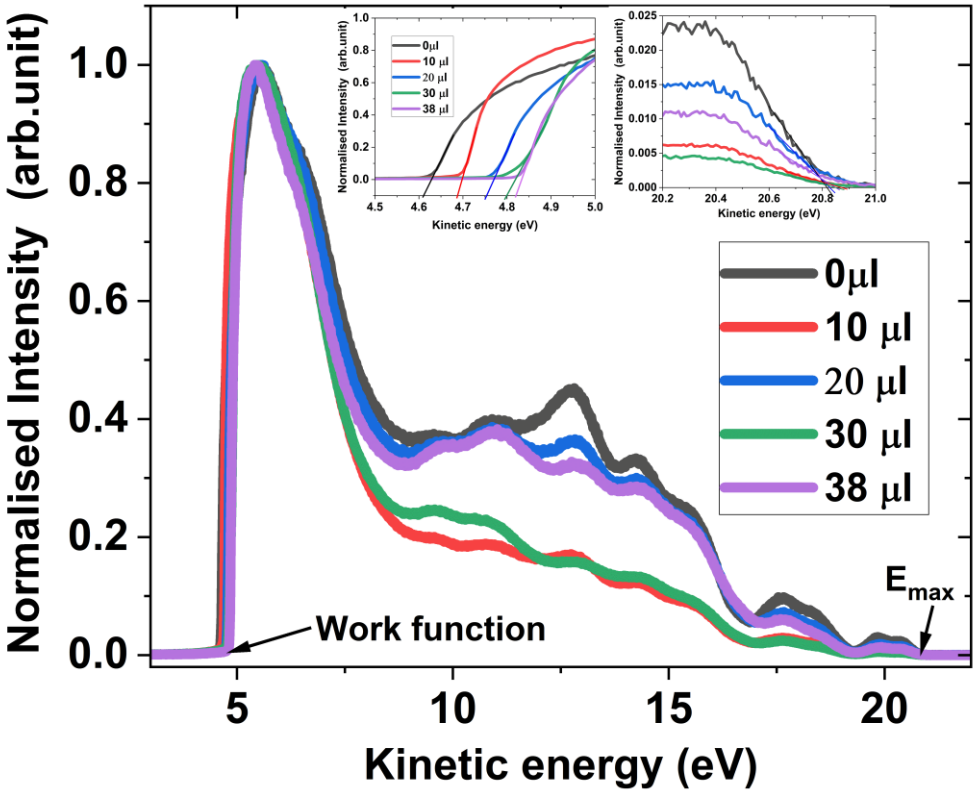

Figure 5.6: UPS spectra of FTO and FTO/Spiro-OMETAD as a work function of FK209 additive.

Table 5. 3: Band properties of Spiro-OMETAD modified with FK209 additive. The table also contains the VB and Fermi level of $MAPbI_3$

FK209 (µl)	VB (eV) (Spiro-OMETAD)	Fermi level (eV) (Spiro-OMETAD)	VB (eV) ($MAPbI_3$)	Fermi level (eV) ($MAPbI_3$)
0	-4.97	-4.6	-5.56	-4.02
10	-5.04	-4.67		
20	-5.12	-4.75		
30	-5.18	-4.78		
38	-5.22	-4.82		

Equation (5.1) was used to compute the VB mismatch between Spiro-OMETAD and $MAPbI_3$ and results show that the VB mismatch decreased as the amount of FK209 additive increased. Hence, the VB mismatch decreased from 0.59 eV to 0.34 eV as the FK209 additive rose from 0 to 38 µl. These results imply that there could be less reduction

in V_{oc} for PSCs based on 38 µl of FK209 [187]. Furthermore, these results demonstrate that HTL modified with 38 µl of FK209 additive has the least VB mismatching relative to the $MAPbI_3$ and could result in devices with the best performance [370].

$$\text{VB mismatch} = \text{VB}_{\text{Spiro-OMETAD}} - \text{VB}_{\text{MAPbI3}} \quad (5.1)$$

The results indicate that the difference between the work function and VB remained constant and independent of the quantity of FK209 additive incorporated in the Spiro-OMETAD films. These results suggest that the Fermi level and VB shifted proportionally when the FK209 additive increased.

Figure 5.7(a) presents the FTIR spectra of the HTL films as a function of the amount of FK209. The results showed that peaks occurred at 827.49, 1038.74, 1247.02, 1465.95, 1509.35 and 1606.76 cm^{-1}, despite the amount of FK209. These peaks agree with the peaks reported in [371]. Therefore, no appearance of new peaks after adding FK209 could indicate that adding a small amount of FK209 additive does not change the peak position of Spiro-OMETAD. Figures 5.7(b) and 5.7(c) present the transmittance and the corresponding Tauc plots of Spiro-OMETAD films as a function of the amount of FK209 additive. The transmittance spectra show that the intensity minima at about 512 nm decreased steadily as the amount of FK209 additive increased. The decrease in intensity minima suggests that the proportion of Spiro-OMETAD molecules oxidised to Spiro-$OMETAD^+$ increased with the amount of the FK209 additive [368,369]. Therefore, the minima at 512 nm represent Spiro-$OMETAD^+$ as reported in [372,373].

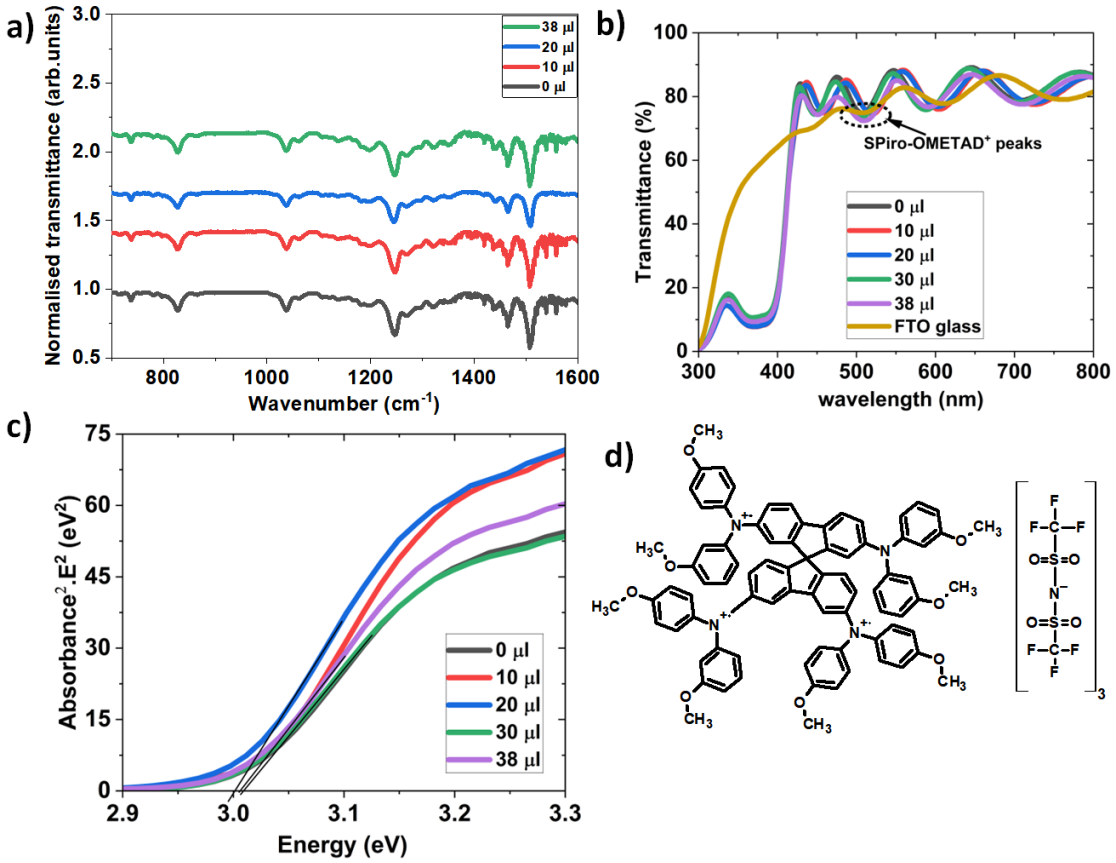

Figure 5. 7: (a) FTIR spectra of Spiro-OMETAD (b) Transmittance spectra and absorbance of Spiro-OMETAD^{+} (c) Tauc plot as a function of FK209 doping and (d) Spiro-OMETAD molecule Oxidised by FK209 additive.

The Tauc plots also show that the E_g of the Spiro-OMETAD films remains practically unchanged when the amount of FK209 additive increased from 0 µl to 38 µl. The E_g remained virtually the same, probably because only a small amount of the additive was added. The E_g of about 3.0 eV achieved in this study closely agrees with the 2.99 eV reported in [366]. Figure 5.7(d) shows the molecule of Spiro-OMETAD oxidised by FK209. The image indicates that one molecule of FK209 additive introduces three positive charges in a molecule of Spiro-OMETAD.

5.4.3. Photovoltaic performance of the devices

This study determines a suitable FK209 additive to be added in Spiro-OMETAD to achieve perovskite solar cells with satisfactory performance. Figures 5.8(a) - 5.8(d) show the energy band diagrams of each device layer as obtained using UPS measurement. The

energy band diagrams demonstrate that the VB mismatch between HTL and $MAPbI_3$ decreases with the increase in the FK209 additive.

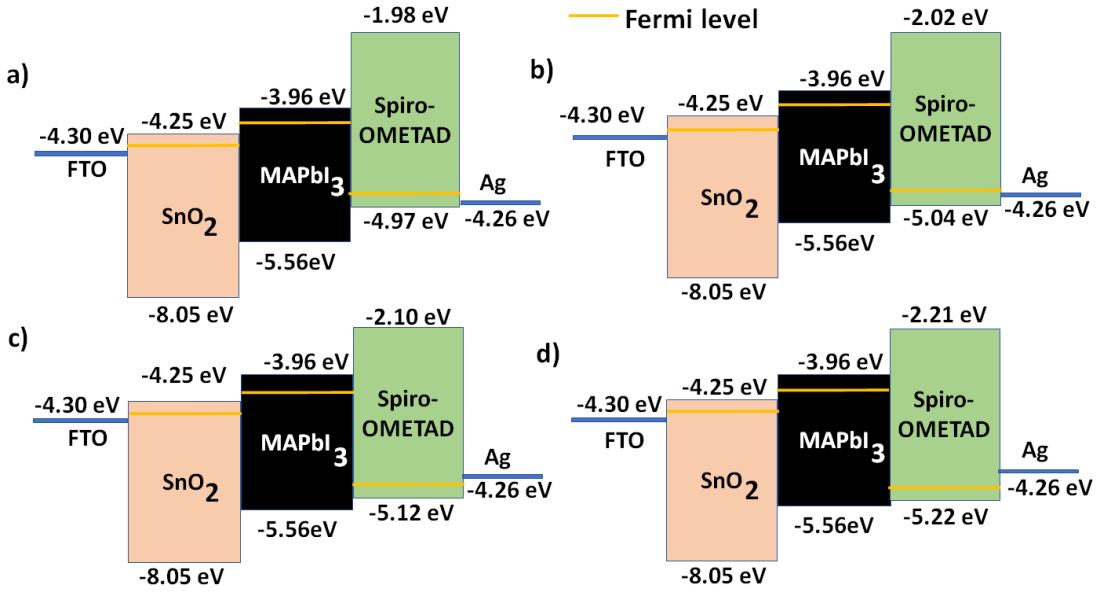

Figure 5.8: VB mismatch between Spiro-OMETAD and $MAPbI_3$ layers for Spiro-OMETAD modified with (a) 0 µl (b) 10 µl (c) 20 µl and (d) 38 µl of FK209 additives.

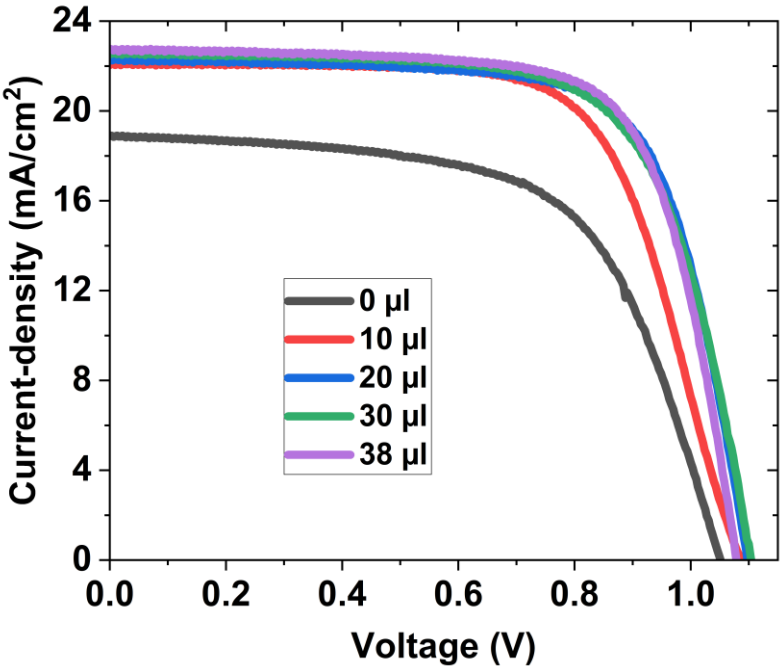

Figure 5.9: J-V curves of best devices as a function of FK209 additive incorporated in Spiro-OMETAD

Table 5.4: Photovoltaic parameters of the devices for different FK209 doping (the rows denoted "Best" represent the data obtained from the best solar cells of the batch; the rows denoted "Av" represent the average of all cells)

FK209 (µl)		V_{oc}(V)	J_{sc} (mA/cm^2)	FF (%)	R_{dc_f} (Ω)	R_{dc_r} (kΩ)	PCE (%)
0.0	Best	1.05	18.90	61.66	81	11.9	12.26
	Av	1.02±0.02	17.62±1.44	58.30±1.76			10.56±1.22
10.0	Best	1.09	22.13	66.99	77	18.2	16.15
	Ave	1.07±0.01	21.45±1.07	66.11±1.16			15.24±1.02
20.0	Best	1.10	22.33	70.93	47	33.3	17.43
	Av	1.08±0.03	22.05±0.54	67.37±2.77			16.07±1.26
30.0		1.11	22.61	68.80	50	11.1	17.16
		1.10±0.01	22.13±0.77	67.03±2.14			16.36±1.15
38.0	Best	1.08	22.76	71.42	45	59.0	17.54
	Av	1.06±0.01	22.20±0.86	70.41±0.61			16.61±0.70

The J-V characteristics of the devices were measured at 1000 W/m^2. Figure 5.9 presents the J-V curves of the devices as a function of the amount of FK209 additive. Table 5.4 summarises the device parameters. The results show that the devices' J_{sc}, FF and PCE increased when the amount of FK209 additive in the HTL rose from 0 to 38 µl. Device performance improved because HTL became more conductive due to the oxidation of Spiro-OMETAD films by the FK209 additive. In addition, the conductivity of the Spiro-OETAD films increased because the FK209 additive increased hole carrier density in the HTLs by creating additional hole carriers [369]. Hence, the improved charge extraction resulted in a reduction of R_{dc_f}. Studies have also proven that increasing the amount of FK209 additive in Spiro-OMETAD leads to an increase in the conductivity of HTLs [369,374,375]. However, a slight decrease in FF when the Spiro-OMETAD was modified with 30 µl of FK209 additive could be because the devices corresponding to this amount were fabricated during the revision period.

The results also show that the V_{oc} increased when the amount of FK209 additive rose from 0 to 30 µl before decreasing slightly with a further increase in the amount of FK209 additive. The initial rise in V_{oc} with FK209 additive from 0 to 30 µl is probably because

of the reduction in VB mismatch at the HTL/$MAPbI_3$ interface. V_{oc} increased when the offset between the VB of HTL and $MAPbI_3$ decreased because the reduction in VB mismatch encourages charge extraction and minimises the recombination arising from the backward flow of holes [376]. However, the available data could not explain the observed decrease in V_{oc} when the FK209 additive increased from 30 µl to 38 µl. This study demonstrates that increasing the amount of FK209 additive in Spiro-OMETAD results in PSCs with improved PCE.

5.5. Summary

This chapter investigated the effect of solution parameters on the performance of perovskite solar cells (PSCs). The study shows that the efficiency of devices started decreasing when the concentration of perovskite solution exceeded 1.5 M. The results also indicated that the efficiency reduced when the concentration of $SnCl_2.2H_2O$ surpasses 15 mg/ml. The data also showed that devices performed best when Spiro-OMETAD solutions contained 38 µl of FK209 additive (300 mg/ml in ethane nitrile). These results demonstrated that devices prepared using 15 mg/ml of $SnCl_2.2H_2O$ solution, 1.50 M of $MAPbI_3$ solutions and Spiro-OMETAD modified with 38 µl of FK209 additive achieved the best PCE. Hence, Chapters 6-8 will employ these parameters for all the investigations.

Chapter 6: Optimum silver contact sputtering parameters for efficient perovskite solar cell

6.1. Introduction

This chapter investigates the optimum sputtering parameters for depositing silver contacts for efficient perovskite solar cells (PSCs). The deposition of silver contact on the Spiro-OMETAD layer using magnetron sputtering is a challenging task because it can induce damage to this organic layer. Therefore, this study systematically investigated how sputtering power, argon flow rate, sputtering duration, and argon pressure for depositing Ag contacts affect the performance of perovskite solar cells. This investigation is the first comprehensive study to determine the optimal condition for depositing Ag contacts on perovskite solar cells.

6.2. Film and device fabrication

The SnO_2 and $MAPbI_3$ layers were prepared using the parameters described in Section 5.4.1. The HTLs were prepared using the parameters described in Section 5.3.1. Ag contacts with active areas of 0.15 cm^2 were deposited on HTLs using the sputtering parameters specified in sections 6.3, 6.4, 6.5 and 6.6. All the perovskite solar cells prepared in this chapter have FTO/SnO_2/$MAPbI_3$/Spiro-OMETAD/Ag structures. Section 3.2 in Chapter 3 provides more information on the device fabrication process.

6.3. Influence of sputtering power on the performance of devices

This study aims to investigate how the sputtering power for depositing the Ag contact affects the performance of PSCs. This study is crucial because sputtering power affects the deposition rate, kinetic energy and the sizes of metal particles, which can induce severe damage to the organic layers. Ag contacts were prepared by varying the sputtering power from 1.0 to 5.0 W while keeping the argon flow rate, sputtering duration and argon pressure at 15 standard cubic centimetres per minute (sccm), 60 minutes and 5 millitorrs (mTorr), respectively. Subsections 6.3.1 and 6.3.2 discuss the properties of prepared Ag films and devices, respectively.

6.3.1. Properties of the prepared silver films

The AFM, 4-Probe and UV-Vis spectrometer were used to study Ag films deposited on glass substrates. Figures 6.1(a) – 6.1(e) present the AFM images of Ag films as a function of sputtering power.

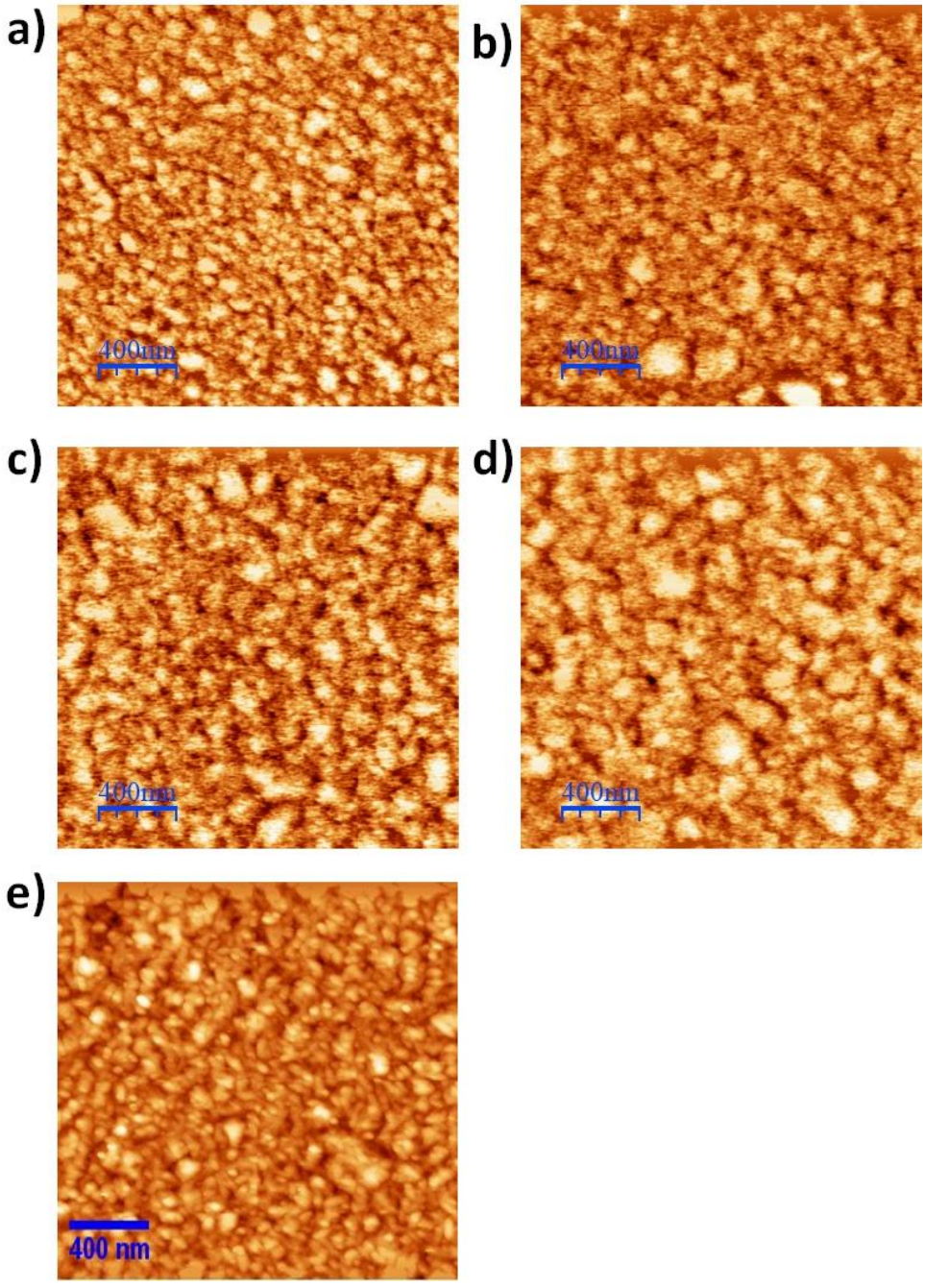

Figure 6.1: AFM images of Ag films sputtered at a sputtering power of (a) 1.0 W, (b) 2.0 W, (c) 3.0 W, (d) 4.0 W and (e) 5.0 W. The films were deposited on glass substrates at 5 mTorr and 15 sccm for 60 minutes.

The AFM images show that the surface smoothness of the films decreased steadily as the sputtering power was increased from 1.0 W to 5.0 W. This observation is relatively consistent with the results reported in [377]. Hence, the Ag films deposited at 1.0 W exhibit the smoothest surface.

Figure 6.2(a) shows the RMS roughness derived from the AFM images using WSxM and Gwyddion software. The results indicate that the RMS roughness increased as the sputtering power was increased from 1.0 W to 5.0 W. This suggests that the surface smoothness of the films decreased as the sputtering power increased.

Figure 6.2(b) shows the XRD spectra of Ag films deposited on glass substrates using different sputtering power. The XRD spectra show that all films have crystalline structures and that the peak intensity grows with increased sputtering power. The increase in peak intensity suggests that the film thickness increases with the rise in sputtering power. The results also demonstrate that the preferred crystal growth direction occurred at about 38°, indicating that it is independent of the sputtering power. The Ag films deposited at 1.0 W, 2.0 W, 3.0 W, 4.0 W and 5.0 W have normalised intensities of 0.3231, 0.4635, 0.5605, 0.5959 and 1.0000, respectively.

Table 6.1: XRD parameters of Ag films as a function of sputtering power. The films were deposited on glass substrates at 15 sccm and 5 mTorr for 60 minutes.

Power (W)	Normalised intensity	2θ (°)	FWHM (°)	Grain size (nm)
1.0	0.3231	38.2073	0.2765	33.7854
2.0	0.4635	38.1247	0.2301	40.5784
3.0	0.5605	38.1307	0.2225	41.9674
4.0	0.5959	38.1203	0.2214	42.1727
5.0	1.0000	38.1549	0.2180	42.8370

Using Origin Lab Software, this project extracted the peak positions (2θ) and full width at half maximum (FWHM, β) from the XRD spectra. Equation (2.18) presents the expression for calculating the grain sizes (z) from β and θ. Table 6.1 shows the 2θ, β and

z parameters for films as a function of sputtering power. These results indicate that the FWHM decreased while the grain size increased with increased sputtering power.

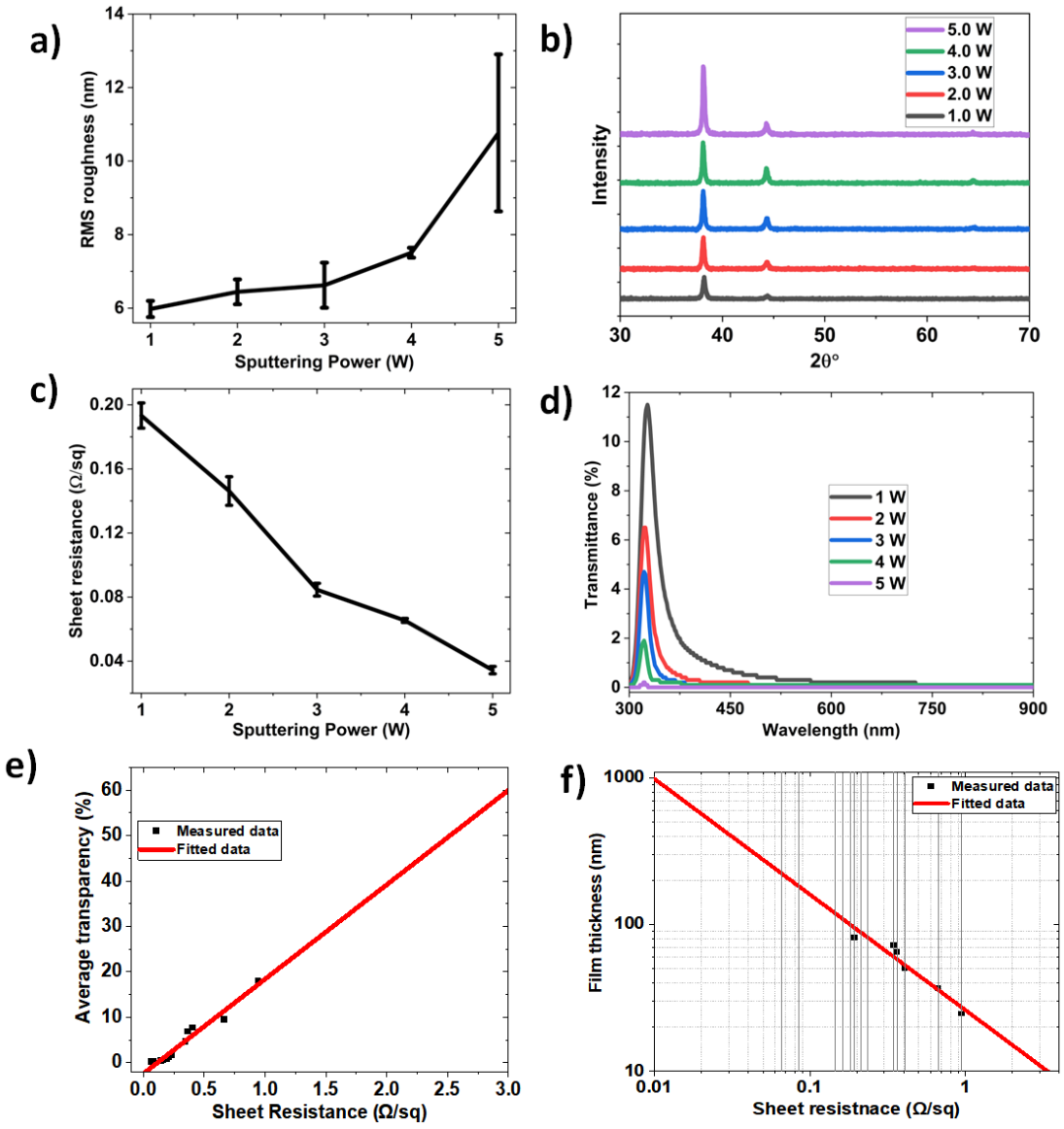

Figure 6.2: (a) RMS roughness, (b) XRD pattern, (c) sheet resistance, (d) transmittance, (e) average transparency, and (f) thickness of Ag films deposited on glass substrates as a function of sheet resistance.

Figure 6.2(c) presents the sheet resistance of the Ag films measured using a 4-Probe. The results show that the average sheet resistance of the Ag films decreased from 0.193 Ω/sq. to 0.0344Ω/sq. as the sputtering power was increased from 1.0 W to 5.0 W. This is likely because an increase in sputtering power led to a rise in the film thickness, resulting in reduced sheet resistance of the film.

Figure 6.2(d) shows the transmittance spectra of Ag films at different sputtering power. The data indicate that all the Ag films have low transparency in the 300 nm – 900 nm wavelength range. Figure 6.2(e) shows that films deposited at 1.0 W, 2.0 W, 3.0 W, 4.0 W and 5.0 W have average transparencies of 0.9%, 0.4%, 0.3%, 0.2% and 0.01% over 300 nm – 900 nm wavelength, respectively. The results also indicated the presence of transmittance maxima at about 344 nm. The position and appearance of the maxima achieved in this study are consistent with those reported elsewhere [378]. In addition, the results indicate that the height of the maxima increased with the reduction in sputtering power and, consequently, the film thickness. This observation agrees with the maxima trends reported in [379].

AFM images of thin Ag films were captured at the edge glass/Ag interface. The AFM images were processed using WSxM and Gwydion software. Figure 6.2(f) presents the measured and extrapolated thickness of Ag films as a function of sheet resistance. The results indicate that as sheet resistance decreased, the film thickness increased. Hence, films deposited at 1.0 W, 2.0 W, 3.0 W, 4.0 W and 5.0 W have estimated thicknesses of 95 nm, 120 nm, 184 nm, 223 nm, and 360 nm, respectively.

The cross-sectional images of fabricated devices were studied using a scanning electron microscope (SEM) to ascertain the damaging effect of sputtering power on HTLs. Figures 6.3(a) – 6.3(d) present the cross-sectional SEM images of the devices as a function of sputtering power. Table 6.2 summarises the film thicknesses extracted from the SEM images using ImageJ. The SEM studies indicate that the HTL thickness was reduced from 156 nm to 75 nm when the Ag sputtering power increased from 1.0 W to 4.0 W (see Table 6.2). The SEM results suggest that the HTL suffered damage, and the degree of damage is proportional to the sputtering power. The Table also presented the thicknesses of the FTO and $MAPbI_3$ films from the SEM images.

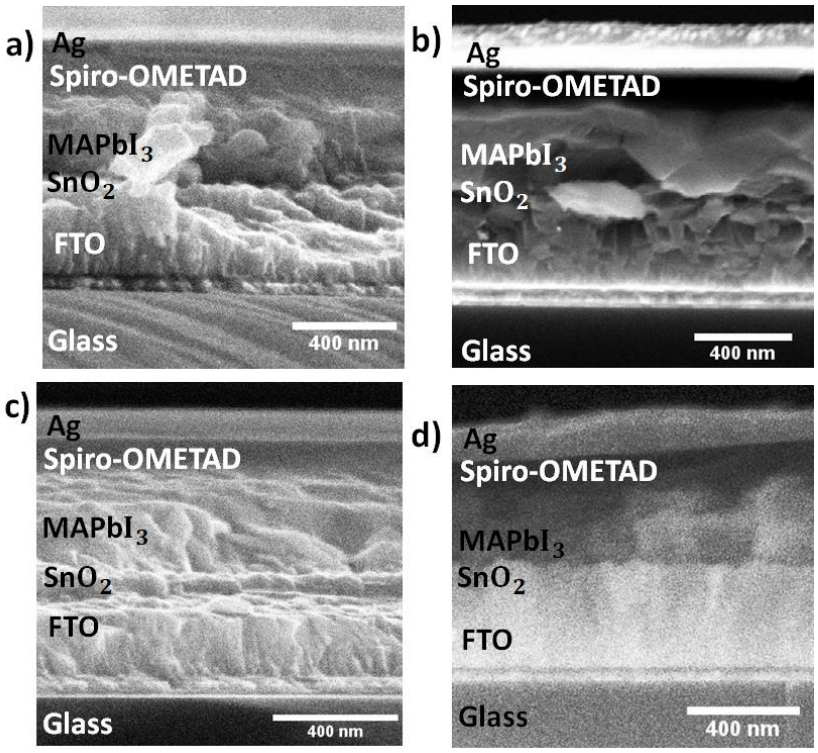

Figure 6.3: Cross-sectional SEM images of the devices with Ag contacts deposited at a sputtering power of (a) 1.0 W, (b) 2.0 W, (c) 3.0 W and (d) 4.0 W. The films were deposited at 5 mTorr, 15 sccm for 60 minutes.

Table 6.2: Thicknesses of FTO, $MAPbI_3$ and Spiro-OMETAD films estimated from SEM images using ImageJ. The Ag films were deposited at 15 sccm and 5 mTorr for 60 minutes.

Sputtering power (W)	Average film thickness (nm)		
	FTO	$MAPbI_3$	Spiro-OMETAD
1.0	400	343	156
2.0	400	396	120
3.0	400	355	101
4.0	400	355	75

6.3.2. Photovoltaic performance of the devices

The impedance spectra of the devices were measured at 1000 W/m^2 and 1.0 V. Junction capacitances were extracted from the IS plots using ZSimpWin software. Figure 6.4(a)

shows the junction capacitance of the devices as a function of the sputtering power. The results show that the junction capacitance of the devices reduced as the sputtering power increased. This observation could be due to degradation in charge extraction arising from damages to the HTL, as indicated by the SEM measurements in Figures 6.3(a) - 6.3(d). Consequently, this suggests a decrease in carrier density as the sputtering power increases.

The J-V measurement was conducted at 1000 W/m^2. Figure 6.4(b) shows the PSCs' J-V curves as a function of the sputtering power. Table 6.3 summarises the photovoltaic parameters of the devices prepared. The photovoltaic parameters indicate that as the sputtering power increased from 1.0 to 2.0 W, the solar cells' fill factor (FF) decreased slightly, and the short-circuit current density (J_{sc}) increased. At the same time, the open-circuit voltage (V_{oc}) remained practically the same. The improvement in J_{sc} is possible because of the reduction in the sheet resistance of the Ag contact, as shown in Figure 6.2(c). These results suggest that good contact conductivity could be crucial in achieving high electrical currents. The decrease in FF and PCE may be attributed to a slight drop in charge extraction (see Figure 6.4(a)) due to a minor reduction in HTL thickness arising from increased sputtering power, as shown in Figure 6.3(b). However, the V_{oc} showed no notable change because the HTL damage and Ag doping into HTL/perovskite layers were negligible. Since the reduction in FF is more significant than the improvement in J_{sc}, the PCE of devices with contacts deposited at 2.0 W slightly deteriorated.

When the sputtering power increased from 2.0 to 3.0 W, the V_{oc} and FF decreased further while the J_{sc} slightly increased. The significant reduction in V_{oc} and FF is due to more acute HTL damage that has led to a decrease in HTL thickness, as shown by SEM images in Figures 6.3(b) and 6.3(c). Few reports have proven that HTL damages result in severe recombination and poor device performance [58]. Consequently, the damaged HTL reduces charge density, as indicated by the drop in junction capacitance [64]. However, the J_{sc} is increased further, probably because of thinner barriers (HTL) and a further reduction in the sheet resistance of the Ag contact. Hence, the combined effect of FF and V_{oc} degradation counteracted the improvement in J_{sc}, leading to a significant decrease in PCE of the devices with Ag contacts deposited at 3.0 W.

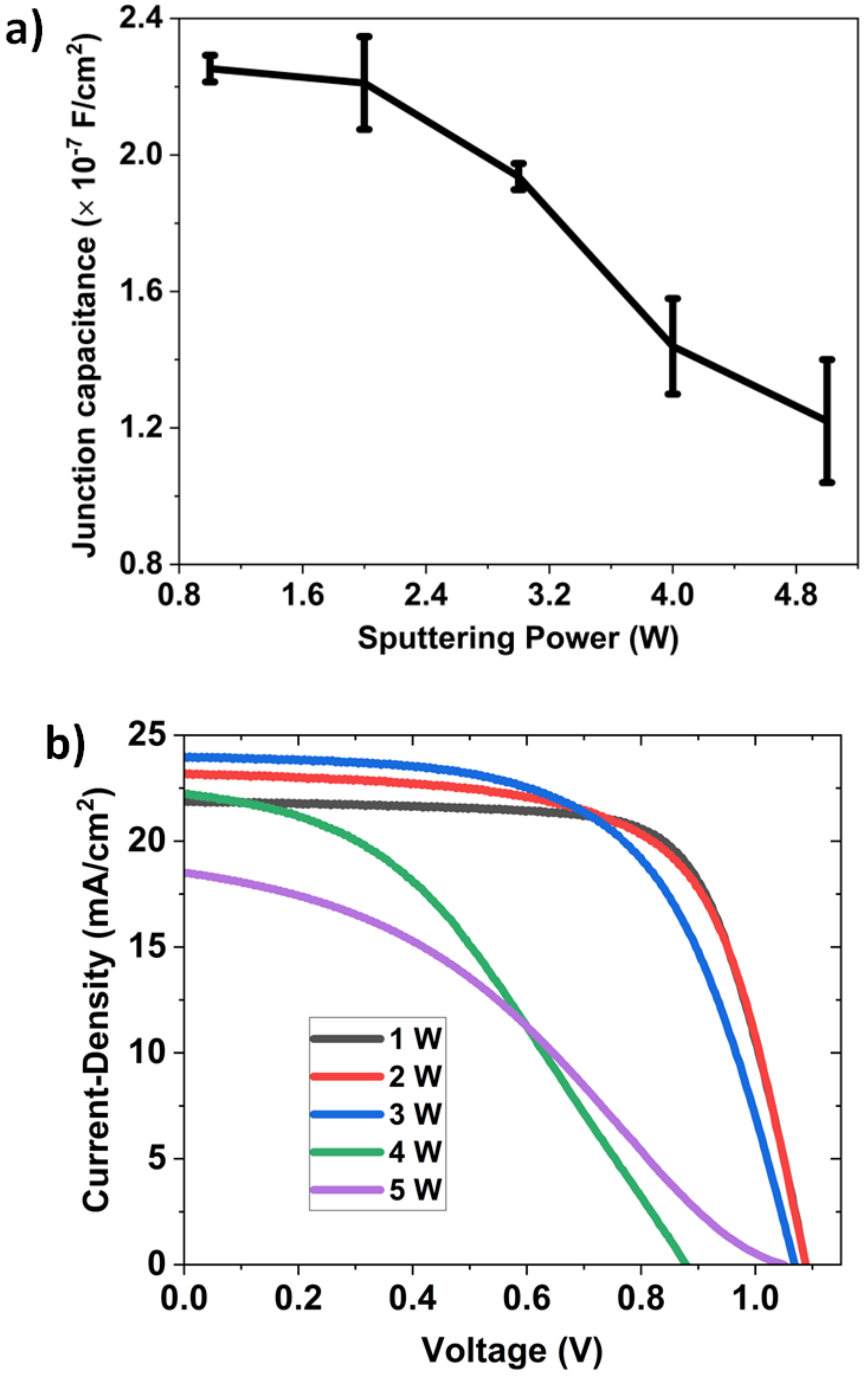

Figure 6.4: (a) Junction capacitance and (b) J-V curves of the best devices as a function of sputtering power for PSCs with Ag contacts. The Ag contacts of the devices were deposited at 15 sccm and 5 mTorr for 60 minutes.

Table 6.3: Photovoltaic parameters of the devices with Ag contacts deposited using different sputtering powers (the rows denoted "Best" represent the data obtained from the best solar cells of the batch; the rows denoted "Av" represent the average of all cells). The Ag contacts of the devices were deposited at 15 sccm and 5 mTorr for 60 minutes.

Sputtering Power (W)		V_{oc} (V)	J_{sc} (mA/cm^2)	FF (%)	R_{dc_f} (Ω)	R_{dc_r} (kΩ)	PCE (%)
1.0	Best	1.09	21.90	70.55	55	40.0	16.82
	Av	1.08±0.01	21.44±0.61	69.08±0.85			16.01±0.5
2.0	Best	1.09	23.21	65.24	55	12.5	16.49
	Av	1.08±0.01	22.40±1.10	62.28±4.35			15.08±0.83
3.0	Best	1.07	23.96	60.00	67	8.9	15.41
	Av	1.07±0.01	23.13±0.74	60.08±1.66			15.05±0.29
4.0	Best	0.88	22.29	38.75	164	1.6	7.61
	Av	0.86±0.03	21.22±0.85	37.62±1.00			6.88±0.38
5.0	Best	1.05	18.55	35.18	498	1.4	6.86
	Av	0.69±0.36	18.06±3.59	33.23±5.69			3.81±1.83

With a further increase in the sputtering power from 3.0 to 4.0 W, the devices' PCE drastically decreased due to a significant reduction in V_{oc} and FF, even though the sheet resistance of the Ag contact was further reduced. The considerable decrease in V_{oc} and FF is likely due to severe damage to organic HTL by Ag particles during high sputtering power. Sputtering Ag contacts at 4.0 W reduces HTL thickness to about 75 nm (see Figure 6.3(d) and Table 6.2). A consequence of the damage to the HTL is an increase in charge recombination that leads to a decrease in charge carrier density (junction capacitance) of the devices [64]. Further, J_{sc}, FF, and PCE reduced when the sputtering power increased from 4.0 W to 5.0 W. However, the available data could not explain a slight increase in the V_{oc} of best devices for sputtering power above 4.0W. The results from this study seem to indicate that the difference in the sheet resistance of Ag films deposited using 1.0 W and 5.0 W has little influence on the performance of the perovskite solar cells. This observation could be because the sheet resistance obtained from Ag films deposited at 1.0 W is already sufficiently low (0.193 Ω/sq.). Hence, further improvement in sheet resistance of Ag films deposited at 5.0 W only introduces severe degradation in J_{sc}, FF

and V_{oc}. This study suggests that 1.0 W is the most suitable sputtering power for depositing Ag contacts at sputtering conditions of 5.0 mTorr, 15 sccm and 60 minutes. Since this magnetron sputtering equipment does not support sputtering power below 1.0 W, the study could not be extended below 1.0 W.

6.4. Dependence of device performances on the argon flow rate

This study investigates the dependence of PSC performances on the argon flow rate for depositing Ag contacts. The films and devices were prepared by varying the argon flow rate from 5 sccm to 25 sccm while the argon pressure, sputtering power and duration were kept at 5.0 mTorr, 1.0 W and 60 minutes, respectively. Subsection 6.4.1 discusses the properties of Ag films, while subsection 6.4.2 analyses the photovoltaic characteristics of PSCs.

6.4.1. Properties of the prepared silver films

AFM, XRD, 4-Probe and UV-Vis spectrometer were used to study Ag films deposited on glass substrates. Figures 6.5(a) – 6.5(e) show the AFM images of the Ag films as a function of the Ar flow rate. The AFM images suggest that the surface smoothness of films increased as the argon flow rate was increased from 5.0 sccm to 20.0 sccm before slightly decreasing as the argon flow rate increased to 25.0 sccm. This observation could be because of the increase in grain interconnections as the deposition rate increased.

The AFM images were analysed using WSxM and Gwyddion software to obtain the roughness parameters. Figure 6.6(a) presents the RMS parameters of the films prepared at different argon flow rates. The results show that the RMS roughness of the films decreased as the argon flow rate increased from 5.0 sccm to 20.0 sccm before slightly increasing when the argon flow rate further increased to 25.0 sccm. The observed decrease in RMS with the increase in argon flow rate is likely because of the improvement in surface coverage and grain connectivity. However, the available data could not explain why the RMS roughness increased slightly when the argon flow rate increased beyond 20 sccm.

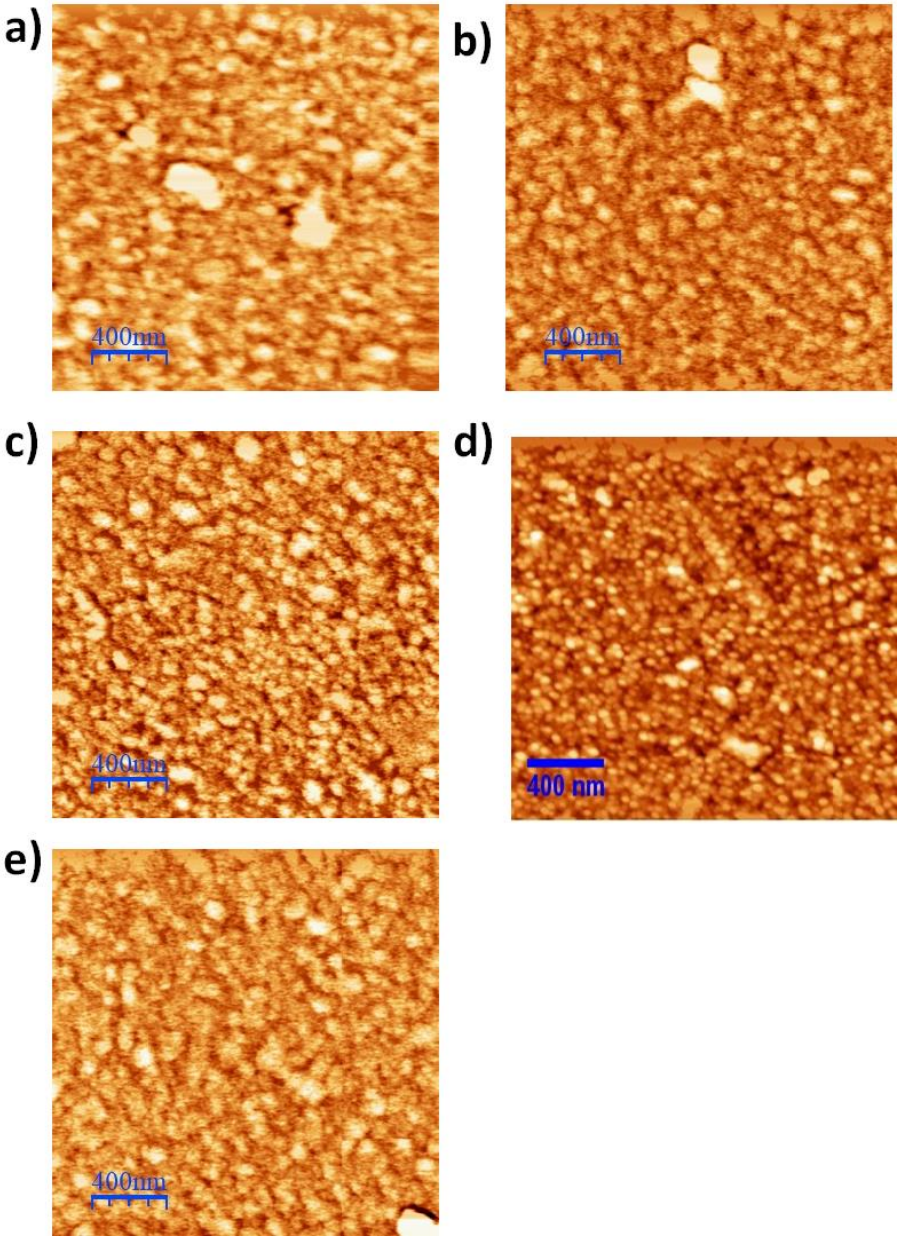

Figure 6.5: AFM images of Ag films sputtered at an argon flow rate of (a) 5 sccm, (b) 10 sccm, (c) 15 sccm, (d) 20 sccm and (e) 25 sccm. The films were deposited on glass substrates at 5 mTorr and 1.0 W for 60 minutes.

Figure 6.6(b) shows the XRD spectra of Ag films deposited on glass substrates. The XRD spectra indicate clearly that all the films have crystalline structures and that the intensity increased when the argon flow rate increased. The increase in intensity is possible because of an increase in film thickness. Table 6.4 presents features of the XRD spectra relative

to the flow rate. The results show that the grain sizes increased and FWHM decreased as the argon flow rate increased from 5 to 25 sccm.

Table 6.4: XRD parameters of Ag films deposited at different argon flow rates. The films were deposited on glass substrates at 1.0 W and 5.0 mTorr for 60 minutes.

Argon flow rate (sccm)	Normalised intensity	2θ (°)	FWHM (°)	Grain size (nm)
5.0	0.5358	38.2137	0.2861	32.6569
10.0	0.6737	38.2001	0.2828	33.0320
15.0	0.7507	38.2073	0.2765	33.7854
20.0	0.7772	38.2355	0.2607	35.8199
25.0	1.0000	38.2355	0.2593	36.0364

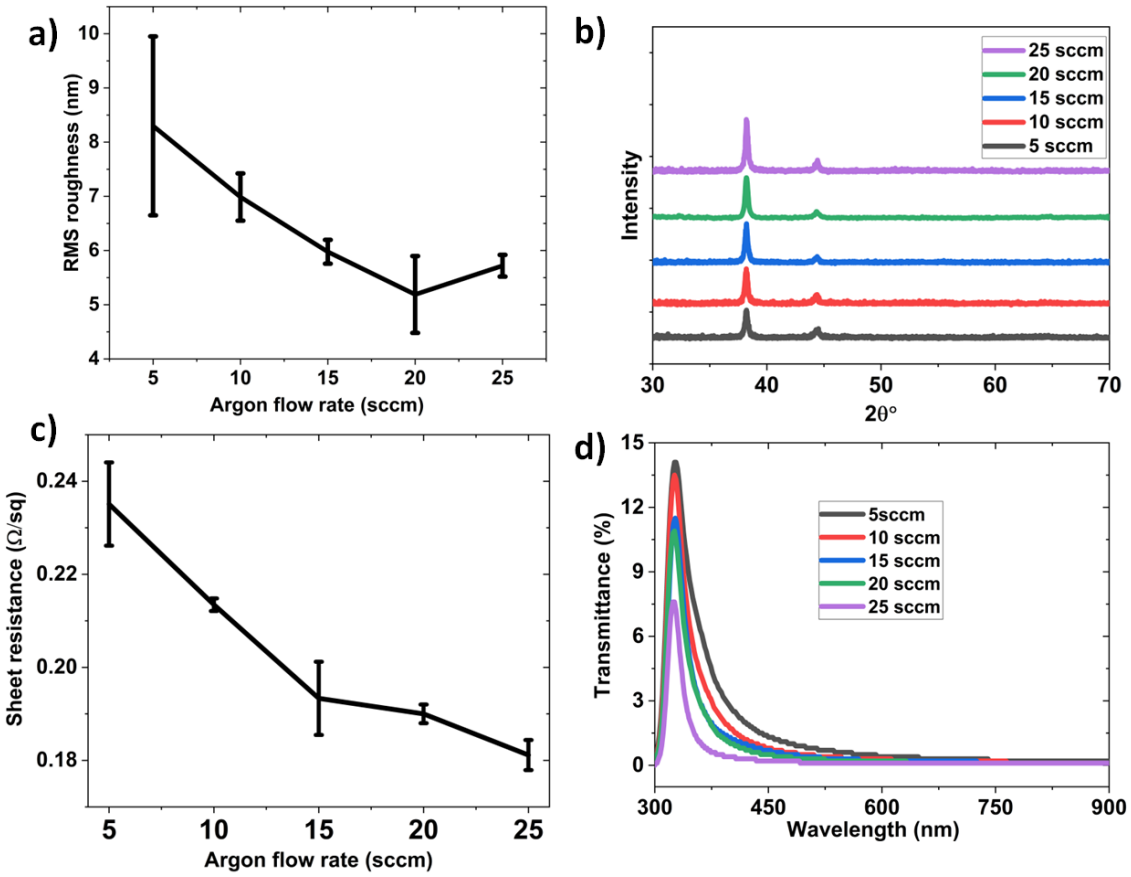

Figure 6.6: (a) Root-Mean Square roughness, (b) XRD pattern, (c) sheet resistance and (d) transmittance of Ag films as a function of argon flow rate. The Ag films were deposited on glass substrates at 1 W, five mTorr for 60 minutes.

Figure 6.6(c) presents the sheet resistance of the Ag films. The resistance data show that the average sheet resistance of the Ag films decreased from 0.235 Ω/sq. to 0.181 Ω/sq. as the argon flow rate increased from 5.0 sccm to 25.0 sccm. The decrease in sheet resistance is a consequence of the increase in film thickness resulting from an increase in deposition rate.

Figure 6.6(d) shows the transmittance of Ag films deposited at different argon flow rates. The results indicate that the transparency of the films was relatively low at 300 nm – 900 nm wavelength. Hence, Ag films deposited at 25 sccm and 5.0 sccm have average transparencies of 0.8% and 1.6%, respectively. The results also demonstrated the presence of maxima at about 344 nm, just like the data reported in subsection 6.2.1. The results also show that the intensity of the maxima increases with a reduction in the argon flow rate, suggesting that it is a function of film thickness. Ag thicknesses estimated from Figure 6.2(f) indicate that the film thickness increased from 82 nm to 101 nm as the argon flow rate increased from 5.0 sccm to 25.0 sccm.

6.4.2. Photovoltaic performance of the devices

J-V measurements of the devices were studied immediately after fabrication. Figure 6.7(a) presents the junction capacitance of the PSCs with Ag contacts deposited at different argon flow rates. The results show that the junction capacitance reached the maximum at an argon flow rate of 15.0 sccm before decreasing when the flow rate increased to 25.0 sccm. These results suggest that devices with Ag contact deposited at 15.0sccm could achieve the best charge extraction and PCE.

Figure 6.7(b) presents J-V curves of PSCs as a function of argon flow rate, while Table 6.5 summarises device parameters. The results show that the J_{sc} of the devices improved as the argon flow rate increased from 5.0 to 25.0 sccm. The J_{sc} may have improved due to a reduction in sheet resistance of the Ag films as the argon flow rate was increased (see Figure 6.6(c)). The results also show that V_{oc} remained virtually constant when the argon flow rate increased from 5.0 to 20.0 sccm. However, the V_{oc} decreased when the argon flow rate increased to 25.0 sccm. This observation is likely due to slight damage to HTL, resulting in reduced charge extraction (see Figure 6.7(a)).

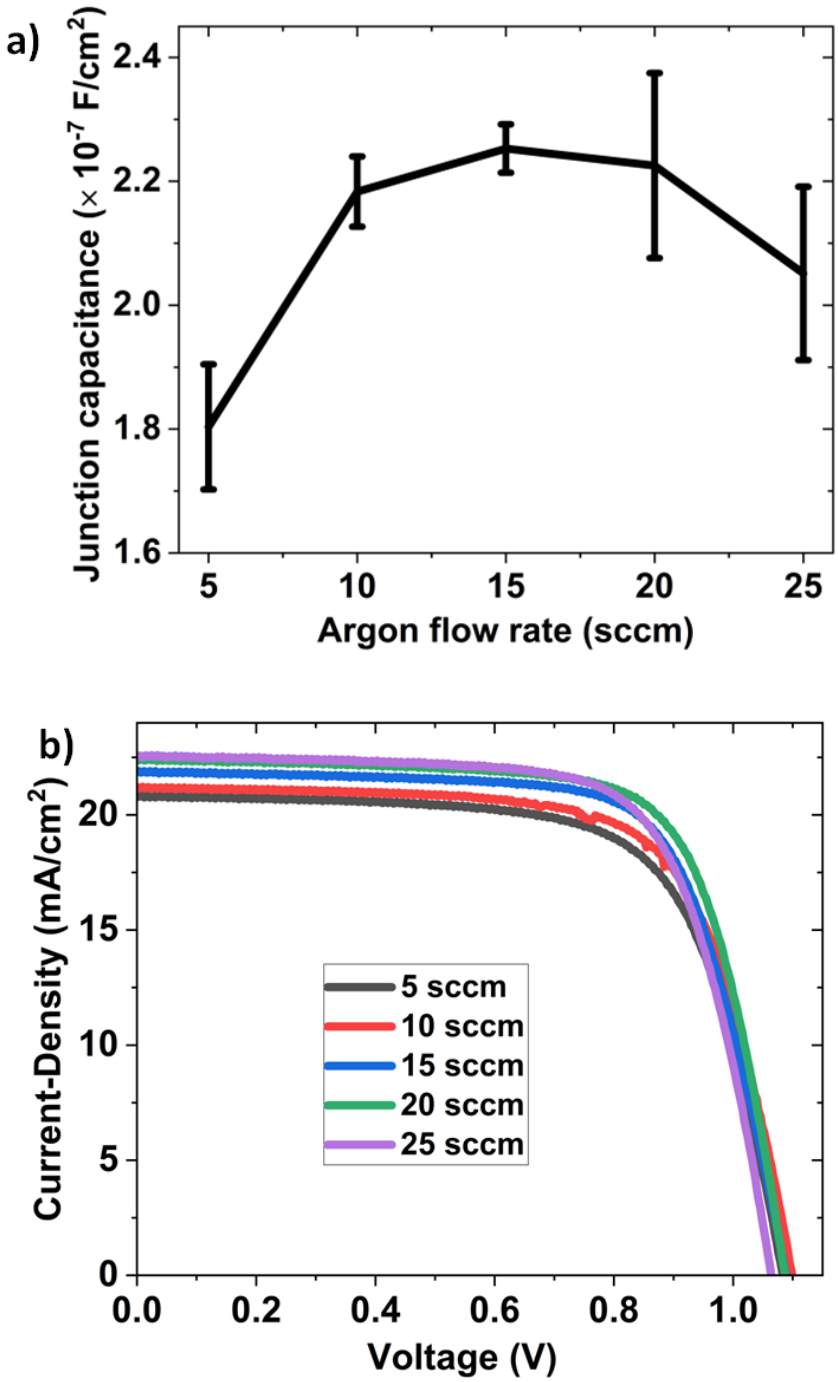

Figure 6.7: (a) Junction capacitance of devices and (b) J-V curves of best devices with Ag contacts deposited at different argon flow rates. The Ag contacts of the devices were deposited at 1.0 W and 5.0 mTorr for 60 minutes.

Table 6.5: Photovoltaic parameters of devices with Ag contacts deposited using different argon flow rates (the rows denoted "Best" represent the data obtained from the best solar cells of the batch; the rows denoted "Av" represent the average of all cells). The Ag contacts of the devices were deposited at 1.0 W and 5.0 mTorr for 60 minutes.

Argon flow rate (sccm)		V_{oc} (V)	J_{sc} (mA/cm^2)	FF (%)	R_{dc_f} (Ω)	R_{dc_r} (kΩ)	PCE (%)
	Best	1.09	20.84	68.22	55	7.4	15.44
5.0	Av	1.09±0.01	20.42±1.18	64.71±2.66			14.39±1.21
	Best	1.10	21.22	69.03	56	22.6	16.12
10.0	Av	1.08±0.02	20.63±0.73	65.82±2.71			14.70±0.97
	Best	1.09	21.90	70.55	55	40.0	16.82
15.0	Av	1.08±0.01	21.44±0.61	69.08±0.85			16.01±0.52
	Best	1.09	22.44	71.64	46	18.2	17.49
20.0	Av	1.08±0.00	21.16±2.01	70.26±0.99			16.13±1.70
	Best	1.06	22.56	70.32	49	21.9	16.91
25.0	Av	1.06±0.01	23.01±0.99	63.27±5.12			15.45±0.97

On the other hand, at 5.0 sccm, the V_{oc} of the devices was slightly reduced, probably due to the high sheet resistance of the Ag films, which led to poor carrier collection. The results also indicate that the FF showed an increasing trend as the argon flow rate increased from 5.0 to 20.0 sccm before decreasing as the argon flow rate increased to 25.0 sccm. The decrease in sheet resistance (see Figure 6.6(b)) of the Ag films with an increase in the argon flow rate, helps improve the charge carrier extraction. However, the severity of HTL damage increased with the argon flow rate because of an increase in deposition rate. The rise in HTL damage leads to the deterioration of the charge carrier extraction (see Figure 6.7(a)). In summary, 20.0 sccm appears to be the most suitable argon flow rate for preparing Ag contact using magnetron sputtering for conditions under 5.0 mTorr, 1.0 W and 60 minutes.

6.5. Optimal sputtering duration for efficient perovskite solar cells

This study aims to determine the optimal sputtering duration for depositing Ag contact on PSCs to achieve good efficiency. The sputtering time for Ag contact deposition varied from 20 to 100 minutes, whereas the sputtering power, argon flow rate and argon pressure were kept constant at 1.0 W, 15.0 sccm and 5.0 mTorr, respectively. Subsection 6.5.1 presents the properties of the prepared Ag films, while subsection 6.5.2 discusses the results obtained from the photovoltaic characterisation of PSCs.

6.5.1. Properties of the prepared silver films

Initially, the Ag films deposited on glass substrates were studied using AFM. Figures 6.8(a) – 6.8(e) show the AFM images of Ag films. The AFM images show that the surface smoothness of the films decreased steadily as the sputtering duration increased. Hence, the films deposited for 20 minutes have the smoothest surfaces.

Figure 6.9(a) shows the RMS roughness of the films deposited for different durations. The results indicate that the RMS roughness of the films increased when the sputtering duration was increased from 20 to 40 minutes, remaining more or less the same as the sputtering time increased to 80 minutes. However, an increase in sputtering duration from 80 minutes to 100 minutes caused a slight rise in RMS roughness. The available data could not explain the slight increase in the RMS roughness when the sputtering duration increased beyond 80 minutes. These results indicate that films deposited for 20 minutes have the smallest grain sizes and the smoothest surfaces.

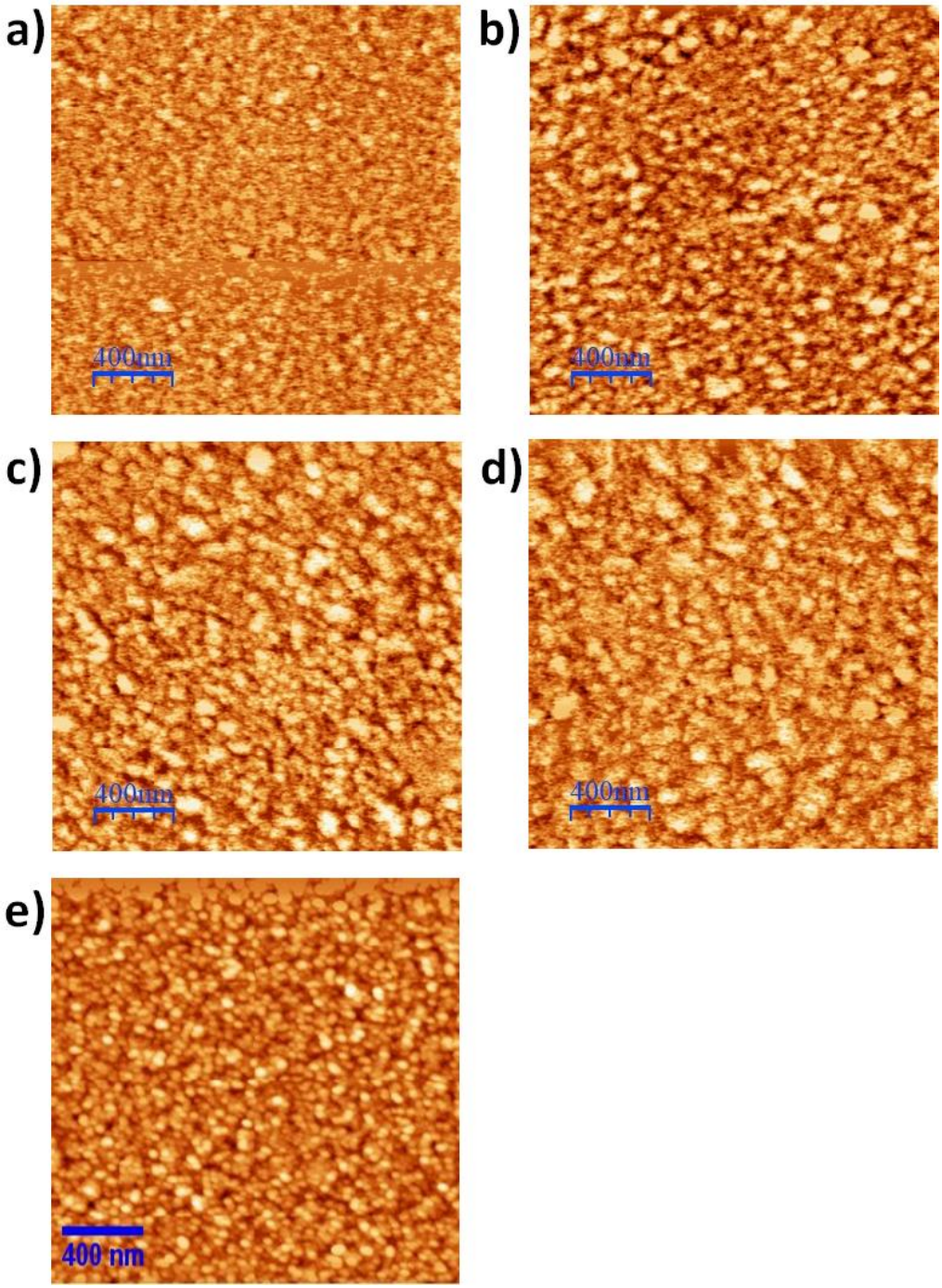

Figure 6.8: AFM images of Ag films sputtered for (a) 20 minutes, (b) 40 minutes, (c) 60 minutes, (d) 80 minutes and (e) 100 minutes. The films were deposited on glass substrates at 5.0 mTorr, 15 sccm and 1.0 W.

Figure 6.9(b) presents the XRD spectra of Ag films on glass substrates as a function of sputtering duration. The XRD spectra demonstrate that all the films have crystalline structures and that the intensity of the films increased with the sputtering period. The increase in the intensity of the spectra with sputtering time suggests an increase in film

thickness with sputtering duration. The increase in film thickness with increased sputtering duration occurred because the long sputtering time allowed the deposition of many more Ag particles. The results also indicate that the sputtering time does not affect the preferred crystal growth direction. Table 6.6 shows FWHM and the grain sizes of the films deposited for different durations. The results indicate that the grain sizes increased while the FWHM decreased when the deposition duration increased.

Table 6.6: XRD parameters of Ag films as a function of sputtering duration. The films were deposited on glass substrates at 1.0 W, 5.0 mTorr and 15 sccm.

Sputtering duration (min)	Normalised intensity	2θ (°)	FWHM (°)	Grain size (nm)
20.0	0.1888	38.2005	0.4164	22.4374
40.0	0.3056	38.2148	0.3118	29.9631
60.0	0.6360	38.2073	0.2765	33.7854
80.0	0.7506	38.1161	0.2640	35.3766
100.0	1.0000	38.2139	0.2526	36.9675

Figure 6.9(c) gives the sheet resistance of the Ag films as a function of sputtering duration. The graph shows that the average sheet resistance of the Ag films decreased from 0.943 Ω/sq. to 0.100 Ω/sq. as the sputtering time increased from 20 to 100 minutes. The decrease in sheet resistance is likely because of increased film thickness with increased sputtering duration.

Figure 6.9(d) shows the transmittance of Ag films deposited at different sputtering durations. The results reveal that films deposited for 20 and 40 minutes have good transparency over 300 – 900 nm. Hence, an average transparency of 18.04% was achieved for films deposited for 20 minutes (see Figure 6.2(e)). The results also indicate the transmittance maxima shift with the increase in film thickness for the very thin films.

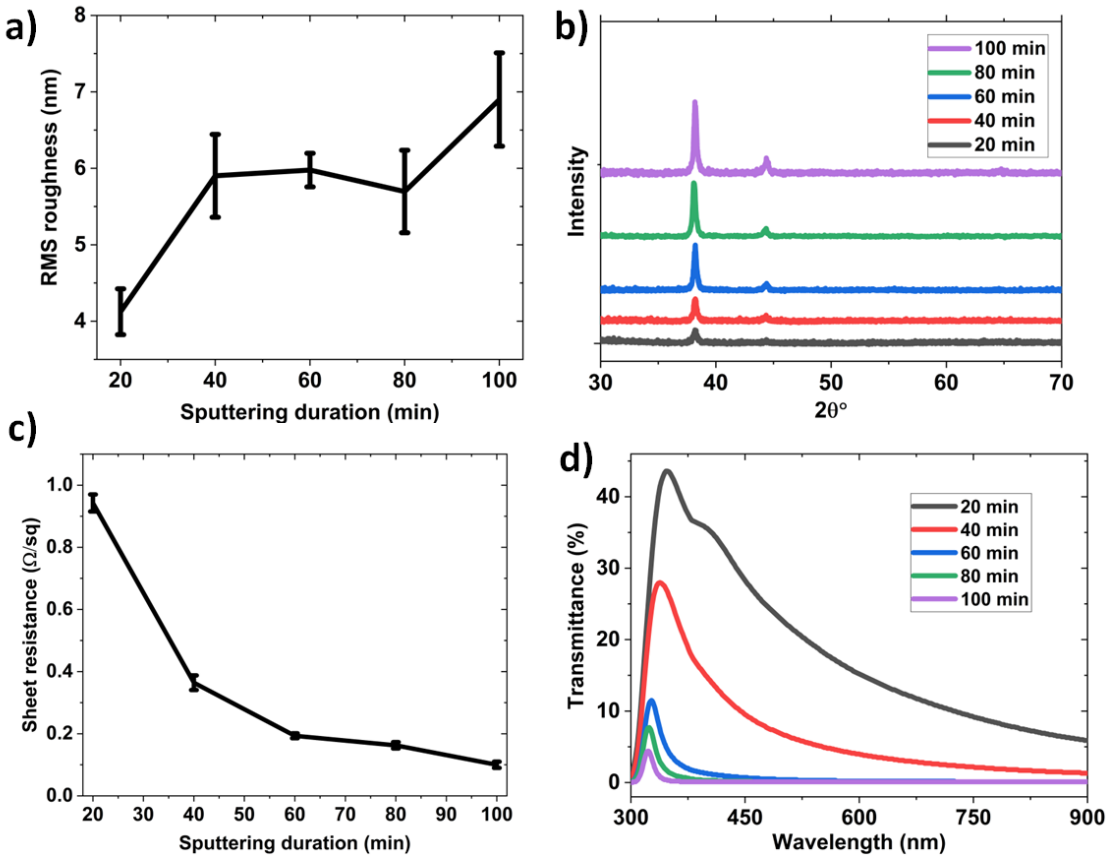

Figure 6.9: (a) Root-Mean Square roughness, (b) XRD pattern, (c) sheet resistance and (d) transmittance of Ag films as a function of sputtering duration. The films were deposited on glass substrates at 1 W and 5.0 mTorr for 15 sccm.

Thickness estimated from Figure 6.2(f) demonstrates that film thickness increased from 27 nm to 160 nm when the deposition time increased from 20 to 100 minutes. These results are consistent with the rise in XRD intensity, which indicates an increase in film thickness.

6.5.2. Photovoltaic performance of the devices

The devices were studied using the IS technique to understand their charge extraction characteristics. Figure 6.10(a) presents the junction capacitance of devices as a function of sputtering duration. The results indicate that the junction capacitance, related to the carrier density and charge extraction efficiency, peaked at 40 minutes before reducing steadily as the sputtering duration increased beyond 40 minutes. This observation suggests that the devices with Ag contacts deposited for 40 minutes will likely achieve

the best performance. Figure 6.10(b) shows the J-V curves of PSCs as a function of sputtering durations, while Table 6.7 summarises the photovoltaic parameters of the devices.

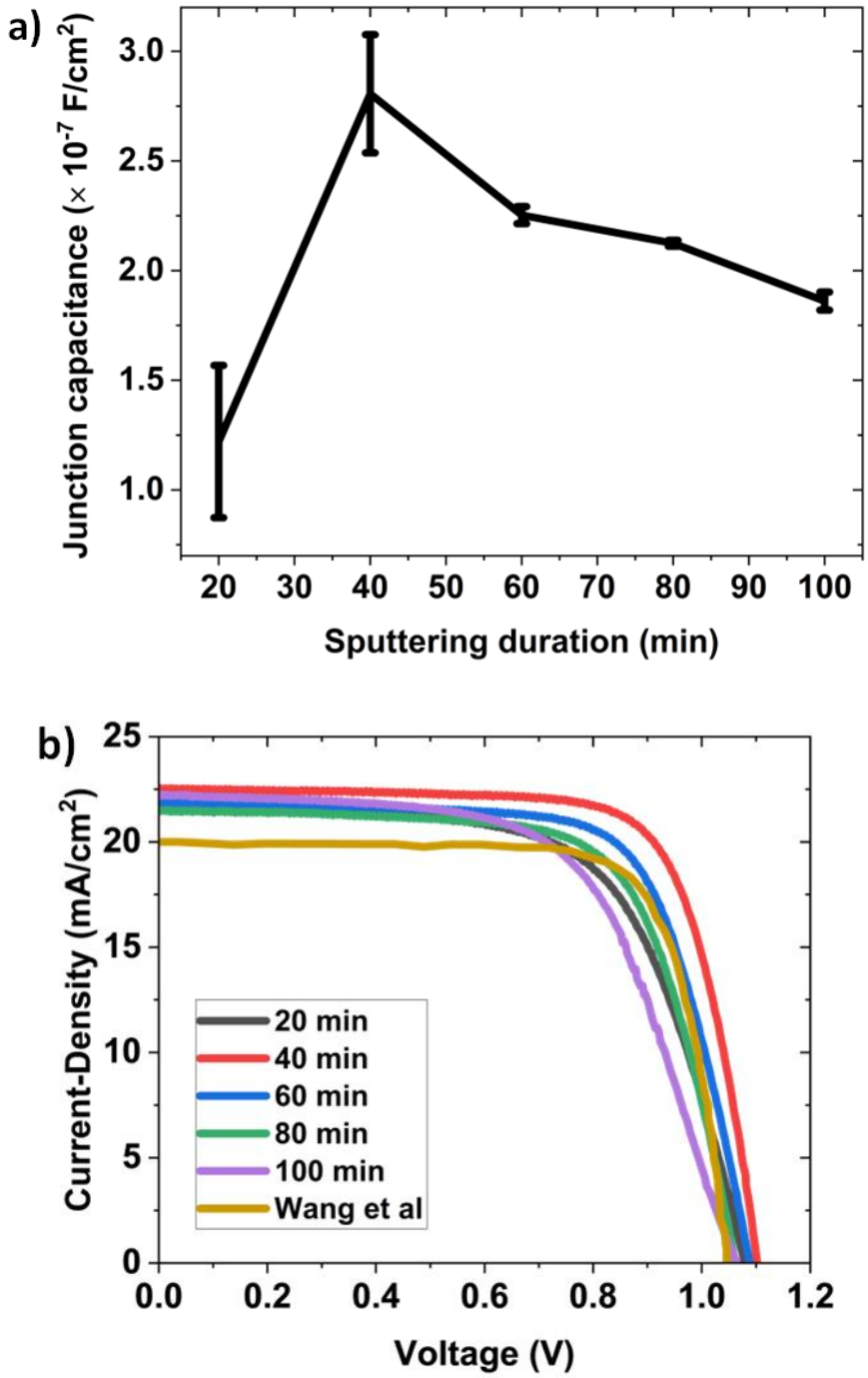

Figure 6.10: (a) Junction capacitances of devices and (b) J-V curves of the best devices as a function of Ag sputtering duration and the J-V curve from the literature [62]. The Ag contacts of the devices were deposited at 1.0 W, 5.0 mTorr and 15 sccm.

Table 6.7: Photovoltaic parameters of devices with Ag contacts deposited using different sputtering durations (the rows denoted "Best" represent the data obtained from the best solar cells of the batch; the rows denoted "Av" represent the average of all cells). The Ag contacts of the devices were deposited at 1 W, 5.0 mTorr and 15 sccm. The data obtained by Wang et al [62] is also included as a reference for comparison.

Sputtering duration (min)		V_{oc} (V)	J_{sc} (mA/cm^2)	FF (%)	R_{dc_f} (Ω)	R_{dc_r} (kΩ)	PCE (%)
20	Best	1.08	21.73	64.04	68	7.1	15.02
	Av	1.08±0.01	19.65±1.06	65.27±2.20			13.84±0.56
40	Best	1.10	22.56	73.70	45	60.0	18.35
	Av	1.09±0.02	22.18±0.93	70.25±2.29			16.99±0.98
60	Best	1.09	21.90	70.55	55	40.0	16.82
	Av	1.08±0.01	21.44±0.61	69.08±0.85			16.01±0.52
80	Best	1.06	21.53	68.69	55	15.1	15.73
	Av	1.04±0.02	21.28±1.03	65.93±1.76			14.53±0.49
100	Best	1.07	22.25	60.94	90	5.3	14.46
	Av	1.06±0.01	21.76±0.64	57.49±4.89			13.26±1.53
Ref-2[62]		1.057	19.88	76.00			15.97

The photovoltaic parameters show that as the deposition duration increased from 20 to 60 minutes, the V_{oc}, J_{sc}, and FF of the devices reached maximum values at a sputtering time of 40 minutes, resulting in a remarkable PCE of 18.35% for PSCs prepared in the air at high relative humidity. This result may be due to improved carrier extraction, as Figure 6.10(a) demonstrates. As shown in Table 6.7, this efficiency corresponds to a favourable combination of lowest R_{dc_f}, highest R_{dc_r} and high junction capacitance. The key reason for the significant improvement in the PCE is the substantial reduction in the power losses associated with the R_{dc_f} and R_{dc_r}. Depositing the Ag contacts for 40 minutes makes it possible to achieve Ag contacts with sufficiently low sheet resistance (Figure 6.9(c)) without considerable damage to the HTL and the interfacial quality between the HTL and Ag film, which are prone to damage by particle impact or stress. With a further increase in sputtering duration from 60 to 100 minutes, the FF and PCE of the devices further

degraded. This observation is because the HTL becomes further damaged due to the prolonged impact of the Ag particles on the organic transport layer.

Although the V_{oc} and J_{sc} increased slightly when the duration increased to 100 minutes (which cannot be explained by the available data), the PCE of the best devices decreased from 18.35% to 14.46% due to a significant decrease in FF. The results also show that deposition at any other sputtering time would increase the series resistance and decrease shunt resistance, as revealed in Table 6.7. This study suggests that 40 minutes is the best sputtering duration for depositing Ag contacts at the conditions under investigation. The PCE achieved in this study represents an improvement in efficiency over devices with Ag contact deposited using magnetron sputtering reported by Wang et al. [62].

6.6. Suitable argon pressure for preparing perovskite solar cells

This study aims to establish the suitable argon pressure for sputtering Ag contacts on perovskite solar cells. The argon pressure for sputtering Ag contacts was varied from 4 mTorr to 12 mTorr while keeping the sputtering power, duration and argon flow rate at 1.0 W, 40 minutes and 15.0 sccm, respectively. Subsection 6.6.1 presents the properties of Ag films, and subsection 6.6.2 shows the results from the J-V measurements of the PSCs.

6.6.1. Properties of the prepared silver films

Ag films sputtered on glass substrates were studied, and Figures 6.11(a) – 6.11(d) show the AFM images of Ag films as a function of argon pressure. The AFM images indicate that the grain sizes of the films decreased steadily as the argon pressure increased, agreeing with the report in [380]. In addition, the deposition rate decreased when argon pressure increased because more Ag particles suffered scattering and obstruction from the increased number of Ar ions in the chamber. Hence, a fewer number of Ag particles get to the substrate, resulting in a reduction in the rate of film deposition.

Figure 6.12(a) shows the RMS roughness extracted from the AFM images. The results demonstrated that the RMS roughness of the films increased significantly as the argon pressure increased from 4 mTorr to 10 mTor. This observation is likely because the grains are poorly interconnected at low argon pressure, resulting in uncovered areas. However,

the available data could not explain the slight fall in the film roughness when the pressure increased to 12 mTorr.

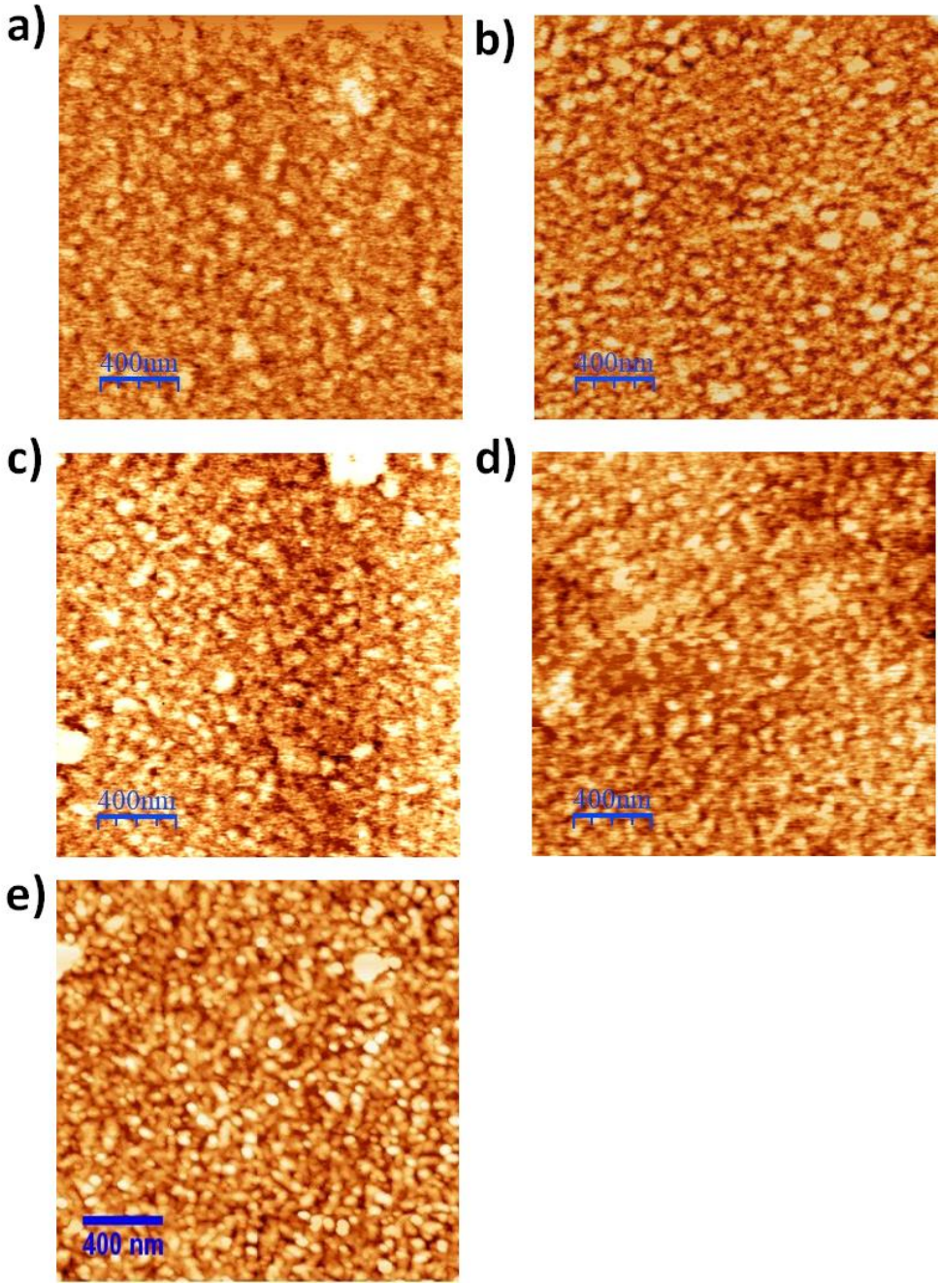

Figure 6.11: AFM images of Ag films sputtered at (a) 4 mTorr (b) 5 mTorr (c) 7 mTorr (d) 10 mTorr and (e) 12 mTorr. The films were deposited on glass substrates at 15 sccm and 1.0 W for 40 minutes.

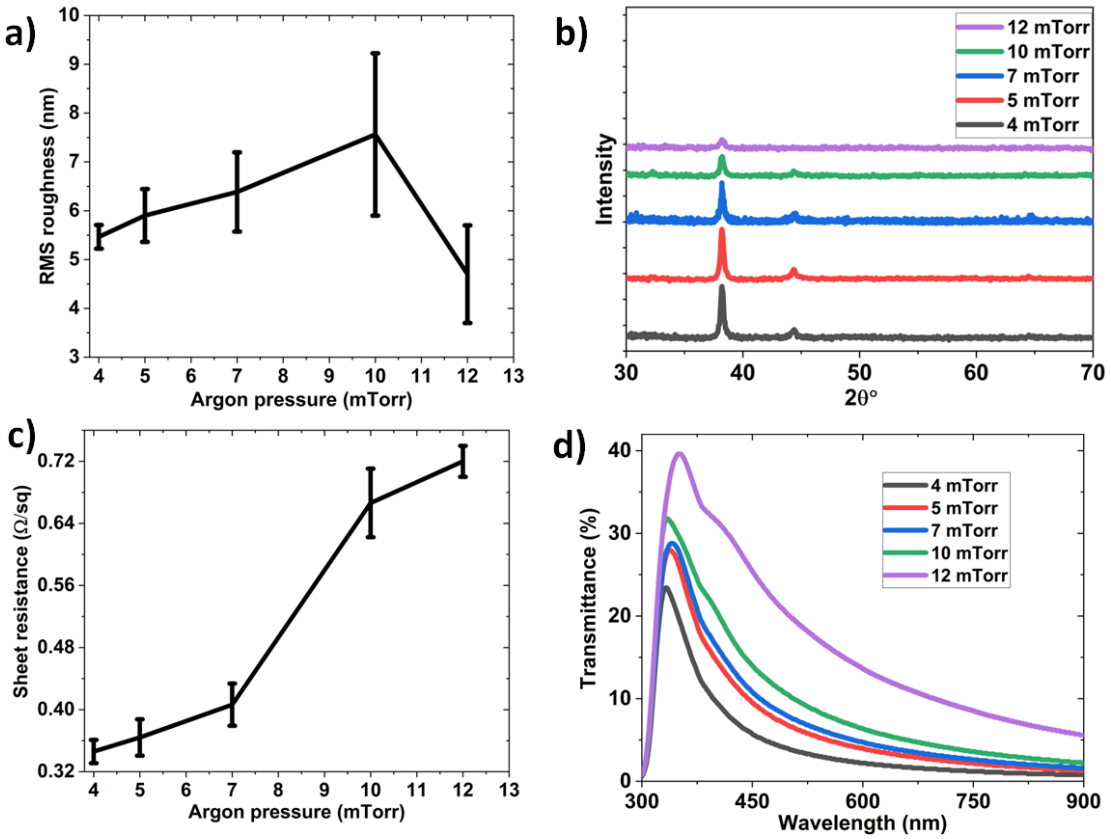

Figure 6.12: (a) Root-Mean Square roughness, (b) XRD pattern, (c) sheet resistance and (d) transmittance of Ag films as a function of argon pressure. The films were deposited on glass substrates at 1 W, 15sccm and 40 minutes.

Figure 6.12(b) illustrates the XRD spectra of Ag films deposited on the glass. The XRD spectra demonstrate that all the films have crystalline structures and that the intensity of the films decreased with the increase in argon pressure. The decrease in the intensity as argon pressure increased suggests that the film thickness dropped as the argon pressure increased. This result is expected because the number of Ag particles obstructed from getting to the substrate by the Ar ions will increase when the argon pressure increases. The results also indicate that films have the same preferred crystal growth direction independent of the argon pressure. Table 6.8 presents FWHM and the grain sizes obtained from the XRD spectra. The results show that the FWHM increased while the grain size of the films decreased as the argon flow rate increased.

Table 6.8: XRD parameters of Ag films as a function of argon pressure. The films were deposited on glass substrates at 15 sccm and 1 W for 40 minutes.

Argon pressure (mTor)	Normalised intensity	2θ (°)	FWHM (°)	Grain size (nm)
4.0	1.0000	38.2309	0.2792	33.4610
5.0	0.9714	38.2148	0.3118	29.9631
7.0	0.7571	38.2323	0.3255	28.7035
10.0	0.3905	38.2190	0.3491	26.7484
12.0	0.1810	38.2263	0.4167	22.4118

Figure 6.12(c) presents the sheet resistance of the Ag films measured using 4-Probe. The results show that the average sheet resistance of the Ag films increased from 0.346 Ω/sq. to 0.720 Ω/sq. as the argon pressure was increased from 4 to 12 mTorr. These results agree with the report that sheet resistance of sputtered metal films increased as the argon pressure was increased [380]. The high sheet resistance achieved at high argon pressure is likely because of a reduction in film thickness arising from the obstruction of the Ag particles by Ar ions [58]. Figure 6.12(d) shows that over 300 nm – 900 nm wavelength, Ag films deposited have good transparency that improved when the argon pressure increased. Hence, the average transparency of the films increased from 4.58% to 9.49% when the argon pressure increased from 4 to 10 mTorr (see Figure 6.2(e)). The results also show that the transmittance maxima shifted with the film thickness. The transmittance spectra also indicate that the maxima's intensity increases as the argon pressure increases. The thicknesses estimated from Figure 6.2(f) show that film thickness decreased from 61 nm to 32 nm when argon pressure was increased from 4 to 12 mTorr. These results are consistent with the report that the film thickness decreases as the argon pressure is increased [381].

6.6.2. Photovoltaic performance of the devices

Figure 6.13(a) presents the junction capacitance of the devices extracted from the IS measurements. The results indicate that the junction capacitance of the devices peaked at 5.0 mTorr. These results demonstrate that devices with contacts deposited at 5.0 mTorr may have the best photovoltaic performance.

I-V measurements were also conducted on the devices at 1000 W/m^2. Figure 6.13(b) presents the J-V curves of PSCs as the argon pressure was increased from 4 to 12 mTorr. Table 6.9 summarises the device parameters obtained from the characterisation. The results show that the V_{oc} and FF of the devices increased when the argon pressure was changed from 4.0 to 5.0 mTorr while the J_{sc} slightly improved. The lower V_{oc}, FF achieved at 4.0 mTorr may be attributed to possible HTL damage due to deposition at low argon pressure, which results in a high deposition rate. The HTL damage results in poor charge carrier extraction, as indicated by reduced junction capacitance in Figure 6.13(a) [63]. This observation is because, at 4.0 mTorr, Ag particles suffer less scattering by Ar ions. Therefore, more Ag particles reach the HTL surface with high impact. On the other hand, the J_{sc} increased slightly, probably due to the improved conductivity of Ag films arising from improved film coverage (see sheet resistance in Figure 6.12(c)). When the argon pressure is 5.0 mTorr, the kinetic energy of Ag particles is reduced due to increased scattering by Ar ions, resulting in less damage to the HTL and, consequently, improvement in V_{oc}, and FF, resulting in improved PCE.

As the argon pressure increased from 5 mTorr to 12 mTorr, the FF, V_{oc}, and J_{sc} of the devices decreased steadily. The steady reduction in FF, V_{oc} and J_{sc} as argon pressure increased above 5.0 mTorr arises from a significant decrease in sheet resistance of Ag films (see Figure 6.12(c)), resulting in poor charge carrier extraction as suggested by the reduced junction capacitance. These results obtained in this study show that the argon pressure significantly influences the performance of the PSCs, and 5.0 mTorr is the optimum pressure for depositing Ag contacts.

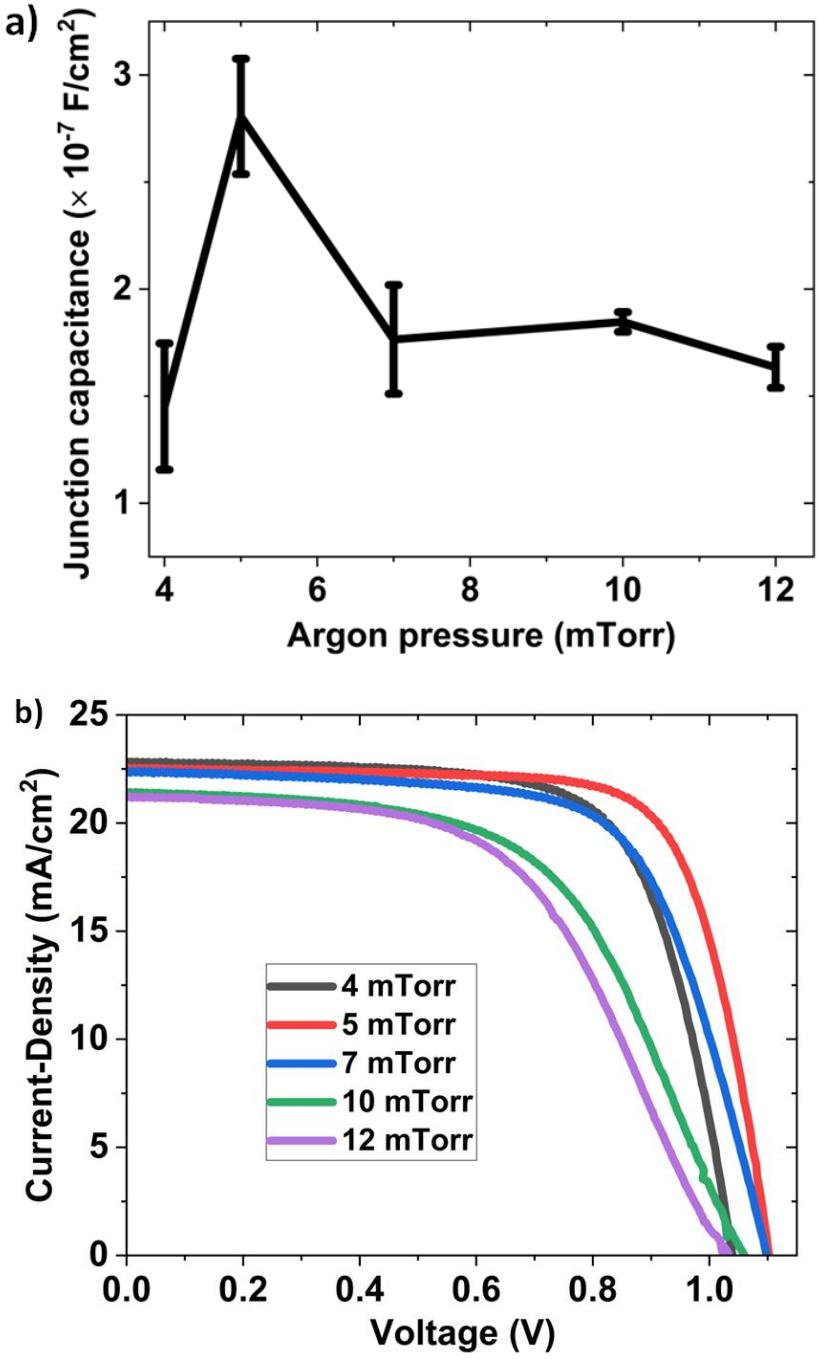

Figure 6.13: (a) Junction capacitance and (b) J-V curves of the devices with Ag contacts deposited at different argon pressures. The Ag contacts were deposited at 1.0 W and 15 sccm for 40 minutes.

Table 6.9: Photovoltaic parameters of devices with Ag contacts deposited using different argon pressures (the rows denoted "Best" represent the data obtained from the best solar cells of the batch; the rows denoted "Av" represent the average of all cells). The Ag contacts of the devices were deposited at 1 W, 15sccm and 40 minutes.

Ar pressure (mTorr)		V_{oc} (V)	J_{sc} (mA/cm^2)	FF (%)	R_{dc_f} (Ω)	R_{dc_r} (kΩ)	PCE (%)
4.0	Best	1.04	22.86	69.70	46	14.4	16.57
	Av	1.04±0.01	21.56±0.97	68.93±1.19			15.52±0.86
5.0	Best	1.10	22.56	73.70	45	60.0	18.35
	Av	1.09±0.02	22.18±0.93	70.25±2.29			16.99±0.98
7.0	Best	1.10	22.42	66.57	64	29.3	16.43
	Av	1.08±0.01	20.24±1.68	64.59±1.76			14.19±1.35
10.0	Best	1.06	21.43	56.3	122	8.4	12.80
	Av	1.04±0.02	21.06±0.25	57.23±0.98			12.51±0.21
12.0	Best	1.03	21.23	54.50	149	10.0	11.96
	Av	1.04±0.01	21.03±0.20	51.43±2.44			11.28±0.48

6.7. Summary

This study investigated the effects of sputtering parameters on the performances of perovskite solar cells with silver contacts deposited using magnetron sputtering. The parameters investigated were sputtering power, argon flow rate, sputtering duration, and argon pressure. The results indicated that the device with silver contacts deposited at a sputtering power of 1.0 W, argon flow rate of 15sccm, sputtering duration of 40 minutes and argon pressure of 5mTorr achieved the best performance. The results also show that sputtering power significantly impacts the device performance and the properties of Ag films.

Chapter 7: Novel CPFS Additive for Improving the Stability of perovskite solar cells

7.1. Introduction

This chapter describes a novel chlorodimethyl(pentafluorophenyl)silane (CPFS) additive process for improving the stability of perovskite solar cells (PSCs) prepared in the air at high relative humidity. Improving perovskite solar cells' stability is crucial as this will enhance the commercialisation prospect. CPFS is chosen for this study because it is miscible with dimethyl methanamide (DMM) and contains fluoride and silyl groups. These functional groups readily form crosslinking bonds with perovskite, thereby strengthening the chemical structure and minimising the decomposition in the presence of moisture. To my knowledge, this is the first application of CPFS additive in PSC fabrication.

This chapter includes a description of the physical properties of methylammonium lead iodide ($MAPbI_3$) films and the photovoltaic performance and stability of the devices. Finally, the chapter will summarise the observation and the conclusion.

7.2. Properties of CPFS and crosslinking bond formation

Chlorodimethyl(pentafluorophenyl) silane (CPFS) contains fluoride and silyl groups, which form crosslinking bonds with perovskites [44,57]. It hydrolyses in water to produce hydroxydimethyl(pentafluorophenyl) silane and hydrogen chloride, as shown in Figure 7.1(a). Figure 7.1(b) shows the formation of crosslinking bonds between the perovskite and hydroxydimethyl(pentafluorophenyl) silane. These crosslinking bonds strengthen the perovskite structure, thereby minimising its decomposition rate. CPFS additive also provides surface passivation against moisture intrusion into perovskite layers [51–53].

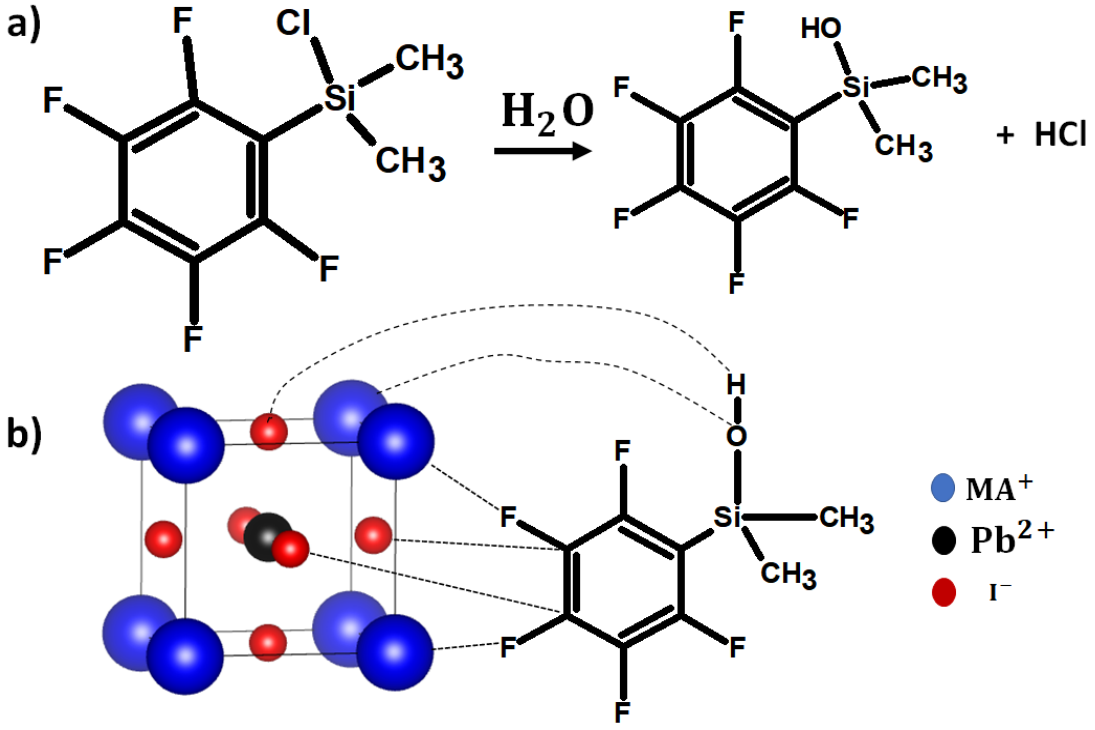

Figure 7.1: (a) Hydrolysis of chlorodimethyl(pentafluorophenyl)silane in water and (b) formation of crosslinking bonds between perovskite and hydrolysed chlorodimethyl(pentafluorophenyl)silane

7.2. Film and device fabrication

The devices fabricated in this study have FTO/SnO_2/$MAPbI_3$/Spiro-OMETAD/Ag structures. SnO_2 films were deposited on FTO substrates from 15 mg/ml of $SnCl_2.2H_2O$ solutions. $MAPbI_3$ films were deposited on SnO_2 films from 1.50 M solutions of $MAPbI_3$ solution containing 0 µl, 3 µl, 6 µl, 9 µl and 15 µl of CPFS additive, respectively. In addition, the perovskite films were treated with150 µl of methyl ethanoate antisolvent. HTLs were deposited on $MAPbI_3$ layers from an HTL solution containing 90 mg Spiro-OMeTAD, 36 µl of MPPD, and 38 µl of FK209 solution (300 gm/ml in ethane nitrile) and 22 µl of Li-TFSI solution (520 mg/ml in ethane nitrile) in 1 ml of chlorobenzene. All the solution-processed films were deposited in ambient air of 50-55% relative humidity. Finally, Ag contacts with active areas of 0.15 cm^2 were deposited on HTLs at sputtering power, argon flow, argon pressure and sputtering duration of 1.0 W, 15 sccm and 5.0 mTorr, respectively, for 40 minutes. Chapter 3 (Section 3.2) presents the details of the device fabrication process.

7.3. Properties of the prepared $MAPbI_3$ films

$MAPbI_3$ films were deposited on FTO substrates from $MAPbI_3$ solutions modified with 0 µl, 3 µl, 6 µl, 9 µl and 15 µl of CPFS additives. The films were examined using AFM, UV-Vis spectrometer, FTIR and XRD techniques.

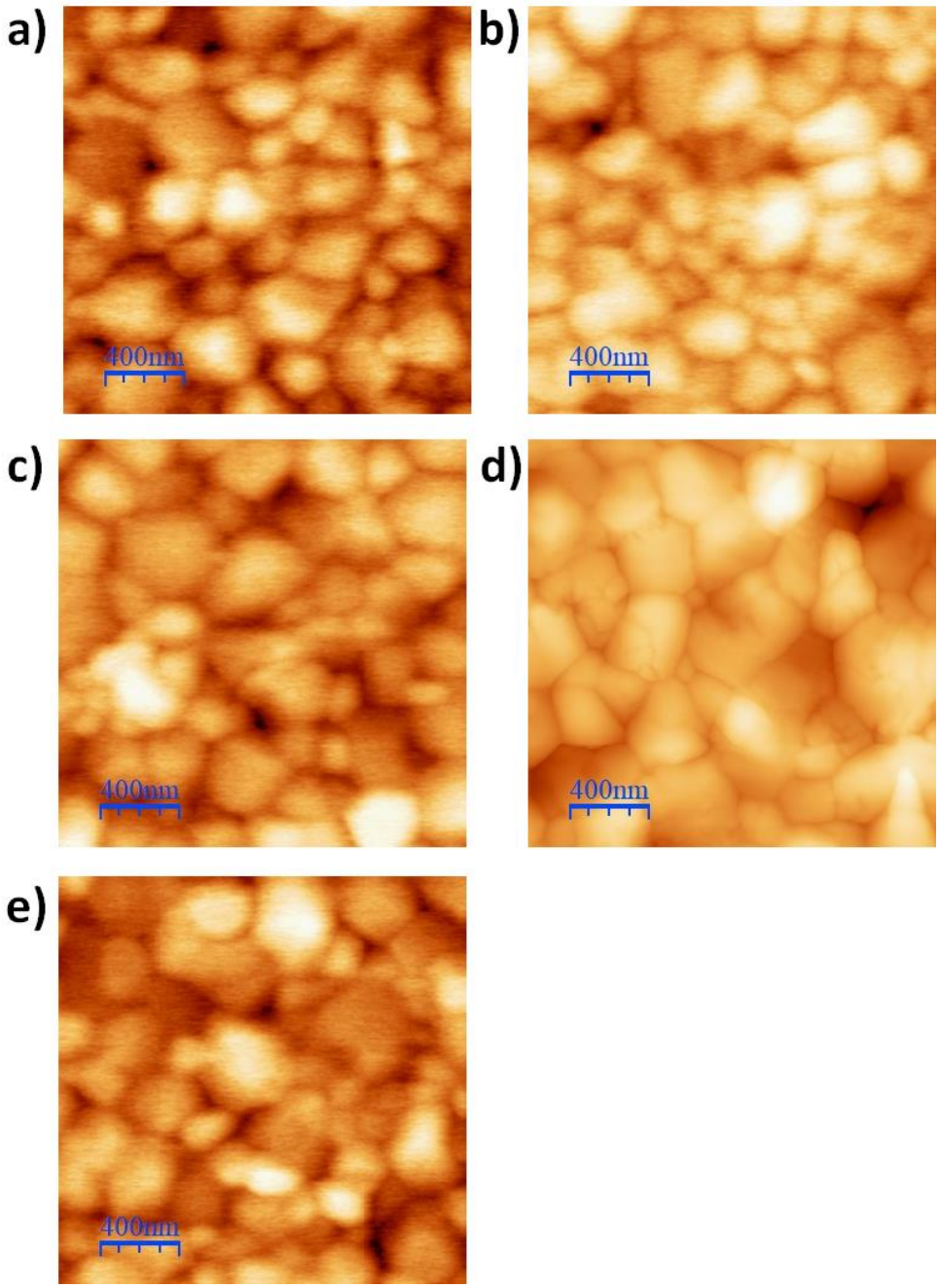

Figure 7.2: AFM images of $MAPbI_3$ films modified with (a) 0 µl, (b) 3 µl, (c) 6 µl (d) 9 µl and (e) 15 µl of CPFS additive.

Figures 7.2(a) - 7.2(e) present the AFM images of $MAPbI_3$ films as a function of CPFS proportion. The films modified with CPFS additive appeared to have slightly larger grain sizes than the control films. This enlarged grain is probably because of the delay in the nucleation process, which results in films with increased grain sizes, as reported in [382]. The results also show that all the films have suitable morphologies. The enhanced surface coverage of films modified with CPFS additive is likely because of the delay in the nucleation process. Reports have shown that a slight delay in the nucleation process can result in films with improved surface morphology [43]. The enhanced image quality of films modified with 9 µl of CPFS additive could be due to using a more advanced AFM machine in the image capturing.

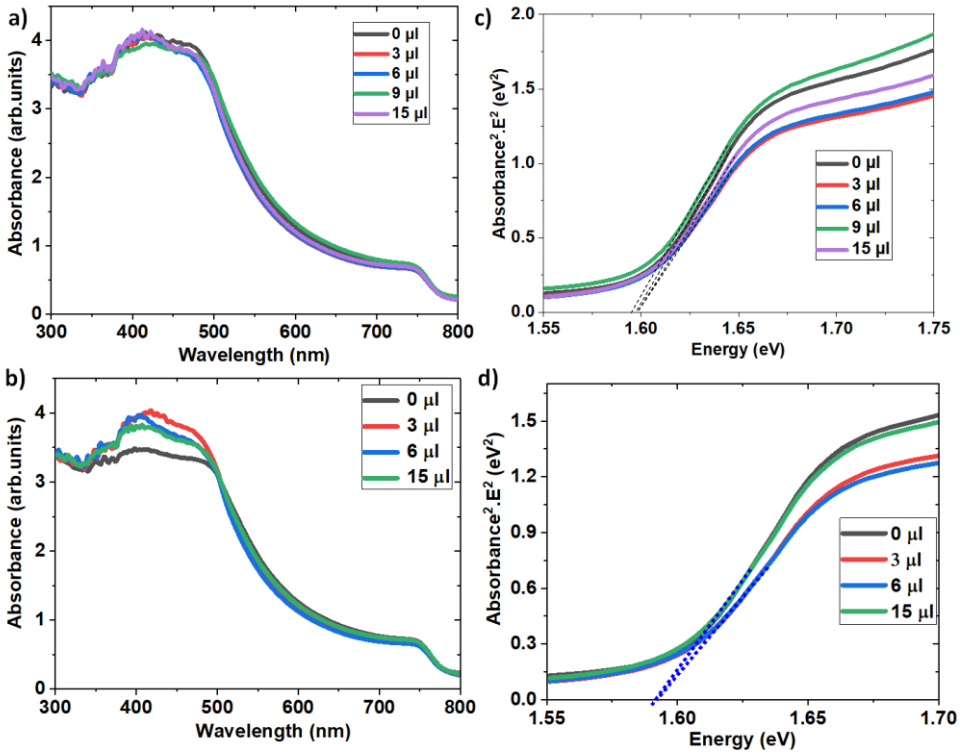

Figure 7.3: (a) Absorbance spectra at 0 hours, (b) Tauc plots at 0 hours, (c) absorbance spectra at 840 hours and (d) Tauc plots at 840 hours of $MAPbI_3$ films as a function of the amount of CPFS additive.

Figures 7.3(a) - 7.3(d) present the absorbance spectra and the Tauc plots of $MAPbI_3$ films deposited on FTO substrates at 0 hours and after 840 hours of storage. Figure 7.3(a) shows that the initial absorbance spectra of the $MAPbI_3$ films were not significantly affected by the proportion of CPFS additive in the $MAPbI_3$ material. Over 300 – 780 nm wavelength,

the control samples (i.e., $MAPbI_3$ films without CPFS additive) have an average absorbance of 2.29 arb. units, while the $MAPbI_3$ films with 3 µl, 6 µl, 9 µl and 15 µl of CPFS additives show similar absorbance values, which are 2.21, 2.21, 2.30 and 2.25 arb. units, respectively.

Figure 7.3(b) shows that the E_g value of all the films appeared to be about 1.6 eV and independent of the CPFS proportion. This result suggests that the energy band structure of the $MAPbI_3$ is not affected by the amount of CPFS additive incorporated in the $MAPbI_3$ materials. Figure 7.3(c) shows that the average absorbance of the control $MAPbI_3$ films decreased by about 7.61% after 840 hours of storage compared to an average decrease of 1.13%, 3.04% and 3.23% for the films with 3 µl, 6 µl and 15 µl of CPFS additive, respectively. The results also show that the degradation is wavelength-dependent, significantly reducing absorbance over the 350 - 500 nm range. However, this degradation does not considerably affect the E_g of the material, as shown in Figure 7.3(d), where the E_g values of the films only decreased slightly. These results suggest that modifying $MAPbI_3$ material with a suitable amount of CPFS enhances the optical stability of $MAPbI_3$ films. A study has reported using UV-Vis measurement to identify degradation in $MAPbI_3$ films [383].

Figures 7.4(a) and 7.4(b) present the FTIR spectra measured at 0 hours and after 456 hours of storage from $MAPbI_3$ films deposited on Ag substrates. Figure 7.4(a) shows that the FTIR peak positions of $MAPbI_3$ films occurred at 910, 1469 and 3180 cm^{-1} ((N-H stretching) and appeared to be independent of the CPFS proportion. These peaks are consistent with 910.43, 1469.81 and 3180.72 cm^{-1} reported in [384]. These results demonstrate that incorporating a minute amount of CPFS additive in $MAPbI_3$ films does not change the bond types in $MAPbI_3$ films.

Figure 7.4(b) reveals that the peak at 3180 cm^{-1} was reduced by about 65% after 456 hours of storage for the control films, in contrast with peak reduction of 38%, 50% and 79% observed for films altered with 3 µl, 6 µl and 15 µl of CPFS additive, respectively. The results also indicate that as the peaks of $MAPbI_3$ degrade, a new peak that matches the silver iodide (AgI) peak reported elsewhere [385] occurred at 3457 cm^{-1}. Reports have shown that $MAPbI_3$ reacts with the silver substrate to form AgI [229,386]. The degradation of $MAPbI_3$ films deposited on the Ag substrate appeared faster than those deposited on FTO substrates (see UV-Visible and FTIR studies). This observation agrees

with the report by Kato et al. that Ag hastens the degradation of $MAPbI_3$ films as they react to form AgI [229]. Research has demonstrated using FTIR to study the degradation of $MAPbI_3$ films [383].

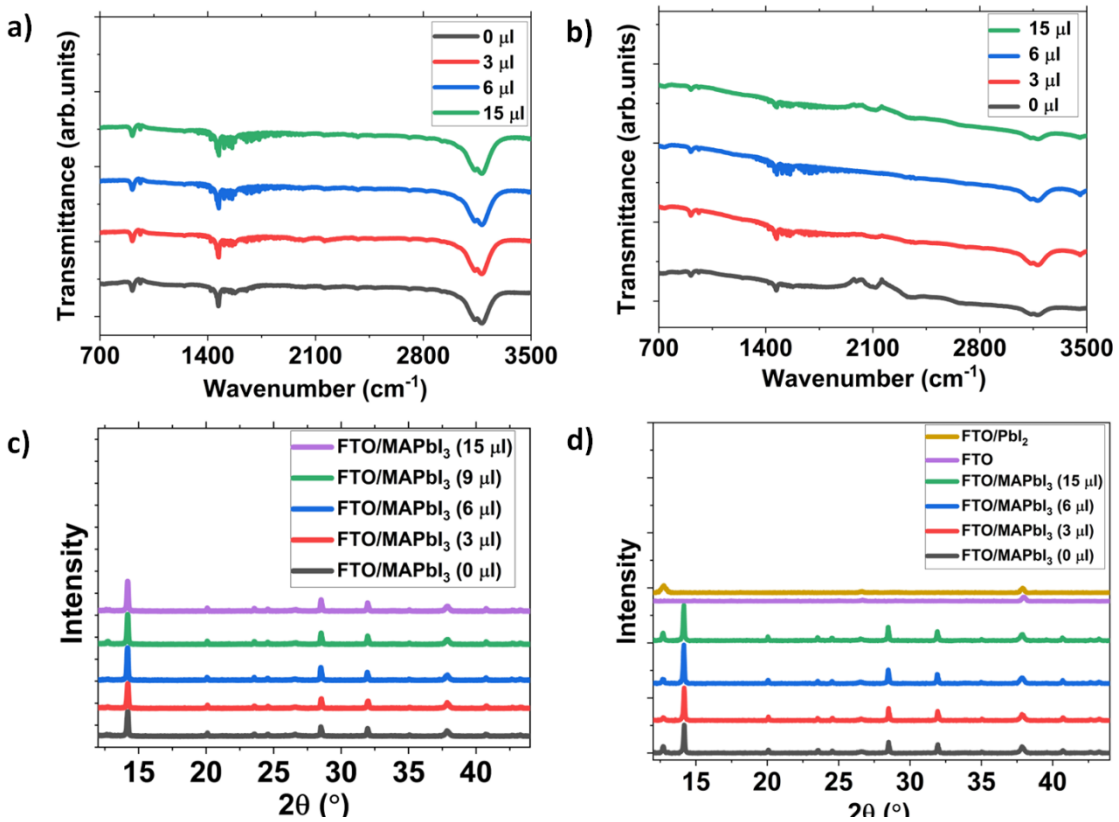

Figure 7.4: (a) FTIR spectra of $MAPbI_3$ at 0 hours (b) FTIR spectra of $MAPbI_3$ at 456 hours (c) XRD pattern of $MAPbI_3$ at 0 hours and (d) XRD pattern of $MAPbI_3$ at 384 hours.

Figures 7.4(c) and 7.4(d) show the XRD pattern of $MAPbI_3$ films deposited on FTO substrates at 0 hours and after 384 hours of storage. Figure 7.4(c) indicates that $MAPbI_3$ peaks occur at 2θ =14.02° (preferred orientation), 28.4° and 31.8° for all the films, independent of the amount of CPFS additive incorporated [137,358]. The results also indicate that the intensity grew as the proportion of CPFS additive increased. This observation suggests that increasing the amount of CPFS additive results in an increase in film thickness. Using FTO peak intensities (37.9°) as references, Figure 7.4(d) reveals that after 384 hours of storage, the peak intensity of $MAPbI_3$ (14.02°) degraded by about 8.18% for control $MAPbI_3$ films while the peaks of films altered with 3 µl, 6 µl and 15µl of CPFS additive reduction by 0%, 5.15% and 5.61%, relative to the first-day

measurement. These results suggest that some of the $MAPbI_3$ molecules decomposed to form PbI_2, as revealed by the appearance of PbI_2 peaks at 12.82° [387,388]. The XRD spectra also demonstrate that the $MAPbI_3$ films modified with 3µl of CPFS were the most chemically stable, as indicated by the insignificant appearance of the PbI_2 peak after 384 hours. These results demonstrate that altering $MPAbI_3$ with a suitable amount of CPFS additive enhances the stability of $MAPbI_3$ films. The $MAPbI_3$ films treated with 9 µl CPFS additive were fabricated and characterised during the revision period, but their stability has not been studied.

7.4. Photovoltaic performance of the devices

The photovoltaic parameters of devices were studied at 1000 W/m^2. Figure 7.5 presents the J-V curve of the best devices as a function of the amount of CPFS additive, while Table 7.1 summarises the electrical parameters of the devices. The results show that the FF and PCE of the devices decreased steadily as the amount of CPFS additive increased from 0 to 15 µl. The available data cannot explain the causes for a decrease in FF with increasing CPFS additive.

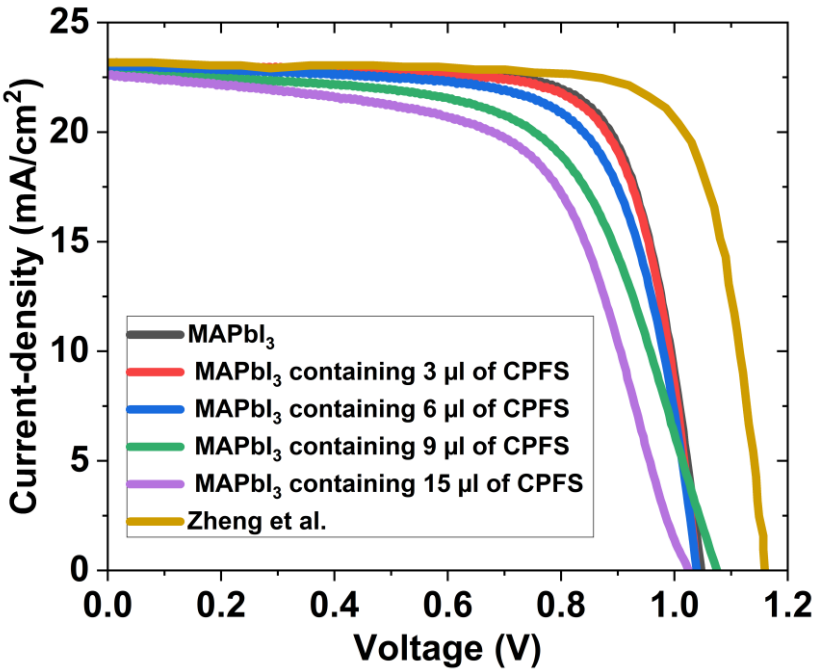

Figure 7.5: J-V curves of best devices as a function of CPFS proportion in this project and 3-aminopropyltrimethoxysilane in literature [44].

Table 7.1: Photovoltaic parameters of devices as a function of CPFS additive (the rows denoted "Best" represent the data obtained from the best solar cells of the batch; the rows denoted "Av" represent the average of all cells). The data obtained by Zheng et al [44] is also included as a reference for comparison.

Perovskite material		**V_{oc}(V)**	**J_{sc} (mA/cm^2)**	**FF (%)**	**R_{dc_f} (Ω)**	**R_{dc_r} (kΩ)**	**PCE (%)**
$MAPbI_3$ +	Best	1.05	23.19	74.11	73	13.4	18.07
0µl CPFS	Av	1.03±0.01	21.87±1.05	73.62±0.68			16.57±1.05
$MAPbI_3$ +	Best	1.04	23.06	74.29	71	60.9	17.82
3µl CPFS	Av	1.03±0.01	21.47±0.85	71.82±2.00			15.89±1.01
$MAPbI_3$ +	Best	1.04	22.85	70.6	81	30.4	16.85
6µl CPFS	Av	1.03±0.01	21.90±0.74	70.18±2.85			15.80±0.75
$MAPbI_3$ +	Best	1.08	22.65	62.29	80	6.7	15.18
9µl CPFS	Av	1.08±0.002	22.76±.30	60.43±1.60			14.82±0.44
$MAPbI_3$ +	Best	1.03	22.65	60.98	90	3.0	14.14
15µl CPFS	Av	1.02±0.01	22.15±0.50	59.56±1.42			13.45±0.71
Ref-3 [44]	Best	1.12	22.36	76.80			19.31

The control devices achieved the best PCE of 18.07%, compared to 17.82%, 16.85%, 15.18% and 14.14% obtained for devices fabricated from $MAPbI_3$ films modified with 3 µl, 6 µl, 9 µl and 15 µl of CPFS additive, respectively. These efficiencies represent about 0.25%, 1.22% and 3.93% loss in PCE relative to the control devices as the CPFS additive increased from 3 µl to 15 µl. The available data could not explain the reduced photovoltaic parameters observed in the devices modified with CPFS immediately after fabrication. Hence, further studies are required to provide a convincing explanation. This study demonstrates that altering $MAPbI_3$ films with CPFS additive does not improve the PCE of devices immediately after fabrication. Zheng et al. [44] reported a higher PCE using a silane additive approach. However, as different perovskite materials, antisolvents, silane additives and laboratory conditions were used, it is difficult to directly compare these results.

7.5. Device stability

This study measured the J-V properties of the devices after 0, 336, 504, 672, 840, 1008, 1176 and 1344 hours of storage in a desiccator using an irradiance of 1000 W/m^2. The V_{oc}, J_{sc}, FF and PCE of the devices were determined from the J-V data. Figures 7.6(a) - 7.6(d) present the devices' normalised V_{oc}, J_{sc}, FF and PCE as a function of storage duration. Figure 7.6(a) shows that the V_{oc} of the devices remains practically unchanged after 1344 hours for both control devices and devices modified with CPFS additive. These results agree with the V_{oc} degradation reported in [34,38,333].

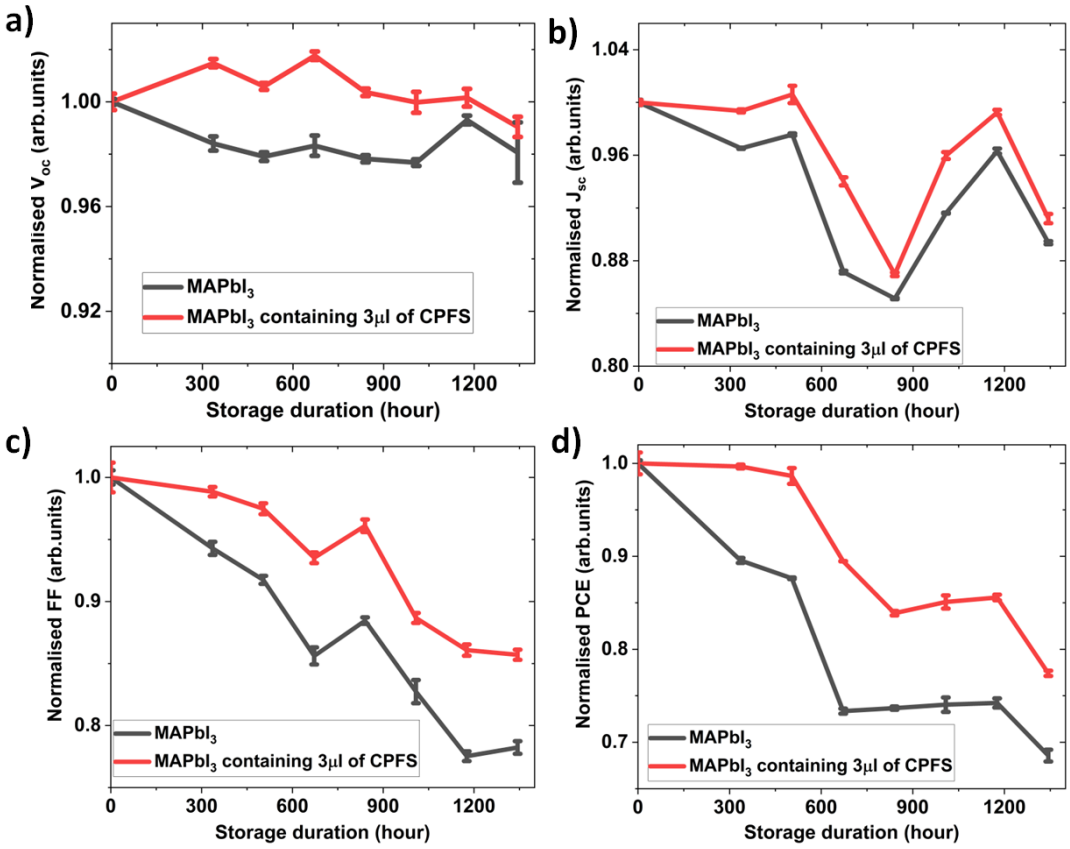

Figure 7.6: (a) Normalised V_{oc}, (b) normalised J_{sc}, (c) normalised FF and (d) normalised PCE as a function of CPFS proportion. The devices were stored in a desiccator for 1344 hours.

Figure 7.6(b) shows that the J_{sc} has a general decreasing trend with time for both devices. Nevertheless, the J_{sc} degradation in the devices modified with CPFS additive is less significant than the degradation of the control devices. The average J_{sc} of the control devices degraded by about 11% after about 1344 hours of storage, compared to about 9%

degradation for the devices modified with 3 µl of CPFS additive, representing an improvement of 2% for the devices modified with CPFS additive. The J_{sc} of the control devices degraded severely because more $MAPbI_3$ molecules decomposed in the presence of moisture, reducing photon absorption (see Figure 7.3 (b)).

The J_{sc} of the devices modified with 3 µl of CPFS additive suffered less degradation. This can be attributed to the crosslinking bonds between $MAPbI_3$ and CPFS that minimise the decomposition of $MAPbI_3$ molecules in the presence of moisture. The negligible degradation in the absorbance of $MAPbI_3$ films modified with 3 µl of CPFS (see Figure 7.3 (b)) provides evidence of the reduced decomposition. This result demonstrates that the crosslinking bond between $MAPbI_3$ and CPFS additive enhances the J_{sc} stability.

Figure 7.6(c) shows that devices modified with 3 µl of CPFS additive have improved FF stability relative to control devices. The average FF of the PSCs with 3 µl of CPFS additive decreased by about 15% after 1344 hours, compared to about 22% degradation for the control devices. This result represents about a 7% enhancement in FF stability against the control device. The average FF of the control devices degraded significantly because many $MAPbI_3$ molecules in the control devices decomposed to produce excess localised PbI_2 particles, which acted as additional recombination sites and decreased the charge extraction of the PSCs [389,390]. The increase in PbI_2 particles is evident from the increase in the intensity of PbI_2 in the XRD pattern. The FF of the devices based on $MAPbI_3$ films modified with 3 µl of CPFS additive suffered less degradation because the films generated fewer PbI_2 particles. The negligible increase in the intensity of PbI_2 peaks of $MAPbI_3$ films modified with 3 µl of CPFS (see Figure 7.4 (d)) provides evidence of the formation of fewer PbI_2 particles.

Figure 7.6(d) shows that the devices with CPFS additive exhibit improved stability compared to the control devices. The average PCE of the perovskite solar cells with 3 µl of CPFS additive degraded by only 23%, compared to about 33% in the control devices. This degradation represents an improvement in PCE stability of about 10% for devices based on films treated with CPFS additives. The poor stability of PCE in the control devices is caused by a severe decomposition of $MAPbI_3$ molecules in the presence of moisture (see Figures 7.3 (b) and 7.4(d)). The severe deterioration of $MAPbI_3$ molecules leads to decreased photon absorption and increased recombination sites, reducing the PCE. The PCE of the devices modified with CPFS additive suffered less degradation due

to a reduced decomposition by the crosslinking bonds formed between $MAPbI_3$ and CPFS.

These results demonstrate that altering $MAPbI_3$ films with 3 µl of CPFS additive improves the average J_{sc}, FF and PCE stability by 2%, 7% and 10%, respectively, compared to the control devices. This stability enhancement is probably because CPFS readily forms crosslinking, strong ionic and intermolecular bonds with perovskite molecules, thereby enhancing the bond strength and protection against moisture, as reported in [51–53]. This study demonstrates that a novel CPFS additive enhances the stability of perovskite solar cells prepared in the air at high relative humidity. The stability of the devices prepared from $MAPbI_3$ modified with 9 µl of CPFS was not studied because the result was obtained and added during the revision period.

7.6. Summary

This chapter described a novel attempt to use chlorodimethyl(pentafluorophenyl)silane additive in the fabrication process for improving the stability of perovskite solar cells (PSCs) prepared in ambient air of high relative humidity. The results showed enhanced stability of perovskite films and the devices based on $MAPbI_3$ modified with 3 µl of CPFS additive. However, it does not lead to an improvement in the power conversion efficiency of the devices. These studies demonstrate the benefit of CPFS additive in fabricating perovskite solar cells in ambient air of high relative humidity. It also provides insights into silane additives' application for enhancing perovskite solar cells' stability.

Chapter 8: Humidity-resistant antisolvent process for perovskite solar cells

8.1. Introduction

This chapter aims to develop a humidity-resistant antisolvent process for preparing perovskite solar cells (PSCs) with improved efficiency and stability at high relative humidity. Antisolvent treatment is necessary for PSC fabrication because it induces the crystallisation of perovskite/dimethyl sulphur (IV) oxide ($MAPbI_3$/DMSO) adduct in dimethyl methanamide (DMM). At high relative humidity, antisolvents with high water solubility and vapour pressure protect the adduct from moisture interaction and accelerate the evaporation of DMM during perovskite film deposition. Therefore, developing a suitable process for fabricating PSCs in ambient air of high humidity is beneficial to the low-cost and large-scale fabrication of PSCs.

This chapter investigates the effect of using different volumes of methyl ethanoate (MET) antisolvent on the properties of $MAPbI_3$ films and the performance of the perovskite solar cells. It also explored the influence of MET, chlorobenzene (CBZ), trichloromethane (TCM), methyl ethanoate (MET) and methylbenzene (MBZ) antisolvents on $MAPbI_3$ films and device characteristics. Finally, this chapter also studies how mixing methyl ethanoate and trichloromethane antisolvents affects the efficiency and stability of perovskite solar cells.

8.2. Chemical structures and properties of antisolvents

The properties of antisolvents significantly affect their effectiveness when preparing perovskite films at high relative humidity. Antisolvent with high vapour pressure and water solubility is beneficial in minimising the moisture influence on the $MAPbI_3$ films during deposition. In addition, antisolvent with moderate dipole moment can remove the DMM without severely altering the stoichiometry of DMSO in $MAPbI_3$/DMSO adduct. However, if an antisolvent has a low dipole moment, it cannot remove the DMM efficiently. On the other hand, if an antisolvent has a high dipole moment, it will not only remove the DMM but also change the stoichiometry of DMSO in the $MAPbI_3$/DMSO adduct. Figures 8.1 (a) – 8.1 (d) present the chemical structures of CBZ, TCM, MET and MBZ, respectively. The properties of these antisolvents are summarised in Table 8.1. The

bonds between carbon and highly electronegative chloride and oxygen atoms make CBZ, TCM and MET polar, while MBZ is non-polar. The high dipole moment of MET, arising from the C=O bond makes it more aggressive in removing DMSO. Still, the high-water solubility and vapour pressure of MET gives it an advantage over CBZ and TCM during high-humidity fabrication.

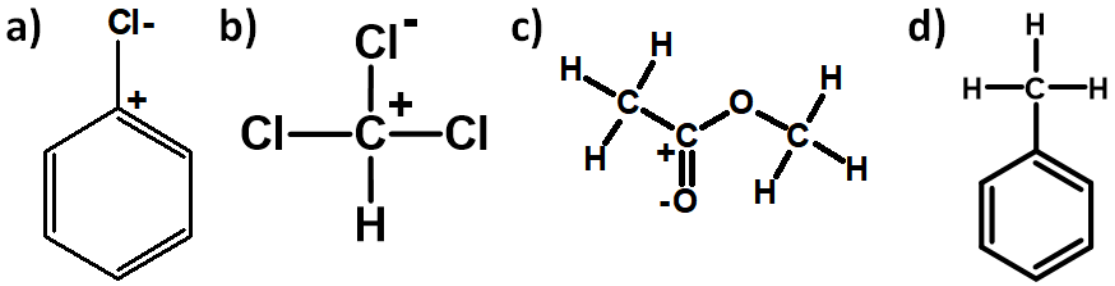

Figure 8.1: Chemical structures of (a) chlorobenzene (b) trichloromethane (c) methyl ethanoate and (d) methylbenzene

Table 8.1: Properties of chlorobenzene, trichloromethane, methyl ethanoate and methylbenzene [250,251]

Antisolvent	Vapour pressure (mmHg) at 23℃	Water solubility (%) at 23℃	Boiling point (℃)	Dipole moment (D)
Chlorobenzene	9	0.05	131.00	1.55
Trichloromethane	160	0.50	61.15	1.04
Methyl ethanoate	173	25.00	56.90	1.71
Methylbenzene	21	0.07	110.00	0.38

8.3. Suitable methyl ethanoate volume for efficient perovskite solar cells

This study aims to establish how the volume of methyl ethanoate antisolvent used for treating $MAPbI_3$ affects the efficient PSCs prepared in ambient air. Methyl ethanoate was employed in this study because it has high vapour pressure and water solubility beneficial for high-humidity fabrication. This study is the first to investigate how the volume of methyl ethanoate antisolvent for preparing $MAPbI_3$ films affects the performance of PSCs. Subsection 8.2.1 discusses the preparation of devices, while subsections 8.2.2 and

8.2.3 describe the results obtained from characterising $MAPbI_3$ films and devices, respectively.

8.3.1. Film and device fabrication

A 15 mg/ml of $SnCl_2.2H_2O$ solution was used to deposit SnO_2 layers on FTO substrates. $MAPbI_3$ films were spin-coated on SnO_2 layers from 1.50 M solutions of methylammonium lead iodide ($MAPbI_3$). This study used 80, 100, 150, 200, and 250 µl of methyl ethanoate antisolvent to treat $MAPbI_3$ films after 15 seconds of spinning. HTL was deposited on $MAPbI_3$ layers from an HTL solution containing 90 mg Spiro-OMETAD, 36 µl of MPPD, 38 µl of FK209 solution (300 gm/ml ethane nitrile) and 22 µl of Li-TFSI solution (520 mg/ml in ethane nitrile) in 1 ml of chlorobenzene. All the solution-processed processes were carried out in the air (48-50% relative humidity). Finally, Ag contacts with active areas of 0.15 cm^2 were deposited on HTLs at sputtering power, argon flow, argon pressure and sputtering duration of 1.0 W, 15 sccm and 5.0 mTorr, respectively, for 60 minutes. Chapter 3 (Section 3.2) presents the details of the fabrication process.

8.3.2. Properties of the prepared $MAPbI_3$ films

Figures 8.2(a) – 8.2(d) present the images of $MAPbI_3$ films on FTO substrates as a function of methyl ethanoate volume. Figure 8.2(a) shows that the film treated with 80 µl of methyl ethanoate has significantly inferior quality, as indicated by its greyish appearance. This observation could be due to the application of insufficient antisolvent, which probably results in poor extraction of DMM and incomplete $MAPbI_3$/DMSO adduct crystallisation [391]. Figure 8.2(b) shows that as the volume of methyl ethanoate increased to 100 µl, the quality of the film appeared to have improved. Hence, the image shows that the grey appearance observed in Figure 8.2(a) has become darker. Figure 8.2(c) shows no observable change in the formation of the films treated with 100 and 150 µl of methyl ethanoate. There is no noticeable change because normal eyes cannot differentiate the minute changes in the quality of films from the image. Figure 8.2(d) reveals that as the volume of antisolvent increased from 150 to 200 µl, the coatings appeared slightly more greyish. Consequently, AFM, XRD and a UV-Visible spectrometer were employed to investigate the films further.

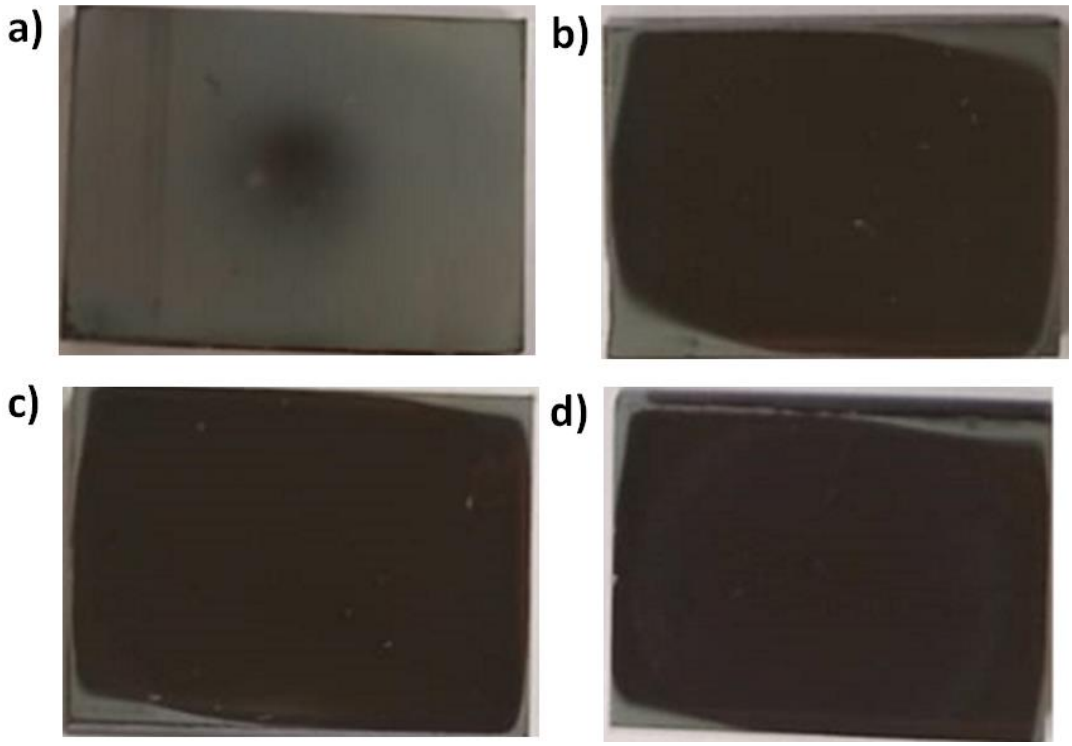

Figure 8.2: Images of $MAPbI_3$ films treated with (a) 80 µl (b) 100 µl (c) 150 µl and (d) 200 µl of methyl ethanoate.

Figures 8.3(a) – 8.3(e) present $MAPbI_3$ films studied using AFM. The AFM images in Figures 8.3(b) - 8.3(e) show that films treated with 100, 150, 200 and 250 µl of methyl ethanoate appeared to have similar morphology. Conversely, Figure 8.3(a) indicates that the AFM image of the films treated with 80 µl of methyl ethanoate appeared to have the worst surface roughness. Insufficient antisolvent could likely impede the formation of smooth $MAPbI_3$/Spiro-OMETAD interfaces, resulting in poor device performance [392].

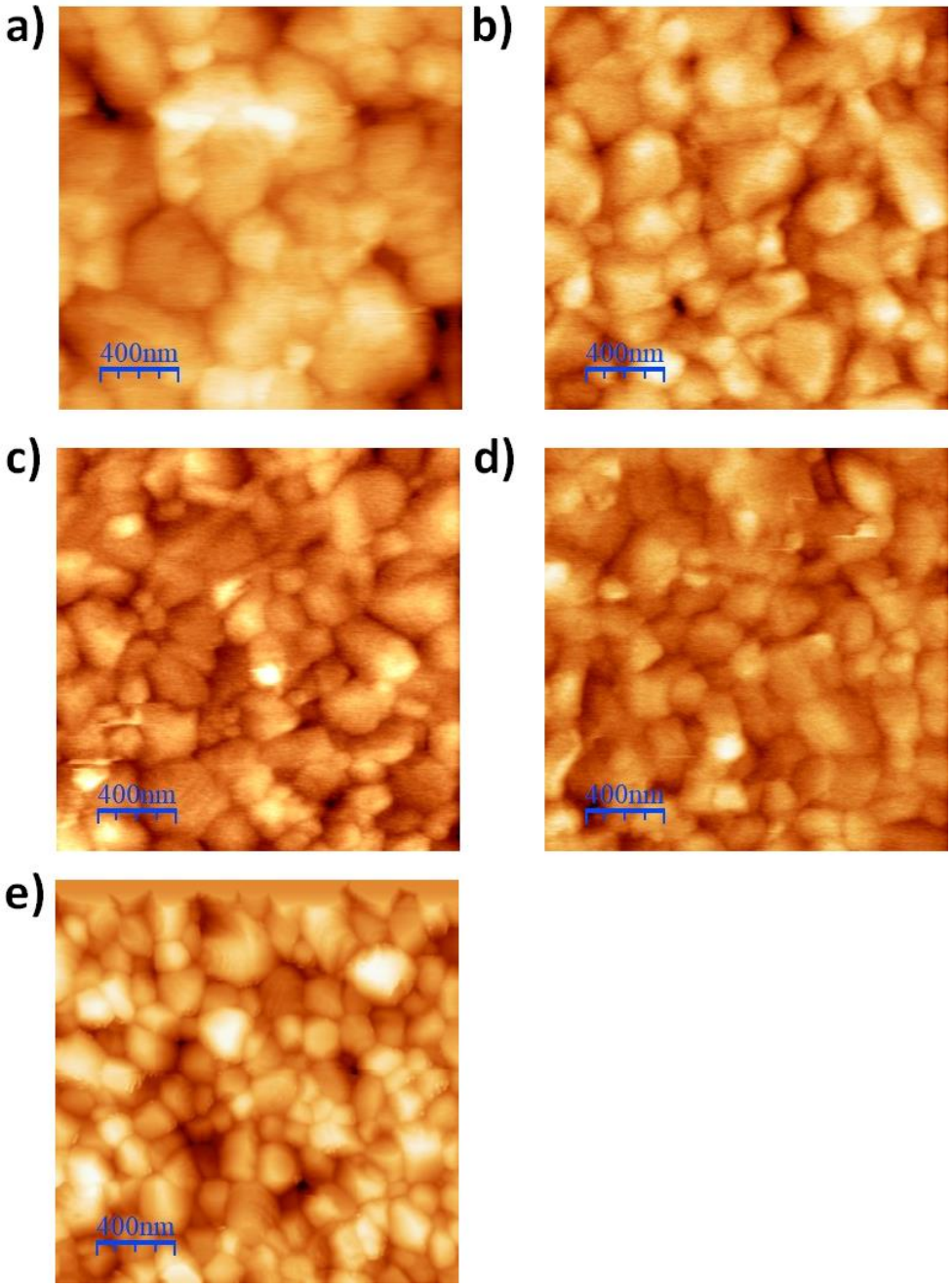

Figure 8.3: AFM images of $MAPbI_3$ films treated with (a) 80 µl, (b) 100 µl (c), 150 µl, (d) 200 µl of methyl ethanoate, and (e) 250 µl of methyl ethanoate

These images indicate that the surface smoothness of the films increased significantly as the volume of methyl ethanoate increased from 80 to 150 µl. However, the surface smoothness decreased slightly when the volume of methyl ethanoate further increased from 100 to 250 µl. This decrease in smoothness is possible because using 200 or 250 µl of MET causes excess removal of DMSO from the $MAPbI_3$/DMSO adducts, resulting in

fast nucleation and rough surfaces. These results suggest that 150 µl is a suitable volume of methyl ethanoate for depositing $MAPbI_3$ films with excellent surface smoothness. This conclusion is probably accurate for experiments using 15 mm×20 mm substrates at high humidity. Furthermore, the low surface roughness of the films treated with 150 µl will likely lead to devices with low R_{dc_f} and high R_{dc_r} and, thus, good photovoltaic performance [175,355,393–397].

The RMS of $MAPbI_3$ films were extracted from the AFM images using WSxM and Gwyddion software. Figure 8.4(a) shows the RMS roughness of the coatings as a function of the volume of methyl ethanoate. The results indicate that the roughness of the films decreased significantly when the volume of methyl ethanoate increased from 80 to 100 µl. The film roughness remained virtually the same when the MET volume increased from 100 to 150 µl. However, RMS roughness increased slightly when the volume of methyl ethanoate rose from 150 to 250 µl. Films treated with 80 µl of methyl ethanoate are roughest because an insufficient amount of antisolvents was used. These results suggest that 150 µl is a suitable volume of methyl ethanoate for depositing $MAPbI_3$ films with excellent morphology and surface smoothness. This conclusion is accurate for experiments using 15 mm×20 mm substrates at high humidity. The low surface roughness of the films treated with 150 µl will likely lead to devices with low R_{dc_f} and high R_{dc_r} and, thus, good photovoltaic performance [175,355,393–397].

The films were also studied using the XRD method. Figure 8.4(b) shows the XRD pattern of FTO and $MAPbI_3$ films on FTO substrates as a function of the volume of methyl ethanoate. The results show that all the $MAPbI_3$ films have crystalline structures and that their peak intensity (preferred direction), relative to FTO peak intensity (preferred direction), attained a maximum value at 100 µl. Relative to FTO, $MAPbI_3$ peaks of 0.8, 1.08, 0.95 and 0.84 resulted from films treated with 80, 100, 150 and 200 µl, respectively. These results suggest that $MAPbI_3$ films treated with 100 µl of methyl ethanoate have the thickest films. Films treated with 80 µl of methyl ethanoate seem to have low peak intensity, indicating poor crystallinity due to insufficient antisolvent. The results also show that the peak intensity of the films decreased when the amount of methyl ethanoate increased from 100 to 200 µl. Therefore, the XRD measurement suggests that the film thickness decreased when the antisolvent volume increased beyond 100 µl.

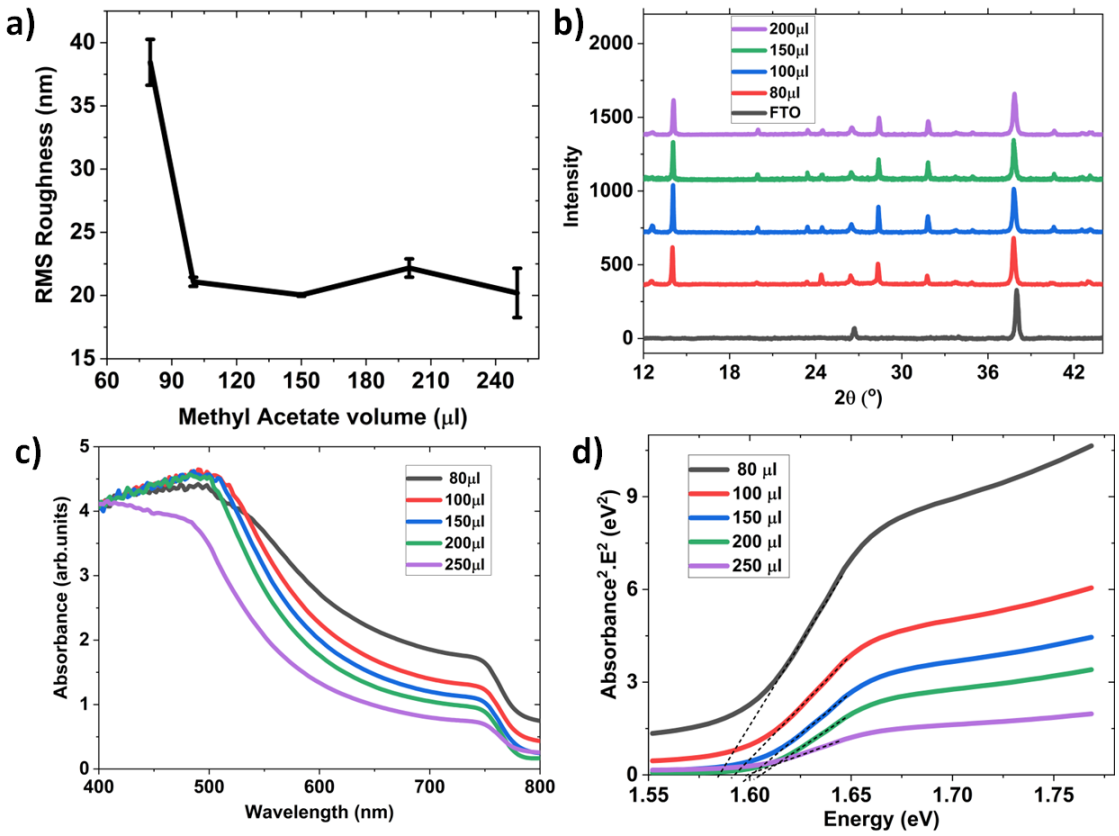

Figure 8.4: (a) RMS roughness, (b) XRD spectra, (c) Absorbance spectra and (d) Tauc plot of $MAPbI_3$ films as a function of methyl ethanoate volume. FTO substrate (TEC-8) was used for this XRD study.

Figures 8.4(c) and 8.4(d) show the absorbance spectra and the corresponding Tauc plots of $MAPbI_3$ films as a function of antisolvent volume. These results indicate that for wavelengths above 480 nm, the absorbance of the $MAPbI_3$ films decreased as the volume of methyl ethanoate increased from 80 to 250 µl. This reduced absorbance is due to the removal of MAI molecules by antisolvent, which reduces film thickness [137,205,335,336]. Below 480 nm, all the films appeared to have almost the same absorbance. The $MAPbI_3$ films treated with 80 µl of methyl ethanoate have the highest average absorbance. The Tauc plots also show that the E_g of the $MAPbI_3$ films varied from 1.58 to 1.61 eV as the volume of methyl ethanoate was increased from 80 to 250 µl, decreasing slightly when the antisolvent volume increased to 250 µl. The available data could not explain E_g's variation with the methyl ethanoate volume.

8.3.3. Photovoltaic performance of the devices

Figure 8.5 presents the J-V curves of the devices as a function of the volume of methyl ethanoate. Table 8.2 summarises the device parameters. The results show that when the volume of methyl ethanoate increased from 80 to 150 µl, the V_{oc} and FF of the devices increased while the J_{sc} decreased. The improvement in V_{oc} and FF arises from enhanced charge carrier extraction [398–400].

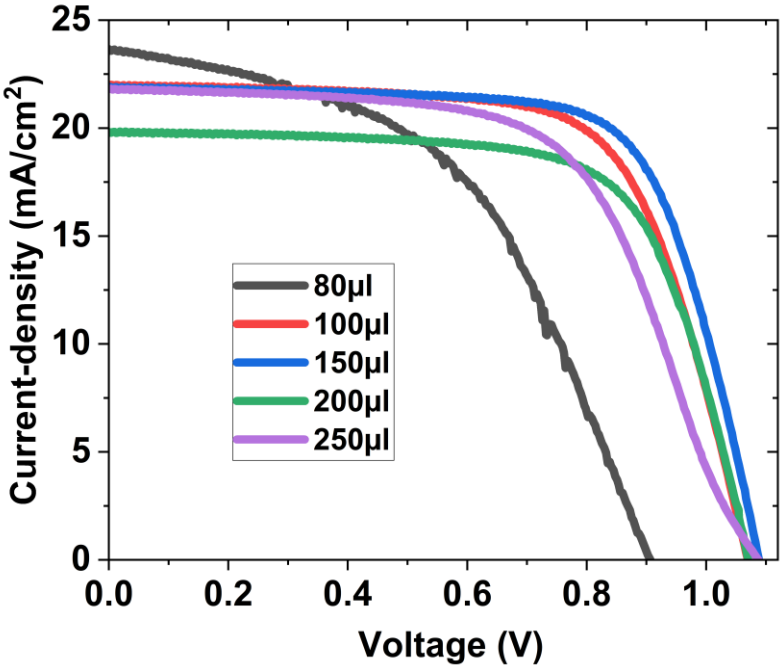

Figure 8.5: J-V curves of the best devices as a function of the volume of methyl ethanoate antisolvent.

Table 8.2: Photovoltaic parameters of the device as a function of methyl ethanoate volume (the rows denoted "Best" represent the data obtained from the best solar cells of the batch; the rows denoted "Av" represent the average of all cells)

Volume (µl)		**V_{oc}(V)**	**J_{sc} (mA/cm^2)**	**FF (%)**	**R_{dc_f} (Ω)**	**R_{dc_r} (kΩ)**	**PCE (%)**
80	Best	0.91	23.68	49.07	100	1.4	10.56
	Av	0.90±0.02	22.53±1.38	47.10±1.62			9.56±0.72
100	Best	1.07	22.00	67.89	60	23.4	15.99
	Av	1.05±0.02	21.44±0.41	63.20±5.01			14.31±1.58
150	Best	1.09	21.90	70.55	55	40.0	16.82
	Av	1.08±0.01	21.44±0.61	69.08±0.85			16.01±0.52
200	Best	1.07	19.84	68.61	60	11.1	14.61
	Av	1.07±0.01	19.18±0.46	66.62±1.99			13.64±0.58
250	Best	1.09	21.83	60.40	81	8.4	14.35
	Av	1.05±0.05	21.94±0.19	59.58±1.08			13.69±0.94

The charge extraction from the devices improved because of the reduction in surface roughness, which minimises the R_{dc_f} and maximises the R_{dc_r}. On the other hand, the J_{sc} obtained decreased due to reduced photon absorbance (see Figure 8.4(c)). Consequently, the enhancement in both V_{oc} and FF overcompensates the degradation in J_{sc}, thereby increasing the PCE of the devices. As the volume of methyl ethanoate rose from 150 to 200 µl, the devices' V_{oc}, PCE, FF and J_{sc} decreased. The V_{oc} and FF of the devices treated with 200 µl were low, probably due to increased surface roughness [401]. Large surface roughness led to significant interface resistance at the $MAPbI_3$/Spiro-OMETAD interface, thereby resulting in an increase in R_{dc_f} and a decrease in R_{dc_r}. In addition, the decline in J_{sc} could be due to a reduction in light absorption and an increase in current leakage. The absorbance of the films treated with 200 µl of methyl ethanoate dropped because the film thickness reduced and the E_g increased [36].

8.4. Suitable antisolvents for preparing perovskite solar cells in humid air

This study explores suitable antisolvents for preparing efficient perovskite solar cells at high relative humidity. Having successfully established the optimal volume of methyl

ethanoate (MET) required for preparing PSCs in ambient air, chlorobenzene (CBZ), trichloromethane (TCM), MET and methylbenzene (MBZ) antisolvents were comparatively studied to establish their suitability for preparing PSCs at high relative humidity. These antisolvents were selected for this study because they are readily available and have wide application in perovskite solar cells. Subsection 8.4.1 presents device fabrication, while subsections 8.4.2, 8.4.3 and 8.4.4 discuss the results from characterising $MAPbI_3$ films and devices.

8.4.1. Film and device fabrication

The devices were fabricated using the same conditions and parameters described in Section 8.3.1, except for $MAPbI_3$ films treated with 150 µl of either CBZ, TCM, MET or MBZ antisolvents. Chapter 3 (Section 3.2) presents the details of the device fabrication process.

8.4.2. Properties of the prepared $MAPbI_3$ films

AFM, UV-Vis spectrometer, XRD and FTIR techniques were used to study $MAPbI_3$ films treated with CBZ, TCM, MET, or MBZ antisolvents. Figures 8.6(a) – 8.6(d) present the images of $MAPbI_3$ films deposited on FTO substrates. Figure 8.6(a) indicates that films treated with CBZ have some degree of haziness, indicating the presence of pinholes, light scattering characteristics and poor qualities [34]. The observed poor film quality could be due to low vapour pressure and water solubility of CBZ (see Table 8.1), which make it less effective in protecting the $MAPbI_3$/DMSO adducts against moisture during deposition [37].

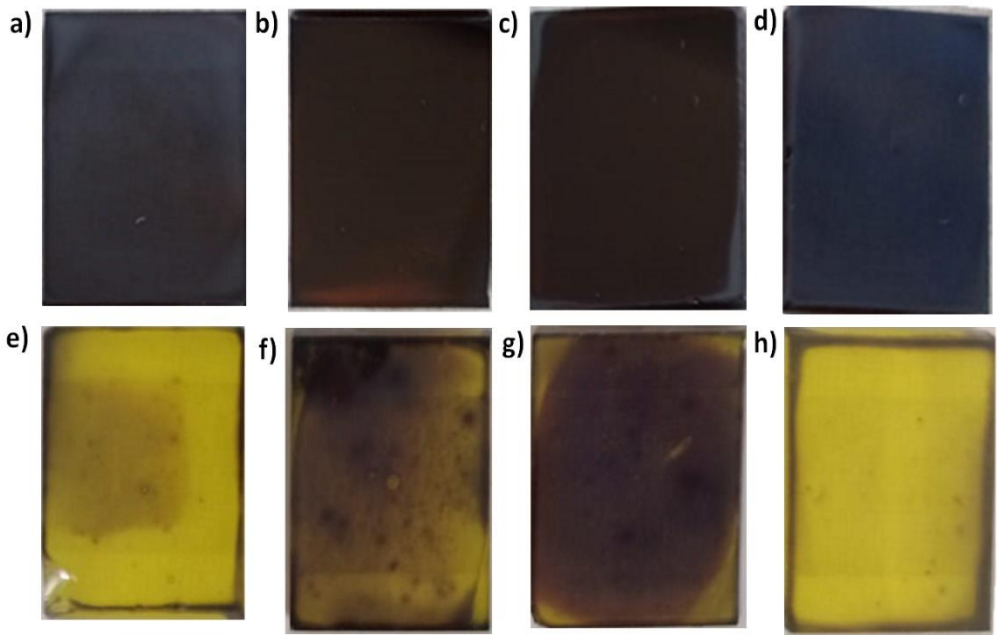

Figure 8.6: Images of annealed $MAPbI_3$ films (a) treated with CBZ on day 1 (b) treated with TCM on day 1 (c)treated with MET on day 1 (d) treated with MBZ on day 1 © treated with CBZ on day 65 (f) treated with TCM on day 65 (g) treated with MET on day 65 and (h) treated with MBZ on day 65.

Figure 8.6(b) shows that perovskite films treated with TCM have improved qualities. The film quality could have improved because TCM has high vapour pressure, which makes it relatively effective in protecting the $MAPbI_3$/DMSO adducts against moisture interference during film deposition (see Table 8.1). Similarly, TCM has moderate dipole moments that can induce the crystallisation of the $MAPbI_3$/DMSO adducts from the solution without extracting a significant amount of DMSO from the adduct. Figure 8.6(c) shows that films treated with MET have excellent qualities (dark and reflecting). This is because methyl ethanoate has very high vapour pressure and water solubility, which makes it quite effective in protecting films against moisture interference [402].

Figure 8.6(d) also indicates that films treated with methylbenzene have poor morphology, as demonstrated by the high haziness of the prepared films. The inferior quality of films treated with methylbenzene is likely due to two factors. Methylbenzene has a relatively low dipole moment, which makes it ineffective in inducing the crystallisation in perovskite solution. This could result in a prolonged nucleation process and rewetting, which prolonged the exposure of the adducts to the humid environment. Secondly,

methylbenzene has considerably low vapour pressure and water solubility, which makes it ineffective in protecting the $MAPbI_3$/DMSO adducts against moisture [37].

Figures 8.6(–) - 8.6(h) show the images of the $MAPbI_3$ films captured after 65 days of storage in a desiccator. The images show that films treated with trichloromethane or methyl ethanoate were the least bleached after 65 days. Nevertheless, films treated with MET were less bleached than those treated with TCM because MET antisolvent has high water solubility and dipole moment. The results indicate that films treated with chlorobenzene or methylbenzene bleached significantly after the same period. However, films treated with chlorobenzene appeared to have been bleached less than those treated with MBZ. MBZ has quite a low dipole moment, low vapour pressure and water solubility, which make it less valuable as an antisolvent relative to CBZ. These results demonstrate that MET treatment results in films with enhanced stability.

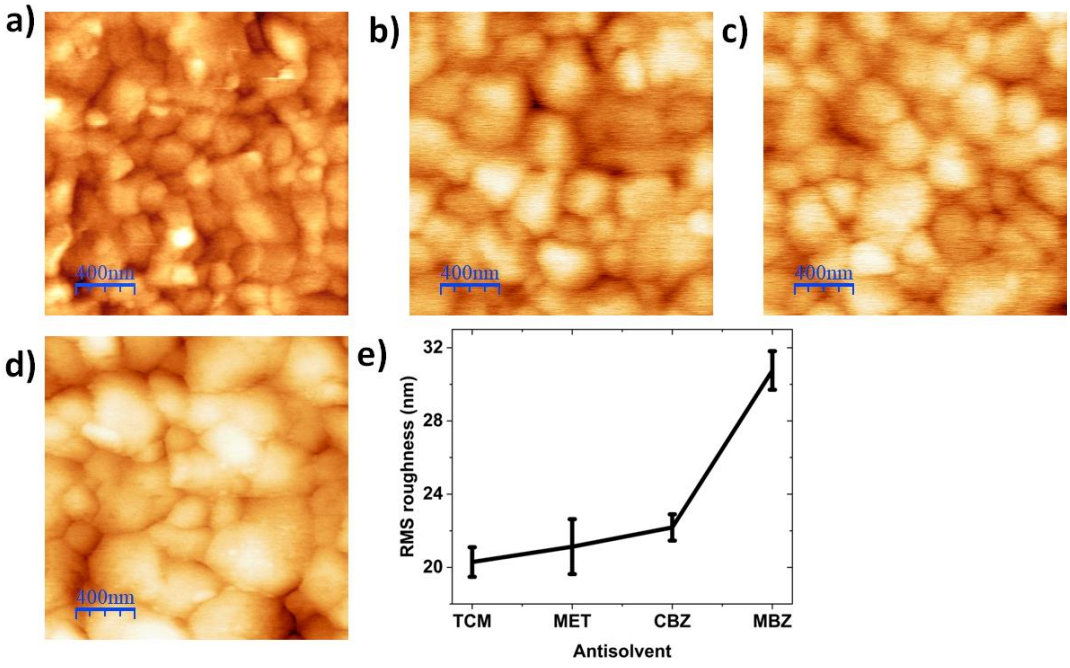

Figure 8.7: AFM images of $MAPbI_3$ films treated with (a) CBZ, (b) TCM, (c) MET, (d) MBZ and (e) RMS roughness of $MAPbI_3$ films immediately after deposition annealing.

Figures 8.7(a) – 8.7(d) present the AFM images of the films captured immediately after preparation. The AFM images show that the films treated with methyl ethanoate and trichloromethane have good qualities. In contrast, films treated with CBZ and MBZ antisolvents appear to have poor morphology.

The RMS roughness of the films was extracted from the AFM images using WSxM software. Figu©8.7(e) shows that the films treated with MET and TCM have low RMS roughness relative to the films treated with CBZ, while films treated with MBZ have significantly the largest RMS roughness. Films treated with MET, TCM, CBZ, and MBZ showed RMS roughness of 21 nm, 20 nm, 22 nm, and 32 nm, respectively. These results suggest that devices based on films treated with TCM, MET, or CBZ could have low interface resistance because of reduced RMS roughness [355].

Figures 8.8(a) –8.8(b) present the absorbance spectra and the Tauc plots of the $MAPbI_3$ films treated with different antisolvents. The absorbance spectra show that for wavelengths above 500 nm, the films treated with MBZ and CBZ have the highest absorbance. The absorbance seems higher in films treated with MBZ and CBZ antisolvents because these films cause more light scattering. On the other hand, the results show that films treated with trichloromethane or methyl ethanoate have higher absorbance over the wavelength ranging from 400 nm - 500nm. Still, the available data could not explain the reason for this observation. Further investigation is needed.

Figure 8.8(b) shows that the E_g of the $MAPbI_3$ films is slightly antisolvent-dependent. The E_g varies from 1.55 eV -1.61 eV, with the films treated with MBZ having the lowest E_g and those treated with MA having the widest E_g. The reason for this observation is not yet understood.

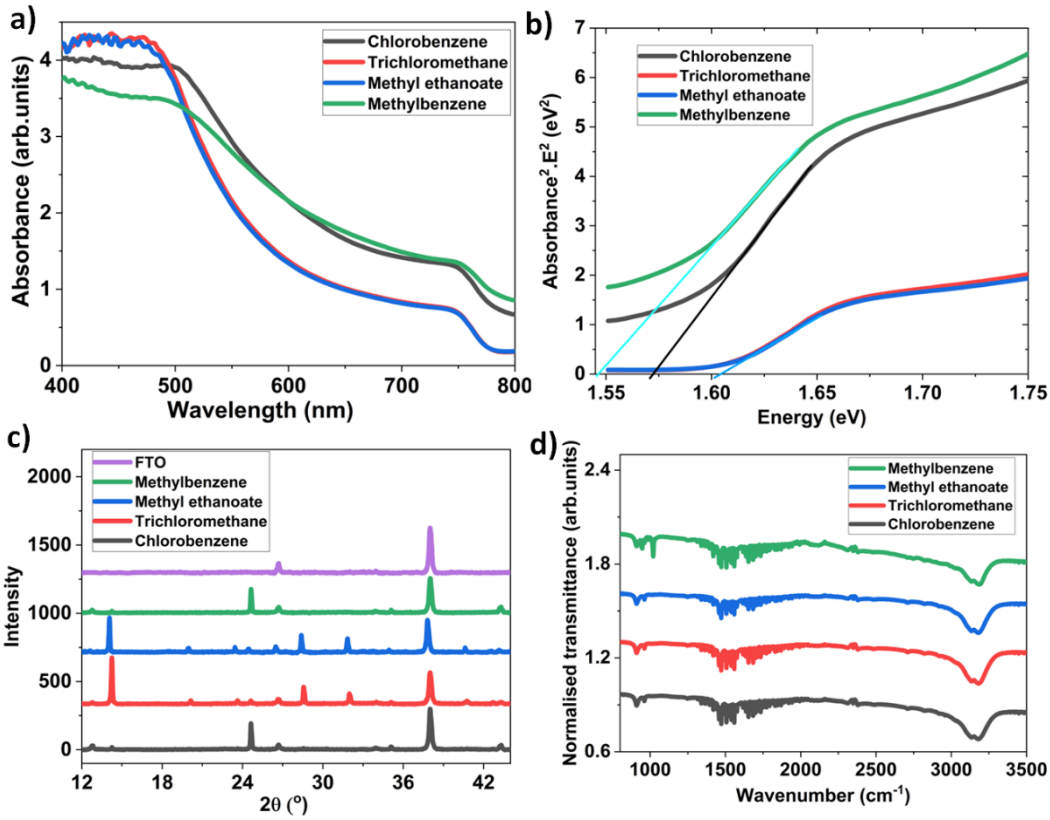

Figure 8.8: (a) Absorbance spectra, (b) Tauc plots, (c) XRD spectra and (d) FTIR spectra of $MAPbI_3$ films immediately after preparation for different antisolvents. FTO substrate (TEC-8) was used for this XRD study.

Figures 8.8(c) – 8.8(d) show the XRD and FTIR spectra of films treated with different antisolvents. The XRD spectra in Figure 8.8(c) indicate that the $MAPbI_3$ films treated with MET and TCM have a preferred crystal growth direction at 14.02°, consistent with the preferred direction reported for the films prepared in the glovebox [403]. These results suggest that MET and TCM are suitable for preparing perovskite films at high relative humidity. In contrast, the preferred crystal growth direction appeared at 24.8° for the films treated with CBZ and MBZ. The results also indicate that CBZ and MBZ may not be suitable for preparing quality $MAPbI_3$ films at high relative humidity [403]. The FTIR spectra in Figure 8.8(d) reveal that all the films have peaks at 910, 1470 and 3181 cm^{-1}. These peaks closely agree with 920, 1500 and 3200 cm^{-1} reported in [384]. The results also indicate the presence of a peak at 1020 cm^{-1} in films treated with methylbenzene. This peak represents a CH_3 rocking, as reported in [404].

8.4.3. Photovoltaic performance of the devices

Figure 8.9 shows the J-V curves of the devices prepared using different antisolvents, while Table 8.3 summarises the photovoltaic parameters of the devices. The results show that devices treated with MET achieved the best PCE and V_{oc} while those treated with MBZ had the lowest PCE and V_{oc}. The devices treated with MET attained high V_{oc} probably because of the reduced carrier recombination, interface resistance and wide E_g (see Figures 8.7(e) and 8.8(b)). These results are consistent with reports that the V_{oc} of photovoltaic devices increases with E_g [73,112].

Similarly, devices treated with CBZ, TCM, MET, and MBZ have virtually the same J_{sc}. Also, the devices treated with CBZ, MBZ and MET have nearly the same FF, while those treated with MBZ have poor FF. The reduced V_{oc} and FF of the devices treated with MBZ are likely due to an increased RMS roughness, as reported in [349,405].

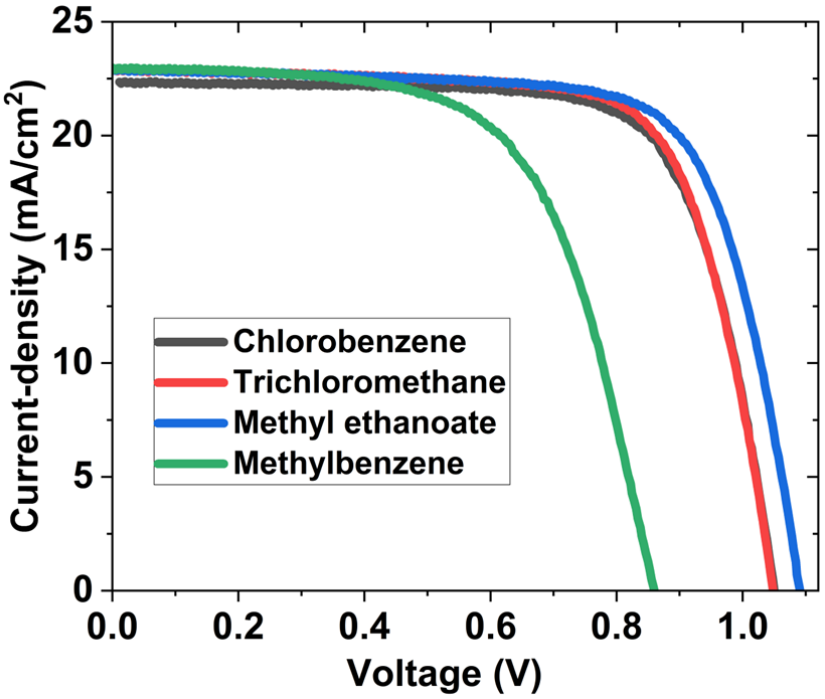

Figure 8.9: J-V curves of the best devices treated using different antisolvents.

Table 8.3: Photovoltaic parameters of the devices treated using different antisolvent (the rows denoted "Best" represent the data obtained from the best solar cells of the batch; the rows denoted "Av" represent the average of all cells)

Antisolvent		**V_{oc}(V)**	**J_{sc} (mA/cm^2)**	**FF (%)**	**R_{dc_f} (Ω)**	**R_{dc_r} (kΩ)**	**PCE (%)**
CBZ	Best	1.04	22.38	72.26	43	13.5	16.80
	Av	0.99±0.04	22.12±0.32	69.61±2.02			15.31±1.10
TCM	Best	1.05	22.93	72.32	45	36.2	17.42
	Av	1.04±0.01	22.66±0.44	71.62±0.80			16.91±0.39
MET	Best	1.09	22.93	72.17	45	25.0	18.10
	Av	1.09±0.00	22.49±0.43	71.18±1.16			17.50±0.51
MBZ	Best	0.86	23.00	62.46	51	10.0	12.37
	Av	0.86±0.01	22.71±0.30	59.04±2.37			11.57±0.59

8.4.4. Device stability

The J-V measurement was performed after 0, 192, 360, 528, 696 and 864 hours of storage in a desiccator. The devices' V_{oc}, J_{sc}, FF and PCE were determined from the measured J-V characteristics. Figures 8.10(a) - 8.10(d) present the normalised V_{oc}, J_{sc}, FF and PCE as a function of antisolvent and storage time. Figure 8.10 (a) indicates that the V_{oc} of the devices degraded only slightly after 864 hours, and it appeared to be independent of the antisolvent applied.

Conversely, Figure 8.10(b) shows that the average J_{sc} of the devices treated with MBZ degraded by about 57% after 864 hours, while the J_{sc} of devices treated with other antisolvents degraded more slowly. The severe degradation in the J_{sc} of devices based on $MAPbI_3$ films treated with MBZ can be attributed to the decomposition of a significant amount of $MAPbI_3$ molecules, leading to reduced photon absorption. The quick deterioration of the films treated with MBZ could be due to multitudes of pinholes that act as moisture entry points. On the other hand, the high vapour pressure and water solubility of MET result in compact films with fewer entry points for moisture and, therefore, fewer decomposition of $MAPbI_3$ molecules. Hence, the average J_{sc} of the

devices based on films treated with MET degraded by only 6%, while the devices prepared from films treated with CBZ and TCM decreased by about 22% and 8%, respectively.

Figure 8.10(c) also indicates that the average FF of devices fabricated from films treated with MBZ degraded by 53% after 864 hours compared to 25%, 21% and 10% for the devices prepared from $MAPbI_3$ treated with CBZ, TCM, and MET antisolvents, respectively. PSCs from films treated with MBZ have the worst FF degradation because many PbI_2 particles, which act as carrier recombination sites, were produced from the decomposition of $MAPbI_3$ molecules. The devices treated with MET exhibit the lowest degradation in FF because films treated with MET generated the least PbI_2, which could act as localised recombination sites.

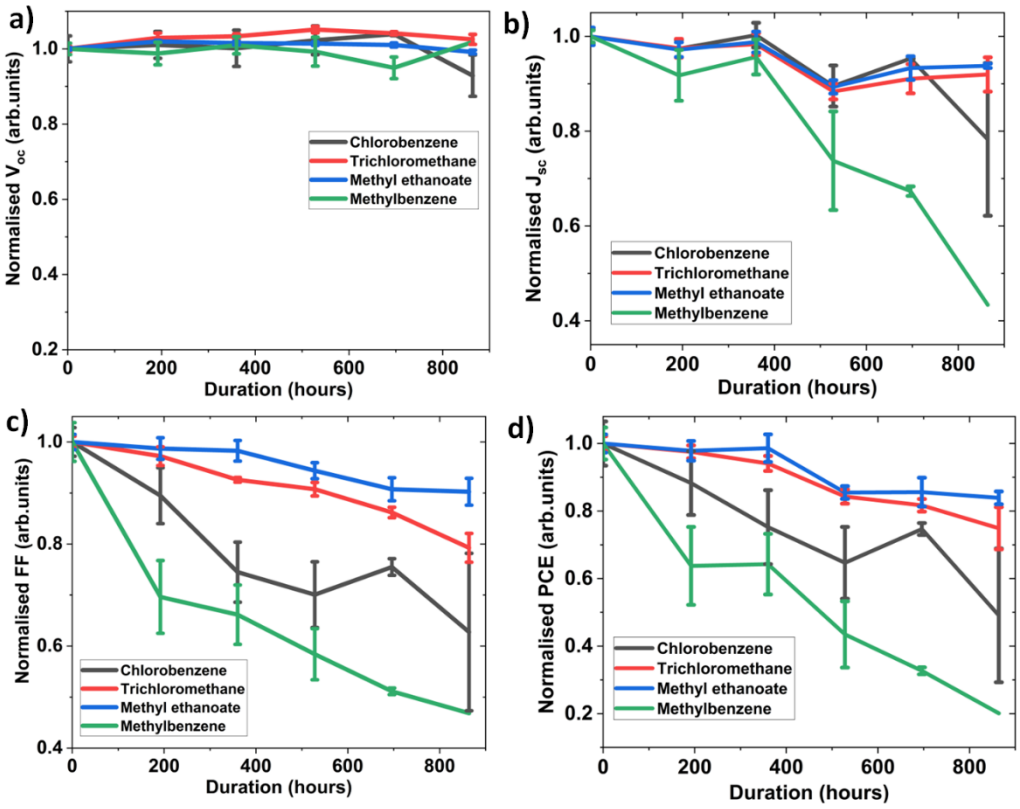

Figure 8.10: Normalised (a) V_{oc} (b) J_{sc} (c) FF and (d) PCE of devices, all parameters as a function of antisolvent and storage duration.

Figure 8.10(d) shows that the average PCE of the devices prepared from films treated with MET degraded by 16% after 864 hours compared to PCE degradation of 25% for the devices based on films treated with TCM. The results also show that the average PCE

of the devices prepared from films treated with CBZ and MBZ degraded by 51% and 80%, respectively. The observed degradation in PCE of the devices is a result of the combined degradation of both J_{sc} and FF. Devices treated with MET are the most stable because the antisolvent protects the $MAPbI_3$/DMSO adducts from moisture interference during deposition. Similarly, the devices treated with TCM also showed a reasonable level of stability. MET and TCM protect $MAPbI_3$/DMSO adducts against moisture due to their high vapour pressure at room temperature, but MET has better protection than TCM due to its high-water solubility. Low vapour pressure and water solubility of CBZ and MBZ limit their ability to protect $MAPbI_3$/DMSO adducts against moisture interference during fabrication. Consequently, the devices treated with CBZ and MBZ have the worst stability overall. However, the devices treated with CBZ appeared more stable than those treated with MBZ. The low dipole moments of MBZ cause the films treated with it to suffer from a slow nucleation process and rewetting. This slow nucleation process and rewetting prolong the exposure of the $MAPbI_3$/DMSO to moisture, resulting in poor film quality and stability. These results demonstrate that devices treated with MET have the best J_{sc}, FF and PCE stability and, therefore, the most suitable antisolvents for preparing PSCs in ambient air among the antisolvents studied.

8.5. Improving the stability and PCE of PSCs using mixed antisolvents

This study investigates how mixing methyl ethanoate and trichloromethane antisolvents affects the PCE and stability of PSCs prepared at high relative humidity. Combining these antisolvents reduces the solubility of DMSO in the resultant antisolvent and ensures that the optimal amount remains in the $MAPbI_3$/DMSO adducts. This process could enhance the quality of $MAPbI_3$ films and improve the efficiency and stability of PSCs prepared in ambient air.

8.5.1. Film and device fabrication

The devices in this study were prepared using the same parameters and conditions described in Section 8.3.1. In addition, however, the $MAPbI_3$ films were treated with methyl ethanoate mixed with trichloromethane (0%, 15%, 30%, 45%, and 60%). Chapter 3 (section 3.2) presents the details of the device fabrication process.

8.5.2. Properties of the prepared $MAPbI_3$ films

Figure 8.11(a) shows the image of $MAPbI_3$ film before the application of antisolvent and annealing. The films seem yellow due to lead iodide in the solution since the perovskite films have not formed. Figures 8.11(b) - 8.11(e) show the image of $MAPbI_3$ films after applying antisolvents but before annealing. The film images show that the colour of the unannealed films became lighter as the proportion of trichloromethane increased from 0% to 45%. The results indicate that films treated with methyl ethanoate (100%) are deep brown, suggesting partial perovskite formation even before annealing. This observation is probably because a substantial proportion of the DMSO was extracted from the $MAPbI_3$/DMSO adducts by the methyl ethanoate due to its high dipole moment. Removing a considerable proportion of DMSO from the $MAPbI_3$/DMSO adducts fastens the nucleation process. Consequently, dark brown films formed as a substantial proportion of $MAPbI_3$/DMSO adducts have been partially converted to perovskite, even before annealing [204]. Conversely, the films treated with antisolvent containing methyl ethanoate (55%) and trichloromethane (45%) appeared light. This observation indicates a delay in the nucleation process and that it may take longer annealing to complete perovskite formation than films treated with methyl ethanoate.

Figures 8.11(f) – 8.11(i) present the images of the $MAPbI_3$ films after applying antisolvent and annealing. All the images appear dark, suggesting that they have good qualities. Hence, the possible differences in film quality are not visually noticeable. Consequently, more advanced instruments like AFM and SEM are required to identify any possible change in the film qualities.

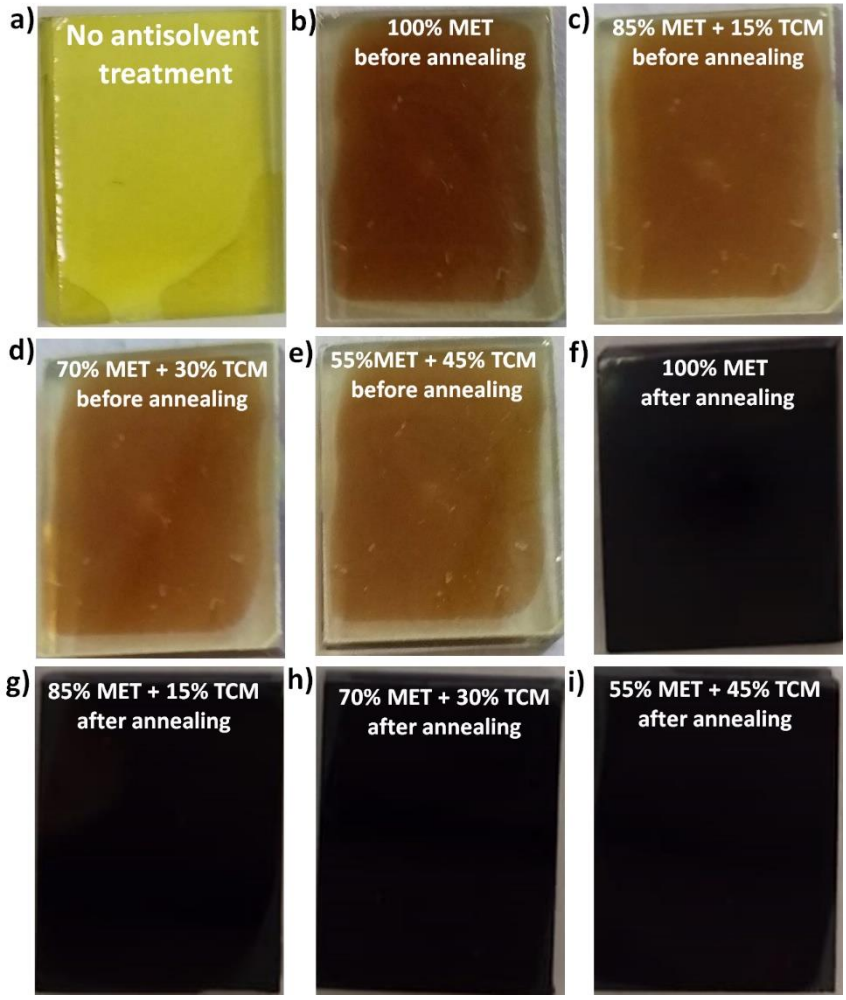

Figure 8.11: Images of $MAPbI_3$ films treated with methyl ethanoate (MET) only and treated using the mixture of methyl ethanoate with trichloromethane (TCM) before and after annealing. The films were deposited at 4000 rpm for 30 seconds and annealed at 110℃ for 15 minutes under 50-55% RH.

The $MAPbI_3$ films were examined using FE-SEM to inspect their surface morphology. Figures 8.12(a) - 8.12(d) show the SEM images of films treated with a different mixture of methyl ethanoate and trichloromethane. The SEM images show that all the films have good crystallinity, morphology, and compactness. Furthermore, a detailed inspection shows that the films treated with methyl ethanoate (85%) mixed with trichloromethane (15%) have a smoother surface than those treated with methyl ethanoate (100%). This is because the solubility of DMSO in the mixed antisolvent decreased, leading to a more optimised DMSO amount in the $MAPbI_3$/DMSO adduct.

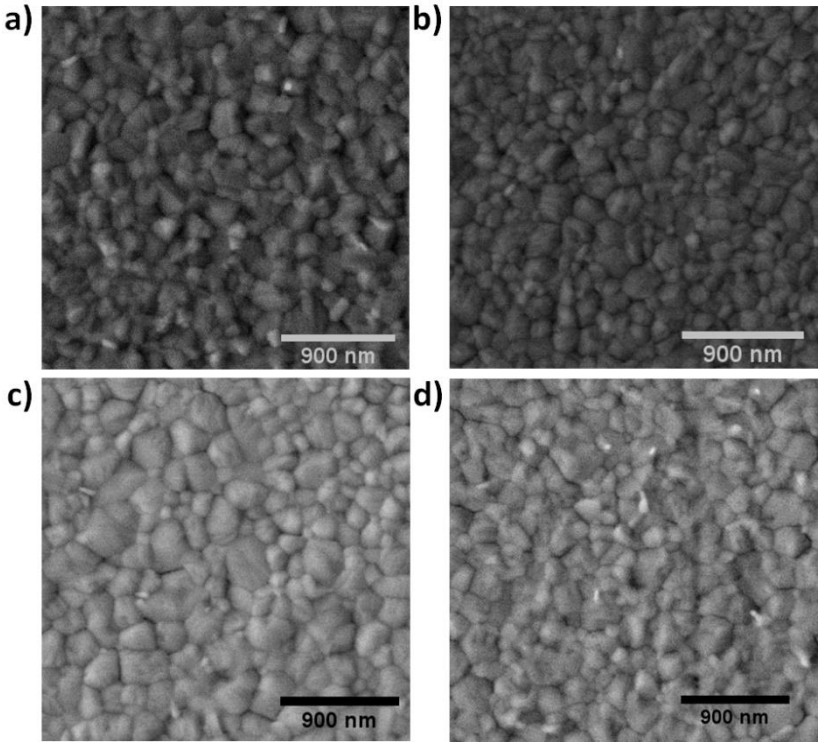

Figure 8.12: SEM images of $MAPbI_3$ films treated with methyl ethanoate mixed with (a) 0% trichloromethane, (b) 15% trichloromethane, (c) 30% trichloromethane and (d) 45% trichloromethane.

The results indicate that grain size increased as the trichloromethane proportion increased from 15% to 30%. This is because the solubility of DMSO in the mixed antisolvents decreased, leaving slightly more DMSO in the $MAPbI_3$/DMSO adduct. More DMSO slowed the speed of the nucleation process slightly and resulted in larger crystals, which are beneficial to improving the power conversion efficiency. However, the slow nucleation process in the $MAPbI_3$/DMSO adduct with excess DMSO may result in pinholes and defects between larger grains, which open pathways for moisture penetration and degradation in the stability. Furthermore, the grain size and surface smoothness degraded when the trichloromethane percentage increased from 30% to 45%. In addition, the solubility of DMSO in the mixed antisolvents was reduced further, leaving excess DMSO in the $MAPbI_3$/DMSO adduct. Excess DMSO delays the nucleation process, causes rewetting and, consequently, a degradation in the film quality [35,36,406]. These results indicate that the perovskite films treated using methyl ethanoate mixed with 15%

and 30% trichloromethane have the best quality regarding surface smoothness, grain size, and compactness.

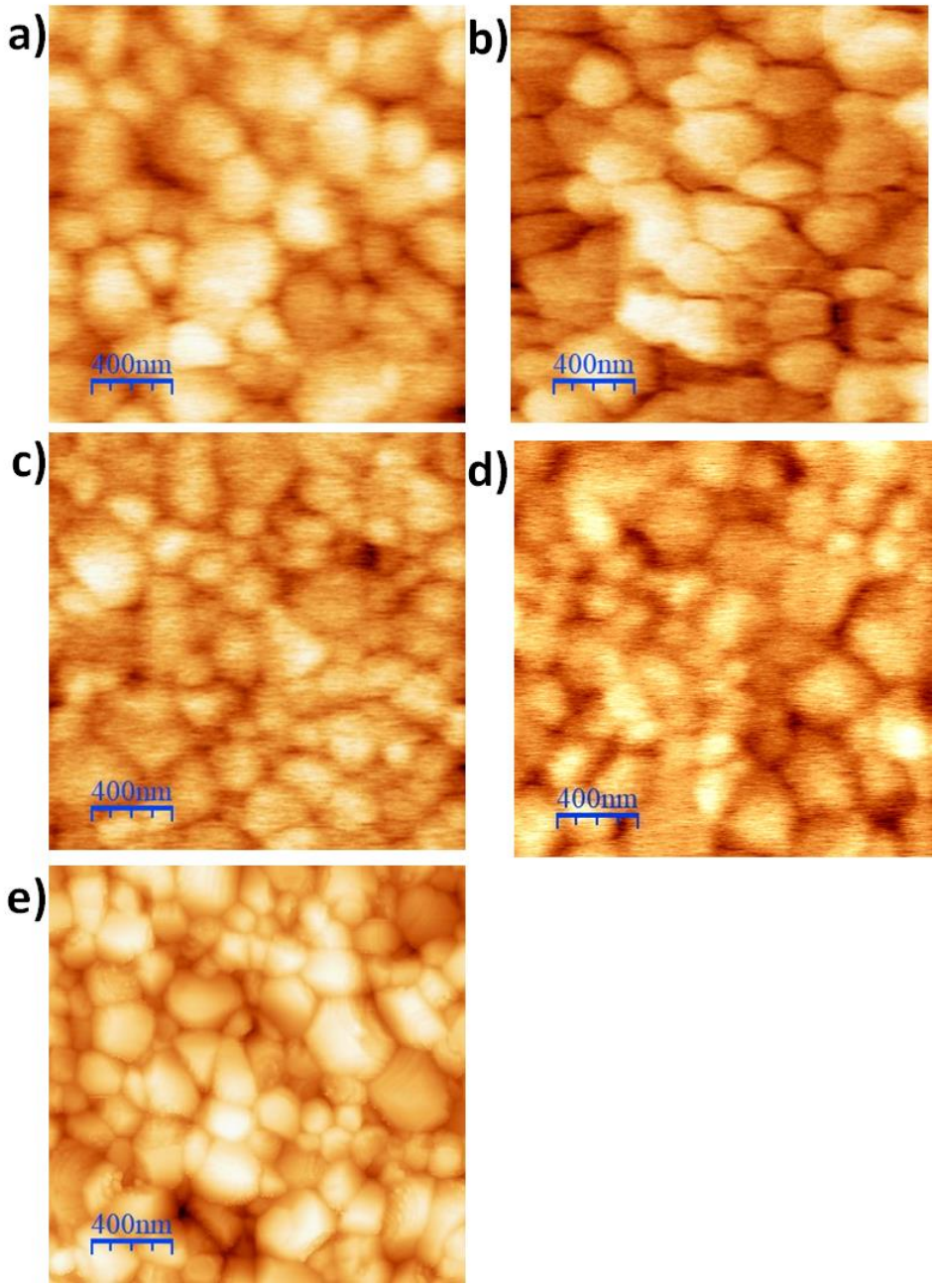

Figure 8.13: AFM images of $MAPbI_3$ films treated with methyl ethanoate mixed with (a) 0% trichloromethane, (b) 15% trichloromethane, (c) 30% trichloromethane, (d) 45% trichloromethane and (d) 60% trichloromethane.

Figures 8.13(a) – 8.13(d) show the AFM images for the films treated using the methyl ethanoate mixed with 0%, 15%, 30%, 45% and 60% of trichloromethane, respectively.

The AFM images indicate that all the films exhibit good morphology of typical perovskite films. However, the films treated with methyl ethanoate (70%) mixed with trichloromethane (30%) have the best surface smoothness. AFM image analysis using WSxM and Gwyddion software confirms this observation. Figure 8.14(a) shows that films treated with methyl ethanoate (70%) mixed with trichloromethane (30%) and methyl ethanoate (85%) mixed with trichloromethane (15%) achieved the lowest RMS roughness. Figure 8.14(b) showed the decrease in the solubility of DMSO in the mixed antisolvent when the proportion of TCM increased, indicating that the film smoothness improvement could be related to DMSO solubility in the antisolvent.

Figures 8.14(c) and 8.14(d) show the XRD data of $MAPbI_3$ films on FTO substrates taken at 0 hours and after 384 hours of storage, respectively. The results obtained at 0 hours show that $MAPbI_3$ peaks occurred at 2θ =14.1°, 28.4° and 31.8° and were independent of the mixed antisolvent composition. These peaks agree with the peaks reported elsewhere [358]. The peak at 14.02°is the preferred crystal growth direction for the $MAPbI_3$ films, while the peak at 37.9° is the preferred crystal direction for the FTO layer. The XRD measurements show that the ratio of the $MAPbI_3$ peak intensity at 14.02° to the FTO peak intensity at 37.9° increased with an increase in the trichloromethane proportion. The result indicates that the thickness of $MAPbI_3$ films increased when the amount of trichloromethane in the antisolvent mixture increased.

Moreover, the XRD spectra measured after 384 hours (see Figure 8.14(d)) show that the peak intensity of $MAPbI_3$ (14.02°) relative to the peak intensity of FTO (37.9°) degraded by about 9% for the films treated with the methyl ethanoate. However, films treated using methyl ethanoate mixed with 15%, 30% and 45% of trichloromethane degraded by 0%, 0% and 15%, respectively. This result indicates that the $MAPbI_3$ films treated using MET mixed with 15% and 30% trichloromethane remained unchanged. Conversely, the films treated with methyl ethanoate (100%) or methyl ethanoate (55%) mixed with trichloromethane (45%) degraded. Figure 8.14(d) shows that the PbI_2 phase emerges for all films after 384 hours of storage. The PbI_2 peaks indicate the decomposition of $MAPbI_3$ due to moisture penetration [407]. Furthermore, the PbI_2 peaks revealed that films treated with methyl ethanoate (85%) mixed with trichloromethane (15%) were the most stable and produced the least amount of PbI_2 particles after 384 hours.

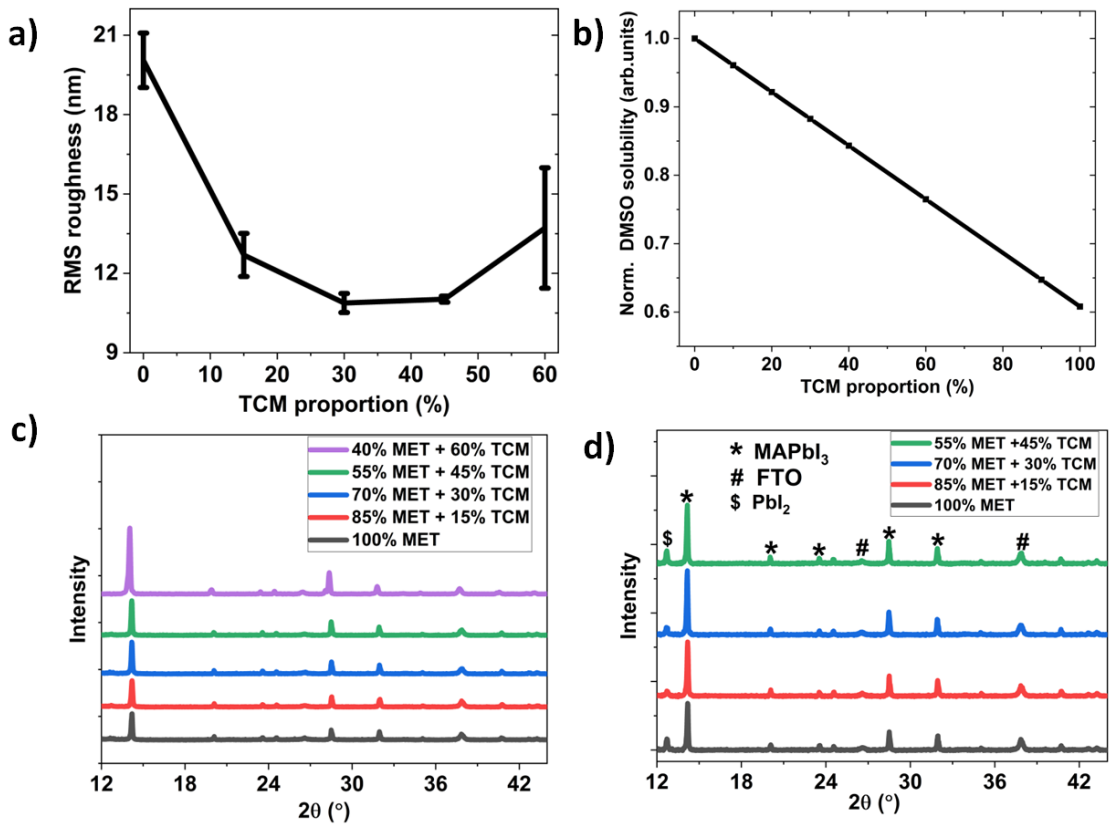

Figure 8.14: The effect of trichloromethane (TCM) proportion mixed with methyl ethanoate (MET) on (a) RMS roughness of $MAPbI_3$ films, (b) solubility of DMSO in the resultant antisolvent, (c) XRD spectra of $MAPbI_3$ films at 0 hours and (d) XRD spectra of $MAPbI_3$ films after 384 hours storage.

The UV-Visible measurement was conducted on $MAPbI_3$ films treated using MET mixed with different proportions of TCM antisolvents after 0 and 384 hours of storage. Figures 8.15(a) - 8.15(d) show the measured absorbance spectra and the related Tauc plots. The results obtained at 0 hours show that over the wavelength range of 400 nm – 500 nm, the $MAPbI_3$ films treated using the MET mixed with TCM antisolvents have better absorbance than those treated with methyl ethanoate (100%). Hence, films treated with methyl ethanoate (100%) have an average absorbance of 1.725 compared to 1.77, 1.81, 1.75 and 1.799 obtained from films treated with methyl ethanoate mixed with 15, 30, 45% and 60% of TCM. These results indicate that the absorbance of the $MAPbI_3$ films seems independent of the mixed antisolvent composition. Furthermore, the Tauc plots show that the energy bandgap (E_g) of $MAPbI_3$ films is about 1.59 eV and independent of the mixed antisolvent composition.

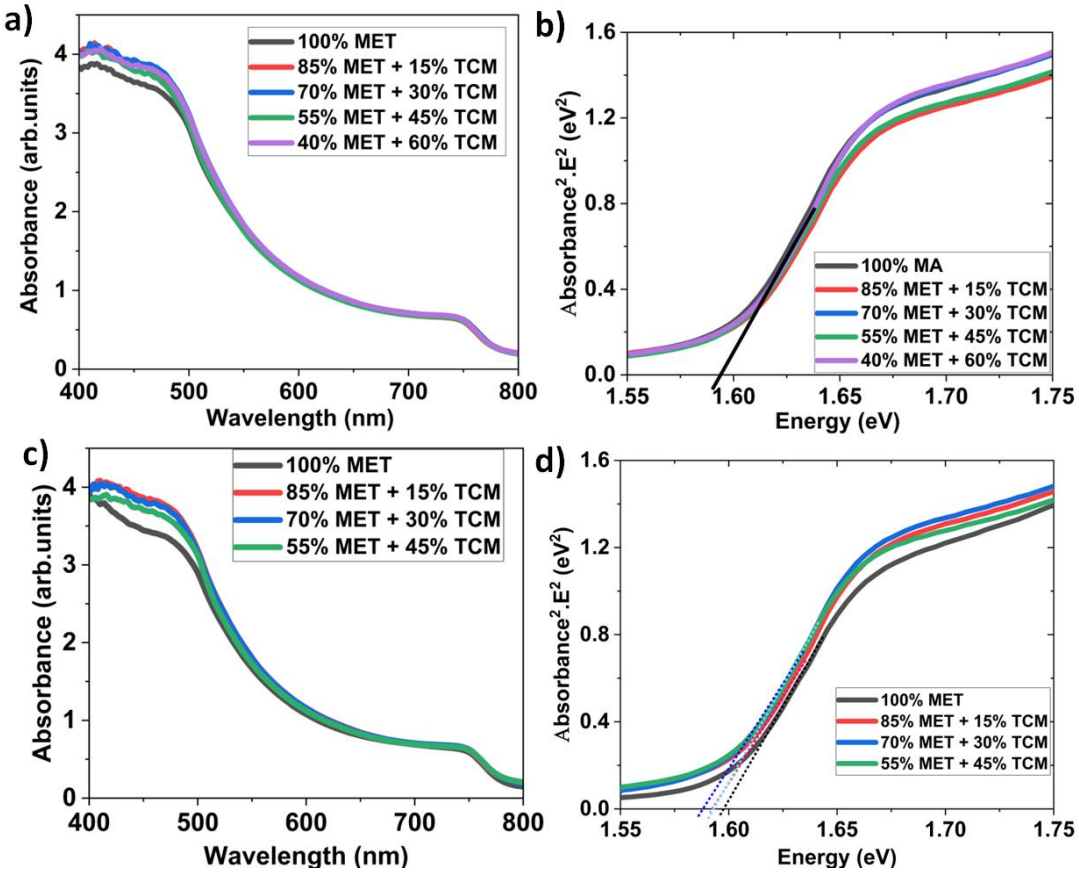

Figure 8.15: (a) Absorbance of $MAPbI_3$ films after 0 hours, (b) Tauc plots of $MAPbI_3$ films after 0 hours, (c) absorbance of $MAPbI_3$ films after 360 hours, and (d) Tauc plots of $MAPbI_3$ films after 360 hours. The $MAPbI_3$ films were treated with methyl ethanoate (MET) mixed with different proportions of trichloromethane (TCM)

The UV-Visible measurements after 360 hours show that the average absorbance of the films treated with methyl ethanoate (100%) degraded by about 5%. Conversely, the films treated with methyl ethanoate mixed with 15%, 30% and 45% trichloromethane suffered average absorbance degradation of 0%, 2% and 2%, respectively. Hence, the films treated with methyl ethanoate (85%) mixed with trichloromethane (15%) suffered the least degradation. The improved surface smoothness of these films (SEM image in Figure 8.12(b)) suppresses moisture ingress and $MAPbI_3$ decomposition. The improvement in the surface smoothness of the $MAPbI_3$ could be beneficial in improving the stability and efficiency of the PSCs. It should be noted that the films treated with methyl ethanoate (40%) mixed with trichloromethane (60%) were fabricated and investigated during the revision period. Hence, their stability was not investigated because it is challenging to

ensure that the films are exposed to the same environmental conditions as the other films during the previous stability testing.

8.5.3. Photovoltaic performance of the devices

The impedance characteristics of the devices were measured using illumination of 1000 W/m^2 and a DC bias of 1.0 V. The junction capacitances of the PSCs were extracted from the impedance data using ZSimpWin software and presented in Figure 8.16(a). The results show that the junction capacitance increased as the TCM proportion increased from 0 to 30%, attaining the maximum at 30% trichloromethane. These results indicate that devices treated with methyl ethanoate (70%) mixed with trichloromethane (30%) have the best charge extraction. The results also showed a further decrease in junction capacitance when the trichloromethane proportion increased from 45% to 60%.

Figure 8.16(b) presents the J-V curves of the best devices for different trichloromethane proportions. Table 8.4 summarises the critical photovoltaic parameters for these devices and the average values of all devices. The results show that the devices' average J_{sc}, FF and PCE increased slightly when the trichloromethane proportion increased from 0% to 30%. The J_{sc} increased because an increase in light absorption ((see Figure 8.15(a))) increases charge generation while low R_{dc_f} minimises leakage current via the R_{dc_r}. A decrease in the R_{dc_f} value could result from the reduction in interface resistance, which depends on the surface roughness of the $MAPbI_3$ films. An increase in the FF indicates an improvement in carrier extraction. The junction capacitance results in Figure 8.15(a) support this explanation. The results show that devices treated with methyl ethanoate (70%) mixed with trichloromethane (30%) have the best PCE, despite having similar surface smoothness as devices treated with methyl ethanoate (85%) mixed with trichloromethane (15%). This observation might be because the devices treated with methyl ethanoate (70%) mixed with trichloromethane (30%) have slightly larger grains. Films with good coverage and large grain sizes result in better device performance due to the reduced grain boundaries, which act as recombination sites [45,50,260].

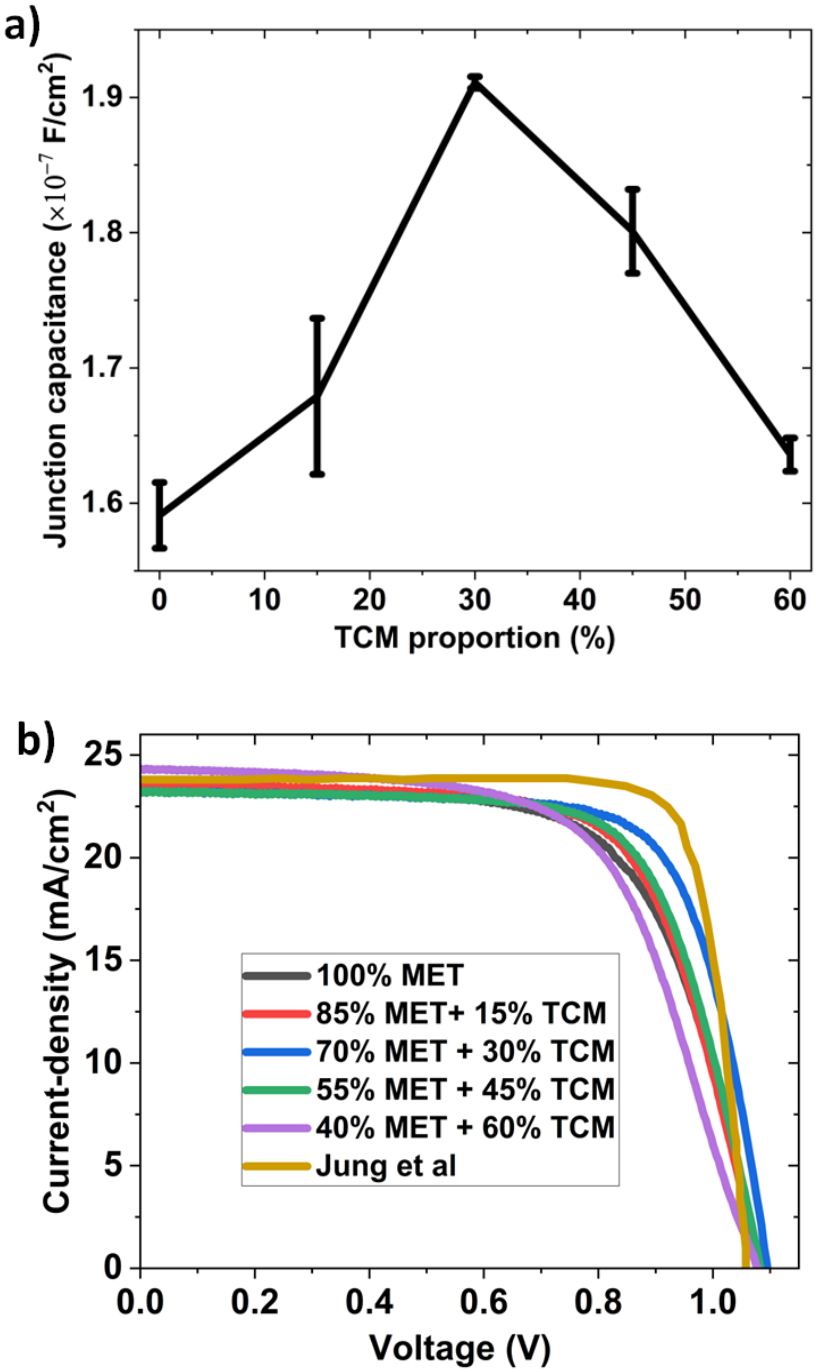

Figure 8.16: (a) Junction capacitance and (b) J-V curves of the devices treated with methyl ethanoate mixed with trichloromethane and J-V curve in the literature [39]. The devices were prepared at 50 -55% RH

Table 8.4: Photovoltaic parameters of the device treated with methyl ethanoate mixed with trichloromethane (the rows denoted "Best" represent the data obtained from the best solar cells of the batch; the rows denoted "Av" represent the average of all cells). The data by Jung et al [39] is also included as a reference for comparison.

Antisolvent		**V_{oc} (V)**	**J_{sc} (mA/cm2)**	**FF (%)**	**Rd_{c_f} (Ω)**	**Rd_{c_r} (kΩ)**	**PCE (%)**
100% MET	Best	1.10	23.49	66.08	57	13.9	17.13
	Av	1.09±0.02	21.99±1.02	64.72±1.37			15.48±0.92
85% MET + 15% TCM	Best	1.08	23.62	67.70	57	19.5	17.34
	Av	1.09±0.02	22.66±1.10	65.92±3.38			16.21±1.15
70% MET + 30% TCM	Best	1.10	23.26	72.76	42	20.0	18.55
	Av	1.09±0.02	22.70±0.93	69.59±2.05			17.16±0.94
55% MET + 45% TCM	Best	1.09	23.27	69.66	55	13.0	17.59
	Av	1.09±0.01	22.33±1.36	68.20±1.77			16.55±1.06
40% MET + 60% TCM	Best	1.09	24.34	62.33	81	10.4	16.46
	Av	1.07±0.02	24.18±0.21	61.52±0.84			15.92±0.34
Ref-4 [39]	Best	1.08	24.82	82.15			22.06

When the trichloromethane proportion increased from 30 to 45%, the V_{oc} and FF of the devices decreased slightly while the J_{sc} remained practically the same. The J_{sc} remained almost the same since there was only a minor difference in the average absorbance between these films. However, the FF and V_{oc} of the devices decreased when the TCM proportion increased to 45%. This is likely due to a reduced charge carrier extraction, as indicated by the junction capacitance in Figure 8.16(a). The degradation of FF and V_{oc} causes a decrease in the PCE of the devices treated with methyl ethanoate (55%) mixed with TCM (45%). A further increase in trichloromethane from 45% to 60% led to a decrease in V_{oc} and FF, probably because of the reduced charge extraction. These results show that devices treated with methyl ethanoate mixed with 30% TCM have slightly better performance immediately after fabrication. Jung et al. [39] have reported a higher

PCE using a similar approach. However, it is difficult to compare directly because the perovskite materials, antisolvents, contact materials, contact deposition method, and laboratory conditions are different.

8.5.4. Device stability

This study investigates how mixing methyl ethanoate and trichloromethane affects the stability of PSCs prepared in ambient air. The J-V parameters of the devices were measured after 0, 216, 360 and 552 hours of storage in a desiccator. The devices' Voc, Jsc, FF and PCE were determined from the J-V data. Figures 8.17(a)–8.17(d) present the devices' normalised V_{oc}, J_{sc}, FF and PCE as a function of TCM proportion in the methyl ethanoate. Figure 8.17(a) shows that the V_{oc} remains virtually unchanged after 552 hours of storage for all devices. The V_{oc} remained stable for all the PSCs, probably because the work function of both FTO substrates and the Ag contacts did not change after degradation [93]. However, there is no available data to confirm this assumption.

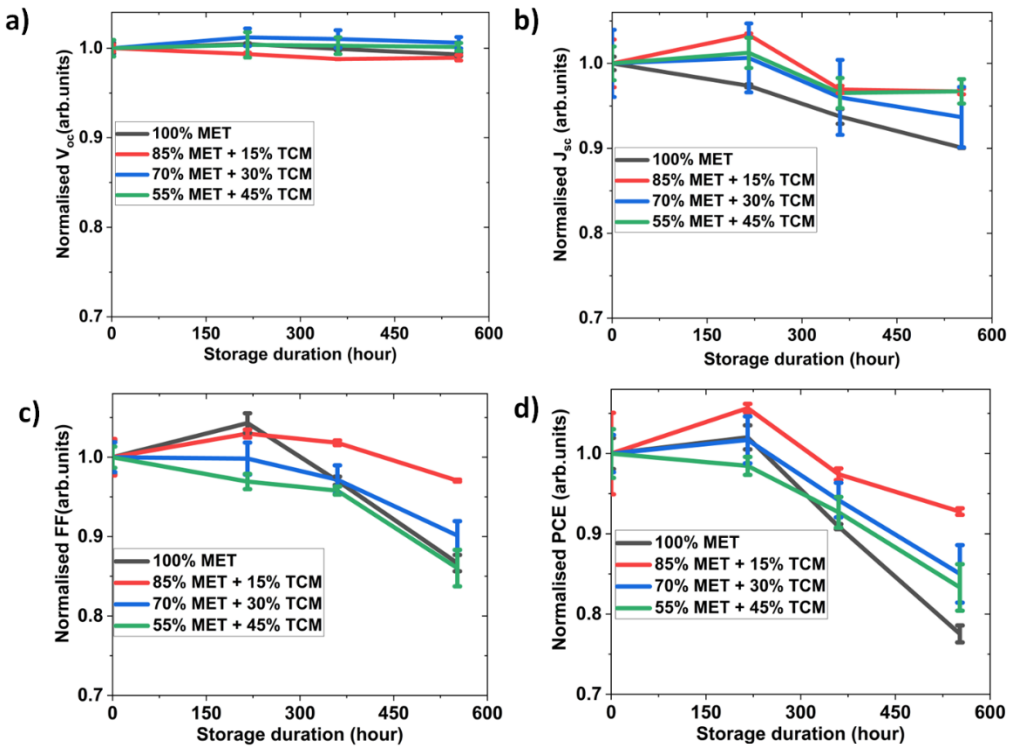

Figure 8.17: Normalised (a) V_{oc}, (b) J_{sc}, (c) FF, and (d) PCE as a function of storage duration for the devices treated with methyl ethanoate mixed with different proportions of trichloromethane.

In contrast, Figure 8.17(b) shows that J_{sc} decreases with time for all devices. However, the devices treated with the mixed antisolvents degraded more slowly than those treated with the methyl ethanoate (100%). The J_{sc} of the devices treated with methyl ethanoate (100%) degraded by about 10% after 552 hours. Conversely, PSCs treated with methyl ethanoate mixed with 15%, 30% and 45% trichloromethane deteriorated only by 3%, 6% and 4%, respectively. Figure 8.17(c) shows that the device treated with methyl ethanoate (85%) mixed with trichloromethane (15%) suffered the least FF degradation of 3%, while devices treated with methyl ethanoate (100%) degraded most by 13%. The devices treated using methyl ethanoate mixed with 30% and 45% trichloromethane show 10% and 14% FF degradation, respectively. Figure 8.17(d) shows that the device treated with methyl ethanoate (100%) has the worst PCE stability, with a degradation of 22% after 552 hours. In comparison, PSCs treated with methyl ethanoate mixed with 15% trichloromethane suffered PCE degradation of 7%. The results also show that the devices treated with methyl ethanoate mixed with 30% and 45% trichloromethane degraded by 15% and 17%, respectively. These results demonstrate that all the devices treated with methyl ethanoate mixed with trichloromethane have improved stability over devices treated with methyl ethanoate (100%). Consequently, devices treated with methyl ethanoate (85%) mixed with trichloromethane (15%) exhibit the most improved stability. These results demonstrate a clear correlation between stability and surface smoothness. The study also reveals that the degradation of perovskite solar cells is associated with the decomposition of $MAPbI_3$ films. Therefore, using appropriate antisolvent mixtures for treatment could mitigate the deterioration. Note: the stability data for the devices treated with methyl ethanoate mixed with 60% trichloromethane was not available as explained in section 8.5.2.

8.6. Summary

This chapter investigated the effects of antisolvent treatments on the efficiency and stability of perovskite solar cells prepared in ambient air. The study on how the volume of methyl ethanoate affects the performance of devices showed that devices based on films treated with 150 µl methyl ethanoate have the best efficiency. Investigation into applying CBZ, TCM, MET, and MBZ antisolvents in PSCs indicated that devices based on films treated with MET exhibited the best efficiency and stability. In contrast, devices treated with MBZ demonstrated the worst device performance. Finally, the study also

showed that devices based on films treated with methyl ethanoate (70%) mixed with trichloromethane (30%) have the best efficiency. In comparison, devices treated with methyl ethanoate (85%) mixed with trichloromethane (15%) demonstrated the best stability. These studies provide a valuable guide in applying antisolvents for fabricating perovskite solar cells in the air.

Chapter 9: Conclusions and future work

9.1. Conclusions

This project represents the first attempt at Cardiff University to fabricate perovskite solar cells. It involves establishing laboratory facilities and developing fabrication processes specifically for perovskite solar cell fabrication in ambient air at high relative humidity, which has low-cost and large-scale fabrication applications. An efficiency of 18.55% was achieved, which is comparable with the highest efficiency of perovskite solar cells fabricated in the air. This outcome was achieved through a series of systematic investigations of the effects of fabrication parameters on the performance of perovskite solar cells, which include silver contact sputtering parameters, chlorodimethyl(pentafluorophenyl)silane additive, methyl ethanoate volume, different antisolvents and mixed antisolvent of methyl ethanoate and trichloromethane. The major findings of this research project are summarised as follows:

1. Preliminary studies were conducted to determine how components and preparation processes affect the performance of air-fabricated perovskite solar cells with sputtered silver contact. The results suggest that the sputtering power of silver contact has the most significant impact on the PCE of perovskite solar cells. It was also noted that the choice of FTO glass, annealing temperature and process of SnO_2 and $MAPbI_3$ significantly influence the efficiency of PSCs. This work established the benchmark components and procedures for preparing perovskite solar cells in main studies.

2. A study investigated the effect of solution parameters on the efficiency of perovskite solar cells prepared at high relative humidity. The results suggested that using 15 mg/ml of $SnO_2.2H_2O$, 1.5 M of $MAPbI_3$ and 90 mg/ml of Spiro-OMETAD modified with 38 µl of FK209 solution (300 mg/1ml of ethane nitrile) is an appropriate combination for obtaining efficient devices. This combination achieved a power conversion efficiency of 17.54%. The work established a benchmark and provided a foundation for further optimisation study and improvement.

3. A systematic investigation was performed to determine the optimum parameters for depositing Ag contacts using magnetron sputtering for preparing efficient perovskite solar cells. The results show that the best power conversion efficiency of 18.40% was obtained using a sputtering power of 1.0 W, an argon flow rate of 15sccm, a sputtering duration of 40 minutes and an argon pressure of 5mTorr. The results also showed that selecting appropriate sputtering power is the most crucial factor in Ag contact deposition to minimise possible damage to HTL layers. This work demonstrates that magnetron sputtering can be employed to prepare the Ag contacts of perovskite solar cells if appropriate sputtering parameters are identified and applied.

4. A novel chlorodimethyl (pentafluorophenyl)silane additive process was developed for preparing efficient and stable perovskite solar cells in the air at high relative humidity. The results demonstrate reasonable efficiency and stability for perovskite solar cells prepared from $MAPbI_3$ films modified with chlorodimethyl (pentafluorophenyl)silane. Hence, devices based on films modified with 3 µl of chlorodimethyl (pentafluorophenyl)silane exhibited a power conversion efficiency of 17.82%, compared to 18.07% achieved for control devices. Furthermore, **t**he results indicate that devices modified with 3 µl of chlorodimethyl (pentafluorophenyl)silane have the best photovoltaic stability after 1350 hours of storage. Consequently, power conversion efficiency, short-current density, and fill factor of the devices modified with 3 µl of chlorodimethyl (pentafluorophenyl)silane degraded by about 23%, 9% and 15%, respectively, relative to degradation of 33%, 11% and 22% achieved for control devices. The results also revealed that the open-circuit voltage of the devices remains virtually unchanged and appeared independent of the chlorodimethyl (pentafluorophenyl)silane modification. The study also indicated that the average absorbance of $MAPbI_3$ films modified with chlorodimethyl (pentafluorophenyl)silane degraded by about 1.13% compared to 7.61% degradation for control films after 840 hours of storage. These results demonstrate the benefits of this new chlorodimethyl (pentafluorophenyl)silane-modified process for preparing high-quality perovskite films at high relative humidity and uncontrolled atmosphere, relevant low-cost and large-scale manufacturing.

5. An investigation was conducted on the effect of the volume of methyl ethanoate antisolvent on the power conversion efficiency of perovskite solar cells prepared in the air. The results show that the films treated with 100 or 150 µl of methyl ethanoate have low surface roughness, while those treated with 80 µl appeared rough. Furthermore, the photovoltaic characteristic indicated that devices treated with 150 µl of methyl ethanoate achieved the best power conversion efficiency. Hence, devices treated with 150 µl of methyl ethanoate achieved the best power conversion efficiency of 16.82%. These results demonstrate that treating devices with 150 µl of methyl ethanoate achieves quality perovskite films and efficient devices in ambient air, which is relevant for low-cost and large-scale manufacturing.

6. A study was conducted on the effect of chlorobenzene, trichloromethane, methyl ethanoate and methylbenzene antisolvents on the stability and power conversion efficiency of perovskite solar cells prepared at 40-43% relative humidity. The results show that perovskite films treated with either trichloromethane or methyl ethanoate have low surface roughness, while films treated with methylbenzene appeared rough. As a result, devices treated with methyl ethanoate or trichloromethane have improved efficiency and stability at moderately high relative humidity. Hence, devices treated with methyl ethanoate and trichloromethane achieved the best power conversion efficiency of 18.10% and 17.42%, respectively. In contrast, devices treated with chlorobenzene and methylbenzene achieved PCE of 16.80% and 12.37% in ambient air. Results also show that devices treated with methyl ethanoate and trichloromethane suffered PCE degradation of 16% and 25% after 864 hours of storage compared to the degradation of 51% and 80% achieved from devices treated with chlorobenzene and methylbenzene, respectively. These results demonstrate the effectiveness of methyl ethanoate and trichloromethane antisolvents in preparing high-quality perovskite films at high relative humidity.

7. This study developed a new mixed methyl ethanoate/trichloromethane antisolvent process for fabricating high-quality perovskite films at high relative humidity (> 50%). It chose methyl ethanoate and trichloromethane for this investigation because it has high water solubility and vapour pressure, facilitating moisture extraction around the films in a high-humidity environment. Furthermore, trichloromethane was selected because it has a relatively low dipole moment that enables adjustment of the solubility of DMSO in the mixed antisolvent when mixed with methyl ethanoate. As a result, this new mixed antisolvent process could enhance the efficiency and stability of the perovskite solar cells fabricated at high relative humidity. The results show that the surface roughness of the perovskite films was significantly improved when methyl ethanoate and trichloromethane were mixed in appropriate proportions. The devices treated with methyl ethanoate (70%) mixed with trichloromethane (30%) exhibit the best PCE of 18.55% compared to 17.13% for those treated with methyl ethanoate only. In addition, devices treated with the methyl ethanoate (85%) mixed with trichloromethane (15%) suffered slow PCE degradation of 7% after 552 hours of storage, compared to PCE degradation of 22% for the devices treated with methyl ethanoate only. These results demonstrate the usefulness and benefits of this new mixed antisolvent for fabricating high-quality perovskite films at high relative humidity, paving the way for low-cost manufacturing that does not require a controlled atmosphere.

9.2. Future work

These studies demonstrated that highly efficient perovskite solar cells could be prepared by selecting suitable solution parameters for solution-processed layers, optimising magnetron sputtering parameters for depositing metal contacts, and modifying magnetron sputtering parameters for depositing metal contacts perovskite layers with chlorodimethyl(pentafluorophenyl)silane and using mixed methyl ethanoate/ trichloromethane antisolvent. However, future studies still need to address a few research questions. To assist in further investigation, the required aspects of the studies are:

1. To develop an approach for enhancing the conductivity of low-temperature processed tin (IV) oxide films without significantly affecting the transparency of

films. This may facilitate the application of thick tin (IV) oxide films as electron transport layers to enhance smooth surfaces and transmittance.

2. To study the deposition of the metal contacts at high argon pressure. This may facilitate high conductive and smooth metal contact deposition with negligible damage to the organic hole transport layers or hole transport layer/perovskite interface. In addition, contact deposition at high pressure reduces the speed of particles and minimises the damage to the organic layers.

3. To explore the optimum annealing regime for chlorodimethyl (pentafluorophenyl)silane-modified perovskite films. The significant improvement in the efficiency of the devices modified with chlorodimethyl (pentafluorophenyl)silane after a few days suggests an incomplete nucleation process during annealing. Therefore, optimising the annealing temperature and duration may facilitate the preparation of devices with enhanced performance.

4. To explore a more environmentally friendly alternative to trichloromethane in preparing mixed antisolvent for perovskite solar cells preparation. This may facilitate the removal of toxic trichloromethane from the process.

5. To explore degradation pathways in perovskite solar cells using monochromatic efficiency studies. This may facilitate the improvement in the stability of perovskite solar cells.

References

[1] Damle A. An introduction to the utilization of membrane technology in the production of clean and renewable power. Membr. Clean Renew. Power Appl., Woodhead Publishing Limited; 2013, p. 3–43. https://doi.org/10.1533/9780857098658.1.3.

[2] IEA. Global Energy Review 2020. IEA, Paris 2020. https://www.iea.org/reports/global-energy-review-2020.

[3] O'Neill S. Global CO2 Emissions Level Off in 2019, With a Drop Predicted in 2020. Engineering 2020:2019–20. https://doi.org/10.1016/j.eng.2020.07.005.

[4] Liu Z. R&D on Global Energy Interconnection and Practice. Glob Energy Interconnect 2015:273–342. https://doi.org/10.1016/b978-0-12-804405-6.00007-5.

[5] Chapin DM, Fuller CS, Pearson GL. A new silicon p-n junction photocell for converting solar radiation into electrical power [3]. J Appl Phys 1954;25:676–7. https://doi.org/10.1063/1.1721711.

[6] Yoshikawa K, Kawasaki H, Yoshida W, Irie T, Konishi K, Nakano K, et al. Silicon heterojunction solar cell with interdigitated back contacts for a photoconversion efficiency over 26%. Nat Energy 2017;2. https://doi.org/10.1038/nenergy.2017.32.

[7] Sinke WC. Development of photovoltaic technologies for global impact. Renew Energy 2019;138:911–4. https://doi.org/10.1016/j.renene.2019.02.030.

[8] Schachinger M. Module Price Index. PV Mag Int 2019. https://www.pv-magazine.com/features/investors/module-price-index/ (accessed September 12, 2020).

[9] PVinsights. Solar PV Cell Weekly Spot Price. PVinsights 2022. http://pvinsights.com/ (accessed February 4, 2022).

[10] Nayak PK, Mahesh S, Snaith HJ, Cahen D. Photovoltaic solar cell technologies: analysing the state of the art. Nat Rev Mater 2019;4:269–85. https://doi.org/10.1038/s41578-019-0097-0.

[11] Field IE, Bhatia SC. Thin-Film Silicon Photovoltaics Learn more about Thin-Film Silicon Photovoltaics Solar photovoltaic systems Thin-Film Silicon Solar Cells1

2014;m.

[12] Wikipedia. Thin-film solar cell. Wikipedia 2020. https://en.wikipedia.org/wiki/Thin-film_solar_cell (accessed September 12, 2020).

[13] NREL. Best Research-Cell Efficiencies. Natl Renew Energy Lab 2020:1. https://www.nrel.gov/pv/cell-efficiency.html.

[14] Qin X, Zhao Z, Wang Y, Wu J, Jiang Q, You J. Recent progress in stability of perovskite solar cells. J Semicond 2017;38:1–8. https://doi.org/10.1088/1674-4926/38/1/011002.

[15] De Maria A, La Ferrara V, Mercaldo LV, Bobeico E, Di Luccio T, Delli Veneri P. Solution-processed perovskite thin films for planar solar cells under ambient conditions. 18th Ital. Natl. Conf. Photonic Technol. Rome, Italy, 2016, p. 3–6.

[16] Song T, Chen Q, Zhou HH-P, Jiang C, Wang H-H, (Michael) Yang Y, et al. Perovskite solar cells: film formation and properties. J Mater Chem A 2015;3:9032–50. https://doi.org/10.1039/C4TA05246C.

[17] Zhang N, Sun W, Rodrigues SP, Wang K, Gu Z, Wang S, et al. Highly Reproducible Organometallic Halide Perovskite Microdevices based on Top-Down Lithography. Adv Mater 2017;29:9–10. https://doi.org/10.1002/adma.201606205.

[18] Mora-Seró I, Garcia-Belmonte G, Boix PP, Vázquez MA, Bisquert J. Impedance spectroscopy characterisation of highly efficient silicon solar cells under different light illumination intensities. Energy Environ Sci 2009;2:678–86. https://doi.org/10.1039/b812468j.

[19] Yin WJ, Shi T, Yan Y. Unique properties of halide perovskites as possible origins of the superior solar cell performance. Adv Mater 2014;26:4653–8. https://doi.org/10.1002/adma.201306281.

[20] Hutter EM, Gélvez-Rueda MC, Osherov A, Bulović V, Grozema FC, Stranks SD, et al. Direct-indirect character of the bandgap in methylammonium lead iodide perovskite. Nat Mater 2017;16:115–20. https://doi.org/10.1038/nmat4765.

[21] Hodes G, Kamat P V. Understanding the Implication of Carrier Diffusion Length

in Photovoltaic Cells. J Phys Chem Lett 2015;6:4090–2. https://doi.org/10.1021/acs.jpclett.5b02052.

[22] Nelson J. The Physics of Solar Cells. 1st ed. London: Imperial College Press; 2003.

[23] Kojima A, Teshima K, Shirai Y, Miyasaka T. Organometal Halide Perovskites as Visible-Light Sensitizers for Photovoltaic Cells. J Am Chem Soc 2009;131:6050–1. https://doi.org/10.1021/ja809598r.

[24] Yoo JJ, Seo G, Chua MR, Park TG, Lu Y, Rotermund F, et al. Efficient perovskite solar cells via improved carrier management. Nature 2021;590:587–93. https://doi.org/10.1038/s41586-021-03285-w.

[25] Conings B, Drijkoningen J, Gauquelin N, Babayigit A, D'Haen J, D'Olieslaeger L, et al. Intrinsic Thermal Instability of Methylammonium Lead Trihalide Perovskite. Adv Energy Mater 2015;5:1–8. https://doi.org/10.1002/aenm.201500477.

[26] Tai Q, You P, Sang H, Liu Z, Hu C, Chan HLW, et al. Efficient and stable perovskite solar cells prepared in ambient air irrespective of the humidity. Nat Commun 2016;7:1–8. https://doi.org/10.1038/ncomms11105.

[27] Wang Q, Zheng X, Deng Y, Zhao J, Chen Z, Huang J. Stabilizing the α-Phase of CsPbI3Perovskite by Sulfobetaine Zwitterions in One-Step Spin-Coating Films. Joule 2017;1:371–82. https://doi.org/10.1016/j.joule.2017.07.017.

[28] Yi C, Luo J, Meloni S, Boziki A, Ashari-Astani N, Grätzel C, et al. Entropic stabilization of mixed A-cation ABX 3 metal halide perovskites for high performance perovskite solar cells. Energy Environ Sci 2016;9:656–62. https://doi.org/10.1039/C5EE03255E.

[29] Stoumpos CC, Malliakas CD, Kanatzidis MG. Semiconducting tin and lead iodide perovskites with organic cations: Phase transitions, high mobilities, and near-infrared photoluminescent properties. Inorg Chem 2013;52:9019–38. https://doi.org/10.1021/ic401215x.

[30] Gao F, Li C, Qin L, Zhu L, Huang X, Liu H, et al. Enhanced performance of tin halide perovskite solar cell by addition of lead thiocyanate. RSC Adv 2018;8:14025–30. https://doi.org/10.1039/C8RA00809D.

[31] Xiang J, Wang K, Xiang B, Cui X. Sn 2+ —Stabilization in MASnI 3 perovskites by superhalide incorporation. J Chem Phys 2018;148:124111. https://doi.org/10.1063/1.5023737.

[32] Ran C, Xi J, Gao W, Yuan F, Lei T, Jiao B, et al. Bilateral Interface Engineering toward Efficient 2D-3D Bulk Heterojunction Tin Halide Lead-Free Perovskite Solar Cells. ACS Energy Lett 2018;3:713–21. https://doi.org/10.1021/acsenergylett.8b00085.

[33] Noh JH, Im SH, Heo JH, Mandal TN, Seok S Il. Chemical management for colorful, efficient, and stable inorganic-organic hybrid nanostructured solar cells. Nano Lett 2013;13:1764–9. https://doi.org/10.1021/nl400349b.

[34] Troughton J, Hooper K, Watson TM. Humidity resistant fabrication of CH3NH3PbI3perovskite solar cells and modules. Nano Energy 2017;39:60–8. https://doi.org/10.1016/j.nanoen.2017.06.039.

[35] Chen J, Ren J, Li Z, Wang H, Hao Y. Mixed antisolvents assisted treatment of perovskite for photovoltaic device efficiency enhancement. Org Electron Physics, Mater Appl 2018;56:59–67. https://doi.org/10.1016/j.orgel.2018.01.009.

[36] Tu Y, Wu J, He X, Guo P, Luo H, Liu Q, et al. Controlled growth of CH3NH3PbI3films towards efficient perovskite solar cells by varied-stoichiometric intermediate adduct. Appl Surf Sci 2017;403:572–7. https://doi.org/10.1016/j.apsusc.2017.01.240.

[37] Yang F, Kapil G, Zhang P, Hu Z, Kamarudin MA, Ma T, et al. Dependence of Acetate-Based Antisolvents for High Humidity Fabrication of CH3NH3PbI3Perovskite Devices in Ambient Atmosphere. ACS Appl Mater Interfaces 2018;10:16482–9. https://doi.org/10.1021/acsami.8b02554.

[38] Wang F, Ye Z, Sarvari H, Park SM, Abtahi A, Graham K, et al. Humidity-insensitive fabrication of efficient perovskite solar cells in ambient air. J Power Sources 2019;412:359–65. https://doi.org/10.1016/j.jpowsour.2018.11.013.

[39] Jung K, Oh K, Kim DH, Choi JW, Kim KC, Lee MJ. Ambient-air fabrication of stable mixed cation perovskite planar solar cells with efficiencies exceeding 22% using a synergistic mixed antisolvent with complementary properties. Nano Energy 2021;89:106387. https://doi.org/10.1016/j.nanoen.2021.106387.

[40] Chen P, Bai Y, Wang S, Lyu M, Yun J-H, Wang L. In Situ Growth of 2D Perovskite Capping Layer for Stable and Efficient Perovskite Solar Cells. Adv Funct Mater 2018;1706923:1706923. https://doi.org/10.1002/adfm.201706923.

[41] Cai Y, Wang S, Sun M, Li X, Xiao Y. Mixed cations and mixed halide perovskite solar cell with lead thiocyanate additive for high efficiency and long-term moisture stability. Org Electron 2018;53:249–55. https://doi.org/10.1016/j.orgel.2017.11.045.

[42] Hsiao K-C, Jao M-H, Li B-T, Lin T-H, Liao SH-C, Wu M-C, et al. Enhancing Efficiency and Stability of Hot Casting p–i–n Perovskite Solar Cell via Dipolar Ion Passivation. ACS Appl Energy Mater 2019;2:4821–32. https://doi.org/10.1021/acsaem.9b00486.

[43] Oku T, Nomura J, Suzuki A, Tanaka H, Fukunishi S, Minami S, et al. Fabrication and characterization of CH 3 NH 3 PbI 3 perovskite solar cells added with polysilanes. Int J Photoenergy 2018;2018. https://doi.org/10.1155/2018/8654963.

[44] Zheng R, Zhao S, Zhang H, Li H, Zhuang J, Liu X, et al. Defect passivation grain boundaries using 3-aminopropyltrimethoxysilane for highly efficient and stable perovskite solar cells. Sol Energy 2021;224:472–9. https://doi.org/10.1016/j.solener.2021.06.001.

[45] Jiang Q, Zhao Y, Zhang X, Yang X, Chen Y, Chu Z, et al. Surface passivation of perovskite film for efficient solar cells. Nat Photonics 2019;13. https://doi.org/10.1038/s41566-019-0398-2.

[46] Noel NK, Abate A, Stranks SD, Parrott ES, Burlakov VM, Goriely A, et al. Enhanced photoluminescence and solar cell performance via Lewis base passivation of organic-inorganic lead halide perovskites. ACS Nano 2014;8:9815–21. https://doi.org/10.1021/nn5036476.

[47] Zhu X, Yang D, Yang R, Yang B, Yang Z, Ren X, et al. Superior stability for perovskite solar cells with 20% efficiency using vacuum co-evaporation. Nanoscale 2017;9:12316–23. https://doi.org/10.1039/c7nr04501h.

[48] Fu Q, Tang X, Huang B, Hu T, Tan L, Chen L, et al. Recent Progress on the Long-Term Stability of Perovskite Solar Cells. Adv Sci 2018;5. https://doi.org/10.1002/advs.201700387.

[49] Xu M, Feng J, Ou XL, Zhang ZY, Zhang YF, Wang HY, et al. Surface Passivation of Perovskite Film by Small Molecule Infiltration for Improved Efficiency of Perovskite Solar Cells. IEEE Photonics J 2016;8:1–7. https://doi.org/10.1109/JPHOT.2016.2608619.

[50] Alidaei M, Izadifard M, Ghazi ME, Roghabadi FA, Ahmadi V. Interfacial defect passivation in CH3NH3PbI3 perovskite solar cells using modifying of hole transport layer. J Mater Sci Mater Electron 2019;0:0. https://doi.org/10.1007/s10854-019-01009-5.

[51] Bai Y, Dong Q, Shao Y, Deng Y, Wang Q, Shen L, et al. Enhancing stability and efficiency of perovskite solar cells with crosslinkable silane-functionalized and doped fullerene. Nat Commun 2016;7:1–9. https://doi.org/10.1038/ncomms12806.

[52] Li Z, Guo J, Li Z, Han W, Ren G, Liu C, et al. Incorporating self-Assembled silane-crosslinked carbon dots into perovskite solar cells to improve efficiency and stability. J Mater Chem A 2020;8:5629–37. https://doi.org/10.1039/d0ta00123f.

[53] Lefler BM, May SJ, Fafarman AT. Role of fluoride and fluorocarbons in enhanced stability and performance of halide perovskites for photovoltaics. Phys Rev Mater 2020;4:1–24. https://doi.org/10.1103/PhysRevMaterials.4.120301.

[54] Li B, Ferguson V, Silva SRP, Zhang W. Defect Engineering toward Highly Efficient and Stable Perovskite Solar Cells. Adv Mater Interfaces 2018;5:1–25. https://doi.org/10.1002/admi.201800326.

[55] Saliba M, Grancini G, Wojciechowski K, Snaith HJ, Abate A, Petrozza A, et al. Supramolecular Halogen Bond Passivation of Organic–Inorganic Halide Perovskite Solar Cells. Nano Lett 2014;14:3247–54. https://doi.org/10.1021/nl500627x.

[56] Stewart RJ, Grieco C, Larsen A V., Doucette GS, Asbury JB. Molecular Origins of Defects in Organohalide Perovskites and Their Influence on Charge Carrier Dynamics. J Phys Chem C 2016;120:12392–402. https://doi.org/10.1021/acs.jpcc.6b03472.

[57] Zhao S, Qin M, Xiang Y, Wang H, Xie J, Gong L, et al. Bifunctional Effects of Trichloro(octyl)silane Modification on the Performance and Stability of a Perovskite Solar Cell via Microscopic Characterization Techniques. ACS Appl

Energy Mater 2020;3:3302–9. https://doi.org/10.1021/acsaem.9b02306.

[58] Mo Y, Shi J, Zhou P, Li S, Bu T, Cheng Y-B, et al. Efficient Planar Perovskite Solar Cells via a Sputtered Cathode. Sol RRL 2019;3:1900209. https://doi.org/10.1002/solr.201900209.

[59] Baudet E, Sergent M, Němec P, Cardinaud C, Rinnert E, Michel K, et al. Experimental design approach for deposition optimization of RF sputtered chalcogenide thin films devoted to environmental optical sensors. Sci Rep 2017;7:1–14. https://doi.org/10.1038/s41598-017-03678-w.

[60] Benetti D, Nouar R, Nechache R, Pepin H, Sarkissian A, Rosei F, et al. Combined magnetron sputtering and pulsed laser deposition of TiO2 and BFCO thin films. Sci Rep 2017;7:2–10. https://doi.org/10.1038/s41598-017-02284-0.

[61] Wahl T, Hanisch J, Ahlswede E. Comparison of the Al back contact deposited by sputtering, e-beam, or thermal evaporation for inverted perovskite solar cells. J Phys D Appl Phys 2018;51. https://doi.org/10.1088/1361-6463/aab0d8.

[62] Wang L, Li GR, Zhao Q, Gao XP. Non-precious transition metals as counter electrode of perovskite solar cells. Energy Storage Mater 2017;7:40–7. https://doi.org/10.1016/j.ensm.2016.11.007.

[63] Behrouznejad F, Shahbazi S, Taghavinia N, Wu H, Diau EW. A study on utilizing different metals as the back contact of CH3NH3PbI3 perovskite solar cells. J Mater Chem A 2016;4:13488–98. https://doi.org/10.1039/c6ta05938d.

[64] Yang S, Yu Y, Ni Z, Lei L, Li M, Wei Q, et al. Influence of hole transport material/metal contact interface on perovskite solar cells. Nanotechnology 2018;29:255201. https://doi.org/10.1088/1361-6528/aab795.

[65] Jeong I, Jin Kim H, Lee BS, Jung Son H, Young Kim J, Lee DK, et al. Highly efficient perovskite solar cells based on mechanically durable molybdenum cathode. Nano Energy 2015;17:131–9. https://doi.org/10.1016/j.nanoen.2015.07.025.

[66] Jiang Q, Sheng X, Shi B, Feng X, Xu T. Nickel-Cathoded Perovskite Solar Cells. J Phys Chem C 2014;118:25878–83. https://doi.org/10.1021/jp506991x.

[67] Towler BF. Solar Power. Power Gener. Technol. 3rd ed., 2019, p. 296.

https://doi.org/10.1016/B978-0-08-102631-1.00013-4.

[68] Madhumitha Jaganmohan. projected global energy consumption by source. Statista 2021. https://www.statista.com/statistics/222066/projected-global-energy-consumption-by-source/.

[69] Graetzel M, Janssen RAJ, Mitzi DB, Sargent EH. Materials interface engineering for solution-processed photovoltaics. Nature 2012;488:304–12. https://doi.org/10.1038/nature11476.

[70] SERI, Hersch P, Zweibel K. Basic photovoltaic principles and methods. 1982. https://doi.org/10.2172/5191389.

[71] Park N-GG, Grätzel M, Miyasaka T. Organic-inorganic halide perovskite photovoltaics: From fundamentals to device architectures. Org Halide Perovskite Photovoltaics From Fundam to Device Archit 2016:1–366. https://doi.org/10.1007/978-3-319-35114-8.

[72] Backus CE. Solar Cells. 1st ed. New York: 1976.

[73] Rühle S. Tabulated values of the Shockley-Queisser limit for single junction solar cells. Sol Energy 2016;130:139–47. https://doi.org/10.1016/j.solener.2016.02.015.

[74] Philipps SP, Dimroth F, Bett AW. High-Efficiency III-V Multijunction Solar Cells. Second Edi. Elsevier Ltd; 2013. https://doi.org/10.1016/B978-0-12-386964-7.00012-3.

[75] Liu L, Chen N, Bai Y, Cui M, Zhang H, Gao F, et al. Quantum efficiency and temperature coefficients of GaInP/GaAs dual-junction solar cell. Sci China, Ser E Technol Sci 2009;52:1176–80. https://doi.org/10.1007/s11431-008-0203-9.

[76] Lee MM, Teuscher J, Miyasaka T, Murakami TN, Snaith HJ. Efficient Hybrid Solar Cells Based on Meso-Superstructured Organometal Halide Perovskites. Science (80-) 2012;338:643–7. https://doi.org/10.1109/TMAG.2004.832490.

[77] Esen V, Sağlam Ş, Oral B. Light sources of solar simulators for photovoltaic devices: A review. Renew Sustain Energy Rev 2017;77:1240–50. https://doi.org/10.1016/j.rser.2017.03.062.

[78] Bazzi AM, Klein Z, Sweeney M, Kroeger KP, Shenoy PS, Member S, et al. Solid-State Solar Simulator. IEEE Trans Ind Appl 2012;48:1195–202.

[79] Moshinsky M. What is an air mass 1.5 spectrum. IEEE Conf. Photovolt. Spec., 1990, p. 1085–8.

[80] ASTM. ASTM G173-03 Reference Spectra Derived from SMARTS v. 2.9.2. Am Soc Test Mater 2012. https://www.astm.org/Standards/G173.htm (accessed January 21, 2021).

[81] Thompson BC, Fréchet JMJ. Polymer-fullerene composite solar cells. Org Photovoltaics 2008;47:58–77. https://doi.org/10.1002/anie.200702506.

[82] Hellmann T, Das C, Abzieher T, Schwenzer JA, Wussler M, Dachauer R, et al. The Electronic Structure of MAPI-Based Perovskite Solar Cells: Detailed Band Diagram Determination by Photoemission Spectroscopy Comparing Classical and Inverted Device Stacks. Adv Energy Mater 2020;10. https://doi.org/10.1002/aenm.202002129.

[83] Aram TN, Asgari A, Mayou D. Charge separation in organic solar cells: Effects of Coulomb interaction, recombination and hole propagation. EPL (Europhysics Lett 2016;115:18003. https://doi.org/10.1209/0295-5075/115/18003.

[84] Sassi G. Theoretical analysis of solar cells based on graded band-gap structures. J Appl Phys 1983;54:5421–7. https://doi.org/10.1063/1.332723.

[85] Silvestre S. Strategies for Fault Detection and Diagnosis of PV Systems. Adv. Renew. Energies Power Technol., vol. 1. 1st ed., Elsevier Inc.; 2018, p. 231–55. https://doi.org/10.1016/B978-0-12-812959-3.00007-1.

[86] Rosa-Clot M, Tina GM. Introduction to PV Plants. Submerg. Float. Photovolt. Syst. 1st ed., Academic Press; 2018, p. 33–64. https://doi.org/10.1016/b978-0-12-812149-8.00003-x.

[87] Chin VJ, Salam Z, Ishaque K. Cell modelling and model parameters estimation techniques for photovoltaic simulator application: A review. Appl Energy 2015;154:500–19. https://doi.org/10.1016/j.apenergy.2015.05.035.

[88] Priyanka, Lal M, Singh SN. A new method of determination of series and shunt resistances of silicon solar cells. Sol Energy Mater Sol Cells 2007;91:137–42. https://doi.org/10.1016/j.solmat.2006.07.008.

[89] Subbiah AS, Halder A, Ghosh S, Mahuli N, Hodes G, Sarkar SK. Inorganic hole

conducting layers for perovskite-based solar cells. J Phys Chem Lett 2014;5:1748–53. https://doi.org/10.1021/jz500645n.

[90] Quansah D, Adaramola M, Takyi G, Edwin I. Reliability and Degradation of Solar PV Modules—Case Study of 19-Year-Old Polycrystalline Modules in Ghana. Technologies 2017;5:22. https://doi.org/10.3390/technologies5020022.

[91] Das S, Alford TL. Optimization of the zinc oxide electron transport layer in P3HT:PC61BM based organic solar cells by annealing and yttrium doping. RSC Adv 2015;5:45586–91. https://doi.org/10.1039/C5RA05258K.

[92] Eze MC, Ugwuanyi G, Li M, Eze HU, Rodriguez GM, Evans A, et al. Optimum silver contact sputtering parameters for efficient perovskite solar cell fabrication. Sol Energy Mater Sol Cells 2021;230:111185. https://doi.org/10.1016/j.solmat.2021.111185.

[93] Wu N, Wu Y, Walter D, Shen H, Duong T, Grant D, et al. Identifying the Cause of Voltage and Fill Factor Losses in Perovskite Solar Cells by Using Luminescence Measurements. Energy Technol 2017;5:1827–35. https://doi.org/10.1002/ente.201700374.

[94] Park H, Kim Y, Kim H. PV Cell Model by Single-diode Electrical Equivalent Circuit. J Electr Eng Technol 2016;11:1323–31.

[95] Eze VHU, Iloanusi ON, Eze MC, Osuagwu CC. Maximum power point tracking technique based on optimized adaptive differential conductance. Cogent Eng 2017;4:1–13. https://doi.org/10.1080/23311916.2017.1339336.

[96] Cejer M a, Weng L. Choosing the Optimal Source Measurement Unit Instrument for Your Test and Measurement Application 2012;44139:1–16.

[97] Fonash S. Solar cell device physics. 2nd ed. Burlington: Elsevier Inc.; 2010.

[98] Boix PP, Ajuria J, Etxebarria I, Pacios R, Bisquert J. Role of ZnO Electron-Selective Layers in Regular and Inverted Bulk Heterojunction Solar Cells. J Phys Chem Lett 2011;2:407–11.

[99] Dittrich T. Materials Concepts for Solar Cells. vol. 40. 2015. https://doi.org/10.1557/mrs.2015.134.

[100] Nozik AJ, Luther JM, Law M, Beard MC, Reese MO, Song Q, et al. Schottky Solar

Cells Based on Colloidal Nanocrystal Films. Nano Lett 2008;8:3488–92. https://doi.org/10.1021/nl802476m.

[101] Zhao D, Sexton M, Park HY, Baure G, Nino JC, So F. High-efficiency solution-processed planar perovskite solar cells with a polymer hole transport layer. Adv Energy Mater 2015;5:1–5. https://doi.org/10.1002/aenm.201401855.

[102] Dupré O, Niesen B, De Wolf S, Ballif C. Field Performance versus Standard Test Condition Efficiency of Tandem Solar Cells and the Singular Case of Perovskites/Silicon Devices. J Phys Chem Lett 2018;9:446–58. https://doi.org/10.1021/acs.jpclett.7b02277.

[103] Qi B, Wang J. Fill factor in organic solar cells. Phys Chem Chem Phys 2013;15:8972–82. https://doi.org/10.1039/c3cp51383a.

[104] Pujahari RM. Solar cell technology. Energy Mater. 1st ed., Elsevier Ltd; 2021, p. 27–60. https://doi.org/10.1016/b978-0-12-823710-6.00007-8.

[105] Wu J, Lan Z, Lin J, Huang M, Huang Y, Fan L, et al. Counter electrodes in dye-sensitized solar cells. Chem Soc Rev 2017;46:5975–6023. https://doi.org/10.1039/C6CS00752J.

[106] Lattante S. Electron and Hole Transport Layers: Their Use in Inverted Bulk Heterojunction Polymer Solar Cells. Electronics 2014;3:132–64. https://doi.org/10.3390/electronics3010132.

[107] Fahrenbruch AL, Bube RH. Fundamentals of Solar Cells. New York: Academic Press; 1983.

[108] Da Y, Xuan Y, Li Q. Quantifying energy losses in planar perovskite solar cells. Sol Energy Mater Sol Cells 2018;174:206–13. https://doi.org/10.1016/j.solmat.2017.09.002.

[109] Asghar MI, Zhang J, Wang H, Lund PD. Device stability of perovskite solar cells – A review. Renew Sustain Energy Rev 2017;77:131–46. https://doi.org/10.1016/j.rser.2017.04.003.

[110] Hahn G, Joos S. State-of-the-Art Industrial Crystalline Silicon Solar Cells. Semicond. Semimetals, vol. 90. 1st ed., Elsevier Inc.; 2014, p. 1–72. https://doi.org/10.1016/B978-0-12-388417-6.00005-2.

[111] Shockley W, Queisser H. Detailed balance limit of efficiency of p-n junction solar cells. Renew Energy Four Vol Set 2018;2–4:35–54. https://doi.org/10.4324/9781315793245-44.

[112] Joseph J. Lofersky. Theoretical Considerations Governing the Choice of the Optimum Semiconductor for Photovoltaic Solar Energy Conversion. J Appl Phys 1956;777.

[113] Eperon GE, Stranks SD, Menelaou C, Johnston MB, Herz LM, Snaith HJ. Formamidinium lead trihalide: a broadly tunable perovskite for efficient planar heterojunction solar cells. Energy Environ Sci 2014;7:982. https://doi.org/10.1039/c3ee43822h.

[114] Green MA. Self-consistent optical parameters of intrinsic silicon at 300 K including temperature coefficients. Sol Energy Mater Sol Cells 2008;92:1305–10. https://doi.org/10.1016/j.solmat.2008.06.009.

[115] Wen Y, Tang YG, Yan GQ. Large grain size CH3NH3PbI3 film for perovskite solar cells with hydroic acid additive. AIP Adv 2018;8. https://doi.org/10.1063/1.5048424.

[116] Sidhik S, Pasarán AC, Rosiles Pérez C, López-Luke T, De La Rosa E. Modulating the grain size, phase and optoelectronic quality of perovskite films with cesium iodide for high-performance solar cells. J Mater Chem C 2018;6:7880–9. https://doi.org/10.1039/c8tc02923g.

[117] Ellingson RJ, Almutawah ZS, Yan Y, Watthage SC, Subedi KK, Ahangharnejhad RH, et al. Enhanced Grain Size and Crystallinity in CH3NH3PbI3 Perovskite Films by Metal Additives to the Single-Step Solution Fabrication Process. MRS Adv 2018;3:3237–42. https://doi.org/10.1557/adv.2018.413.

[118] Adachi S. Optical dispersion relations for GaP, GaAs, GaSb, InP, InAs, InSb, Al xGa1-xAs, and In1-xGaxAs yP1-y. J Appl Phys 1989;66:6030–40. https://doi.org/10.1063/1.343580.

[119] Treharne RE, Seymour-Pierce A, Durose K, Hutchings K, Roncallo S, Lane D. Optical design and fabrication of fully sputtered CdTe/CdS solar cells. J Phys Conf Ser 2011;286. https://doi.org/10.1088/1742-6596/286/1/012038.

[120] Phillips LJ, Rashed AM, Treharne RE, Kay J, Yates P, Mitrovic IZ, et al.

Dispersion relation data for methylammonium lead triiodide perovskite deposited on a (100) silicon wafer using a two-step vapour-phase reaction process. Data Br 2015;5:926–8. https://doi.org/10.1016/j.dib.2015.10.026.

[121] Stelling C, Singh CR, Karg M, König TAF, Thelakkat M, Retsch M. Plasmonic nanomeshes: Their ambivalent role as transparent electrodes in organic solar cells. Sci Rep 2017;7:1–13. https://doi.org/10.1038/srep42530.

[122] Frick JJ, Kushwaha SK, Cava RJ, Bocarsly AB. Characterization of Primary Carrier Transport Properties of the Light-Harvesting Chalcopyrite Semiconductors CuIn(S1-xSex)2. J Phys Chem C 2017;121:17046–52. https://doi.org/10.1021/acs.jpcc.7b03152.

[123] Poncé S, Li W, Reichardt S, Giustino F. First-principles calculations of charge carrier mobility and conductivity in bulk semiconductors and two-dimensional materials. Reports Prog Phys 2020;83. https://doi.org/10.1088/1361-6633/ab6a43.

[124] Li D, Sun F, Liang C, He Z. Effective approach for reducing the migration of ions and improving the stability of organic-inorganic perovskite solar cells. J Alloys Compd 2018;741:489–94. https://doi.org/10.1016/j.jallcom.2018.01.082.

[125] Quan LN, Yuan M, Comin R, Voznyy O, Beauregard EM, Hoogland S, et al. Ligand-Stabilized Reduced-Dimensionality Perovskites. J Am Chem Soc 2016;138:2649–55. https://doi.org/10.1021/jacs.5b11740.

[126] Park N-G, Grätzel M, Miyasaka T, Zhu K, Emery K. Towards stable and commercially available perovskite solar cells. Nat Energy 2016;1:16152. https://doi.org/10.1038/nenergy.2016.152.

[127] Lee JC, Chai J Da, Lin ST. Assessment of density functional methods for exciton binding energies and related optoelectronic properties. RSC Adv 2015;5:101370–6. https://doi.org/10.1039/c5ra20085g.

[128] Shen Y, Gupta MC. Investigation of electrical characteristics of P3HT:PCBM organic solar cells. Conf Rec IEEE Photovolt Spec Conf 2012:2770–4. https://doi.org/10.1109/PVSC.2012.6318167.

[129] Tsybeskov L. Nanocrystalline Silicon for Optoelectronic Applications. MRS Bull 1998:33–8.

[130] Lin ZH, Wang TY, Stringfellow GB, Taylor PC. Exciton binding energies in GaInAs/InP quantum wells determined by thermally modulated photoluminescence. Appl Phys Lett 1988;52:1590–2. https://doi.org/10.1063/1.99090.

[131] Baranowski M, Plochocka P. Excitons in Metal-Halide Perovskites. Adv Energy Mater 2020;10. https://doi.org/10.1002/aenm.201903659.

[132] Kane SN, Mishra A, Dutta AK. Preface: International Conference on Recent Trends in Physics (ICRTP 2016). J Phys Conf Ser 2016;755. https://doi.org/10.1088/1742-6596/755/1/011001.

[133] Strzałkowski K, Zakrzewski J, Maliński M. Determination of the exciton binding energy using photothermal and photoluminescence spectroscopy. Int J Thermophys 2013;34:691–700. https://doi.org/10.1007/s10765-012-1382-y.

[134] Franco R. The binding energy of light excitons in spherical quantum dots under hydrostatic pressure 2007;53:189–93.

[135] Schubert EF. LED basics : Electrical properties. Light. diodes, 2012, p. 59–85.

[136] Wurfel U, Cuevas A, Wurfel P. Charge carrier separation in solar cells. IEEE J Photovoltaics 2015;5:461–9. https://doi.org/10.1109/JPHOTOV.2014.2363550.

[137] Chen Y, Wu W, Ma R, Wang C. Perovskites fabricated with volatile anti-solvents for more efficient solar cells. J Mol Struct 2018;1175:632–7. https://doi.org/10.1016/J.MOLSTRUC.2018.08.021.

[138] He R, Huang X, Chee M, Hao F, Dong P. Carbon-based perovskite solar cells: From single-junction to modules. Carbon Energy 2019;1:109–23. https://doi.org/10.1002/cey2.11.

[139] Thambidurai M, Foo S, Muhammed Salim KM, Harikesh PC, Bruno A, Jamaludin NF, et al. Improved photovoltaic performance of triple-cation mixed-halide perovskite solar cells with binary trivalent metals incorporated into the titanium dioxide electron transport layer. J Mater Chem C 2019;7:5028–36. https://doi.org/10.1039/c9tc00555b.

[140] Meng L, You J, Guo T, Yang Y. Recent Advances in the Inverted Planar Structure of Perovskite Solar Cells 2016. https://doi.org/10.1021/acs.accounts.5b00404.

[141] Saleheen M, Arnab SM, Kabir MZ. Analytical model for voltage-dependent photo and dark currents in bulk heterojunction organic solar cells. Energies 2016;9. https://doi.org/10.3390/en9060412.

[142] Heo JH, Han HJ, Kim D, Ahn TK, Im SH. Hysteresis-less inverted CH 3 NH 3 PbI 3 planar perovskite hybrid solar cells with 18.1% power conversion efficiency. Energy Environ Sci 2015;8:1602–8. https://doi.org/10.1039/C5EE00120J.

[143] Shi LX, Wang ZS, Huang Z, Sha WEI, Wang H, Zhou Z. The effects of interfacial recombination and injection barrier on the electrical characteristics of perovskite solar cells. AIP Adv 2018;8:1–19. https://doi.org/10.1063/1.5021293.

[144] Yan W, Li Y, Li Y, Ye S, Liu Z, Wang S, et al. High-performance hybrid perovskite solar cells with open circuit voltage dependence on hole-transporting materials. Nano Energy 2015;16:428–37. https://doi.org/10.1016/j.nanoen.2015.07.024.

[145] Hill IG, Kahn A. Energy level alignment at interfaces of organic semiconductor heterostructures. J Appl Phys 1998;84:5583. https://doi.org/10.1063/1.368864.

[146] Yang WS, Park B, Jung EH, Jeon NJ. Iodide management in formamidinium-lead-halide – based perovskite layers for efficient solar cells. Science (80-) 2017;356:1376–9. https://doi.org/10.1126/science.aan2301.

[147] Sha WEI, Ren X, Chen L, Choy WCH. The efficiency limit of CH3NH3 PbI3 perovskite solar cells. Appl Phys Lett 2015;106:221104. https://doi.org/10.1063/1.4922150.

[148] Jeong M, Choi IW, Go EM, Cho Y, Kim M, Lee B, et al. Stable perovskite solar cells with efficiency exceeding 24.8% and 0.3-V voltage loss. Science (80-) 2020;369:1615–20.

[149] Min H, Lee DY, Kim J, Kim G, Lee KS, Kim J, et al. Perovskite solar cells with atomically coherent interlayers on SnO2 electrodes. Nature 2021;598:444–50. https://doi.org/10.1038/s41586-021-03964-8.

[150] Im JH, Lee CR, Lee JW, Park SW, Park NG. 6.5% Efficient Perovskite Quantum-Dot-Sensitized Solar Cell. Nanoscale 2011;3:4088–93. https://doi.org/10.1039/c1nr10867k.

[151] Jeon NJ, Na H, Jung EH, Yang TY, Lee YG, Kim G, et al. A fluorene-terminated hole-transporting material for highly efficient and stable perovskite solar cells. Nat Energy 2018;3:682–9. https://doi.org/10.1038/s41560-018-0200-6.

[152] Burschka J, Pellet N, Moon SJ, Humphry-Baker R, Gao P, Nazeeruddin MK, et al. Sequential deposition as a route to high-performance perovskite-sensitized solar cells. Nature 2013;499:316–9. https://doi.org/10.1038/nature12340.

[153] Nicholson B, Verma S, Med P, S S. Interface engineering of highly efficient perovskite solar cells. Science (80-) 2014;345:542–6.

[154] Noller HF, Fredrick K, Ippolito JA, Ban N, Moore PB, Steitz TA, et al. Efficient Hybrid Solar Cells Based on Meso-Superstructured Organometal Halide Perovskites. Science (80-) 2012;338:643–7.

[155] Yang WS, Noh JH, Jeon NJ, Kim YC, Ryu S, Seo J, et al. High-performance photovoltaic perovskite layers fabricated through intramolecular exchange. Science (80-) 2015;348:1234–7. https://doi.org/10.1126/science.aaa9272.

[156] Saliba M, Matsui T, Seo J-YY, Domanski K, Correa-Baena J-PP, Nazeeruddin MK, et al. Cesium-containing triple cation perovskite solar cells: improved stability, reproducibility and high efficiency. Energy Environ Sci 2016;9:1989–97. https://doi.org/10.1039/C5EE03874J.

[157] Watson BL, Rolston N, Bush KA, Leijtens T, McGehee MD, Dauskardt RH. Cross-Linkable, Solvent-Resistant Fullerene Contacts for Robust and Efficient Perovskite Solar Cells with Increased J SC and V OC. ACS Appl Mater Interfaces 2016;8:25896–904. https://doi.org/10.1021/acsami.6b06164.

[158] Zhu Y, Deng K, Sun H, Gu B, Lu H, Cao F, et al. TiO $_2$ Phase Junction Electron Transport Layer Boosts Efficiency of Planar Perovskite Solar Cells. Adv Sci 2018;1700614:1700614. https://doi.org/10.1002/advs.201700614.

[159] Wahid S, Islam M, Rahman MSS, Alam MK. Transfer Matrix Formalism-Based Analytical Modeling and Performance Evaluation of Perovskite Solar Cells. IEEE Trans Electron Devices 2017;64:5034–41. https://doi.org/10.1109/TED.2017.2763091.

[160] Tiwana P, Docampo P, Johnston MB, Snaith HJ, Herz LM. Electron mobility and injection dynamics in mesoporous ZnO, SnO 2, and TiO 2

films used in dye-sensitized solar cells. ACS Nano 2011;5:5158–66. https://doi.org/10.1021/nn201243y.

[161] Zhou Y, Xu W, Li J, Yin C, Liu Y, Zhao B, et al. Vacancy defects and optoelectrical properties for fluorine tin oxide thin films with various SnF 2 contents. J Appl Phys 2018;123:025706. https://doi.org/10.1063/1.5004209.

[162] Swallow JEN, Williamson BAD, Whittles TJ, Birkett M, Featherstone TJ, Peng N, et al. Self-Compensation in Transparent Conducting F-Doped SnO2. Adv Funct Mater 2017;1701900:1–10. https://doi.org/10.1002/adfm.201701900.

[163] Andersson A, Johansson N, Broms P, Yu N, Lupo D, Salaneck WR. Fluorine tin oxide as an alternative to indium tin oxide in polymer LEDs. Adv Mater 1998;10:859–63. https://doi.org/10.1002/(SICI)1521-4095(199808)10:11<859::AID-ADMA859>3.0.CO;2-1.

[164] Kumar MH, Yantara N, Dharani S, Graetzel M, Mhaisalkar S, Boix PP, et al. Flexible, low-temperature, solution processed ZnO-based perovskite solid state solar cells. Chem Commun 2013;49:11089. https://doi.org/10.1039/c3cc46534a.

[165] Hamasha MM, Dhakal T, Alzoubi K, Albahri S, Qasaimeh A, Lu S, et al. Stability of ITO thin film on flexible substrate under thermal aging and thermal cycling conditions. IEEE/OSA J Disp Technol 2012;8:383–8. https://doi.org/10.1109/JDT.2011.2176532.

[166] Kalyanasundaram K. Dye-Sensitized Solar Cell. 1st ed. Boca Raton: CRC Press; 2010.

[167] Sigma-Aldrich. Fluorine-doped Tin Oxide (FTO) Glass 2018.

[168] TEC15 FTO substrate, TEC 15 glass, Fluorine Doped Tin Oxide (FTO) coated TEC 15 Glass (2.2 mm) n.d.

[169] Technical Datasheet (TDS) FTO COATED GLASS SLIDES n.d.:440026. https://shilpent.com/conductive-glass/21-fto-coated-glass.html (accessed December 27, 2021).

[170] Li W, Zhang W, Van Reenen S, Sutton RJ, Fan J, Haghighirad AA, et al. Enhanced UV-light stability of planar heterojunction perovskite solar cells with caesium bromide interface modification. Energy Environ Sci 2016;9:490–8.

https://doi.org/10.1039/C5EE03522H.

[171] Scanlon DO, Dunnill CW, Buckeridge J, Shevlin SA, Logsdail AJ, Woodley SM, et al. Band alignment of rutile and anatase TiO2. Nat Mater 2013;12:798–801. https://doi.org/10.1038/nmat3697.

[172] Jeon NJ, Noh JH, Yang WS, Kim YC, Ryu S, Seo J, et al. Compositional engineering of perovskite materials for high-performance solar cells. Nature 2015;517:476–80. https://doi.org/10.1038/nature14133.

[173] Ke W, Fang G, Wan J, Tao H, Liu Q, Xiong L, et al. Efficient hole-blocking layer-free planar halide perovskite thin-film solar cells. Nat Commun 2015;6:1–7. https://doi.org/10.1038/ncomms7700.

[174] Li L, Xu C, Zhao Y, Chen S, Ziegler KJ. Improving Performance via Blocking Layers in Dye-Sensitized Solar Cells Based on Nanowire Photoanodes. ACS Appl Mater Interfaces 2015;7:12824–31. https://doi.org/10.1021/acsami.5b02041.

[175] Zheng L, Ma Y, Wang Y, Xiao L, Zhang F, Yang H. Hole Blocking Layer-Free Perovskite Solar Cells with over 15% Efficiency. Energy Procedia 2017;105:188–93. https://doi.org/10.1016/j.egypro.2017.03.300.

[176] Womack G, Kaminski PM, Walls JM. Optical optimization of high resistance transparent layers in thin film cadmium telluride solar cells. Vacuum 2017;139:196–201. https://doi.org/10.1016/j.vacuum.2016.11.031.

[177] Conibeer GJ, Willoughby A. Solar Cell Materials: Developing Technologies. John Wiley & Sons; 2014.

[178] Qin M, Ma J, Ke W, Qin P, Lei H, Tao H, et al. Perovskite Solar Cells Based on Low-Temperature Processed Indium Oxide Electron Selective Layers. ACS Appl Mater Interfaces 2016;8:8460–6. https://doi.org/10.1021/acsami.5b12849.

[179] Hwang I, Yong K. Novel CdS Hole-Blocking Layer for Photostable Perovskite Solar Cells. ACS Appl Mater Interfaces 2016;8:4226–32. https://doi.org/10.1021/acsami.5b12336.

[180] Ke W, Fang G, Liu Q, Xiong L, Qin P, Tao H, et al. Low-temperature solution-processed tin oxide as an alternative electron transporting layer for efficient perovskite solar cells. J Am Chem Soc 2015;137:6730–3.

https://doi.org/10.1021/jacs.5b01994.

[181] Liu D, Kelly TL. Perovskite solar cells with a planar heterojunction structure prepared using room-temperature solution processing techniques. Nat Photonics 2014;8:133–8. https://doi.org/10.1038/nphoton.2013.342.

[182] Jiang Q, Zhang L, Wang H, Yang X, Meng J, Liu H, et al. Enhanced electron extraction using SnO2 for high-efficiency planar-structure HC(NH2)2PbI3-based perovskite solar cells. Nat Energy 2016;2:16177. https://doi.org/10.1038/nenergy.2016.177.

[183] Wang P, Shao Z, Ulfa M, Pauporté T. Insights into the Hole Blocking Layer Effect on the Perovskite Solar Cell Performance and Impedance Response. J Phys Chem C 2017;121:9131–41. https://doi.org/10.1021/acs.jpcc.7b00979.

[184] Ranjan R, Prakash A, Singh AA, Singh AA, Garg A, Gupta RK. Effect of tantalum doping in a TiO_2 compact layer on the performance of planar spiro-OMeTAD free perovskite solar cells. J Mater Chem A 2018;6:1037–47. https://doi.org/10.1039/C7TA09193A.

[185] Mahmood K, Sarwar S, Mehran MT, Taqi M, Sarwar S, Mehran MT. Current status of electron transport layers in perovskite solar cells: materials and properties. RSC Adv 2017;7:17044–62. https://doi.org/10.1039/C7RA00002B.

[186] Tharsika T, Haseeb ASMA, Akbar SA, Mohd Sabri MF, Hoong WY. Enhanced ethanol gas sensing properties of SnO2-core/ZnO-shell nanostructures. Sensors (Switzerland) 2014;14:14586–600. https://doi.org/10.3390/s140814586.

[187] Ono LK, Leyden MR, Wang S, Qi Y. Organometal halide perovskite thin films and solar cells by vapor deposition. J Mater Chem A 2016;4:6693–713. https://doi.org/10.1039/C5TA08963H.

[188] Zheng F, Xu WL, Jin HD, Hao XT, Ghiggino KP. Charge transfer from poly(3-hexylthiophene) to graphene oxide and reduced graphene oxide. RSC Adv 2015;5:89515–20. https://doi.org/10.1039/c5ra18540h.

[189] Barbé J, Tietze ML, Neophytou M, Murali B, Alarousu E, Labban A El, et al. Amorphous Tin Oxide as a Low-Temperature-Processed Electron-Transport Layer for Organic and Hybrid Perovskite Solar Cells. ACS Appl Mater Interfaces 2017;9:11828–36. https://doi.org/10.1021/acsami.6b13675.

[190] Wang Y, Liang Y, Zhang Y, Yang W, Sun L, Xu D. Pushing the Envelope: Achieving an Open-Circuit Voltage of 1.18 V for Unalloyed MAPbI 3 Perovskite Solar Cells of a Planar Architecture. Adv Funct Mater 2018;1801237:1801237. https://doi.org/10.1002/adfm.201801237.

[191] Li JT, Yang DY, Zhu XH, Li X, Chen SQ, Zhao YQ. Influence of Annealing Temperature on Structural, Morphological, Optical and Electrical Properties of Sol-Gel SnO_2 Thin Films. J Nano Res 2018;52:15–20. https://doi.org/10.4028/www.scientific.net/jnanor.52.15.

[192] Singh BP, Kumar R, Kumar A, Gaur J, Singh SP, Tyagi RC. Effect of annealing on properties of transparent conducting tin oxide films deposited by thermal evaporation. Indian J Pure Appl Phys 2013;51:558–62.

[193] Ke W, Zhao D, Cimaroli AJ, Grice CR, Qin P, Liu Q, et al. Effects of annealing temperature of tin oxide electron selective layers on the performance of perovskite solar cells. J Mater Chem A 2015;3:24163–8. https://doi.org/10.1039/c5ta06574g.

[194] Lee Y, Lee S, Seo G, Paek S, Cho KT, Huckaba AJ, et al. Efficient Planar Perovskite Solar Cells Using Passivated Tin Oxide as an Electron Transport Layer. Adv Sci 2018;1800130:1–6. https://doi.org/10.1002/advs.201800130.

[195] Konstantakou M, Perganti D, Falaras P, Stergiopoulos T. Anti-Solvent Crystallization Strategies for Highly Efficient Perovskite Solar Cells. Crystals 2017;7:291. https://doi.org/10.3390/cryst7100291.

[196] McNeill CR, Hwang I, Greenham NC. Photocurrent transients in all-polymer solar cells: Trapping and detrapping effects. J Appl Phys 2009;106. https://doi.org/10.1063/1.3177337.

[197] Sadhanala A, Deschler F, Thomas TH, Dutton SE, Goedel KC, Hanusch FC, et al. Preparation of single-phase films of CH3NH3Pb(I1- xBrx)3with sharp optical band edges. J Phys Chem Lett 2014;5:2501–5. https://doi.org/10.1021/jz501332v.

[198] Chang YH, Park CH. First-principles study of the structural and the electronic properties of the lead-halide-based inorganic-organic perovskite. Journal- Korean Phys Soc · 2004;44:889–93.

[199] Gheno A, Vedraine S, Ratier B, Bouclé J. π-Conjugated Materials as the Hole-Transporting Layer in Perovskite Solar Cells. Metals (Basel) 2016;6:21.

https://doi.org/10.3390/met6010021.

[200] De A, Mondal N, Samanta A. Hole Transfer Dynamics from Photoexcited Cesium Lead Halide Perovskite Nanocrystals: 1-Aminopyrene as Hole Acceptor. J Phys Chem C 2018:acs.jpcc.7b12813. https://doi.org/10.1021/acs.jpcc.7b12813.

[201] Ye M, Hong X, Zhang F, Liu X. Recent advancements in perovskite solar cells: flexibility, stability and large scale. J Mater Chem A 2016;4:6755–71. https://doi.org/10.1039/C5TA09661H.

[202] Elumalai NK, Mahmud MA, Wang D, Uddin A, Mahmud A, Wang D, et al. Perovskite solar cells: Progress and advancements. Energies 2016;9:1–20. https://doi.org/10.3390/en9110861.

[203] Qiu J, Qiu Y, Yan K, Zhong M, Mu C, Yan H, et al. All-solid-state hybrid solar cells based on a new organometal halide perovskite sensitizer and one-dimensional TiO2 nanowire arrays. Nanoscale 2013;5:3245. https://doi.org/10.1039/c3nr00218g.

[204] Ahn N, Son DY, Jang IH, Kang SM, Choi M, Park NG. Highly Reproducible Perovskite Solar Cells with Average Efficiency of 18.3% and Best Efficiency of 19.7% Fabricated via Lewis Base Adduct of Lead(II) Iodide. J Am Chem Soc 2015;137:8696–9. https://doi.org/10.1021/jacs.5b04930.

[205] Huang Z, Wang D, Wang S, Zhang T. Highly efficient and stable MAPbI<inf>3</inf>perovskite solar cell induced by regulated nucleation and ostwald recrystallization. Materials (Basel) 2018;11:20–30. https://doi.org/10.3390/ma11050778.

[206] Seok S Il, Grätzel M, Park N-G. Methodologies toward Highly Efficient Perovskite Solar Cells. Small 2018;1704177:1–17. https://doi.org/10.1002/smll.201704177.

[207] Vivo P, Salunke JK, Priimagi A. Hole-transporting materials for printable perovskite solar cells. Materials (Basel) 2017;10:1–45. https://doi.org/10.3390/ma10091087.

[208] Intaniwet A, Mills CA, Sellin PJ, Shkunov M, Keddie JL, Akarin Intaniwet, et al. Achieving a stable time response in polymeric radiation sensors under charge injection by X-rays. Appl Mater $ Interfaces 2010;2:1692–9. https://doi.org/10.1021/am100220y.

[209] Nguyen WH, Bailie CD, Unger EL, Mcgehee MD. Enhancing the Hole-Conductivity of Spiro-OMeTAD without Oxygen or Lithium Salts by Using Spiro(TFSI) 2 in Perovskite and Dye- Sensitized Solar Cells. J Am Chem Soc 2014;136:10996–1001. https://doi.org/10.1021/ja504539w.

[210] Cappel UB, Daeneke T, Bach U. Oxygen-induced doping of spiro-MeOTAD in solid-state dye-sensitized solar cells and its impact on device performance. Nano Lett 2012;12:4925–31. https://doi.org/10.1021/nl302509q.

[211] Snaith HJ, Grätzel M. Enhanced charge mobility in a molecular hole transporter via addition of redox inactive ionic dopant: Implication to dye-sensitized solar cells. Appl Phys Lett 2006;89:87–90. https://doi.org/10.1063/1.2424552.

[212] Schölin R, Karlsson MH, Eriksson SK, Siegbahn H, Johansson EMJ, Rensmo H. Energy level shifts in spiro-OMeTAD molecular thin films when adding Li-TFSI. J Phys Chem C 2012;116:26300–5. https://doi.org/10.1021/jp306433g.

[213] Lindblad R, Oscarsson J, Fredin K, Eriksson SK, Siegbahn H, Johansson EMJ, et al. Controlling energy level positions in hole conducting molecular films by additives. J Electron Spectros Relat Phenomena 2017. https://doi.org/10.1016/j.elspec.2017.03.009.

[214] Hawash Z, Ono LK, Qi Y. Recent Advances in Spiro-MeOTAD Hole Transport Material and Its Applications in Organic–Inorganic Halide Perovskite Solar Cells. Adv Mater Interfaces 2018;5. https://doi.org/10.1002/admi.201700623.

[215] Ren G, Han W, Deng Y, Wu W, Li Z, Guo J, et al. Strategies of modifying spiro-OMeTAD materials for perovskite solar cells: a review. J Mater Chem A 2021;9:4589–625. https://doi.org/10.1039/d0ta11564a.

[216] Li M, Wang Z-K, Zhuo M-P, Hu Y, Hu K-H, Ye Q-Q, et al. Pb-Sn-Cu Ternary Organometallic Halide Perovskite Solar Cells. Adv Mater 2018;1800258:1800258. https://doi.org/10.1002/adma.201800258.

[217] Gao Y, Dong Y, Huang K, Zhang C, Liu B, Wang S, et al. Highly Efficient, Solution-Processed CsPbI2Br Planar Heterojunction Perovskite Solar Cells via Flash Annealing. ACS Photonics 2018;5:4104–10. https://doi.org/10.1021/acsphotonics.8b00783.

[218] Parida B, Singh A, Oh M, Jeon M, Kang J, Kim H. E ff ect of compact TiO 2 layer

on structural , optical , and performance characteristics of mesoporous perovskite solar cells. Mater Today Commun 2019;18:176–83. https://doi.org/10.1016/j.mtcomm.2018.12.007.

[219] Jodlowski AD, Roldán-Carmona C, Grancini G, Salado M, Ralaiarisoa M, Ahmad S, et al. Large guanidinium cation mixed with methylammonium in lead iodide perovskites for 19% efficient solar cells. Nat Energy 2017;2:972–9. https://doi.org/10.1038/s41560-017-0054-3.

[220] Xu Y, Zhu L, Shi J, Lv S, Xu X, Xiao J, et al. Efficient Hybrid Mesoscopic Solar Cells with Morphology-Controlled $CH_3NH_3PbI_{3-x}Cl_x$ Derived from Two-Step Spin Coating Method. ACS Appl Mater Interfaces 2015;7:2242–8. https://doi.org/10.1021/am5057807.

[221] Fang Y, Wang X, Wang Q, Huang J, Wu T. Impact of annealing on spiro-OMeTAD and corresponding solid-state dye sensitized solar cells. Phys Status Solidi Appl Mater Sci 2014;211:2809–16. https://doi.org/10.1002/pssa.201431366.

[222] Jena AK, Ikegami M, Miyasaka T. Severe Morphological Deformation of Spiro-OMeTAD in $(CH_3NH_3)PbI_3$ Solar Cells at High Temperature. ACS Energy Lett 2017;2:1760–1. https://doi.org/10.1021/acsenergylett.7b00582.

[223] Jiang X, Yu Z, Zhang Y, Lai J, Li J, Gurzadyan GG, et al. High-Performance Regular Perovskite Solar Cells Employing Low-Cost Poly(ethylenedioxythiophene) as a Hole-Transporting Material. Sci Rep 2017;7:1–9. https://doi.org/10.1038/srep42564.

[224] Calió L, Kazim S, Grätzel M, Ahmad S. Hole-Transport Materials for Perovskite Solar Cells. Perovskite Sol Cells 2016;55:14522–45. https://doi.org/10.1002/anie.201601757.

[225] Chowdhury TH, Kaneko R, Kayesh ME, Akhtaruzzaman M, Sopian K Bin, Lee J-J, et al. Nanostructured NiO x as hole transport material for low temperature processed stable perovskite solar cells. Mater Lett 2018;223:109–11. https://doi.org/10.1016/j.matlet.2018.04.040.

[226] Zhang Z, Zhou Y, Cai Y, Liu H, Qin Q, Lu X, et al. Efficient and stable CH3NH3PbI3-x(SCN)x planar perovskite solar cells fabricated in ambient air with

low-temperature process. J Power Sources 2018;377:52–8. https://doi.org/10.1016/j.jpowsour.2017.11.070.

[227] Bastos JP, Manghooli S, Jaysankar M, Tait JG, Qiu W, Gehlhaar R, et al. Low-cost electrodes for stable perovskite solar cells. Appl Phys Lett 2017;110. https://doi.org/10.1063/1.4984284.

[228] Domanski K, Correa-Baena JP, Mine N, Nazeeruddin MK, Abate A, Saliba M, et al. Not All That Glitters Is Gold: Metal-Migration-Induced Degradation in Perovskite Solar Cells. ACS Nano 2016;10:6306–14. https://doi.org/10.1021/acsnano.6b02613.

[229] Kato Y, Ono LK, Lee M V., Wang S, Raga SR, Qi Y. Silver Iodide Formation in Methyl Ammonium Lead Iodide Perovskite Solar Cells with Silver Top Electrodes. Adv Mater Interfaces 2015;2:2–7. https://doi.org/10.1002/admi.201500195.

[230] Zhao L, Kerner RA, Xiao Z, Lin YL, Lee KM, Schwartz J, et al. Redox Chemistry Dominates the Degradation and Decomposition of Metal Halide Perovskite Optoelectronic Devices. ACS Energy Lett 2016;1:595–602. https://doi.org/10.1021/acsenergylett.6b00320.

[231] Niu G, Wang S, Li J, Li W, Wang L. Oxygen doping in nickel oxide for high efficient planar perovskite solar cells. J Mater Chem A 2018;6:4721–8. https://doi.org/10.1039/C8TA00161H.

[232] Liao LS, Hung LS, Chan WC, Ding XM, Sham TK, Bello I, et al. Ion-beam-induced surface damages on tris- (8-hydroxyquinoline) aluminum. Appl Phys Lett 1999;75:1619–21. https://doi.org/10.1063/1.124773.

[233] Derry GN, Kern ME, Worth EH. Recommended values of clean metal surface work functions. J Vac Sci Technol A Vacuum, Surfaces, Film 2015;33:060801. https://doi.org/10.1116/1.4934685.

[234] Ofuonye B, Lee J, Yan M, Sun C, Zuo JM, Adesida I. Electrical and microstructural properties of thermally annealed Ni/Au and Ni/Pt/Au Schottky contacts on AlGaN/GaN heterostructures. Semicond Sci Technol 2014;29. https://doi.org/10.1088/0268-1242/29/9/095005.

[235] Wang Y, Wang S, Chen X, Li Z, Wang J, Li T, et al. Largely enhanced V_{OC} and

stability in perovskite solar cells with modified energy match by coupled 2D interlayers. J Mater Chem A 2018;6:4860–7. https://doi.org/10.1039/C7TA11295E.

[236] Gao H, Bao C, Li F, Yu T, Yang J, Zhu W, et al. Nucleation and crystal growth of organic-inorganic lead halide perovskites under different relative humidity. ACS Appl Mater Interfaces 2015;7:9110–7. https://doi.org/10.1021/acsami.5b00895.

[237] Ogunniran KO, Martins NT. Humidity and Moisture Degradation of Perovskite Material in Solar Cells: Effects on Efficiency. IOP Conf Ser Earth Environ Sci 2021;655. https://doi.org/10.1088/1755-1315/655/1/012049.

[238] Fu Q, Tang X, Huang B, Hu T, Tan L, Chen L, et al. Recent Progress on the Long-Term Stability of Perovskite Solar Cells. Adv Sci 2018;5. https://doi.org/10.1002/advs.201700387.

[239] Shahbazi M, Wang H. Progress in research on the stability of organometal perovskite solar cells. Sol Energy 2016;123:74–87. https://doi.org/10.1016/j.solener.2015.11.008.

[240] Frost JM, Butler KT, Brivio F, Hendon CH, Van Schilfgaarde M, Walsh A. Atomistic origins of high-performance in hybrid halide perovskite solar cells. Nano Lett 2014;14:2584–90. https://doi.org/10.1021/nl500390f.

[241] Christians JA, Miranda Herrera PA, Kamat P V. Transformation of the excited state and photovoltaic efficiency of CH3NH3PbI3 perovskite upon controlled exposure to humidified air. J Am Chem Soc 2015;137:1530–8. https://doi.org/10.1021/ja511132a.

[242] Lang F, Shargaieva O, Brus V V, Neitzert HC, Rappich J, Nickel NH. Influence of Radiation on the Properties and the Stability of Hybrid Perovskites 2018;1702905:1–22. https://doi.org/10.1002/adma.201702905.

[243] Sun M, Zhang F, Liu H, Li X, Xiao Y, Wang S. Tuning the crystal growth of perovskite thin-films by adding the 2-pyridylthiourea additive for highly efficient and stable solar cells prepared in ambient air. J Mater Chem A 2017;5:13448–56. https://doi.org/10.1039/C7TA00894E.

[244] Yang Z, Pan J, Liang Y, Li Q, Xu D. Ambient Air Condition for Room-Temperature Deposition of MAPbI3 Films in Highly Efficient Solar Cells. Small

2018;14:1–6. https://doi.org/10.1002/smll.201802240.

[245] Wang Y, Wu J, Zhang P, Liu D, Zhang T, Ji L, et al. Stitching triple cation perovskite by a mixed anti-solvent process for high performance perovskite solar cells. Nano Energy 2017;39:616–25. https://doi.org/10.1016/j.nanoen.2017.07.046.

[246] Lee KM, Lin CJ, Liou BY, Yu SM, Hsu CC, Suryanarayanan V. Effect of anti-solvent mixture on the performance of perovskite solar cells and suppression hysteresis behavior. Org Electron 2019;65:266–74. https://doi.org/10.1016/j.orgel.2018.08.048.

[247] Yi J, Zhuang J, Ma Z, Guo Z, Zhou W, Zhao S, et al. Regulated perovskite crystallinity via green mixed antisolvent for efficient perovskite solar cells. Org Electron 2019;69:69–76. https://doi.org/10.1016/j.orgel.2019.03.021.

[248] Wang Y, Wu J, Zhang P, Liu D, Zhang T, Ji L, et al. Stitching triple cation perovskite by a mixed anti-solvent process for high performance perovskite solar cells. Nano Energy 2017;39:616–25. https://doi.org/10.1016/j.nanoen.2017.07.046.

[249] Yu Y, Yang S, Lei L, Cao Q, Shao J, Zhang S, et al. Ultrasmooth perovskite film via mixed anti-solvent strategy with improved efficiency. ACS Appl Mater Interfaces 2017;9:3667–76. https://doi.org/10.1021/acsami.6b14270.

[250] NIOSH Pocket Guide to Chemical Hazards. vol. 2005–149. 3rd ed. Ohio: 2007.

[251] Solvent Miscibility Table n.d. https://www.sigmaaldrich.com/chemistry/solvents/solvent-miscibility-table.html (accessed November 29, 2020).

[252] Sun Y, Peng J, Chen Y, Yao Y, Liang Z. Triple-cation mixed-halide perovskites: Towards efficient, annealing-free and air-stable solar cells enabled by Pb(SCN) 2 additive. Sci Rep 2017;7:1–7. https://doi.org/10.1038/srep46193.

[253] Zhao BG, Zhu L, Zhao YL, Yang Y, Song J, Gu XQ, et al. Improved performance of perovskite solar cell by controlling CH3NH3PbI3−xClxfilm morphology with CH3NH3Cl-assisted method. J Mater Sci Mater Electron 2016;27:10869–76. https://doi.org/10.1007/s10854-016-5196-8.

[254] Liu H, Li W, Feng F, Wang S, Lu Z. Improved Efficiency of Perovskite Solar Cells by the Interfacial Modification of the Active Layer. Nanomaterials 2019;9:204. https://doi.org/10.3390/nano9020204.

[255] Bag S, Durstock MF. Large Perovskite Grain Growth in Low-Temperature Solution-Processed Planar p-i-n Solar Cells by Sodium Addition. ACS Appl Mater Interfaces 2016;8:5053–7. https://doi.org/10.1021/acsami.5b11494.

[256] Wang Q, Dong Q, Li T, Gruverman A, Huang J. Thin Insulating Tunneling Contacts for Efficient and Water-Resistant Perovskite Solar Cells. Adv Mater 2016:6734–9. https://doi.org/10.1002/adma.201600969.

[257] Hörantner MT, Nayak PK, Mukhopadhyay S, Wojciechowski K, Beck C, McMeekin D, et al. Shunt-Blocking Layers for Semitransparent Perovskite Solar Cells. Adv Mater Interfaces 2016;3:1–7. https://doi.org/10.1002/admi.201500837.

[258] Salim KMM, Masi S, Gualdrón-Reyes AF, Sánchez RS, Barea EM, Krecmarová M, et al. Boosting Long-Term Stability of Pure Formamidinium Perovskite Solar Cells by Ambient Air Additive Assisted Fabrication. ACS Energy Lett 2021;6:3511–21. https://doi.org/10.1021/acsenergylett.1c01311.

[259] Hwang I, Jeong I, Lee J, Ko MJ, Yong K. Enhancing Stability of Perovskite Solar Cells to Moisture by the Facile Hydrophobic Passivation. ACS Appl Mater Interfaces 2015;7:17330–6. https://doi.org/10.1021/acsami.5b04490.

[260] Zheng X, Chen B, Dai J, Fang Y, Bai Y, Lin Y, et al. Defect passivation in hybrid perovskite solar cells using quaternary ammonium halide anions and cations. Nat Energy 2017;2:17102. https://doi.org/10.1038/nenergy.2017.102.

[261] Alharbi EA, Alyamani AY, Kubicki DJ, Uhl AR, Walder BJ, Alanazi AQ, et al. Atomic-level passivation mechanism of ammonium salts enabling highly efficient perovskite solar cells. Nat Commun 2019;10:1–9. https://doi.org/10.1038/s41467-019-10985-5.

[262] Flack WW, Soong DS, Bell AT, Hess DW. A mathematical model for spin coating of polymer resists. J Appl Phys 1984;56:1199–206. https://doi.org/10.1063/1.334049.

[263] Heredia E, Bojorge C, Casanova J, Cánepa H, Craievich A, Kellermann G. Nanostructured ZnO thin films prepared by sol-gel spin-coating. Appl Surf Sci

2014;317:19–25. https://doi.org/10.1016/j.apsusc.2014.08.046.

[264] Balzarotti R, Cristiani C, Francis LF. Spin coating deposition on complex geometry substrates: Influence of operative parameters. Surf Coatings Technol 2017;330:1–9. https://doi.org/10.1016/j.surfcoat.2017.09.077.

[265] Razza S, Castro-Hermosa S, Di Carlo A, Brown TM. Research Update: Large-area deposition, coating, printing, and processing techniques for the upscaling of perovskite solar cell technology. APL Mater 2016;4. https://doi.org/10.1063/1.4962478.

[266] Gilissen K, Stryckers J, Verstappen P, Drijkoningen J, Heintges GHL, Lutsen L, et al. Ultrasonic spray coating as deposition technique for the light-emitting layer in polymer LEDs. Org Electron Physics, Mater Appl 2015;20:31–5. https://doi.org/10.1016/j.orgel.2015.01.015.

[267] Ossila. Spin Coating : A Guide to Theory and Techniques. Ossila 2021:1–21. https://www.ossila.com/pages/spin-coating?_pos=1&_sid=ac33c4252&_ss=r (accessed January 21, 2021).

[268] Osilla. Spin Coating: Complete Guide to Theory and Techniques. Osilla 2018. https://www.ossila.com/pages/spin-coating?_pos=1&_sid=ac33c4252&_ss=r (accessed January 21, 2021).

[269] Yavari M, Mazloum-Ardakani M, Gholipour S, Tavakoli MM, Turren-Cruz S-H, Taghavinia N, et al. Greener, Nonhalogenated Solvent Systems for Highly Efficient Perovskite Solar Cells. Adv Energy Mater 2018;1800177:1800177. https://doi.org/10.1002/aenm.201800177.

[270] Rizk HA, Elanwar IM. Dipole moments of glycerol, isopropyl alcohol, and isobutyl alcohol. Can J Chem 1968;46:507–13. https://doi.org/10.1139/v68-084.

[271] University of Louisville. Spin Coating Theory. 2013.

[272] Griffin J, Ryan AJ, Lidzey DG. Solution modification of PEDOT:PSS inks for ultrasonic spray coating. Org Electron 2017;41:245–50. https://doi.org/10.1016/j.orgel.2016.11.011.

[273] Barrows AT, Pearson AJ, Kwak CK, Dunbar ADF, Buckley AR, Lidzey DG. Efficient planar heterojunction mixed-halide perovskite solar cells deposited via

spray-deposition. Energy Environ Sci 2014;7:2944–50. https://doi.org/10.1039/C4EE01546K.

[274] Das S, Yang B, Gu G, Joshi PC, Ivanov IN, Rouleau CM, et al. High-Performance Flexible Perovskite Solar Cells by Using a Combination of Ultrasonic Spray-Coating and Low Thermal Budget Photonic Curing. ACS Photonics 2015;2:680–6. https://doi.org/10.1021/acsphotonics.5b00119.

[275] Mattox DM. The Foundations of Vacuum Coating Technology. New York: NOYES PUBLICATIONS WILLIAM ANDREW PUBLISHING; 2003. https://doi.org/10.1016/B978-081551495-4.50015-2.

[276] Behera A, Aich S, Theivasanthi T. Magnetron sputtering for development of nanostructured materials. Elsevier Inc.; 2021. https://doi.org/10.1016/B978-0-12-820558-7.00002-9.

[277] Magnetron T, Features S. Titan Planar Magnetron 2-inch Sputter Source. Source n.d.:2–3.

[278] Raposo M, Ferreira Q, Ribeiro P a. A Guide for Atomic Force Microscopy Analysis of Soft- Condensed Matter. Mod Res Educ Top Microsc 2007:758–69. https://doi.org/10.1002/sia.2294.

[279] Cell F, Kowalski C, Burrows L, Varbel a, Leilani M. Dimension 3100 Manual NanoScope Software Version 5 004-320-000 (standard) Document Revision History : DImension 3100 Manual. Dimens Contemp Ger Arts Lett 2004;000:4–320.

[280] Brucker. MLCT n.d. https://www.brukerafmprobes.com/p-3444-mlct.aspx (accessed November 29, 2021).

[281] Brucker. SCM-PIT-V2 n.d. https://www.brukerafmprobes.com/p-3950-scm-pit-v2.aspx (accessed November 29, 2021).

[282] De Caro, Cosimo; Haller C. UV / VIS Spectrophotometry. 2015.

[283] Kaliva M, Vamvakaki M. Nanomaterials characterization. In: Narain R, editor. Polym. Sci. Nanotechnol., Elsevier Inc.; 2020, p. 401–33. https://doi.org/10.1016/B978-0-12-816806-6.00017-0.

[284] Agilent. The Basics of UV-Vis Spectrophotometry, 2020, p. 36.

[285] Ghobadi N. Band gap determination using absorption spectrum fitting procedure. Int Nano Lett 2013;3:2. https://doi.org/10.1186/2228-5326-3-2.

[286] Kim CE, Moon P, Kim S, Myoung JM, Jang HW, Bang J, et al. Effect of carrier concentration on optical bandgap shift in ZnO:Ga thin films. Thin Solid Films 2010;518:6304–7. https://doi.org/10.1016/j.tsf.2010.03.042.

[287] Yogamalar NR, Chandra Bose A. Burstein-Moss shift and room temperature near-band-edge luminescence in lithium-doped zinc oxide. Appl Phys A Mater Sci Process 2011;103:33–42. https://doi.org/10.1007/s00339-011-6304-5.

[288] Carolan D, Doyle H. Size and emission color tuning in the solution phase synthesis of highly luminescent germanium nanocrystals. J Mater Chem C 2014;2:3562–8. https://doi.org/10.1039/c4tc00319e.

[289] Makuła P, Pacia M, Macyk W. How To Correctly Determine the Band Gap Energy of Modified Semiconductor Photocatalysts Based on UV-Vis Spectra. J Phys Chem Lett 2018;9:6814–7. https://doi.org/10.1021/acs.jpclett.8b02892.

[290] Escobedo-Morales A, Ruiz-López II, Ruiz-Peralta M de L, Tepech-Carrillo L, Sánchez-Cantú M, Moreno-Orea JE. Automated method for the determination of the band gap energy of pure and mixed powder samples using diffuse reflectance spectroscopy. Heliyon 2019;5:1–19. https://doi.org/10.1016/j.heliyon.2019.e01505.

[291] Sindhu R, Binod P, Pandey A. Microbial Poly-3-Hydroxybutyrate and Related Copolymers. Ind. Biorefineries White Biotechnol., Elsevier B.V.; 2015, p. 575–605. https://doi.org/10.1016/B978-0-444-63453-5.00019-7.

[292] Crystran. The Crystran handbook of nfra-red and ultra-violet optical materials. 2020. https://doi.org/10.1017/CBO9781107415324.004.

[293] Bassan P, Mellor J, Shapiro J, Williams KJ, Lisanti MP, Gardner P. Transmission FT-IR chemical imaging on glass substrates: Applications in infrared spectral histopathology. Anal Chem 2014;86:1648–53. https://doi.org/10.1021/ac403412n.

[294] Ashley JMB and EJ. INFRARED REFLECTANCE AND EMITTANCE OF SILVER AND GOLD EVAPORATED IN ULTRAHIGH VACUUM. Appl Opt 221 1965;4:221–4.

[295] Akl AA, Hassanien AS. Microstructure characterization of Al-Mg alloys by X-ray diffraction line profile analysis Alloy 5251 Al Si Fe Cu Mn Mg Cr Zn Al Reminder. Int J Adv Res 2014;2:1–9.

[296] Bunaciu AA, Udriştioiu E gabriela, Aboul-Enein HY. X-Ray Diffraction: Instrumentation and Applications. Crit Rev Anal Chem 2015;45:289–99. https://doi.org/10.1080/10408347.2014.949616.

[297] Akl AA, Hassanien AS. Superlattices and Microstructures Microstructure and crystal imperfections of nanosized CdS x Se 1 À x thermally evaporated thin films. Superlattices Microstruct 2015;85:67–81. https://doi.org/10.1016/j.spmi.2015.05.011.

[298] Itoh E, Iwamoto M, Burghard M, Roth S. Ultraviolet Photoelectron Spectroscopy and Surface Potential of π -conjugated Langmuir-Blodgett Films on Gold Metal Electrode. Jpn J Appl Phys 2000;39:5146–50.

[299] Carle RH. UPS Applications: A Mill Perspective. IEEE Ind Appl Mag 1995;1:12–7. https://doi.org/10.1109/2943.469998.

[300] Opitz A, Bronner M, Brütting W, Himmerlich M, Schaefer JA, Krischok S. Electronic properties of organic semiconductor blends: Ambipolar mixtures of phthalocyanine and fullerene. Appl Phys Lett 2007;90:1–3. https://doi.org/10.1063/1.2742640.

[301] Wikipedia. Ultraviolet photoelectron spectroscopy 2021. https://en.wikipedia.org/wiki/Ultraviolet_photoelectron_spectroscopy (accessed January 2, 2022).

[302] Clementi E, Davis D. Electronic structure of large molecular systems. J Comput Phys 1966;1:223–44. https://doi.org/10.1016/0021-9991(66)90004-0.

[303] Kampen TU, Mendez H, Zahn DRT. Energy Level Alignment at Molecular Semiconductor/GaAs(100) Interfaces: Where is the LUMO? 26th ICPS, IOP Conf Ser 171 2003:H215.

[304] Ni C. Scanning Electron Microscopy (SEM). In: Wang QJ, Chung Y-W, editors. Encycl. Tribol., Boston, MA: Springer US; 2013, p. 2977–82. https://doi.org/10.1007/978-0-387-92897-5_1217.

[305] Ravescientific. Descriptions of Electron Microscope Cathodes and Emitters n.d. https://ravescientific.com/education/32-descriptions-of-electron-microscope-cathodes-and-emitters (accessed January 2, 2022).

[306] Fajardo S, García-Galvan, R. F, Barranco V, Galvan JC, Batlle SF. We are IntechOpen , the world ' s leading publisher of Open Access books Built by scientists , for scientists TOP 1 %. vol. i. 2016. https://doi.org/http://dx.doi.org/10.5772/57353.

[307] Jeong SH, Lee KH. Flexible Field Emitters Based on Carbon Nanotubes and Other Materials. Semicond. Nanomater. Flex. Technol. From Photovoltaics Electron. to Sensors Energy Storage. First Edit, Elsevier Ltd.; 2010, p. 129–58. https://doi.org/10.1016/B978-1-4377-7823-6.00005-2.

[308] Bowler N. Four-point potential drop measurements for materials characterization. Meas Sci Technol 2011;22. https://doi.org/10.1088/0957-0233/22/1/012001.

[309] Ossila. Calculate Sheet Resistance Using the Four-Probe Method n.d. https://www.ossila.com/pages/sheet-resistance-theory (accessed March 23, 2023).

[310] Kjeldby SB, Evenstad OM, Cooil SP, Wells JW. Probing dimensionality using a simplified 4-probe method. J Phys Condens Matter 2017;29. https://doi.org/10.1088/1361-648X/aa8296.

[311] Miccoli I, Edler F, Pfnür H, Tegenkamp C. The 100th anniversary of the four-point probe technique: The role of probe geometries in isotropic and anisotropic systems. J Phys Condens Matter 2015;27:1–3.

[312] Schuetze AP, Lewis W, Brown C, Geerts WJ. A laboratory on the four-point probe technique. Am J Phys 2004;72:149–53. https://doi.org/10.1119/1.1629085.

[313] Swartzendruber LJ. Calculations for Comparing Two-Point and Four-Point Probe Resistivity Measurements on Rectangular Bar-Shaped Semiconductor Samples. Natl Bur Stand 1964:1–25.

[314] Zhang J, Zhang H, Wu J, Zhang J. Membrane/Ionomer Proton Conductivity Measurements. Pem Fuel Cell Test. Diagnosis, 2013, p. 143–70. https://doi.org/10.1016/b978-0-444-53688-4.00005-x.

[315] Ossila. I-V Curves: A Guide to Measurement n.d.

https://www.ossila.com/pages/iv-curves-measurement (accessed April 17, 2023).

[316] Pandiarajan N, Ramaprabha R, Muthu R. Application of circuit model for photovoltaic energy conversion system. Int J Photoenergy 2012;2012. https://doi.org/10.1155/2012/410401.

[317] S. R, O. S, A. K, S. A, B. R, Okelola O, et al. Development and Application of Asphalt Bonded Solar Thermogenerator in Small Scale Agroforestry Based Industry. Sol Radiat 2012. https://doi.org/10.5772/34578.

[318] Oriel-Instruments. LCS-100 Series Small Area Solar Simulators. 2013.

[319] Oriel-Instruments. Oriel Sol3A. 2017.

[320] Dirnberger D. Photovoltaic module measurement and characterization in the laboratory. Perform. Photovolt. Syst. Model. Meas. Assess., Elsevier Ltd.; 2017, p. 23–70. https://doi.org/10.1016/B978-1-78242-336-2.00002-1.

[321] Emery KA. Solar simulators and I-V measurement methods. Sol Cells 1986;18:251–60. https://doi.org/10.1016/0379-6787(86)90124-9.

[322] Feng Y, Bian J, Wang M, Wang S, Zhang C, Dong Q, et al. Interfacial negative capacitance in planar perovskite solar cells: an interpretation based on band theory. Mater Res Bull 2018;107:74–9. https://doi.org/10.1016/J.MATERRESBULL.2018.07.015.

[323] Zarazúa I, Sidhik S, Lopéz-Luke T, Esparza D, De La Rosa E, Reyes-Gomez J, et al. Operating Mechanisms of Mesoscopic Perovskite Solar Cells through Impedance Spectroscopy and J-V Modeling. J Phys Chem Lett 2017;8:6073–9. https://doi.org/10.1021/acs.jpclett.7b02848.

[324] Lv Y, Cai B, Ma Q, Wang Z, Liu J, Zhang W-H. Highly crystalline Nb-doped TiO_2 nanospindles as superior electron transporting materials for high-performance planar structured perovskite solar cells. RSC Adv 2018;8:20982–9. https://doi.org/10.1039/C8RA03559H.

[325] Davidson J. Impedance Spectroscopy of Lithium-Ion Cells Précis of Mini-Project Report. Differences 2011.

[326] Semple J, Georgiadou DG, Wyatt-Moon G, Gelinck G, Anthopoulos TD. Flexible diodes for radio frequency (RF) electronics: A materials perspective. Semicond Sci

Technol 2017;32. https://doi.org/10.1088/1361-6641/aa89ce.

[327] Kumar D, Banerjee A, Patil S, Shukla AK. A 1 V supercapacitor device with nanostructured graphene oxide/polyaniline composite materials. Bull Mater Sci 2015;38:1507–17. https://doi.org/10.1007/s12034-015-0966-0.

[328] Robles-ocampo JB. A Novel Fault Detection and Location Method for PV Arrays based on Frequency Analysis 2019. https://doi.org/10.1109/ACCESS.2019.2920053.

[329] Guerrero A, Bisquert J, Garcia-Belmonte G. Impedance Spectroscopy of Metal Halide Perovskite Solar Cells from the Perspective of Equivalent Circuits. Chem Rev 2021;121:14430–84. https://doi.org/10.1021/acs.chemrev.1c00214.

[330] Rong Y, Ku Z, Mei A, Liu T, Xu M, Ko S, et al. Hole-conductor-free mesoscopic TiO2/CH3NH 3PbI3 heterojunction solar cells based on anatase nanosheets and carbon counter electrodes. J Phys Chem Lett 2014;5:2160–4. https://doi.org/10.1021/jz500833z.

[331] Zhao S, Qin M, Xiang Y, Wang H, Xie J, Gong L, et al. Bifunctional Effects of Trichloro(octyl)silane Modification on the Performance and Stability of a Perovskite Solar Cell via Microscopic Characterization Techniques. ACS Appl Energy Mater 2020;3:3302–9. https://doi.org/10.1021/acsaem.9b02306.

[332] Niu G, Li W, Meng F, Wang L, Dong H, Qiu Y. Study on the stability of CH3NH3PbI3 films and the effect of post-modification by aluminum oxide in all-solid-state hybrid solar cells. J Mater Chem A 2014;2:705–10. https://doi.org/10.1039/c3ta13606j.

[333] Wang G, Liu D, Xiang J, Zhou D, Alameh K, Ding B, et al. Efficient perovskite solar cell fabricated in ambient air using one-step spin-coating. RSC Adv 2016;6:43299–303. https://doi.org/10.1039/c6ra05893k.

[334] Xie L, Chen J, Vashishtha P, Zhao X, Shin GS, Mhaisalkar SG, et al. Importance of Functional Groups in Cross-Linking Methoxysilane Additives for High-Efficiency and Stable Perovskite Solar Cells. ACS Energy Lett 2019;4:2192–200. https://doi.org/10.1021/acsenergylett.9b01356.

[335] Rahaq Y, Moussa M, Mohammad A, Wang H, Hassan A. Highly reproducible perovskite solar cells via controlling the morphologies of the perovskite thin films

by the solution-processed two-step method. J Mater Sci Mater Electron 2018;29:16426–36. https://doi.org/10.1007/s10854-018-9734-4.

[336] Alidaei M, Izadifard M, Ghazi ME, Ahmadi V. Efficiency enhancement of perovskite solar cells using structural and morphological improvement of CH3NH3PbI3 absorber layers. Mater Res Express 2018;5. https://doi.org/10.1088/2053-1591/aaa616.

[337] Xiao M, Zhao L, Geng M, Li Y, Dong B, Xu Z, et al. Selection of an anti-solvent for efficient and stable cesium-containing triple cation planar perovskite solar cells. Nanoscale 2018;10:12141–8. https://doi.org/10.1039/c8nr03580f.

[338] Taylor AD, Sun Q, Goetz KP, An Q, Schramm T, Hofstetter Y, et al. A general approach to high-efficiency perovskite solar cells by any antisolvent. Nat Commun 2021;12:1–11. https://doi.org/10.1038/s41467-021-22049-8.

[339] Wang L, Wang X, Deng LL, Leng S, Guo X, Tan CH, et al. The mechanism of universal green antisolvents for intermediate phase controlled high-efficiency formamidinium-based perovskite solar cells. Mater Horizons 2020;7:934–42. https://doi.org/10.1039/c9mh01679a.

[340] Qin P, He Q, Yang G, Yu X, Xiong L, Fang G. Metal Ions Diffusion at Heterojunction Chromium Oxide/CH3NH3PbI3 Interface on the Stability of Perovskite Solar Cells. Surfaces and Interfaces 2017;10:93–9. https://doi.org/10.1016/j.surfin.2017.12.006.

[341] Bao S, Wu J, He X, Tu Y, Wang S, Huang M, et al. Mesoporous Zn2SnO4 as effective electron transport materials for high-performance perovskite solar cells. Electrochim Acta 2017;251:307–15. https://doi.org/10.1016/j.electacta.2017.08.083.

[342] Li MH, Yum JH, Moon SJ, Chen P. Inorganic p-type semiconductors: Their applications and progress in dye-sensitized solar cells and perovskite solar cells. Energies 2016;9:1–28. https://doi.org/10.3390/en9050331.

[343] Lee H, Rhee S, Kim J, Lee C, Kim H. Surface coverage enhancement of a mixed halide perovskite film by using an UV-ozone treatment. J Korean Phys Soc 2016;69:406–11. https://doi.org/10.3938/jkps.69.406.

[344] Li X, Dai SM, Zhu P, Deng LL, Xie SY, Cui Q, et al. Efficient Perovskite Solar

Cells Depending on TiO2 Nanorod Arrays. ACS Appl Mater Interfaces 2016;8:21358–65. https://doi.org/10.1021/acsami.6b05971.

[345] Atomic force microscopy n.d. https://en.wikipedia.org/wiki/Atomic_force_microscopy (accessed April 17, 2023).

[346] Corning. Corning HPFS® 7979, 7980, 8655 Fused Silica Optical Materials Product Information Specialty Materials Division. 2014.

[347] Fused Silica / Quartz Glass - Properties and Applications of Fused Silica / Quartz Glass by Goodfellow Ceramic & Glass Division. Goodfellow Ceram Glas 2015:1–5. https://www.azom.com/article.aspx?ArticleID=4766 P (accessed September 9, 2018).

[348] Semnani D. Geometrical characterization of electrospun nanofibers. Electrospun Nanofibers, Elsevier Ltd.; 2017, p. 151–80. https://doi.org/10.1016/B978-0-08-100907-9.00007-6.

[349] Pitarch-Tena D, Ngo TT, Vallés-Pelarda M, Pauporté T, Mora-Seró I. Impedance Spectroscopy Measurements in Perovskite Solar Cells: Device Stability and Noise Reduction. ACS Energy Lett 2018;3:1044–8. https://doi.org/10.1021/acsenergylett.8b00465.

[350] Zoppi G, Beattie NS, Major JD, Miles RW, Forbes I. Electrical, morphological and structural properties of RF magnetron sputtered Mo thin films for application in thin film photovoltaic solar cells. J Mater Sci 2011;46:4913–21. https://doi.org/10.1007/s10853-011-5404-0.

[351] Dualeh A, Tétreault N, Moehl T, Gao P, Nazeeruddin MK, Grätzel M. Effect of annealing temperature on film morphology of organic-inorganic hybrid pervoskite solid-state solar cells. Adv Funct Mater 2014;24:3250–8. https://doi.org/10.1002/adfm.201304022.

[352] Chouhan AS, Jasti NP, Avasthi S. Effect of interface defect density on performance of perovskite solar cell: Correlation of simulation and experiment. Mater Lett 2018;221:150–3. https://doi.org/10.1016/j.matlet.2018.03.095.

[353] Chen X, Jiang J, Yan F, Tian S, Li K. A novel low temperature vapor phase hydrolysis method for the production of nano-structured silica materials using

silicon tetrachloride. RSC Adv 2014;4:8703–10. https://doi.org/10.1039/c3ra47018k.

[354] Osuntokun J, Onwudiwe DC, Ebenso EE. Biosynthesis and Photocatalytic Properties of SnO2 Nanoparticles Prepared Using Aqueous Extract of Cauliflower Biosynthesis and Photocatalytic Properties of SnO 2 of Cauliflower. J Clust Sci 2017. https://doi.org/10.1007/s10876-017-1188-y.

[355] Jiang LL, Cong S, Lou YH, Yi QH, Zhu JT, Ma H, et al. Interface engineering toward enhanced efficiency of planar perovskite solar cells. J Mater Chem A 2015;4:217–22. https://doi.org/10.1039/c5ta09231k.

[356] Dittrich T. Basic Characteristics and Characterization of Solar Cells. Mater. Concepts Sol. Cells, 2018, p. 3–43. https://doi.org/10.1142/9781786344496_0001.

[357] Muhammad FF, Yahya MY, Hameed SS, Aziz F, Sulaiman K, Rasheed MA, et al. Employment of single-diode model to elucidate the variations in photovoltaic parameters under different electrical and thermal conditions. PLoS One 2017;12. https://doi.org/10.1371/journal.pone.0182925.

[358] Sun Q, Zhou S, Shi X, Wang X, Gao L, Li Z, et al. Efficiency enhancement of perovskite solar cells via electrospun CuO nanowires as buffer layers. ACS Appl Mater Interfaces 2018:acsami.7b19335. https://doi.org/10.1021/acsami.7b19335.

[359] Banyamin Z, Kelly P, West G, Boardman J. Electrical and Optical Properties of Fluorine Doped Tin Oxide Thin Films Prepared by Magnetron Sputtering. Coatings 2014;4:732–46. https://doi.org/10.3390/coatings4040732.

[360] Mishra PK, Prasad JN, Dave V, Chandra R, Choudhary AK. The significant effect of film thickness on the properties of chalcopyrite thin absorbing films deposited by RF magnetron sputtering. Mater Sci Semicond Process 2015;34:350–8. https://doi.org/10.1016/j.mssp.2015.02.047.

[361] Joo H-Y, Kim HJ, Kim SJ, Kim SY. Spectrophotometric analysis of aluminum nitride thin films. J Vac Sci Technol A Vacuum, Surfaces, Film 1999;17:862. https://doi.org/10.1116/1.582035.

[362] Zheng YZ, Lai X Sen, Luo Y, Zhao EF, Meng FL, Zhang XF, et al. Effects of precursor concentration and annealing temperature on CH3NH3PbI3 film crystallization and photovoltaic performance. J Phys Chem Solids 2017;107:55–

61. https://doi.org/10.1016/j.jpcs.2017.03.020.

[363] Kumar GR, Savariraj AD, Karthick SN, Selvam S, Balamuralitharan B, Kim H, et al. Phase transition kinetics and surface binding states of methylammonium lead iodide perovskite. Phys Chem Chem Phys 2016;18:7284–92. https://doi.org/10.1039/C5CP06232B.

[364] Duan J, Zhang Y, Yu D, Wang F, Dai J. High Performance Inverted Planar MAPbI3 Perovskite Solar Cells with a Simple Annealing Process. ChemNanoMat 2019;5:715–22. https://doi.org/10.1002/cnma.201900097.

[365] Geffroy C, Grana E, Bessho T, Almosni S, Tang Z, Sharma A, et al. p-Doping of a Hole Transport Material via a Poly(ionic liquid) for over 20% Efficiency and Hysteresis-Free Perovskite Solar Cells. ACS Appl Energy Mater 2020;3:1393–401. https://doi.org/10.1021/acsaem.9b01819.

[366] Li Z, Chen J, Li H, Zhang Q, Chen Z, Zheng X, et al. A facilely synthesized "spiro" hole-transporting material based on spiro[3.3]heptane-2,6-dispirofluorene for efficient planar perovskite solar cells. RSC Adv 2017;7:41903–8. https://doi.org/10.1039/c7ra06643k.

[367] Nguyen WH, Bailie CD, Unger EL, McGehee MD. Enhancing the hole-conductivity of spiro-OMeTAD without oxygen or lithium salts by using spiro(TFSI)2 in perovskite and dye-sensitized solar cells. J Am Chem Soc 2014;136:10996–1001. https://doi.org/10.1021/ja504539w.

[368] Burschka J, Kessler F, Nazeeruddin MK, Gra M. Co(III) Complexes as p - Dopants in Solid-State Dye-Sensitized Solar Cells 2013.

[369] Burschka J, Dualeh A, Kessler F, Baranoff E, Cevey-Ha NL, Yi C, et al. Tris(2-(1 H -pyrazol-1-yl)pyridine)cobalt(III) as p-type dopant for organic semiconductors and its application in highly efficient solid-state dye-sensitized solar cells. J Am Chem Soc 2011;133:18042–5. https://doi.org/10.1021/ja207367t.

[370] Shao G. Work Function and Electron Affinity of Semiconductors: Doping Effect and Complication due to Fermi Level Pinning. Energy Environ Mater 2021;4:273–6. https://doi.org/10.1002/eem2.12218.

[371] Wang J, Li J, Xu X, Bi Z, Xu G, Shen H. Promising photovoltaic application of multi-walled carbon nanotubes in perovskites solar cells for retarding

recombination. RSC Adv 2016;6:42413–20. https://doi.org/10.1039/c6ra04743b.

[372] Cappel UB, Gibson EA, Hagfeldt A, Boschloo G. Dye regeneration by Spiro-MeOTAD in solid state dye-sensitized solar cells studied by photoinduced absorption spectroscopy and spectroelectrochemistry. J Phys Chem C 2009;113:6275–81. https://doi.org/10.1021/jp811196h.

[373] Fantacci S, De Angelis F, Nazeeruddin MK, Grätzel M. Electronic and optical properties of the spiro-MeOTAD hole conductor in its neutral and oxidized forms: A DFT/TDDFT investigation. J Phys Chem C 2011;115:23126–33. https://doi.org/10.1021/jp207968b.

[374] Schloemer TH, Christians JA, Luther JM, Sellinger A. Doping strategies for small molecule organic hole-transport materials: impacts on perovskite solar cell performance and stability. Chem Sci 2019;10:1904–35. https://doi.org/10.1039/C8SC05284K.

[375] Xi H, Tang S, Ma X, Chang J, Chen D, Lin Z, et al. Performance Enhancement of Planar Heterojunction Perovskite Solar Cells through Tuning the Doping Properties of Hole-Transporting Materials. ACS Omega 2017;2:326–36. https://doi.org/10.1021/acsomega.6b00465.

[376] Rombach FM, Haque SA, Macdonald TJ. Lessons learned from spiro-OMeTAD and PTAA in perovskite solar cells. Energy Environ Sci 2021;14:5161–90. https://doi.org/10.1039/d1ee02095a.

[377] Chaoumead A, Sung YM, Kwak DJ. The effects of RF sputtering power and gas pressure on structural and electrical properties of ITiO thin film. Adv Condens Matter Phys 2012;2012. https://doi.org/10.1155/2012/651587.

[378] Mukhtar WM, Shaari S, Susthitha Menon P. Propagation of surface plasmon waves at metal thin film/air interface using modified optical waveguiding assembly. Optoelectron Adv Mater Rapid Commun 2013;7:9–13.

[379] Li L, Li L, Chen W, Zheng J, Wang L, Chen Y. Characterization of Silver Nanoparticles Thin Films with Various Thicknesses by AFM. J Mater Sci Chem Eng 2016;04:34–9. https://doi.org/10.4236/msce.2016.41007.

[380] Sagara R, Kawamura M, Kiba T, Abe Y, Kim KH. Characteristics of Ag thin films sputter deposited using Ar or Kr gas under different pressure. Surf Coatings

Technol 2020;388. https://doi.org/10.1016/j.surfcoat.2020.125616.

[381] Jang GS, Ahn SM, Hwang NM. Effects of Sputtering Power, Working Pressure, and Electric Bias on the Deposition Behavior of Ag Films during DC Magnetron Sputtering Considering the Generation of Charged Flux. Electron Mater Lett 2021. https://doi.org/10.1007/s13391-021-00314-8.

[382] Bi D, Yi C, Luo J, Décoppet JD, Zhang F, Zakeeruddin SM, et al. Polymer-templated nucleation and crystal growth of perovskite films for solar cells with efficiency greater than 21%. Nat Energy 2016;1:1–5. https://doi.org/10.1038/nenergy.2016.142.

[383] Abdelmageed G, Jewell L, Hellier K, Seymour L, Luo B, Bridges F, et al. Mechanisms for light induced degradation in MAPbI3 perovskite thin films and solar cells. Appl Phys Lett 2016;109. https://doi.org/10.1063/1.4967840.

[384] Hou X, Huang S, Ou-Yang W, Pan L, Sun Z, Chen X. Constructing Efficient and Stable Perovskite Solar Cells via Interconnecting Perovskite Grains. ACS Appl Mater Interfaces 2017;9:35200–8. https://doi.org/10.1021/acsami.7b08488.

[385] Safaei-Ghomi J, Kakavand-Qalenoei A, Ghasemzadeh MA, Salavati-Niasari M. Efficient one-pot alkylation of imines using nanosilver iodide in aqueous media. Turkish J Chem 2012;36:852–9. https://doi.org/10.3906/kim-1201-40.

[386] Svanström S, Jacobsson TJ, Boschloo G, Johansson EMJ, Rensmo H, Cappel UB. Degradation Mechanism of Silver Metal Deposited on Lead Halide Perovskites. ACS Appl Mater Interfaces 2020;12:7212–21. https://doi.org/10.1021/acsami.9b20315.

[387] Kundu S, Kelly TL. In situ studies of the degradation mechanisms of perovskite solar cells. EcoMat 2020;2:1–22. https://doi.org/10.1002/eom2.12025.

[388] Yang J, Siempelkamp BD, Liu D, Kelly TL. Investigation of CH3NH3PbI3degradation rates and mechanisms in controlled humidity environments using in situ techniques. ACS Nano 2015;9:1955–63. https://doi.org/10.1021/nn506864k.

[389] Merdasa A, Kiligaridis A, Rehermann C, Abdi-Jalebi M, Stöber J, Louis B, et al. Impact of Excess Lead Iodide on the Recombination Kinetics in Metal Halide Perovskites. ACS Energy Lett 2019;4:1370–8.

https://doi.org/10.1021/acsenergylett.9b00774.

[390] Barbé J, Newman M, Lilliu S, Kumar V, Lee HKH, Charbonneau C, et al. Localized effect of PbI2 excess in perovskite solar cells probed by high-resolution chemical-optoelectronic mapping. J Mater Chem A 2018;6:23010–8. https://doi.org/10.1039/c8ta09536a.

[391] Lee KM, Lin CJ, Liou BY, Yu SM, Hsu CC, Suryanarayanan V, et al. Selection of anti-solvent and optimization of dropping volume for the preparation of large area sub-module perovskite solar cells. Sol Energy Mater Sol Cells 2017;172:368–75. https://doi.org/10.1016/j.solmat.2017.08.010.

[392] Chang SH, Huang WC, Chen CC, Chen SH, Wu CG. Effects of anti-solvent (iodobenzene) volume on the formation of CH 3 NH 3 PbI 3 thin films and their application in photovoltaic cells. Appl Surf Sci 2018;445:24–9. https://doi.org/10.1016/j.apsusc.2018.03.123.

[393] Shih YC, Wang L, Hsieh HC, Lin KF. Effect of Fullerene Passivation on the Charging and Discharging Behavior of Perovskite Solar Cells: Reduction of Bound Charges and Ion Accumulation. ACS Appl Mater Interfaces 2018;10:11722–31. https://doi.org/10.1021/acsami.8b03116.

[394] Salado M, Calió L, Contreras-Bernal L, Idígoras J, Anta JA, Ahmad S, et al. Understanding the influence of interface morphology on the performance of perovskite solar cells. Materials (Basel) 2018;11:1–13. https://doi.org/10.3390/ma11071073.

[395] Shao S, Loi MA. The Role of the Interfaces in Perovskite Solar Cells. Adv Mater Interfaces 2020;7. https://doi.org/10.1002/admi.201901469.

[396] Fakharuddin A, Schmidt-Mende L, Garcia-Belmonte G, Jose R, Mora-Sero I. Interfaces in Perovskite Solar Cells. Adv Energy Mater 2017;7. https://doi.org/10.1002/aenm.201700623.

[397] Wong KK, Fakharuddin A, Ehrenreich P, Deckert T, Abdi-Jalebi M, Friend RH, et al. Interface Dependent Radiative and Non-Radiative Recombination in Perovskite Solar Cells. J Phys Chem C 2018:acs.jpcc.8b00998. https://doi.org/10.1021/acs.jpcc.8b00998.

[398] Prochowicz D, Tavakoli MM, Kalam A, Chavan RD, Trivedi S, Kumar M, et al.

Influence of A-site cations on the open-circuit voltage of efficient perovskite solar cells: A case of rubidium and guanidinium additives. J Mater Chem A 2019;7:8218–25. https://doi.org/10.1039/c9ta00272c.

[399] Salado M, Idigoras J, Calio L, Kazim S, Nazeeruddin MK, Anta JA, et al. Interface Play between Perovskite and Hole Selective Layer on the Performance and Stability of Perovskite Solar Cells. ACS Appl Mater Interfaces 2016;8:34414–21. https://doi.org/10.1021/acsami.6b12236.

[400] Prochowicz D, Tavakoli MM, Alanazi AQ, Trivedi S, Tavakoli Dastjerdi H, Zakeeruddin SM, et al. Charge Accumulation, Recombination, and Their Associated Time Scale in Efficient (GUA) x(MA)1-xPbI3-Based Perovskite Solar Cells. ACS Omega 2019;4:16840–6. https://doi.org/10.1021/acsomega.9b01701.

[401] Li C, Wang ZS, Zhu HL, Zhang D, Cheng J, Lin H, et al. Thermionic Emission–Based Interconnecting Layer Featuring Solvent Resistance for Monolithic Tandem Solar Cells with Solution-Processed Perovskites. Adv Energy Mater 2018;8:1–10. https://doi.org/10.1002/aenm.201801954.

[402] Zhang Y, Kirs A, Ambroz F, Lin CT, Bati ASR, Parkin IP, et al. Ambient Fabrication of Organic–Inorganic Hybrid Perovskite Solar Cells. Small Methods 2021;5:1–40. https://doi.org/10.1002/smtd.202000744.

[403] Wang G, Liao L, Chen L, Xu C, Yao Y, Liu D, et al. Perovskite solar cells fabricated under ambient air at room temperature without any post-treatment. Org Electron 2020;86:105918. https://doi.org/10.1016/j.orgel.2020.105918.

[404] Li J, Yang R, Que L, Wang Y, Wang F, Wu J, et al. Optimization of anti-solvent engineering toward high performance perovskite solar cells. J Mater Res 2019;34:2416–24. https://doi.org/10.1557/jmr.2019.122.

[405] Mora-Sero´ I, Bisquert J, Fabregat-Santiago F, Garcia-Belmonte G. Implications of the Negative Capacitance Observed at Forward-Bias in Nanocomposite and Polycrystalline Solar Cells. NANO Lett 2006;6:640–50.

[406] Liu H, Liu HR, Yang F, Yang JE, Song J, Li M, et al. π-Conjugated small molecules enable efficient perovskite growth and charge-extraction for high-performance photovoltaic devices. J Power Sources 2020;448:227420. https://doi.org/10.1016/j.jpowsour.2019.227420.

[407] Boyd CC, Cheacharoen R, Leijtens T, McGehee MD. Understanding Degradation Mechanisms and Improving Stability of Perovskite Photovoltaics. Chem Rev 2019;119:3418–51. https://doi.org/10.1021/acs.chemrev.8b00336.

Appendixes

Appendix A: Other results not included in the main chapters.

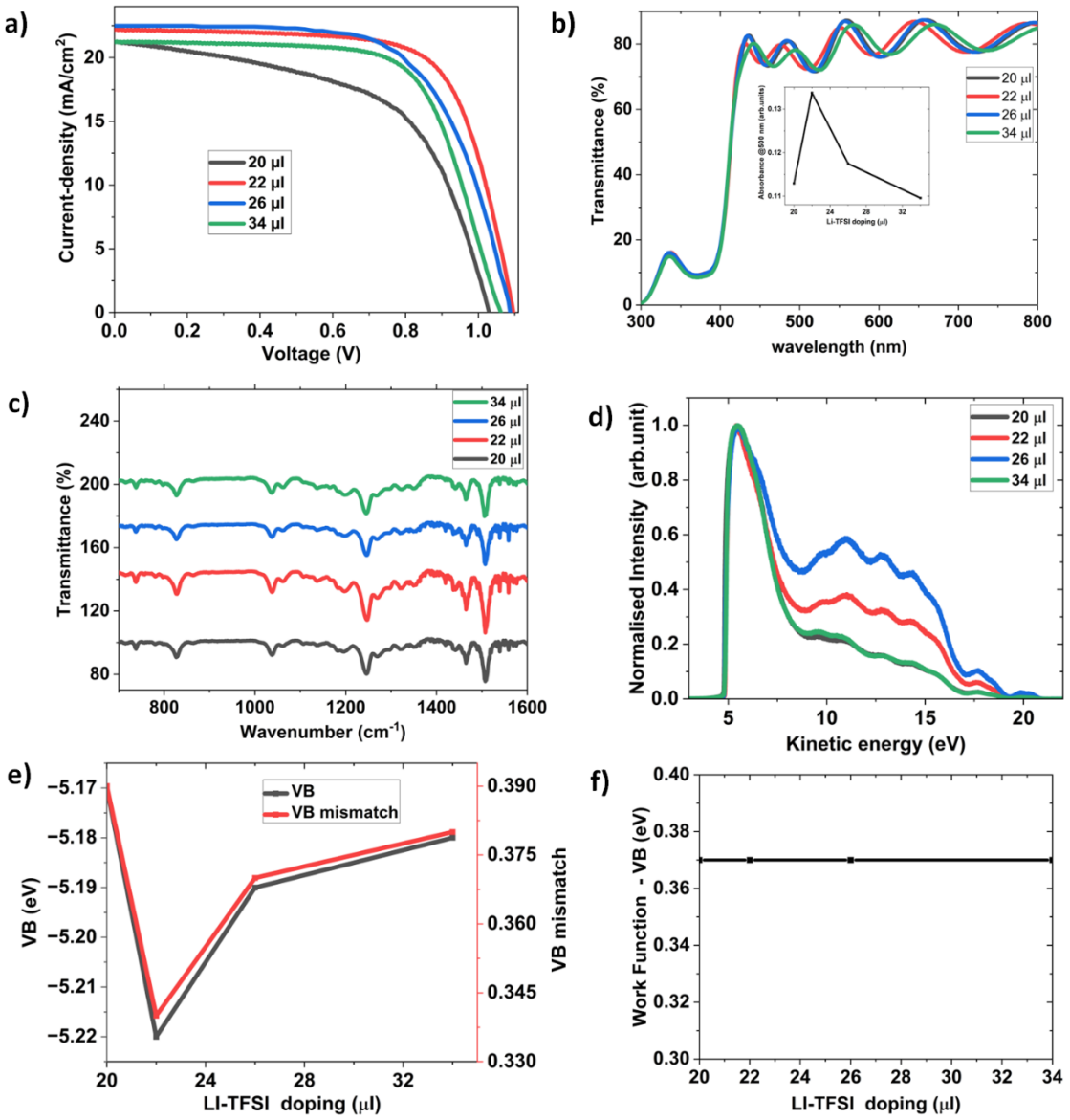

Figure A.1: (a) J-V curve (b) UV-Visible spectra (c) FTIR spectra (d) UPS spectra (e) VB and VB mismatch and (f) difference between work function and VB as a function of Li-TFI proportion in Spiro-OMETAD

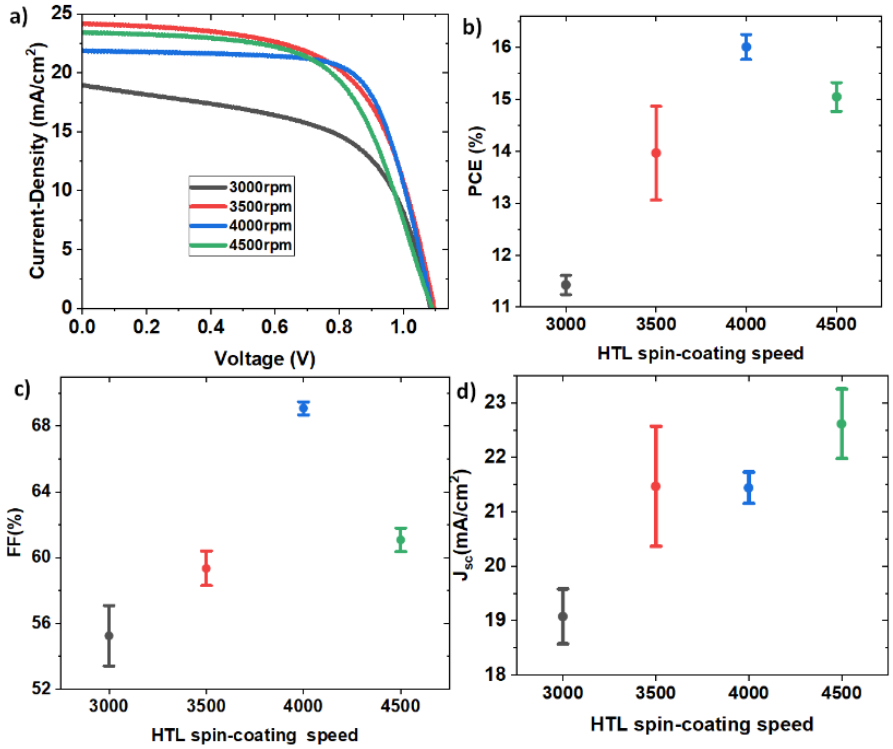

Figure A.2: (a) J-V curves of devices (b) power conversion efficiency (c) fill factor and (d) short-current density as a function of Spiro-OMETAD deposition speed.

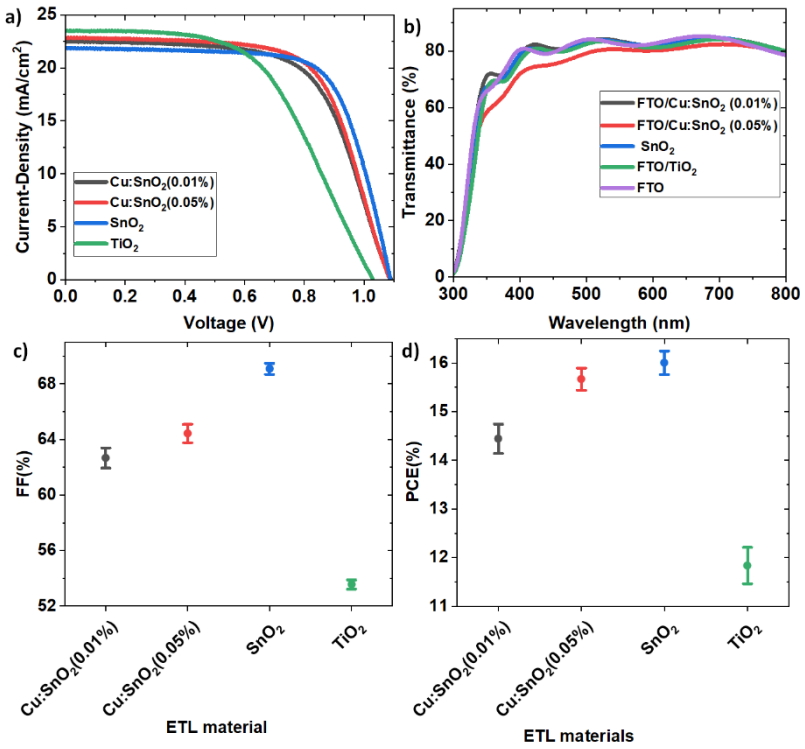

Figure A.3: (a) J-V curves (b) transmittance spectra (c) fill factors and (d) power conversion efficiency of devices as a function of electron transport layers

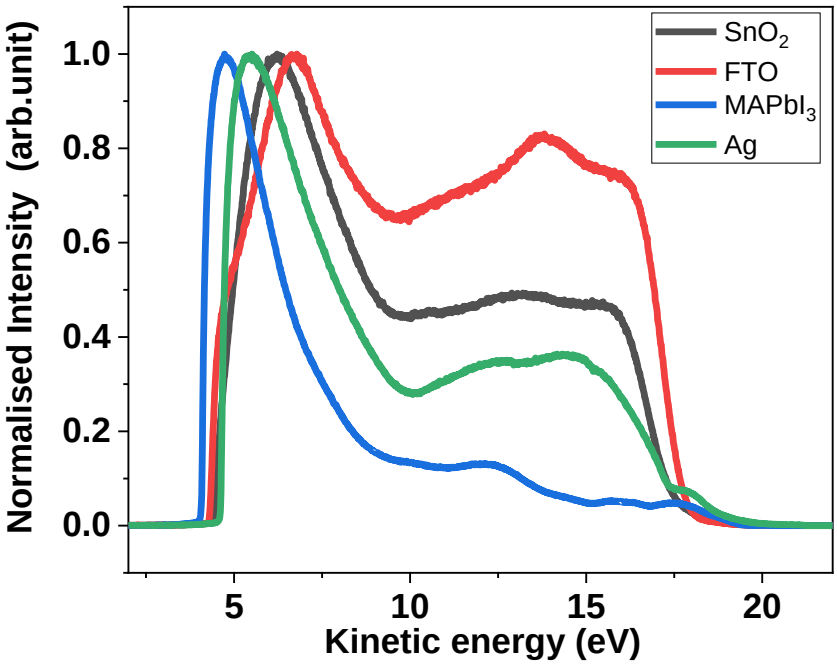

Figure A.4: UPS spectra of SnO_2, FTO, $MAPbI_3$ and Ag. FTO glass substrates were used for SnO_2 and $MAPbI_3$

Appendix B: List of Journal Publications and Conferences

B.1. List of Journal publications

1. Liu, H. et al. π-Conjugated small molecules enable efficient perovskite growth and charge-extraction for high-performance photovoltaic devices. Journal of Power Sources 448, 227420 (2020).

2. Eze, M. C. et al. Optimum silver contact sputtering parameters for efficient perovskite solar cell fabrication. Solar Energy Materials and Solar Cells 230, 111185 (2021).

3. Eze, M. C. et al. Improving the efficiency and stability of in-air fabricated perovskite solar cells using the mixed antisolvent of methyl acetate and chloroform. Organic Electronics 107, 106552 (2022).

4. Effects of sputtering parameters on Morphological, Structural, and electrical properties of silver thin films (Under preparation)

5. Novel CPFS additive process for improving the stability of perovskite solar cells (Under preparation)

B.2. List of conferences

1. Speaking of Science. 3rd May 2018

2. 10th Gregynog 2018- Cardiff School of Engineering PGR Research Conference 26th - 28th June 2018

3 Eze MC, Min G. Understanding the Impact of Libis(trifluoromethanesulfonyl)imide Doping on Spiro-OMeTAD Properties and Perovskite Solar Cell Performance. ICNRE 2020 : XIV. International Conference on Nanomaterials for Renewable Energy (London), 2020, p. 1021.

4. Gregynog Online 2021- Cardiff School of Engineering PGR Research Conference 11th June 2021